

**ANALYTICAL INVESTIGATION OF
FLOW DISTRIBUTION IN HEAT
EXCHANGER MANIFOLDS**

BY

OSMAN KALEEM SIDDIQUI

A Dissertation Presented to the
DEANSHIP OF GRADUATE STUDIES

KING FAHD UNIVERSITY OF PETROLEUM & MINERALS

DHAHRAN, SAUDI ARABIA

In Partial Fulfillment of the
Requirements for the Degree of

DOCTOR OF PHILOSOPHY

In

Mechanical Engineering

MAY, 2018

KING FAHD UNIVERSITY OF PETROLEUM & MINERALS

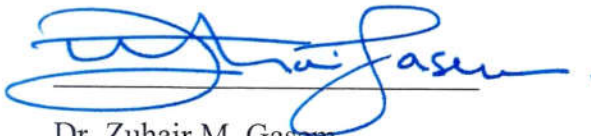
DHAHRAN- 31261, SAUDI ARABIA

DEANSHIP OF GRADUATE STUDIES

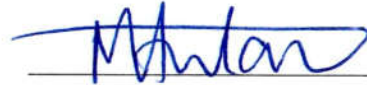
This thesis, written by **Osman Kaleem Siddiqui** under the direction of his thesis advisor and approved by his thesis committee, has been presented to and accepted by the Dean of Graduate Studies, in partial fulfillment of the requirements for the degree of **DOCTOR OF PHILOSOPHY IN MECHANICAL ENGINEERING**.



Dr. Syed M. Zubair
(Advisor)



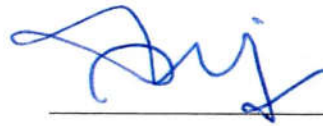
Dr. Zuhair M. Gasem
Department Chairman



Dr. Mohammed A. Antar
(Member)

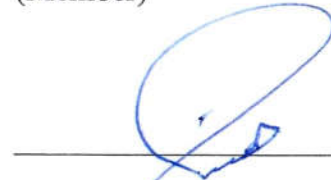


Dr. Salam A. Zummo
Dean of Graduate Studies



Dr. Shahzada Z. Shuja
(Member)

29/8/18
Date



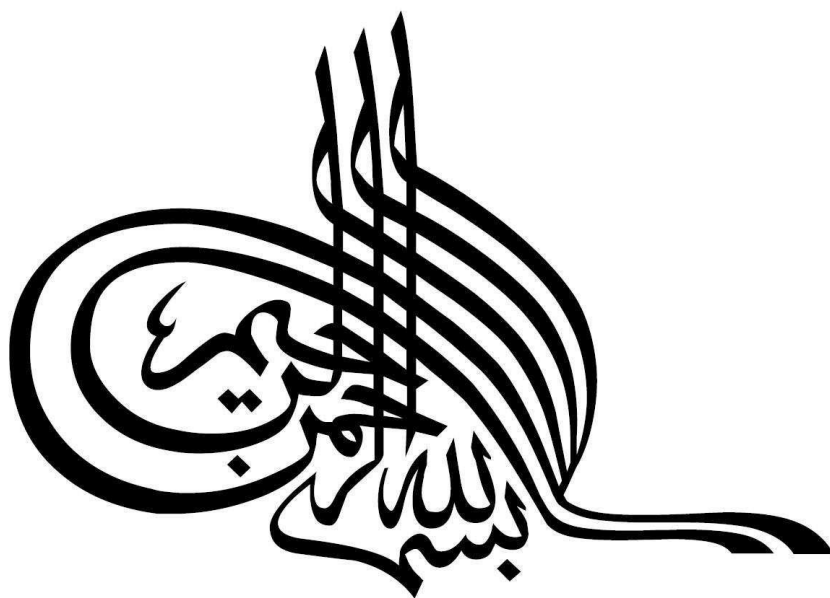
Dr. Haitham M. Bahaidarah
(Member)



Dr. Housam Binous
(Member)

© OSMAN KALEEM SIDDIQUI

2018



*In the name of Allah,
the Most Beneficent,
the Most Merciful*

Dedicated to

My parents, my wife, my daughter, and

all my teachers

ACKNOWLEDGEMENT

In the name of Allah, the Most Gracious, the Most Merciful.

So exalted is He, in whose hand is the realm of all things and to Him you will be returned
(36:83, Al-Quran).

All praise is for Allah, the creator of everything. Thanks are due to Allah, for bestowing me with knowledge and tolerance in completing this work. May Allah accept my efforts and help me in my future endeavors and grant me a place in Paradise, which is the ultimate success.

I would like to acknowledge the facilities, provided by the King Fahd University of Petroleum and Minerals, Dhahran, needed in fulfilling my thesis objectives. I would like to acknowledge the financial support received through the project IN151001, via the Deanship of Scientific Research for this work. In addition, I am grateful to FABLAB Dhahran, and their excellent team, who helped in creating the experimental design.

My deepest gratitude goes to my thesis advisor Dr. Syed Z. Zubair, for all his support, advice and his invaluable time to guide me throughout the duration of my degree. I acknowledge his enduring efforts in developing my professional research skills, through his caring attitude, which are strongly needed for the academic career. I have known very few people so devoted to improving the skills of their students. I find myself honored to work under his supervision and to gain benefit from his distinguished experience.

I am also grateful to Dr. Shahzada Shuja for sharing his experience in numerical software, which improved the ability and quality of my work. I am thankful to Dr. Mohamed A. Antar, Dr. Haitham M. Bahaidarah, and Dr. Housam Binous for their suggestions and guidance in improving my work.

I would like to specially thank Dr. Abdelsalam Al-Sarkhi, for all his help in providing the PIV system for experimental studies. His cooperation was very significant in ensuring the smooth operation of the experimental setup. I am also thankful to Eng. Bahaa Hasan and Eng. Romeo Agua for the technical help in experiments.

I acknowledge the tireless efforts of my parents for guiding me to this status. I am indebted to them for their love and for standing by my side. I also acknowledge the sacrifices made by my wife and daughter during the busy schedule of my degree. They were the source of inspiration for my hard work and kept me pushing through the tough times. Special thanks to my brothers and sister, for sharing all the precious moments of life with me.

I would also like to thank my cousin Dr. Mohsin Siddiqui and his family, in making my stay at KFUPM enjoyable and memorable. I also appreciate all the brotherly support he provided me during the course of my degree.

I also acknowledge my friends Dr. Haider Ali and Dr. Usama Siddiqui for the good times in the department. I am also thankful to all my fellow colleagues and friends who made my time at KFUPM memorable.

TABLE OF CONTENTS

ACKNOWLEDGEMENT.....	v
TABLE OF CONTENTS	vii
LIST OF TABLES	xii
LIST OF FIGURES	xiv
NOMENCLATURE.....	xxii
ABSTRACT (ENGLISH).....	xxv
ملخص الرسالة.....	xxviii
Chapter 1 INTRODUCTION.....	1
1.1 Applications of heat exchangers	2
1.2 Objective	3
1.3 Outline.....	3
Chapter 2 LITERATURE REVIEW	6
2.1 Flow distribution in heat exchanger	6
2.1.1 Manifold design	9
2.1.2 Channel parameters.....	49
2.1.3 Number and location of inlet/outlet ports	57
2.1.4 Perforated plates for secondary flow distribution	66
2.1.5 Flow distribution with two phase flow	75

2.2	Analytical modelling	84
2.3	Literature on split flow and manifold heating	99
2.4	Literature on analogies	102
Chapter 3 GOVERNING EQUATIONS FOR NUMERICAL ANALYSIS.....		110
3.1	Governing equation	110
3.2	Boundary conditions	112
3.3	Assumptions	113
3.4	Thermal-hydraulic parameters	115
3.5	Grid independence study and validation	119
3.5.1	2D Axisymmetric Nusselt number validation.....	121
3.5.2	Grid independence study for the flow distribution manifold.....	129
Chapter 4 SPLIT FLOW WITH MANIFOLD HEATING		132
4.1	Introduction	132
4.2	3D single tube Nusselt number calculation.....	133
4.3	Manifold dividing flow in four smaller tubes	137
4.3.1	Constant surface heat flux.....	138
4.3.2	Constant wall temperature	143
4.4	Single Manifold dividing flow in multiple smaller tubes	145
4.4.1	Constant wall temperature	145

4.4.2	Constant surface heat flux.....	150
4.5	Performance comparison.....	157
Chapter 5	ASSESSMENT OF THERMO-FLUID ANALOGIES	159
5.1	Introduction	159
5.2	Model description.....	160
5.3	Validation	162
5.4	Results and Discussion.....	163
5.4.1	Shear Driven (Couette) Flows	164
5.4.2	Parallel plate flow	166
5.4.3	Internal tube flow	183
5.4.4	Flow over flat plate	195
Chapter 6	FLOW DISTRIBUTION IN CHANNELS – NUMERICAL STUDY 201	
6.1	Model description.....	201
6.2	Flow distribution:	203
6.2.1	U-type arrangement.	203
6.2.2	Z-type arrangement.	208
6.3	Nusselt number and mean temperature calculations	213
6.3.1	U-type Wide manifold	213
6.3.2	Z-type Wide manifold.....	225

6.3.3	Calculation procedures of mean and surface temperatures.....	235
6.4	Chilton- Colburn analogy for the heat exchanger.	239
6.4.1	U-Type	239
6.4.2	Z-Type.....	245
Chapter 7	FLOW DISTRIBUTION IN CHANNELS – EXPERIMENTAL AND ANALYTICAL STUDY	250
7.1	Introduction to Particle image velocimetry	250
7.2	Experimental Setup	252
7.3	Components of PIV system:.....	259
7.3.1	Seeding particles	260
7.3.2	Illumination source (Laser).....	261
7.3.3	High speed camera.....	264
7.3.4	Image processing	266
7.4	Results and discussion.....	268
7.4.1	Velocity profiles comparison.....	269
7.4.2	Flow distribution:.....	271
7.5	Analytical study.....	282
7.5.1	The governing equations.....	282
7.5.2	Results.....	289

Chapter 8	CONCLUSION AND FUTURE WORK	304
8.1	Concluding remarks	304
8.2	Future work directions	308
Appendix A:	UNCERTAINTY ANALYSIS FOR THE PIV MEASUREMENTS.	310
Appendix B:	MATLAB CODES	316
B.1.	Calculation of Nusselt number for non-axisymmetric flows	316
B.2.	Calculation of Nusselt number in channels	320
B.3.	Calculation of Nusselt number in manifold.	321
REFERENCES.....		322
VITA.....		334

LIST OF TABLES

Table 2.1. A summary of the literature on bifurcation type manifold design characteristics.....	18
Table 2.2. A summary of the literature on conservative manifold design characteristics.....	41
Table 2.3. A summary of the literature on channel parameters, affecting flow distribution.	54
Table 2.4. A summary of literature on number and location of inlet/outlet ports, affecting flow distribution.....	64
Table 2.5. A summary of literature on perforated plates for secondary flow distribution, affecting flow distribution.	73
Table 2.6. A summary of literature on flow distribution with two phase flow.....	81
Table 2.7. A summary of the literature on analytical modeling for flow distributing and combing manifolds.....	95
Table 3.1. The input parameters used for the validation.....	119
Table 3.2. The mesh sizes in each axis used for the grid independent study for the flow distribution system.....	131
Table 4.1. Summary of results from the three main cases of split flow.	158
Table 4.2. Comparison of results from the three main cases, with single pipe as base case.....	158
Table 5.1. List of fluids used for analogy assesment, along with their respective properties.....	162
Table 5.2. Comparison of current modeling with the data published in [158].	163
Table 5.3. Data for Couette flow at $Re=1000$ for both constant wall temperature and heat flux.	165
Table 5.4. Data for parallel plate with constant wall temperature.	176
Table 5.5. Data for parallel plate with constant wall flux.....	182
Table 5.6. Data for tube flow with constant wall temperature.....	193
Table 5.7. Data for tube flow with constant wall flux	194
Table 5.8. Data for flat plate with constant wall temperature (2 m from leading edge).....	199
Table 5.9. Data for flat plate with constant wall flux (2 m from leading edge).	199
Table 6.1. The actual and normalized velocities for each channel. U-Type, wide and narrow manifold.....	207
Table 6.2. The actual and normalized velocities for each channel. Z-Type, wide and narrow manifold.....	212

Table 6.3. The mean wall and cross-sectional temperature, U-type narrow manifold and 100 L/hr.	236
Table 6.4. The Nusselt number and Nusselt number star, U-type narrow manifold and 100 L/hr.	237
Table 6.5. The calculated values of mean wall and cross-sectional temperature, U-type narrow manifold and 100 L/hr.	238
Table 6.6. The data for the assessment of Chilton-Colburn analogy for the channels in U-type narrow manifold.....	242
Table 6.7. The data for the assessment of Chilton-Colburn analogy for the U-type narrow manifold.....	244
Table 6.8. The data for the assessment of Chilton-Colburn analogy for the channels in Z-type narrow manifold.	247
Table 6.9. The data for the assessment of Chilton-Colburn analogy for the Z-type narrow manifold.....	249
Table 7.1. Specification of the laser used for illuminating the flow area	265
Table 7.2. Specification of the camera used for the high-speed videos.....	265
Table 7.3. Specification of the lens used with the camera.....	266
Table 7.4. The actual and normalized velocities for each channel. U-Type, wide and narrow manifold for multiple inlet flow rates.....	278
Table 7.5. The actual and normalized velocities for each channel. Z-Type, wide and narrow manifold for multiple inlet flow rates.....	281
Table 7.6. The calculated coefficients of the momentum change and turn loss. U-Type.	287
Table 7.7. The calculated coefficients of the momentum change and turn loss. Z-Type.	288
Table A.1. The characteristics of the sample data for the calculation of channel area uncertainty.....	315

LIST OF FIGURES

Figure 2.1. A cross-section of a catalytic converter, showing flow distribution and convergence [40].	9
Figure 2.2. Schematic for a) conservative and b) bifurcation type manifold structures (Amador et al. [49]).	10
Figure 2.3. Eight flow distributing layouts considered by Alvarado et al. [50]	11
Figure 2.4. The x-velocity contours for a) normal channel b) channels having smaller size inlet and outlet (O-Charoen et al. [52]).	15
Figure 2.5. The schematic of the structural parameters studied by Mohammadi et al. [64]	24
Figure 2.6. The different cases studied by Tonomura et al. [67]	25
Figure 2.7. Three types of triangular manifolds studied by Pan et al. [70]	30
Figure 2.8. The layouts with corresponding velocity distribution in the four cases presented by Vásquez-Alvarez et al. [72]	31
Figure 2.9. The three manifold designs considered by Tong et al. [83].	37
Figure 2.10. Layouts showing a) smaller inlet than the manifold leading to reverse flow in first channel, b) angled inlet, showing recirculation by Tong et al. [83]	38
Figure 2.11. a) Conventional b) modified manifold design by Wasewar et al. [87]	40
Figure 2.12. The three manifold designs considered by Huang et al. [104] for flow uniformity.	59
Figure 2.13. The design layouts for inlet and exit ports studied by Delsman et al. [106] and their corresponding relative standard flow deviation.	61
Figure 2.14. Schematic of the cold-plate, with different inlet configurations. (a) I-arrangement. (b) Z-arrangement. (c) J-arrangement. (d) L-arrangement. (e) Γ -arrangement. (f) Channel configuration of the present simulations. (g) X-Y-Z direction and D_h . Dimensions are shown in mm (Lu and Wang [107]).	61
Figure 2.15. Design layout for the perforations in the secondary header. a) header B is having five while header C has seven openings, b) shows the three-dimensional layout for the secondary header arrangements. (Jiao et al. [111]).	67
Figure 2.16. a) Type B having five holes and b) type C having seven holes in secondary distributor (Zhang and Li [112])	68
Figure 2.17. Layout B and layout C for the perforated baffles used for flow distribution by Wen et al. [115]	70

Figure 2.18. The velocity contours in a) base case and b) secondary baffle (Ismail et al. [119]).....	72
Figure 2.19. a) Parallel b) reverse and c) mixed flow manifold used by Datta and Majumdar [120]	76
Figure 2.20. The secondary cylindrical flue shown with openings at angle θ for upwards vertical flow in channels. The arrangement of with all 16 openings and two configurations for eight opening are also shown. (Marchitto et al. [126]).....	80
Figure 2.21. Momentum balance on the manifold with branching channel (Wang [140]).....	91
Figure 2.22. The three flow field configurations, a) single serpentine with the longest channel length, b) multiple serpentines, with four channels and comparatively smaller channel length, and c) a conventional Z-type arrangement with smaller channel length and a maximum number of channels (Wang and Wang [143]).....	94
Figure 3.1. a) 3D tube flow, illustrating the corresponding boundary conditions, b) the 2D axisymmetric domain used for analysis c) the fine and coarse mesh used for axisymmetric 2D tube flow.	120
Figure 3.2. a) Temperature contours for uniform surface temperature of 500 K, b) temperature and heat flux variation for constant wall surface temperature (similar to [176]).	123
Figure 3.3. Mesh independent test of the axial variation of the Nusselt number for a) constant wall temperature and b) constant heat flux.....	126
Figure 3.4. a) Temperature contours for uniform surface heat flux of 100 W/m^2 and b) the temperature and heat flux variation for constant wall surface heat flux.....	128
Figure 3.5. a) The layout used for the flow distribution system. b) the mesh used for the study (shown near the solid regions.)	130
Figure 3.6. The grid independence test for the flow distribution manifold for eight different combinations.	131
Figure 4.1. Mesh used for three-dimensional tube.	135
Figure 4.2. Temperature contours for a) uniform wall temperature b) uniform surface heat flux.	136
Figure 4.3. Axial Nusselt number variation for full three-dimensional tube.....	137
Figure 4.4. Mesh used for four tube split system.....	138
Figure 4.5. Temperature contours for four tubes subjected to constant surface heat flux a) without manifold heating b) with manifold heating.	141
Figure 4.6. Axial Nusselt number for the tube before and after split for constant heat flux case.....	142

Figure 4.7.	Peripheral Nusselt number variation for the turbulent flow.	142
Figure 4.8.	Temperature contours for four tubes subjected to constant surface temperature a) without manifold heating b) with manifold heating.	144
Figure 4.9.	Axial Nusselt number for the tube before and after split for isothermal wall condition.	145
Figure 4.10.	a) Crossectional view of 37 tube split system, b) Three dimensional view of the 37 tube split system.	147
Figure 4.11.	Temperature contours for a) the channel surface at 500 K with manifold adiabatic, b) all external surfaces at 500 K.	148
Figure 4.12.	Axial Nusselt number variation for the four tubes across the cross-section of 37 tube system a) without manifold isothermal condition b) with manifold isothermal condition.	149
Figure 4.13.	Temperature contours for a) the channel surface at constant surface heat flux with manifold adiabatic, b) all external surfaces at constant surface heat flux.	153
Figure 4.14.	Surface Nusselt number for the four tubes across the cross-section of 37 tube system a) without manifold heating b) with manifold heating....	154
Figure 4.15.	Temperature and heat flux variation for tube 1, after split from manifold.	155
Figure 4.16.	a) Axial Nusselt number variation for the first tube with modified mean temperature. b) Nusselt number variation in the top tube after split.	156
Figure 5.1.	Schematic for the cases under study, a) Couette, b) pipe, c) parallel-plate and d) flat-plate configurations.	161
Figure 5.2.	Plots for the axial development of a) $St \times Pr^{2/3}$, b) Stanton number, c) Nusselt number and d) half of skin friction coefficient. Parallel plate, $Pr=0.74$	168
Figure 5.3.	Plots for the axial development of a) $St \times Pr^{2/3}$, b) Stanton number, c) Nusselt number, and d) half of skin friction coefficient. Parallel plate, $Pr=6.9$	169
Figure 5.4.	Comparison of Reynolds analogy (a, c) and Chilton-Colburn analogy (b, d) when skin friction is based on channel maximum velocity (a, b), or channel average velocity (c, d). Parallel plate, constant wall temperature, $Pr=0.74$	170
Figure 5.5.	Comparison of Reynolds analogy (a, c) and Chilton-Colburn analogy (b, d) when skin friction is based on channel maximum velocity (a, b), or channel average velocity (c, d). Parallel plate, constant wall temperature, $Pr=0.86$	173

Figure 5.6. Comparison of Reynolds analogy (a, c) and Chilton-Colburn analogy (b, d) when skin friction is based on channel maximum velocity (a, b), or channel average velocity (c, d). Parallel plate, constant wall temperature, $Pr=1.0$.	174
Figure 5.7. Comparison of Reynolds analogy (a, c) and Chilton-Colburn analogy (b, d) when skin friction is based on channel maximum velocity (a, b), or channel average velocity (c, d). Parallel plate, constant wall temperature, $Pr=6.9$.	175
Figure 5.8. Comparison of Reynolds analogy (a, c) and Chilton-Colburn analogy (b, d) when skin friction is based on channel maximum velocity (a, b), or channel average velocity (c, d). Parallel plate, constant wall heat flux, $Pr=0.74$.	178
Figure 5.9. Comparison of Reynolds analogy (a, c) and Chilton-Colburn analogy (b, d) when skin friction is based on channel maximum velocity (a, b), or channel average velocity (c, d). Parallel plate, constant wall heat flux, $Pr=0.86$.	179
Figure 5.10. Comparison of Reynolds analogy (a, c) and Chilton-Colburn analogy (b, d) when skin friction is based on channel maximum velocity (a, b), or channel average velocity (c, d). Parallel plate, constant wall heat flux, $Pr=1.0$.	180
Figure 5.11. Comparison of Reynolds analogy (a, c) and Chilton-Colburn analogy (b, d) when skin friction is based on channel maximum velocity (a, b), or channel average velocity (c, d). Parallel plate, constant wall heat flux, $Pr=6.9$.	181
Figure 5.12. Comparison of Reynolds analogy (a, c) and Chilton-Colburn analogy (b, d) when skin friction is based on channel maximum velocity (a, b), or channel average velocity (c, d). Tube flow, constant wall temperature, $Pr=0.74$.	184
Figure 5.13. Comparison of Reynolds analogy (a, c) and Chilton-Colburn analogy (b, d) when skin friction is based on channel maximum velocity (a, b), or channel average velocity (c, d). Tube flow, constant wall temperature, $Pr=0.86$.	185
Figure 5.14. Comparison of Reynolds analogy (a, c) and Chilton-Colburn analogy (b, d) when skin friction is based on channel maximum velocity (a, b), or channel average velocity (c, d). Tube flow, constant wall temperature, $Pr=1.0$.	186
Figure 5.15. Comparison of Reynolds analogy (a, c) and Chilton-Colburn analogy (b, d) when skin friction is based on channel maximum velocity (a, b),	

or channel average velocity (c, d). Tube flow, constant wall temperature, $Pr=6.9$	187
Figure 5.16. Comparison of Reynolds analogy (a, c) and Chilton-Colburn analogy (b, d) when skin friction is based on channel maximum velocity (a, b), or channel average velocity (c, d). Tube flow, constant wall heat flux, $Pr=0.74$	189
Figure 5.17. Comparison of Reynolds analogy (a, c) and Chilton-Colburn analogy (b, d) when skin friction is based on channel maximum velocity (a, b), or channel average velocity (c, d). Tube flow, constant wall heat flux, $Pr=0.86$	190
Figure 5.18. Comparison of Reynolds analogy (a, c) and Chilton-Colburn analogy (b, d) when skin friction is based on channel maximum velocity (a, b), or channel average velocity (c, d). Tube flow, constant wall heat flux, $Pr=1.0$	191
Figure 5.19. Comparison of Reynolds analogy (a, c) and Chilton-Colburn analogy (b, d) when skin friction is based on channel maximum velocity (a, b), or channel average velocity (c, d). Tube flow, constant wall heat flux, $Pr=6.9$	192
Figure 5.20. Plots of (a) the Reynolds analogy and (b) Chilton-Colburn analogy, axial development of (c) Nusselt number, (d) Stanton number, and (e) half of skin friction coefficient. Flat plate, constant wall temperature. ...	197
Figure 5.21. Plots of (a) the Reynolds analogy and (b) Chilton-Colburn analogy, axial development of (c) Nusselt number, (d) Stanton number, and (e) half of skin friction coefficient. Flat plate, constant wall flux.	198
Figure 6.1. The layout used for the flow distribution manifold, a) narrow and b) wide manifold.....	202
Figure 6.2. Velocity distribution comparison among channels between wide and narrow manifold. U-Type and 100 L/hr.....	204
Figure 6.3. Velocity distribution comparison among channels between wide and narrow manifold. U-Type and 200 L/hr.....	205
Figure 6.4. Velocity distribution comparison among channels between wide and narrow manifold. U-Type and 300 L/hr.....	206
Figure 6.5. Velocity distribution comparison among channels between wide and narrow manifold. Z-Type and 100 L/hr.	209
Figure 6.6. Velocity distribution comparison among channels between wide and narrow manifold. Z-Type and 200 L/hr.	210
Figure 6.7. Velocity distribution comparison among channels between wide and narrow manifold. Z-Type and 300 L/hr.	211

Figure 6.8. The a) velocity and b) temperature contour for the case of U-type and 100 L/hr.	216
Figure 6.9. The a) Nusselt number and b) Nusselt number star for the inlet manifold. U-type and 100 L/hr.....	217
Figure 6.10. The a) Nusselt number and b) Nusselt number star for the exit manifold. U-type and 100 L/hr.....	218
Figure 6.11. The a) Nusselt number and b) Nusselt number star for the channels. U-type and 100 L/hr.	219
Figure 6.12. The a) velocity and b) temperature contour for the case of U-type and 200L/hr.	221
Figure 6.13. The a) Nusselt number and b) Nusselt number star for the inlet manifold. U-type and 200 L/hr.....	222
Figure 6.14. The a) Nusselt number and b) Nusselt number star for the exit manifold. U-type and 200 L/hr.....	223
Figure 6.15. The a) Nusselt number and b) Nusselt number star for the channels. U-type and 200 L/hr.	224
Figure 6.16. The a) velocity and b) temperature contour for the case of Z- type and 100L/hr.	226
Figure 6.17. The a) Nusselt number and b) Nusselt number star for the inlet manifold. Z- type and 100 L/hr.	227
Figure 6.18. The a) Nusselt number and b) Nusselt number star for the exit manifold. Z- type and 100 L/hr.	228
Figure 6.19. The a) Nusselt number and b) Nusselt number star for the channels. Z-type and 100 L/hr.	229
Figure 6.20. The a) velocity and b) temperature contour for the case of Z-type and 200L/hr.	231
Figure 6.21. The a) Nusselt number and b) Nusselt number star for the inlet manifold. Z- type and 200 L/hr.	232
Figure 6.22. The a) Nusselt number and b) Nusselt number star for the exit manifold. Z- type and 200 L/hr.	233
Figure 6.23. The a) Nusselt number and b) Nusselt number star for the channels. Z-type and 200 L/hr.	234
Figure 6.24. The comparison of $St \times Pr^{2/3}$ and $C_f/2$ for the channels of U-type normal manifold and 100 L/hr.....	241
Figure 6.25. The comparison of $St \times Pr^{2/3}$ and $C_f/2$ for the inlet and exit manifold sections of the U-type narrow manifold and 100 L/hr.	243
Figure 6.26. The comparison of $St \times Pr^{2/3}$ and $C_f/2$ for the channels of Z-type normal manifold and 100 L/hr.....	246

Figure 6.27. The comparison of $St \times Pr^{2/3}$ and $C_f/2$ for the inlet and exit manifold sections of the Z-type narrow manifold and 100 L/hr.....	248
Figure 7.1. The mechanism of 2D2C PIV https://www.dantecdynamics.com/measurement-principles-of-piv	251
Figure 7.2. Experimental setup for flow distributing manifolds, utilizing PIV.....	253
Figure 7.3. The arrangement of manifold, laser, camera, and pump.	254
Figure 7.4. The pump, and two valve arrangement to control the flow rate.....	255
Figure 7.5. The inlet tank, designed to provide uniform inlet condition.	255
Figure 7.6. The flow distribution system, with options for both Z and U type studies.....	256
Figure 7.7. The laser illuminating the inlet section for velocity measurements	256
Figure 7.8. The design being cut using the CNC machine, the grooves were be fitted with spacers, to create channels.....	258
Figure 7.9. The laser light source (Raypower 2000). Specification are given in Table 7.1.....	262
Figure 7.10. An image of the illumination provided by the laser.	263
Figure 7.11. The image processing step in Dantec Dynamics	268
Figure 7.12. The velocity profile comparison for the numerical modelling and the experimental ones. a) for channel 10 and b) for channel 9. U- type and 100 L/hr.	270
Figure 7.13. Experimental comparison of the velocity distribution between channels for flow rate of 100 L/hr and multiple configurations.	273
Figure 7.14. Experimental comparison of the velocity distribution between channels for flow rate of 200 L/hr and multiple configurations.	274
Figure 7.15. Experimental comparison of the velocity distribution between channels for flow rate of 300 L/hr and multiple configurations.	275
Figure 7.16. Normalized velocity comparisons for difference flow rates for a) wide and b) narrow manifold for U-type.	277
Figure 7.17. Normalized velocity comparisons for difference flow rates for a) wide and b) narrow manifold for Z-type.....	280
Figure 7.18 Comparison between numerical, analytical, and experimental models for the flow rate distribution in the channels.. U-type, wide manifold, 100 L/hr.	291
Figure 7.19. Comparison between analytical and numerical models for the flow rate distribution in the channels. U-type, wide manifold, 200 L/hr.	292
Figure 7.20. Comparison between numerical, analytical, and experimental models for the flow rate distribution in the channels. U-type, wide manifold, 300 L/hr.	293

Figure 7.21. Comparison between numerical, analytical, and experimental models for the flow rate distribution in the channels. U-type, normal manifold, 100 L/hr.	294
Figure 7.22. Comparison between numerical, analytical, and experimental models for the flow rate distribution in the channels. U-type, normal manifold, 200 L/hr.	295
Figure 7.23. Comparison between numerical, analytical, and experimental models for the flow rate distribution in the channels. U-type, normal manifold, 300 L/hr.	296
Figure 7.24. Comparison between numerical, analytical, and experimental models for the flow rate distribution in the channels. Z-type, wide manifold, 100 L/hr.	298
Figure 7.25. Comparison between numerical, analytical, and experimental models for the flow rate distribution in the channels. Z-type, wide manifold, 200 L/hr.	299
Figure 7.26. Comparison between numerical, analytical, and experimental models for the flow rate distribution in the channels. Z-type, wide manifold, 300 L/hr.	300
Figure 7.27. Comparison between numerical, analytical, and experimental models for the flow rate distribution in the channels. Z-type, narrow manifold, 100 L/hr.	301
Figure 7.28. Comparison between numerical, analytical, and experimental models for the flow rate distribution in the channels. Z-type, narrow manifold, 200 L/hr.	302
Figure 7.29. Comparison between numerical, analytical, and experimental models for the flow rate distribution in the channels. Z-type, narrow manifold, 300 L/hr.	303

NOMENCLATURE

A	area (m^2)
C_p	specific heat capacity ($\text{kJ kg}^{-1} \text{K}^{-1}$)
C_f	skin friction coefficient (-)
C_1, C_2	constants for turbulent model Eq.(3.6)
d	hydraulic diameter (m)
f	friction factor
G_k	turbulence kinetic energy generation due to the mean velocity gradients
h	heat transfer coefficient ($\text{W m}^{-2} \text{K}^{-1}$)
k	thermal conductivity ($\text{W m}^{-1} \text{K}^{-1}$)
K	turbulence kinetic energy
\dot{m}	mass flow rate (kg s^{-1})
n	direction normal to the wall
N	number of channels
Nu	Nusselt number (-)
p	pressure (Pa)

Pr	Prandtl number (-)
q''	heat flux ($W\ m^{-2}$)
Q	volumetric flow rate ($m^3\ s^{-1}$)
Re	Reynolds number
St	Stanton number (-)
T	temperature (K)
u	velocity ($m\ s^{-1}$)
w	normalized manifold velocity (-)
x	manifold axial distance

Subscripts

c	channel
e	exit
in	inlet
∞	infinity
m	mean
ε	rate of dissipation
f	fluid

t turbulent

w wall

Greek

β momentum change

ε rate of dissipation ($\text{m}^2 \text{s}^{-3}$)

μ fluid viscosity ($\text{kg m}^{-1} \text{s}^{-1}$)

ρ density (kg m^{-3})

ϕ a general variable

Abbreviations

CFD computational fluid dynamics

MWA mass weighted average

NTU number of transfer units

PIV particle image velocimetry

PV photovoltaic

ABSTRACT (ENGLISH)

Full Name : Osman Kaleem Siddiqui

Thesis Title: : Analytical investigation of flow distribution in heat exchanger manifolds

Major Field : MECHANICAL ENGINEERING

Date of Degree : May 2018

The thermal performance of a plate type heat exchanger is directly linked with the flow distribution in the channels. The channels increase the contact surface area thus improving the thermal performance, however with an accompanied pressure loss due to the split and resulting smaller hydraulic diameter. Flow maldistribution reduces the performance, which can be evaluated based on the peripheral Nusselt number. In this regard, three layouts are considered with single tube as reference. Both constant wall temperature and wall flux conditions have been studied, with additional consideration of the manifold surface heating. It is found that for a combined manifold and tube heating system, non-axisymmetric flow exists in the smaller tubes leading to negative Nusselt number on some surface points. To accommodate such flow behavior, a procedure for proper calculation of mean temperature for Nusselt number is discussed, based on the thermal axis at the minimum temperature for each cross-section. The results for the single tube were validated

with the literature, and it was found that the unrealistic negative values for the Nusselt number no longer exists.

The classical Reynolds and Chilton-Colburn analogies are evaluated for four flow configurations in addition to plate-type heat exchangers. The numerical results show that these analogies should be used with proper attention as an excellent agreement was found for parallel flow and flat plate, while Couette flow and heat exchanger showed large differences.

Two variations of the manifold, wide and narrow are studied using three models, namely, numerical, experimental and analytical. The numerical results show the velocity and temperature distribution, when the heat exchanger is subjected to a flux of 1 kW/m^2 and water as the working fluid. The peripheral Nusselt number contours are also presented, to ascertain the thermal performance of the manifolds and each channel.

The numerical results show that for the U- type design, more flow is found in the initial channels, while for Z-type, more flow is towards the latter channels. By increasing the manifold width, it is found that the flow is more uniformly distributed in comparison to the smaller width. Higher flow rate improves distribution for U-type while it degrades the performance for Z-type. For the experimental study, it has been found that the use of

Particle Image Velocimetry (PIV) system is an excellent tool to measure the velocities in the heat exchanger. The results are in a good agreement for the velocity profiles and flow distribution in the channels. Furthermore, the analytical model is also tested with the calculated flow coefficients. It has been found that the models are in an excellent agreement with the numerical results, and the impact of turn loss coefficient has been found to be significantly affecting the flow distribution.

ملخص الرسالة

الاسم الكامل:

عثمان كليم صديقي

عنوان الرسالة:

دراسة تحليلية لتوزيع التدفق في موزعات المبادلات الحرارية

التخصص:

الهندسة الميكانيكية

تاريخ الدرجة العلمية:

مايو، ٢٠١٨

يرتبط الأداء الحراري للمبادلات الحرارية الصفائحية بشكل مباشر مع توزيع تدفق الموائع في القنوات. إن زيادة مساحة أسطح القنوات الملامسة للمائع تؤدي بطبيعتها الى تحسين الأداء الحراري. ولكن هذا التحسن يصاحبه فقدان بضغط التدفق نتيجة الانقسام الى قنوات ذات قطر هيدروولوكي أصغر. يؤدي سوء توزيع التدفق الى تقليل الأداء الذي يمكن تقييمه على أساس رقم نسلت المحيطي. لقد تمت دراسة كل من درجة الحرارة والتدفق الحراري الثابتين كل على حدة على جدار القنوات، بالإضافة الى تسخين سطح الموزع. ووجد ان هناك تدفق غير محوري على الانابيب الصغيرة في منظومة الموزع والانابيب المسخنة، والذي بدوره يؤدي إلى قيم سالبة لرقم نسلت المحيطي في بعض الأماكن السطحية. لاستيعاب هذا السلوك تم تصحيح حساب درجة الحرارة المتوسطة لرقم نسلت بناءً على المحور الحراري عند أقل درجة حرارة في كل مقطع عرضي، وتم التحقق من صحة النتائج على أنبوب منفرد تم دراسته من قبل، وتبين أن القيم السالبة لرقم نسلت لم تعد موجودة.

لقد تم تقييم متشابهة رقم رينولدز ورقم تشيلتون-كولبرن الكلاسيكية لأربعة تكوينات أساسية للتدفق بالإضافة إلى المبادلات الحرارية الصفائحية، وظهرت النتائج العددية أنه يجب استخدام هذه المتشابهات مع الاخذ بعين الاعتبار الى التوافق الممتاز للتدفق المتوازي والصفائح المسطحة، في حين ان تدفق كويتي والمبادل الحراري اظهروا اختلافات كبيرة.

تمت دراسة اثنين من الموزعات، احدهما عريض والاخر ضيق بواسطة ثلاثة نماذج كالتالي: نموذج عددي ونموذج تجريبي و نموذج تحليلي. أظهرت نتائج النموذج العددي توزيع سرعة الماء المتدفق وحرارته عندما يتعرض المبادل الحراري لتدفق ١ كيلو واط لكل متر مربع. كما تم استعراض كنتورات رقم نسلت المحيطي لتحديد الأداء الحراري للموزع ولكل قناة.

كشفت النتائج الخاصة بالتصميم ذات النوع U انه يوجد المزيد من التدفق في القنوات الأولية، بينما التصميم ذات النوع Z أظهر تدفق أكثر نحو القنوات الأخيرة. كما أظهرت الموزعات العريضة تدفق أكثر انتظاماً من الموزعات الضيقة. ومن خلال زيادة عرض الموزع، تبين أن التدفق يتوزع بشكل أكثر انتظاماً مقارنة مع أنبوب بعرض أصغر، وأظهر معدل التدفق العالي توزيع أكثر انتظاماً في التصميم من النوع U بينما ينخفض الانتظام في تصميم من النوع Z. رجوعاً للدراسة التجريبية، فقد وجد أن استخدام نظام PIV (قياس السرعة باستخدام صور الجسيمات) مناسب جداً لقياس السرعات داخل المبادلات الحرارية. وكانت النتائج في توافق جيد مع توزيع السرعة وتوزيع التدفق في القنوات. أيضاً تم اختبار النموذج التحليلي باستخدام معاملات التدفق المقدرة مسبقاً. وأظهرت نتائج النماذج التحليلية توافق ممتاز مع نتائج النموذج العددي، وقد لوحظ أن معامل الفقدان عند الانعطاف له تأثير كبير في توزيع التدفق..

Chapter 1

INTRODUCTION

A heat exchanger is used when the thermal potential of one medium is needed to be transferred to another medium, with and without the direct interaction or mixing between them. The ability to transfer heat strongly depends on the contact area between the two fluids, the larger area results in more heat transfer. The fluids are typically transferred by a piping network of relatively smaller size, upon entering the heat exchanger it has to be distributed within the heat exchanger so as to increase its contact surface area. Particular care is needed to be focused on this fluid distribution, as the flow rate through each fluid path of the heat exchanger has considerable effects on its performance with regards to the pressure drop and heat transfer [1,2]. The pressure drop in the heat exchanger manifold and channels can be measured experimentally [3], thus providing the information about the flow distribution characteristics.

By making flow uniform throughout the device, it can be ensured that there is no potential area for development of a hot spot. Furthermore, constant mass flow rate throughout the device ensures that all sections of the heat exchanger will provide uniform cooling and the average surface temperature remains low. The distribution of flow depends on the pressure losses associated with each fluid path with the fluid taking the path of least resistance.

Thus, it is important to ensure that all paths have the same resistance so that flow will get uniformly distributed across all the channels. To make flow uniform, the design of the inlet and outlet header is of the highest significance, as its profile will determine how the flow gets distributed.

The parameters that would govern the flow distribution and heat transfer characteristics of heat exchangers include manifold layout and dimensions, channel dimensions, channel-to-manifold area ratio, the aspect ratio of the manifold-to-channels, the phase of the fluid, Reynolds number and secondary distributor systems. These parameters have been studied by numerous authors to improve our understanding of their impact on the thermal-hydraulic performance of micro-channel heat exchangers.

1.1 Applications of heat exchangers

The application of plate type flow distribution device includes cooling of different components like electronic integrated circuits and photovoltaic panels where one side of the channel is exposed to a heated surface. A uniform flow would result in uniform cooling and equally distributed temperature throughout the surface. Typically, higher temperatures lead to performance degradation, hence cooling would enhance the performance. These type of heat exchangers are also used in catalytic converters that need to increase the contact area for the reaction to take place.

1.2 Objective

The objectives of the work done in this thesis are summarized below.

- i. To thoroughly review the literature on the topic of flat plate heat exchangers, with specific attention to the flow and temperature distribution.
- ii. To check the validity of the frictional and heat transfer analogies for various flow configurations.
- iii. To understand the split flow problem, with heating of the manifold.
- iv. To provide a numerical solution of the flow and heat distribution types of U- and Z- layouts.
- v. To validate these designs experimentally, with the use of particle image velocimetry.
- vi. To implement the available analytical model of flow distribution, with proper calculation of governing coefficients.

1.3 Outline

The outline of the work done in this thesis is as follows:

Chapter 1 gives an introduction to the subject matter. It describes the utility of the flow distribution manifolds. The objectives are also defined in this chapter.

Chapter 2 provides a comprehensive literature review into the flow distribution manifolds. The work has been focused on identifying key design parameters that govern the flow distribution, and literature that discusses those key points is presented.

Chapter 3 discusses the governing equation for the numerical solution of flow and energy equations. The equations, assumptions, the thermal-hydraulic parameters, and grid independent studies are presented. The Nusselt numbers are also validated with literature.

Chapter 4 presents the calculation of the Nusselt number for axisymmetric and non-axisymmetric cases. A single tube dividing into multiple tubes is analyzed, where a negative Nusselt number was found. The strategy for dealing with such cases is discussed in detail.

Chapter 5 provides the assessment of heat and momentum analogies for various flow channel arrangements. The skin friction is defined based on either maximum or average velocity and comparisons are made to give a guideline for each case. Some cases are fitting perfectly, while others have shown significant variations.

Chapter 6 deals with the numerical modeling used for the solution of flow distributing manifold. The velocity and temperature distributions are shown, along with the Nusselt number variations, and a newly defined Nusselt number star. The surface plots for a Nusselt number at the inlet and outlet sections of the manifold along with the channels is presented. This approach will assist in the evaluation of the surface and mean temperatures for the whole manifold. In addition, the thermo-fluid analogy is also presented for the inlet and exit manifold along with the channels.

Chapter 7 presents the experimental and analytical study of flow distribution. In the first section, the velocity is measured in channels using Particle Image Velocimetry (PIV). The narrow and wide manifolds are fabricated using CNC and laser cutting machines. The results are compared with the numerical. The second section, deal with the analytical model for the flow distribution manifold. The flow governing coefficients calculated from the previous numerical modelling are presented. The flow distribution results are analyzed with the use of those coefficients.

Chapter 8 presents the conclusion to the work done in this thesis. The scope of future work in this field is also discussed.

Appendix A is related to the uncertainty analysis for the experimental velocity measurements.

Appendix B presents the MATLAB codes and functions used for the Nusselt number calculations.

Chapter 2

LITERATURE REVIEW

The review of literature consists of four sections. First section presents the work done on the flow distribution in manifolds. The second section deals with the analytical models used for the flow distribution. Third section involves the literature on the split flow and manifold heating cases. The fourth section presents the literature on the fluid and heat transfer analogies.

2.1 Flow distribution in heat exchanger

The application of flow distribution manifolds in heat sink has received significant focus to increase the amount of heat that can be dissipated from the heat sinks coupled with electronic components. Knight et al. [4] provided an optimization of the heat sink incorporating microchannels. The objective was to reduce the thermal resistance of the heat sink to enable maximum heat transfer. The parameters of Reynolds number, aspect ratio of the channels and fin-to-width ratio were studied. It was found that if the flowrate is low i.e. laminar within the channels, the resulting pressure drop is small along with reduced thermal resistance. If the pressure drop increases in the flow domain, then there exists an optimal value of thermal resistance which lies in the turbulent region of Reynolds number. An optimization was obtained for the water cooled heat sinks by Goldberg [5], Tuckerman and Pease[6] and Philips [7]. The design optimization leads to a reduction in the thermal

resistance within the range of 10-35% for these heat sinks. Some similar applications to the heat sink are given in [8–15].

In addition to heat sinks, flow distributing manifolds are also being utilized in cooling of solar photovoltaic (PV) panels or solar hybrid photovoltaic thermal (PVT) systems, where cooling of PV panels increases the efficiency [16–25] while the heated fluid is utilized in domestic heating applications [26–33]. A review of cooling the PV panels to reduce the negative impact of higher temperature on the performance was presented by Bahaidarah et al. [34]. Chiou [35] studied the thermal performance variation of a solar collector with non-uniform flow distribution, keeping in view that the uniform flow distribution may not be feasible due to economic and space constraints. A numerical method was developed to study the effect of this non-uniformity on thermal performance. In this regard, a flow non-uniformity parameter was introduced to compare the flow distribution about the mean value. A relation was found existing between the flow non-uniformity parameter and the collector efficiency deterioration, which is expected to be helpful in reducing localized heat concentration. In the study, different collector designs and operating conditions to determine the collector efficiency based on ten flow channels, numbered 1-10 from left side. The first flow model had maximum flow in tube 1, decreasing towards tube 10. The second model had maximum flow in tubes 3 and 4 while decreasing in tubes on both sides. The third model had maximum flow in central tubes 5 and 6, leading to symmetrically decreasing distribution while the fourth model had some tubes plugged to have no flow in them representing the most severe form of non-uniformity. The study showed that the deterioration in collector efficiency was from 2% to 20% for the above flow distribution

models, for flow non-uniformity parameter in between 0.01 and 0.3. Some further research efforts have also been published in the literature for photovoltaic and hybrid thermal collectors [35–39].

Another application of flow distributing systems is for catalytic converters which contain oxidation and reduction agents to reduce the toxic emissions from engine to a lesser toxic form. They utilize flow distributing systems, where the objective is to increase the contact reaction area. A cross-sectional view of the catalytic converter is shown in Figure 2.1, where it can be seen that the inlet manifold incorporates a diffuser to distribute the exhaust gasses followed by a ceramic monolith core that hosts the catalyst to react with the exhaust gasses. Towards the end, a converging manifold is used to connect the exhaust pipe. Agrawal et al. [40] studied the effect of flow maldistribution on the effectiveness of catalytic converter. They compared 85 channels with the reduced scale of only 21 channels and found good agreement for constant velocities. Flow expansion in manifold deteriorates flow distribution while friction in channels improves the flow distribution. Up to 20% deviation was discovered in the central channel as compared to side channels at high Reynolds number. It was found that conversion rates also reduce as the flow maldistribution increases; where the single channel models over-predict the actual conversion rate. The consideration of energy effects improved the flow distribution due to density changes as heat is lost to the surroundings. Some further studies on performance enhancement by improving flow distribution in catalytic converters are given in [41–47].

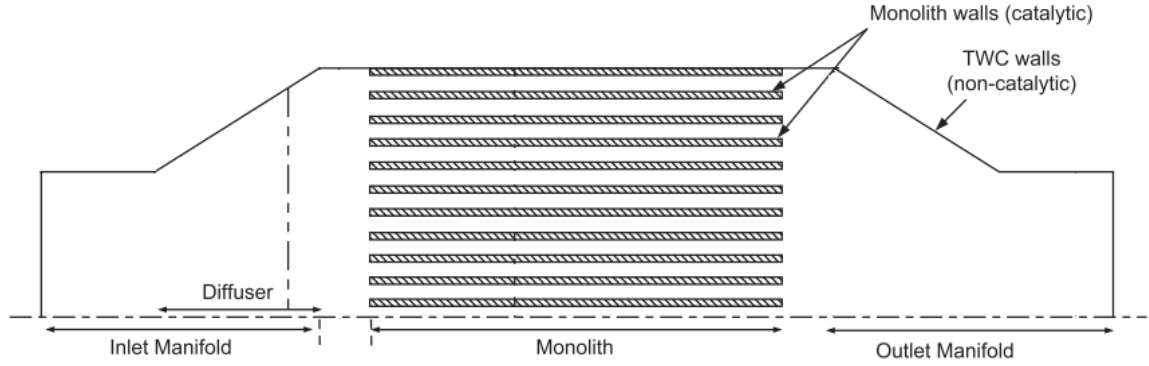


Figure 2.1. A cross-section of a catalytic converter, showing flow distribution and convergence [40].

Various efforts have been put forward by some authors suggesting methods of analytical, numerical and experimental nature for ensuring uniform flow distribution and optimization of heat exchangers so as to keep the losses low with high effectiveness. These research efforts are summarized in Tables 2.1 to 2.7, with detailed discussion in the following sections. The detailed discussion is focused on the manifold design, channel design, location of inlet and outlet connections to the heat exchanger and the use of secondary header. In addition two-phase flow behavior and the analytical modeling has also been discussed in detail.

2.1.1 Manifold design

The basic manifold designs are conservative and bifurcation type, as shown in Figure 2.2. In a conservative design, there is a single manifold region directly connected to the channels distributing the flow. The dashed line in the manifold shows an alternate for improving flow uniformity by making the manifold non-uniform or triangular. In

bifurcation type, the flow from the inlet is divided into two streams; each is then further subdivided into two more till the number of divisions matches the number of channels. This layout is inspired by nature and a detailed description has been given by Bejan and Errera [48], mentioning the presence of this design in trees, cracks in the dry ground, blood circulation system, and lungs, leading to flow uniformity with low flow resistance.

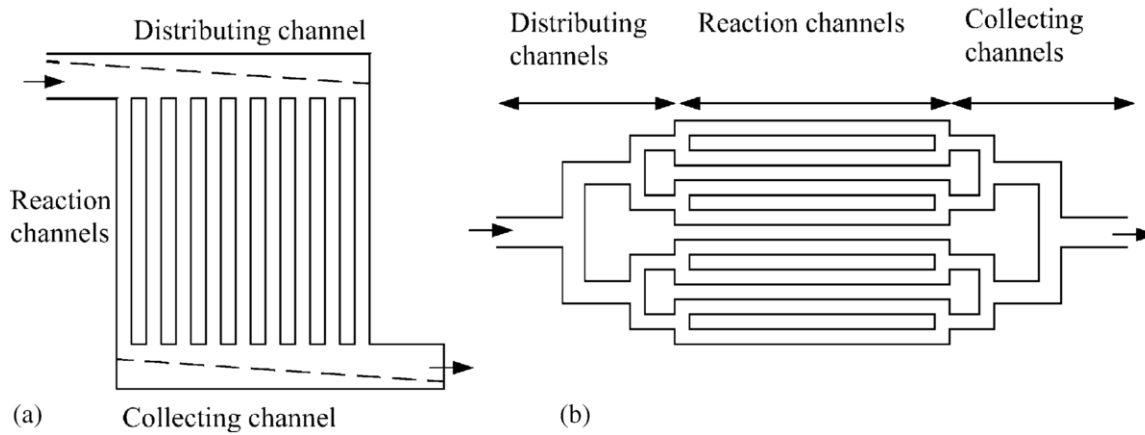


Figure 2.2. Schematic for a) conservative and b) bifurcation type manifold structures (Amador et al. [49]).

2.1.1.1 Bifurcation type manifold

Bifurcation type manifold is a nature-inspired design for flow distribution and is found to be an efficient way of distributing flow in multiples channels. A summary on bifurcation manifolds is given in Table 2.1, with a detailed discussion in the following paragraphs.

Alvarado et al. [50] studied eight different layouts including serpentine, parallel and bifurcation flow patterns for a microchannel based heat sink (Figure 2.3). The numerical modeling was done using ANSYS Fluent [51], a commercial software for numerical solution of the basic mass, momentum and energy equations, resulting in information about

the flow distribution in channels, pumping power needed as well as the uniformity of surface temperature. These parameters are useful in quantifying the performance of such heat exchangers. The findings revealed that the distributor/bifurcation type of manifold results in the lowest pressure loss and surface temperature difference. These parameters make this type manifold suitable for heat sink applications where liquid based cooling is needed.

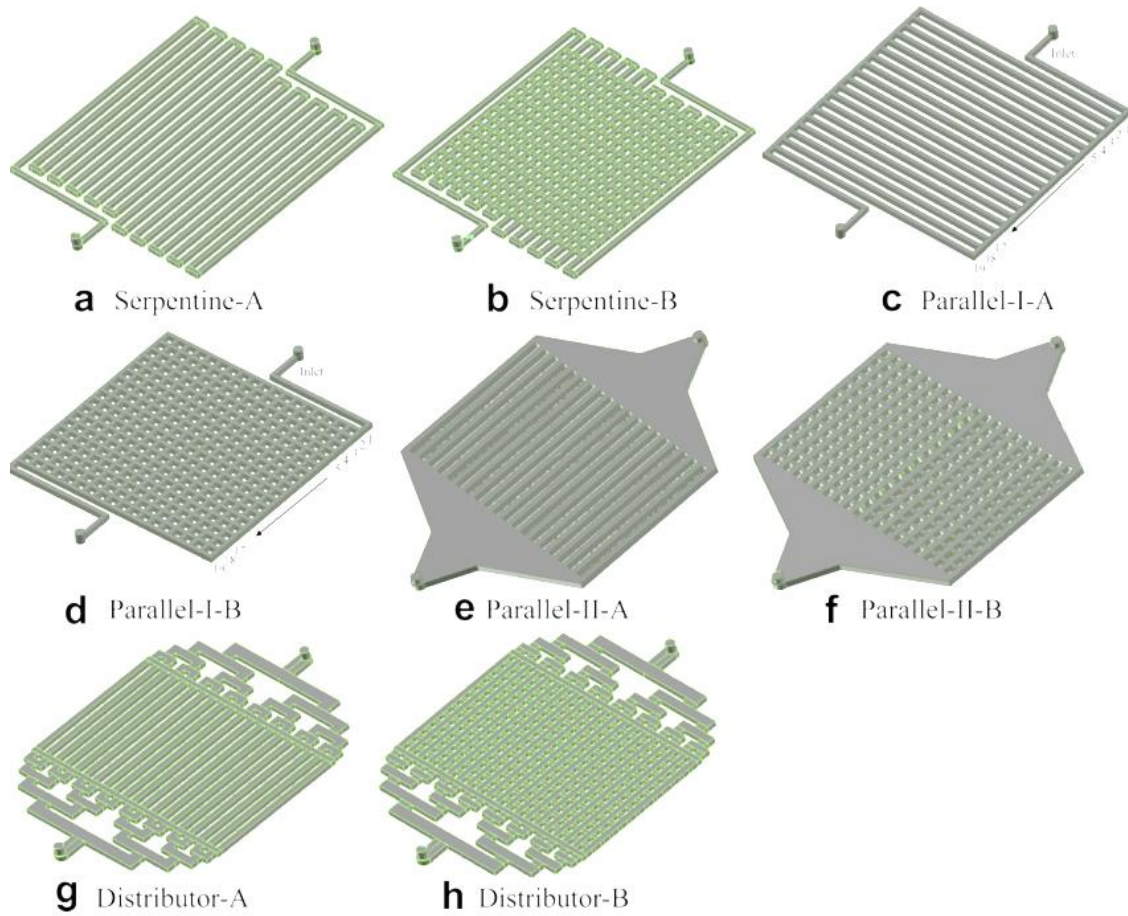


Figure 2.3. Eight flow distributing layouts considered by Alvarado et al. [50]

Another type of layout for bifurcation manifold with inlet and outlet channels parallel to each other is presented by O-Charoen et al. [52], where four inlet and four outlet channels

are studied leading to a total of eight channels. Computational Fluid Dynamics (CFD) software was used for computing the results and had two experimental arrangements for validation. It was found that the alternating channels have flow maldistribution. Figure 2.4(a) shows the layout along the channel axis (x-coordinate) velocity, where it can be seen that near the entry and exit, flow is relatively symmetric while at the middle section stagnation or reverse flow can occur. This is due to the fact that the manifold and tube are of the same size, which causes the majority of flow directed in the first channels while the remaining would just flow towards the ends as it gains momentum in the manifold. Figure 2.4 (b) shows a modification where the channels have smaller inlet and outlet, which increases the pressure loss and improves the flow distribution by reducing the impact of pressure loss in the manifold as compared to that in the channel. It was further revealed that more flow uniformity was obtained when length of the reactor is increased with a decrease in width and depth while increasing the channel width and depth.

A design similar to distributor layout in Figure 2.3 was examined by Saber et al. [53] by terming it as a multi-scale flow distribution. The development of large-scale network of microchannels for application to macro-scaled applications was analyzed by a basic layout and then creating networks with laminar flow and constant temperature operation. The two-scale configuration resulted in lower flow maldistribution and pressure loss, with a limit on the number of channels for each segment for the least pressure loss. The connection between different sections of the geometries was given special attention, as the proper connection can result in uniform flow for any number of sections. Furthermore, increasing the number of flow scales leads to better flow distribution. An additional contribution was

published by Commenge et al. [54] including design charts developed to design a multi-scale network based on a two-scale network. The model was based on flow resistances at every scale and step-by-step procedure that allows calculation of the global parameters, thus assisting in design and evaluation of multiple systems to find the optimum configuration.

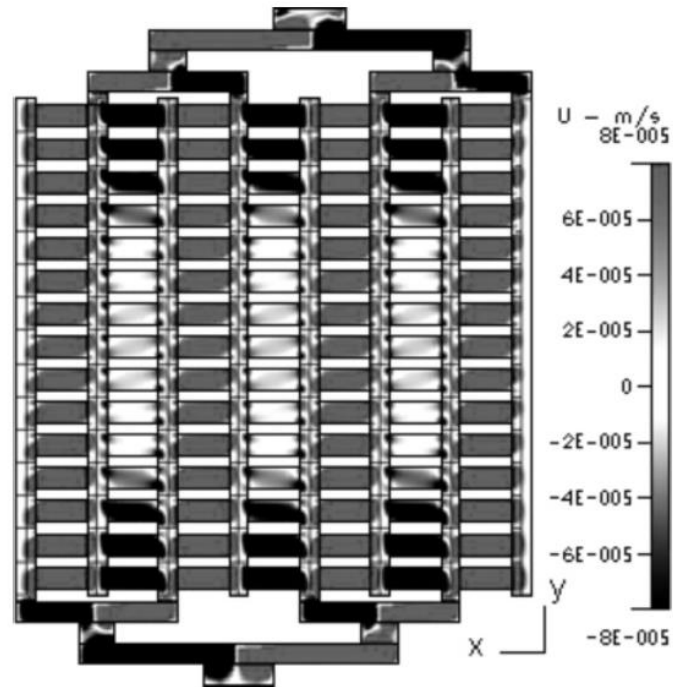
A comparison between the two manifold arrangements i.e. conservative and bifurcation was made by Amador et al. [49] by modeling of the geometries as electrical resistances forming a network and then validated with finite element simulated results. The model has been found to apply to both rectangular and circular cross-sections for the channels, while using two approaches to attain uniform distribution. First, the usage of larger uniform cross-section for the manifold to minimize the pressure drop. Second, the use of variable sized channels was used to make the pressure drop uniform for all the channels. The results show that for lower Reynolds number application, the first method is suitable, while for non-uniform depth cases, the second method is recommended. Also, if the Reynolds number is high, the bifurcation type of manifold is suitable. For the impact of manufacturing tolerance, an assumed design tolerance of 5% was considered by the authors. It was found that for the uniform manifold design, the impact of manufacturing tolerance is not very significant, an increase in non-uniformity by five times results in just 0.5% change in standard deviation. For smaller hydraulic diameter non-linear manifold, the change in standard deviation is from 19.19% to 25.12%, while for large diameter manifold the change is from 1.90% to 5.43%. For 128 channel optimized linear manifold shape, the flow standard deviation was 38.88% without the manufacturing tolerance, it

increased to 65.44% when the design tolerance is accounted for. For the bifurcation type, the impact of design tolerance is small. Their analysis of design tolerance suggested that constant manifold should be used for large or unknown manufacturing tolerances especially in cases when channel blockages are also expected. For smaller manufacturing tolerances, a variable manifold design was suggested.

In addition, Nielson et al. [55] showed the significance of uniform/non-uniform channel size on the performance when subjected to flow maldistribution. It was found that the impact of maldistribution is more amplified when there are non-homogeneous channels. For low thermal conductivities, the impact of non-uniformity is significant, due to absence of conduction between channels. At higher thermal conductivities, the effect of maldistribution is reduced as conduction contributes significantly to heat transfer.

To study the effect of rounded corners and circular bifurcation channels, Liu et al. [56] studied three configurations with a base 90° bend in bifurcation design. The modification to this base case was to round off the bends while the second modification was to make the channels circular. The results showed that a longer length of port after a bend assists in flow uniformity. Also, the channel length-to-width ratio should be higher for upstream channels as they have higher Reynolds number, with Reynolds number decreasing downstream due to the split. Finally, it was found that rounded corner design was the best design for flow distribution, with length-to-diameter ratio of five for all segments.

a)



b)

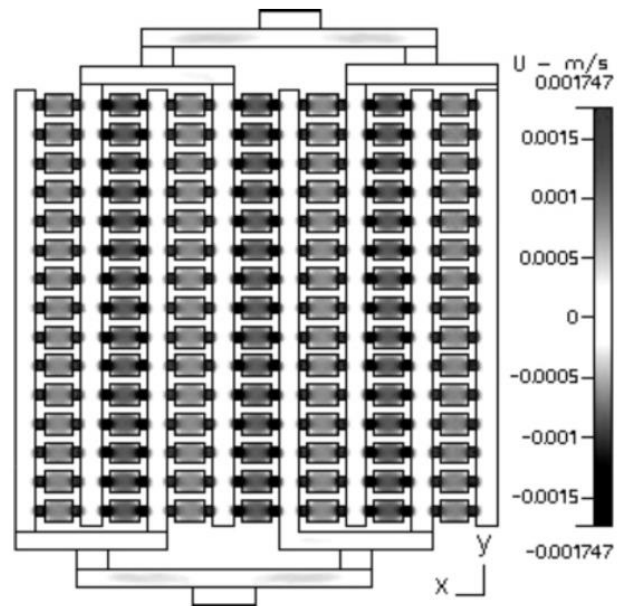


Figure 2.4. The x-velocity contours for a) normal channel b) channels having smaller size inlet and outlet (O-Charoen et al. [52]).

An analytical comparison was presented by Chen and Cheng [57] between parallel channel and bifurcation type design. The results were for three to five branching levels and fractal dimension (D) from 1.1 to 2.0, where the fractal dimension quantifies the relative length of each channel with increasing level of branching. It was found that for fractal dimension of two and five branching levels, heat transfer ability increases by two folds, while the pumping power reduces by about 1.8 times. Hence larger size and more branching levels increase the heat transfer ability while minimizing the pumping power required. In continuation of their work, Chen and Cheng [58] provided experimental verification of the analytical model for a heat sink with dimensions of $20 \times 20 \times 1.4$ mm fabricated on a silicon wafer with micromachining. It was found that the ratio of pumping power of bifurcation to parallel flow channel reduces by 2.8 times while thermal efficiency increases by 2.8 times by increasing the Reynolds number.

Another numerical comparison between serpentine and bifurcation type design was presented by Senn and Poulikakos [59], for water flow at Reynolds number of 20 and 200. It was noticed that a lower pressure loss is for bifurcation in comparison to serpentine for the same surface area. It was further reported that due to multiple turns in the bifurcation, there exists secondary flow motion leading to laminar mixing and better local heat transfer coefficient. Furthermore, heat transfer coefficient increases as the number of branches increase, thereby the total heat transfer was enhanced by increasing the number of branches.

Some design optimization studies were presented by [60,61], and the results were used by Luo et al. [62] to present an experimental comparison of having either pyramid type or bifurcation type manifold at the inlet and outlet of the channels. They used water in laminar flow region ($Re = 50-260$), with pyramid manifold at both inlet and outlet as the base case for comparison purpose. Improvements were found with the use of bifurcation manifold; for example, 30% when both inlet and outlet are bifurcated. For inlet bifurcation and outlet pyramid 15% improvement was observed and 28% with opposite arrangement. With regards to pressure loss, it increased to 72.4% from both pyramids to both bifurcation types. It was concluded that the best design with regard to both heat transfer and pressure loss is with a pyramid type at the inlet and bifurcation type manifold at the outlet.

Table 2.1. A summary of the literature on bifurcation type manifold design characteristics.

Author	Type of study	Specifications	Studies conducted	<ul style="list-style-type: none"> Major outcomes
Alvarado et al. [50]	<p>Numerical</p> <p>Laminar flow</p> <p>Fluid used - water</p>	<p>Number of channels investigated – 21</p> <p>Eight configurations of serpentine, parallel and distributor flow patterns</p>	<p>Re 100-600</p> <p>Flow distribution uniformity,</p> <p>maximum and average temperatures of the heating surfaces,</p> <p>temperature contours on the heating surfaces,</p> <p>thermal resistance,</p> <p>pressure loss,</p> <p>pumping power</p>	<ul style="list-style-type: none"> Distributor A and B designs preferred due to <ul style="list-style-type: none"> a) Low-pressure loss, b) Lower maximum temperature difference, c) Low thermal resistance, and d) Good temperature distribution
O-Charoen et al. [52]	<p>Experimental and Numerical</p> <p>Laminar flow</p> <p>Fluid used - chemicals used in DNA synthesis experiments</p>	<p>Number of channels investigated – 8</p> <p>Headers divided into half and then further half to get four channels for inlet and four channels for outlet.</p>	<p>Microreactor depth, length, and width</p> <p>Microchannel depth and width,</p> <p>Microreactor tapered inlet width and length</p>	<ul style="list-style-type: none"> Alternating columns are highly non-uniform More uniformity when <ul style="list-style-type: none"> a) Increase length of reactor b) Decrease width of reactor c) Decrease depth of reactor d) Increase channel depth e) Increase channel width

Saber et al. [53]	Multiscale network modeling Laminar flow Fluid used - water	Distributing/bifurcation manifolds utilizing multiple passes Number of channels investigated up to 100	Effect of different multi-scale flow distribution configurations on the overall flow resistance	<ul style="list-style-type: none"> • Increase diameter ratio between manifold and channels • Decrease length ratio • Optimum channel number calculation is given for lower pressure loss
Commenge et al. [54]	Multiscale network modeling Laminar flow Fluid used - water	Distributing/bifurcation manifolds utilizing multiple passes Number of channels investigated – 50 and 1000	Two scale network used as base for building multi-scale network	<ul style="list-style-type: none"> • Design charts for flow characteristics
Amador et al. [49]	Electric resistance modeling Laminar and turbulent flow	Manifold and Bifurcation flow distribution	Pressure drop equalization resistance to flow Channels 16, circular and rectangular	<ul style="list-style-type: none"> • Bifurcation better at higher Reynolds number
Liu et al. [56]	Numerical Laminar flow Fluid used – Air	Bifurcation flow distribution Number of channels investigated – 16 Reynolds number - 300 to 600	90°, rounded and circular bends in the bifurcation structure	<ul style="list-style-type: none"> • Longer length after a bend lead to uniformity • Length to channel width ratio should be higher for upstream channels as they have higher Reynolds number • The rounded corner design is best, with length to diameter ratio 5 for are sections

Chen and Cheng [57]	Analytical Laminar flow Fluid used – General	Bifurcation flow distribution Number of bifurcation levels investigated – 3,4,5	90° bends Comparison with parallel channels	<ul style="list-style-type: none"> • Bifurcation has better heat transfer capability, larger diameter and number of branching levels increase heat transfer capability. • Pumping power is less for bifurcation, decreases with larger diameter and number of branching levels
Chen and Cheng [58]	Experimental Laminar and turbulent flow Fluid used – Deionized water	Bifurcation flow distribution Number of bifurcation levels investigated – 4	Impact of Reynolds number 1,449 to 6,503	<ul style="list-style-type: none"> • Thermal efficiency is more as compared to parallel channels • The ratio of pumping power for bifurcation to parallel channel decreases with increasing Reynolds number.
Senn and Poulikakos [59]	Numerical Laminar flow Fluid used - water	Bifurcation flow distribution Number of bifurcation levels investigated – 6 Constant wall heat flux	Reynolds number – 20 and 200 Comparisons of bifurcation and serpentine for same surface area	<ul style="list-style-type: none"> • Bifurcation has half pressure loss as compared to serpentine. • Laminar mixing leads to higher local Nusselt numbers for bifurcation type
Luo et al. [62]	Experimental Laminar flow	Bifurcation flow distribution	Reynolds number – 50 to 260 The combination of inlet and outlet header to be	<ul style="list-style-type: none"> • Improvement in heat transfer coefficient in comparison to both pyramid manifolds <ul style="list-style-type: none"> ▪ Both bifurcation=30% ▪ Inlet bifurcation, outlet pyramid=15%

	Fluid used - water	Number of channels investigated – 128	either pyramid or bifurcation shaped.	<ul style="list-style-type: none"> ▪ Inlet pyramid, outlet bifurcation=28% • Pressure loss for both bifurcation is 72.4% higher than both pyramid. • Inlet Pyramid and outlet bifurcation is found to be the best performing
--	--------------------	---------------------------------------	---------------------------------------	---

2.1.1.2 Conservative manifold design

Contrary to bifurcation type manifold, a conservative type design is simple in fabrication leading to significant efforts in a detailed analysis of every aspect of the manifold design. These efforts are summarized in Table 2.2, with a detailed discussion in this section.

A comprehensive parametric study was conducted by Gandhi et al. [63], with steam acting as the working fluid. The study was focused on variations of pipe diameters for inlet and outlet, header and tube size along with the number of tubes and corresponding pitch. The two major design variations studied included the presence or absence of a channel immediately next to the inlet. Third variation was to add two more tubes to make the total number of tubes ten. Their findings revealed that the flow maldistribution increased when the tube diameter and the flow rate was increased. The first layout was showing most non-uniformity of about 76%, while 3% and 2 % non-uniformity for the second and third type, respectively. It was also reported that by increasing the number of tubes, the flow non-uniformity increases while the reduction in tube diameter improves the flow distribution. The design configuration for ten tubes having header length of 100 mm with inlet and outlet diameter of 50 mm and distance between each tube of 170 mm was deemed the best for uniform flow distribution while also providing more heat transfer area. The experimental investigation of the authors was focused on both water and air as the operating fluid, and the results were within 5- 10% deviation with the numerical modeling. It was also concluded that the effect of having different fluid did not have a significant effect on the flow distribution.

With regards to Z-type flow arrangement, Mohammadi et al. [64] studied triangular manifolds having the inlet and exit port perpendicular to the plane of channels (Figure 2.5). Reynolds number ranged between 5 and 25, and numerical simulations were performed with a commercial software [65]. It was found that for flow distribution, the channel parameters were less significant as compared to the geometrical parameters of the manifold, which includes the smallest section of the manifold and angle of taper. As the Reynolds number becomes low, the presence of optimum corner angle becomes evident. The pressure loss was found to be minimum when the manifold size was maximum (1000 μm) with 15° taper. Furthermore, if the size of inlet manifold is increased, the flow in opposite channels increases and vice versa for the outlet manifold.

A similar study was provided by Minqiang et al. [66] for a three-dimensional model having the triangular manifold in Z-type flow arrangement. It was concluded that more uniform flow distribution was obtained by increasing length and depth while decreasing the width of channels, thus leading to higher aspect ratio. Larger manifold along with larger radius of inlet and outlet ports also resulted in better flow uniformity. Furthermore, a symmetrical design leads to lesser maldistribution as compared to asymmetrical.

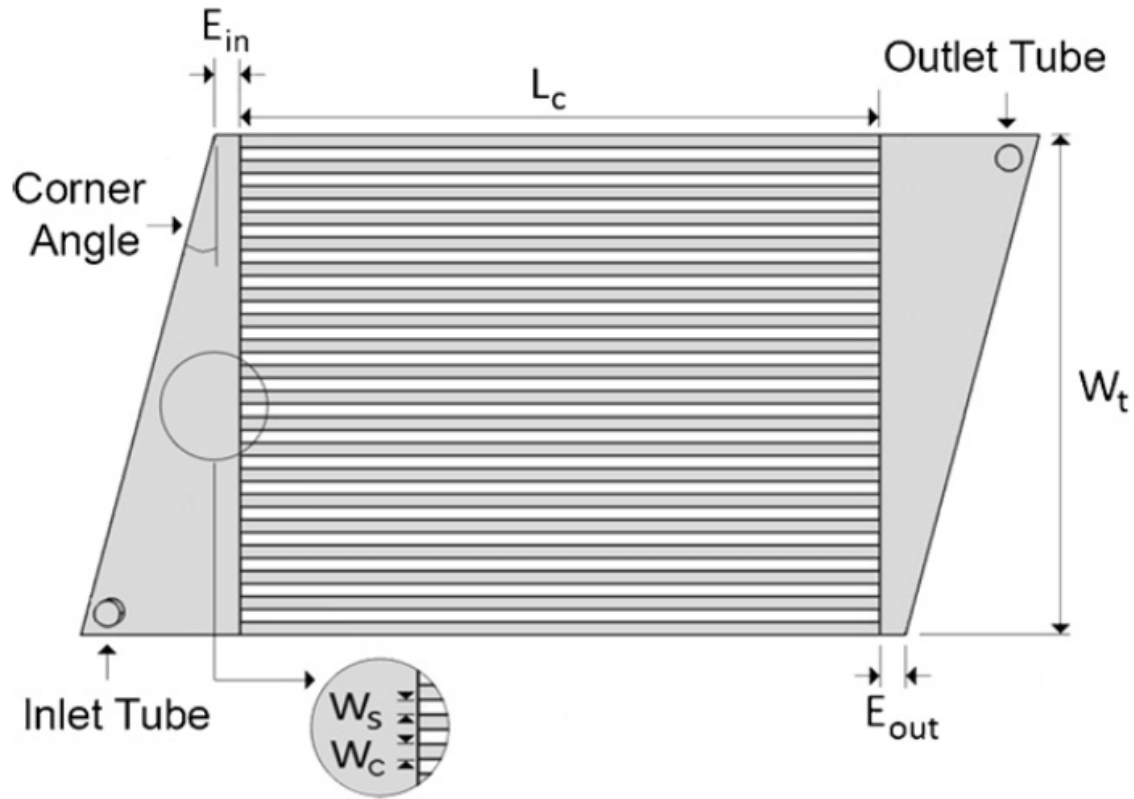


Figure 2.5. The schematic of the structural parameters studied by Mohammadi et al. [64]

A detailed optimization for Z-type flow arrangement in plate-fin micro heat exchangers was provided by Tonomura et al. [67]. The first study showed that the longer length results in more uniform distribution. The reason is that the pressure drop, in the channels, becomes more significant as compared to the pressure loss in the manifold region. Next, the impact of manifold width was studied with four cases, the baseline scenario, double inlet manifold, double outlet, and both inlet and outlet with double manifold width as illustrated in Figure 2.6. The study further showed that the inlet header increment has an adverse influence on the flow distribution while the larger outlet manifold has a positive impact on the flow uniformity by reducing the velocity peaks in the last channels (i.e. opposite to the inlet

side). Hence the outlet should be twice the inlet. Subsequently, a corner optimization by cutting segments of the corner was performed to find the optimum shape. After finding the optimum shape, they proceeded to make the original size same and vary the baffle location according to the optimized channel length obtained earlier. This design (termed Type C) was found to give the best flow distribution for the three velocities considered.

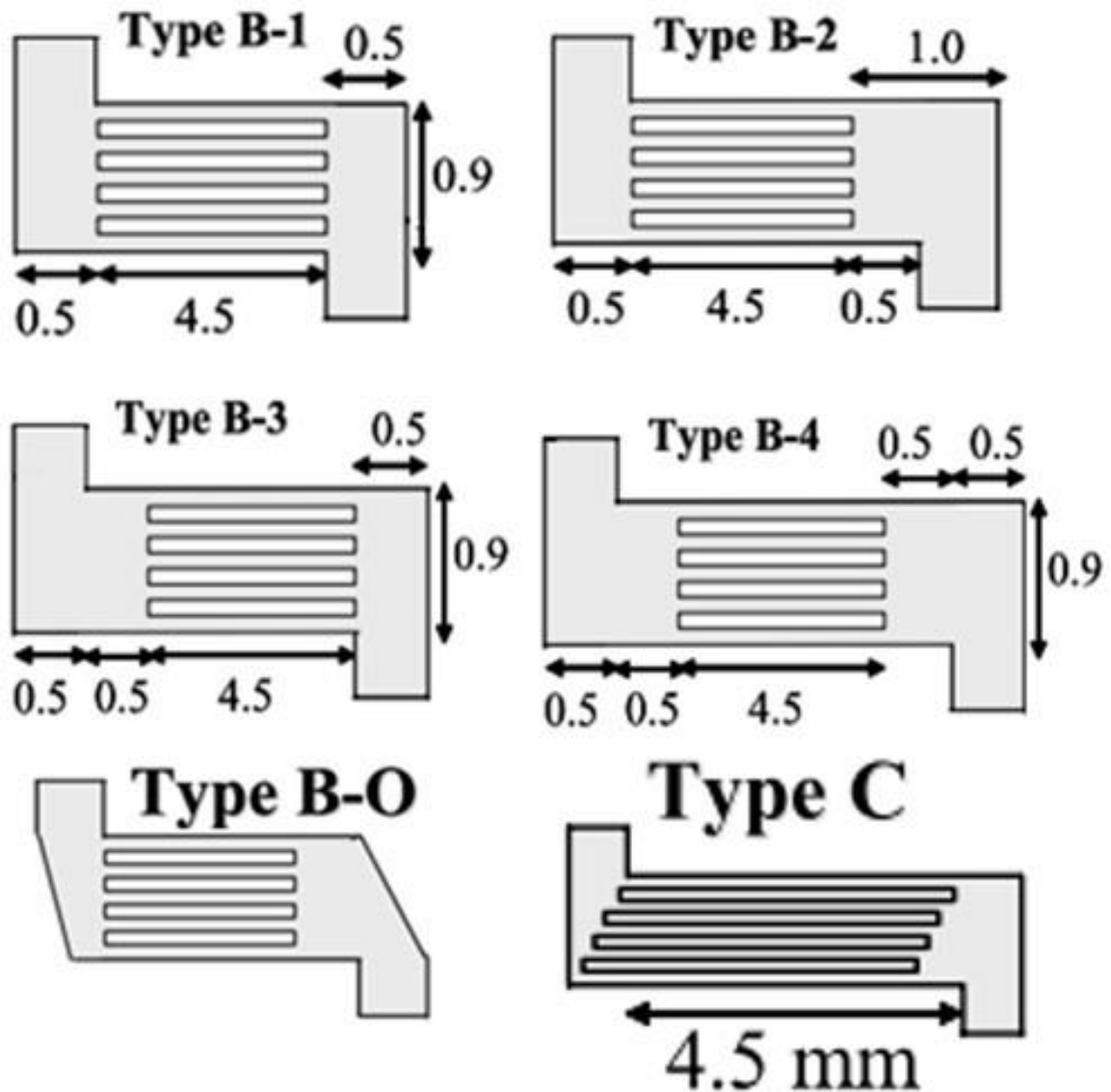


Figure 2.6. The different cases studied by Tonomura et al. [67]

A similar study was conducted by Griffini and Gavrilidis et al. [68] with focus on lower Reynolds number to explore the flow distribution in a manifold for several design layouts. To ensure uniform cooling, the residence times as well as the fluid flow rate in each of the channels, are important aspects to take into consideration for enhanced performance of heat exchangers. The simulations pointed that two-dimensional numerical simulations are not representing the true flow behavior; thus, a complete three-dimensional modeling must be used to understand the overall flow characteristics. The presence of a critical value of Reynolds number was found in both two- and three-dimensional simulations, but it was noticed that there was two order of magnitude difference between the values of critical Reynolds number. This showed that two-dimensional results were giving a higher estimate of the flow maldistribution. Stagnation regions were identified to be forming at the corners of the flow region which can be reduced by utilizing baffle directing the flow towards the stagnation regions. The thickness of the baffles had no effect on the flow distribution mainly due to the lower Reynolds number while increasing the size of both inlet and outlet manifold showed improved flow distribution up to a particular limit after which the flow distribution remained constant. Previous models had the flow inlet and outlet outside the flow channel regions, so the design was modified to bring the inlet and outlet in line with the channel and noticed improved distribution of flow as compared to the original layout.

Solovitz and Jeffrey [69] provided an analytical model to optimize the flow distribution by equating the pressure loss in all the channels. They considered the major pressure loss (frictional, Eq. (2.1)) while ignoring the minor pressure losses (geometrical, Eq. (2.2)) for the analytical model.

$$\Delta p_{maj} = \frac{fL\rho u^2}{2D} \quad (2.1)$$

$$\Delta p_{min} = \frac{K_L u^2}{2} \quad (2.2)$$

Where K_L is the minor pressure loss coefficient and L is the channel length. For fully developed condition, Darcy–Weisbach equation ($f = 64/\text{Re}$) and $V = (4 \times Q)/(\pi D^2)$ led to simplified general expression for the major pressure loss,

$$\Delta p_{maj} = \frac{128\mu L Q}{\pi D^4} \quad (2.3)$$

For uniform distribution, the flow rate in each channel should be same. Therefore, for five identical parallel channels the inlet flow rate is five times the flow in each channel. The major pressure loss components in each section along the paths are added, leading to the following four equations, where the largest segment is not included as it is common for all paths and has no impact on flow distribution.

$$\Delta p_{path,1} = \frac{128\mu L_m(4)Q_c}{\pi D_{m,4}^4} + \frac{128\mu L_m(3)Q_c}{\pi D_{m,3}^4} + \frac{128\mu L_m(2)Q_c}{\pi D_{m,2}^4} + \frac{128\mu L_m(1)Q_c}{\pi D_{m,1}^4} + \frac{128\mu L_c Q_c}{\pi D_c^4} \quad (2.4)$$

$$\Delta p_{path,2} = \frac{128\mu L_m(4)Q_c}{\pi D_{m,4}^4} + \frac{128\mu L_m(3)Q_c}{\pi D_{m,3}^4} + \frac{128\mu L_m(2)Q_c}{\pi D_{m,2}^4} + \frac{128\mu L_c Q_c}{\pi D_c^4} + \frac{128\mu L_m(4)Q_c}{\pi D_{m,4}^4} \quad (2.5)$$

$$\Delta p_{path,3} = \frac{128\mu L_m(4)Q_c}{\pi D_{m,4}^4} + \frac{128\mu L_m(3)Q_c}{\pi D_{m,3}^4} + \frac{128\mu L_c Q_c}{\pi D_c^4} + \frac{128\mu L_m(3)Q_c}{\pi D_{m,3}^4} + \frac{128\mu L_m(4)Q_c}{\pi D_{m,4}^4} \quad (2.6)$$

$$\Delta p_{path,4} = \frac{128\mu L_m(4)Q_c}{\pi D_{m,4}^4} + \frac{128\mu L_c Q_c}{\pi D_c^4} + \frac{128\mu L_m(2)Q_c}{\pi D_{m,2}^4} + \frac{128\mu L_m(3)Q_c}{\pi D_{m,3}^4} + \frac{128\mu L_m(4)Q_c}{\pi D_{m,4}^4} \quad (2.7)$$

Now for each set of two consecutive paths, only one term is different while all other terms are same. Hence for uniform pressure drop, those two terms should be equal. Equating the terms leads to the following simplification

$$\frac{128\mu L_m(1)Q_c}{\pi D_{m,1}^4} = \frac{128\mu L_m(N-1)Q_c}{\pi D_{m,N-1}^4} \quad (2.8)$$

where N is the total number of channels. Further simplification of the common terms leads to the expression for diameter ratio.

$$D_{m,N-1} = (N-1)^{1/4} D_{m,1} \quad (2.9)$$

Similarly, for path two and three, we get the following relation.

$$(2)^{1/4} D_{m,N-2} = (N-2)^{1/4} D_{m,2} \quad (2.10)$$

Hence, a general relation can be written as

$$D_{m,N-k} = \left(\frac{N-k}{k} \right)^{1/4} D_{m,k} \quad (2.11)$$

where m denotes the manifolds, while k is the local channel for which the diameter is to be calculated. To further simplify the ratio, the minimum diameter is used as a reference and all other diameters are calculated from it using the power law

$$D_{m,k} = (k)^{1/4} D_{m,1} \quad (2.12)$$

This rule can be applied to any shape of the channel, as long as the hydraulic diameters are used in these expressions. Thus the equalization of major pressure losses in all flow paths resulted in the relation termed as power law, which is given by Eq. (2.13)

$$D_k = (k)^{1/4} D_1 \quad (2.13)$$

where k is the manifold segment number corresponding to the channel number. With the use of this power law, the results show that step-wise increments in the manifold size result in excellent flow distribution. Another modification was done by linearizing the stepped changes into a straight line joining the smallest and largest segment. This reduced the minor losses due to the sudden shape changes, leading to just 0.8% standard deviation of flow in channels.

After understanding the utility of triangular manifolds, Pan et al. [70] studied three triangular configurations, i.e., obtuse, right and acute angle for the manifold (Figure 2.7). The resistance networks modeling was used, dividing the manifold into rectangular channels and calculated the corresponding resistance for each segment to determine the flow distribution for a triangular manifold. The optimization led to the conclusion that the right-angle manifold is the best performing shape for identical structural parameters. A further study [71] included the effect of having asymmetrical inlet and outlet manifolds using the same model and found that better flow distribution occurs for the symmetrical

manifold. For asymmetrical manifolds, the taper angle has a very significant influence on the flow distribution; larger angles enhance the distribution.

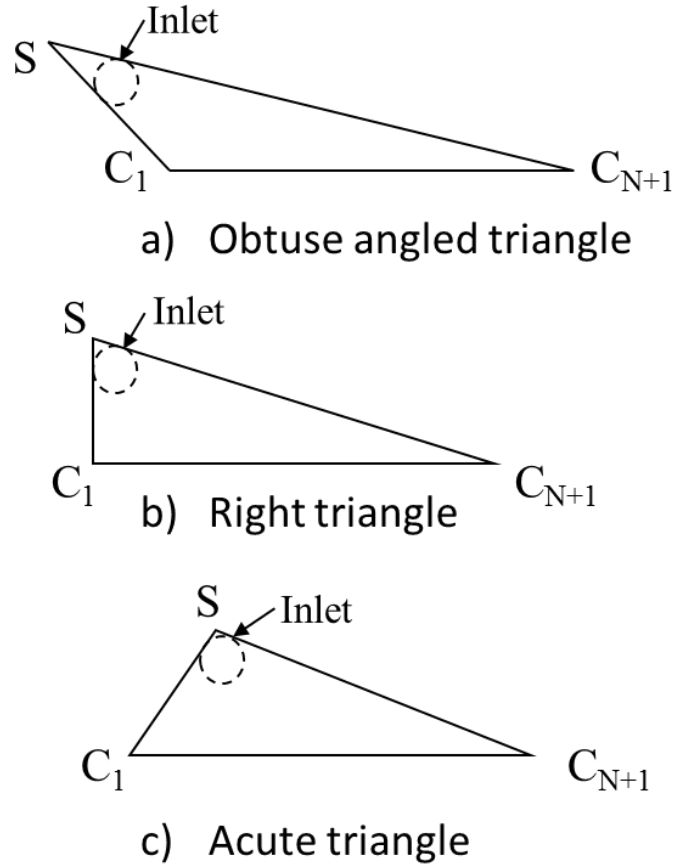


Figure 2.7. Three types of triangular manifolds studied by Pan et al. [70]

Another study for triangular manifolds was presented by Vásquez-Alvarez et al. [72], with four manifold designs i.e., obtuse, isosceles, circular with channels at extremes and circular with baffles at extremes as shown in Figure 2.8. The study revealed that making the manifold circular with inlet at the center had better flow distribution characteristics, but the presence of channels at extremes cause lower flow in them. Further analysis showed that

by having baffles at the extremes, flow becomes even more uniform with same velocity at all channels including the extreme channels.

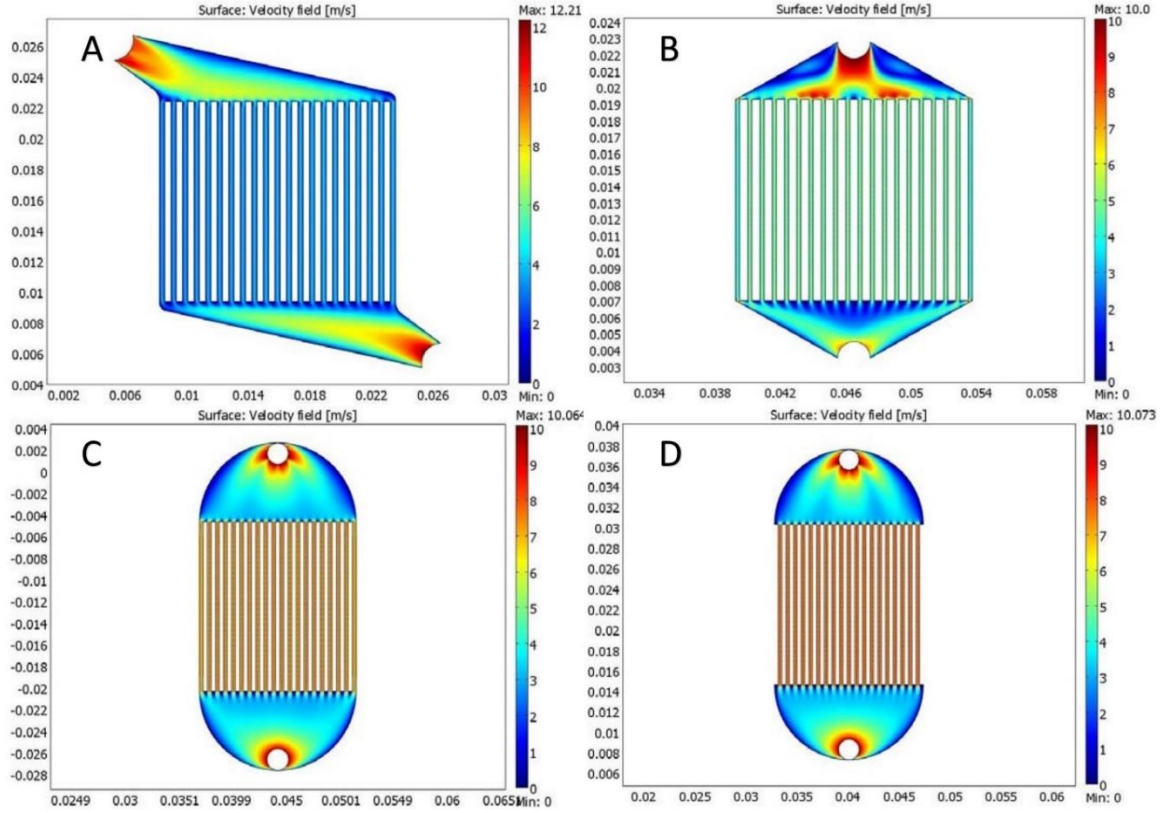


Figure 2.8. The layouts with corresponding velocity distribution in the four cases presented by Vásquez-Alvarez et al. [72]

In another study regarding the manifold shape, Hassan et al. [73] compared numerical and experimental results for five channels of circular cross-section with a diameter of 5 cm, spacing of 22 cm and manifold diameter of 10 cm. The base case had the manifold with constant diameter and results show that the flow has non-uniform distribution with maximum pressure occurring towards the last channel in the manifold. The modification

of tapered manifold was applied, and it was found that the pressure is now more uniformly distributed in the manifold, and results in a relatively uniform flow within the channels. The Reynolds number studied were 100000, 150000, and 200000 which are in the turbulent region, and the results from numerical were found to be matching with the experimental values. For such higher Reynolds numbers, the effect of inlet flow variation becomes less significant for the flow uniformity into the channels.

Another study on the equalization of pressure within the manifold was presented by Perlmutter [74] with an analytical model for the manifold flow. The resulting optimization study was validated by experiments. The design was focused on making the static pressure constant throughout the manifold to ensure flow uniformity. The momentum balance was used with Blasius law for wall shear stress to come up with an equation to represent the outlet header, and a similar momentum balance for the inlet header. The variations studied were, with and without friction, with parallel- and counter-flow arrangements. The optimum results were found when the manifold length-to-height ratio is larger. The overall pressure drops have also been found to be in accordance with the experimental values.

The experimental determination of pressure variation within the manifold was presented by Tereda et al. [75] in addition to velocity variation in the manifold and channels for a plate heat exchanger. A mandrel was inserted into the manifold with taps available for pressure measurements. It was found that as the flow rate increases, the maldistribution of flow increases. This effect was not very significant when a larger manifold is utilized which

also improved the flow distribution and reduced the pressure loss. It was found that pressure variation in the manifolds was dominated by the flow branching effects in comparison with the friction pressure drop.

The effect of manifold width has also received attention for flow uniformity. In this regard, Chen et al. [76] presented a CFD simulated results to understand flow distribution in the stack of Proton exchange membrane. The model considered of 72 channels that were filled with porous medium, while studying the effect of permeability, inlet velocity of air along with the manifold dimensions. The findings revealed that higher inlet velocity increases the flow maldistribution. Decreasing permeability enhances the flow distribution but it also increases the overall pressure drop. Also, for channels with more flow resistance, more pressure drop will occur and result in flow uniformity. The manifold width is a significant parameter, increasing it leads to more flow uniformity while reducing the overall pressure drop.

The effect of area ratio between the manifold and the channel has been studied by Datta and Majumdar [77]. A numerical finite difference procedure of iterative nature was presented to solve the differential equations of continuity and momentum in the longitudinal direction while the integral equation of momentum in the lateral direction. The results have been verified by experimental data available by Bajura and Jones [78]. The model was applied to U- and Z-type flow pattern termed as parallel and reverse flow. The flow in manifold was previously assumed to be parabolic i.e. the end conditions have no

effect on the initial flow. An elliptic model was presented in which the downstream conditions do have an effect on the flow in the upstream. They studied the flow distribution for various set of area ratio and friction parameters, with two-phase flow modeling possible by using effective fluid properties. The experimental data used for the validation and comparison of results was published by Bajura and Jones [78], while also including the basic momentum balance and a mathematical foundation for the analytical solution of the flow distribution equations. The experimental setup used air as working fluid and consisted of eight different flow configurations using 10 or 20 channels with U- and Z-type arrangements. The parameters studied were, varying area ratio and flow resistance, the later was varied by inserting orifice in the flow area.

Another study on the influence of area ratio on the distribution of flow was presented by Choi et al. [79] for liquid cooling modules. The objective of uniform flow arrangement is to reduce the development of hot spots in the modules, using a finite element code to numerically solve the mass and momentum equations for different area ratios. It was shown that as the area ratio increases, the flow in first and last channel increases while decreasing in the middle channels. This is attributed to the static pressure difference along the flow paths which varies due to friction and momentum. For combining manifold both friction and momentum always decreases the pressure whereas for the dividing manifold, friction reduces the pressure while momentum increases it. The study also revealed that area ratio of four produced better flow distribution, the difference in flow rate was 2.75 times between the first and last channels. In continuation of their work, Choi et al. [80] presented the effect of Reynolds number and the manifold width for the flow distribution in cooling

modules to be used in electronic packaging. The largest width ratio of 4.0 resulted in the best flow distribution, where the flow uniformity ratio was 1.2. This larger manifold area also results in less overall pressure drop further increasing the benefits. The dependence on Reynolds number was studied for $Re=5$, 50 and 250, with high non-uniformity at a higher Reynolds number.

In another application on cooling of electronic components, Kim et al. [81] compared rectangular, triangular and trapezoidal manifolds. Eight channels were used with the Reynolds number variation from 50 to 300 studied using a numerical solution software. The rectangular manifold has the problem of concentrating the flow in the last channel which leads to a large flow maldistribution. It was found that for the range of Reynolds number considered, triangular manifold resulted in the best flow distribution. Reynolds number effect on flow distribution was more significant for rectangular manifold as compared to triangular, which resulted in virtually uniform distribution for the range of Reynolds number considered.

Another study on area ratio between channel-to-manifold was studied by Jones and Lior [82] with the use of numerical solution of non-linear equations by neglecting the effect of buoyancy. The study revealed three major flow distribution controlling parameters: (i) the ratio of channel diameter to the manifold diameter, (ii) the number of channels, and (iii) the length of these channels. The flow non-uniformity increased with an increase in the first and second parameter while it was decreasing with the last parameter. The findings

revealed that the flow in initial channels is lowest and then increases along the channels in flow direction for a Z-type configuration, while it reduces for the U-type configuration. The ratio of channel diameter to the manifold diameter is a significant factor, the value of which should be kept as small as possible. After fixing this ratio, the maldistribution increases with the square of the number of channels. The effect of distance between the channels has insignificant effect for the case under study. Increasing the length distributed the flow more uniformly as it decreases the friction pressure changes within the channels. In conclusion, the pressure drop in the channels should be significant as compared to the losses of frictional and inertial losses to make the flow distribute itself uniformly amongst the channels.

A numerical study into non-linear manifolds as a further improvement to triangular manifolds was presented by Tong et al. [83], with the use of eight different parameters that can affect the flow distribution. It was found that channel width increments make the flow distribution better. A linear taper was then studied to demonstrate that as the Reynolds number increases, the optimum taper angle also increases to ensure better distribution. A further study included non-linear patterns, having concave down, concave up and the combination of concave-down followed by concave-up section, as shown in Figure 2.9. It was found that the concave down was the best design but the difference between this design and linear design was not significant and linear may be preferred keeping in view the fabrication cost of a non-linear design. It was found that if a similar taper is introduced in the outlet manifold, this leads to flow non-uniformity thus it is not preferred. Then the width of channels was varied, making last channel smaller than the first channel and found this to be a significant parameter. The flow inlet was made smaller than the inlet manifold

(Figure 2.10) and found a negative impact of the smaller inlet suggesting that the inlet and manifold should be of same dimensions. The inlet at an angle to the manifold (Figure 2.10) led to reverse flow in first few channels while rounding off the corners of the entrance of each channel had a negative influence discouraging further investigations.

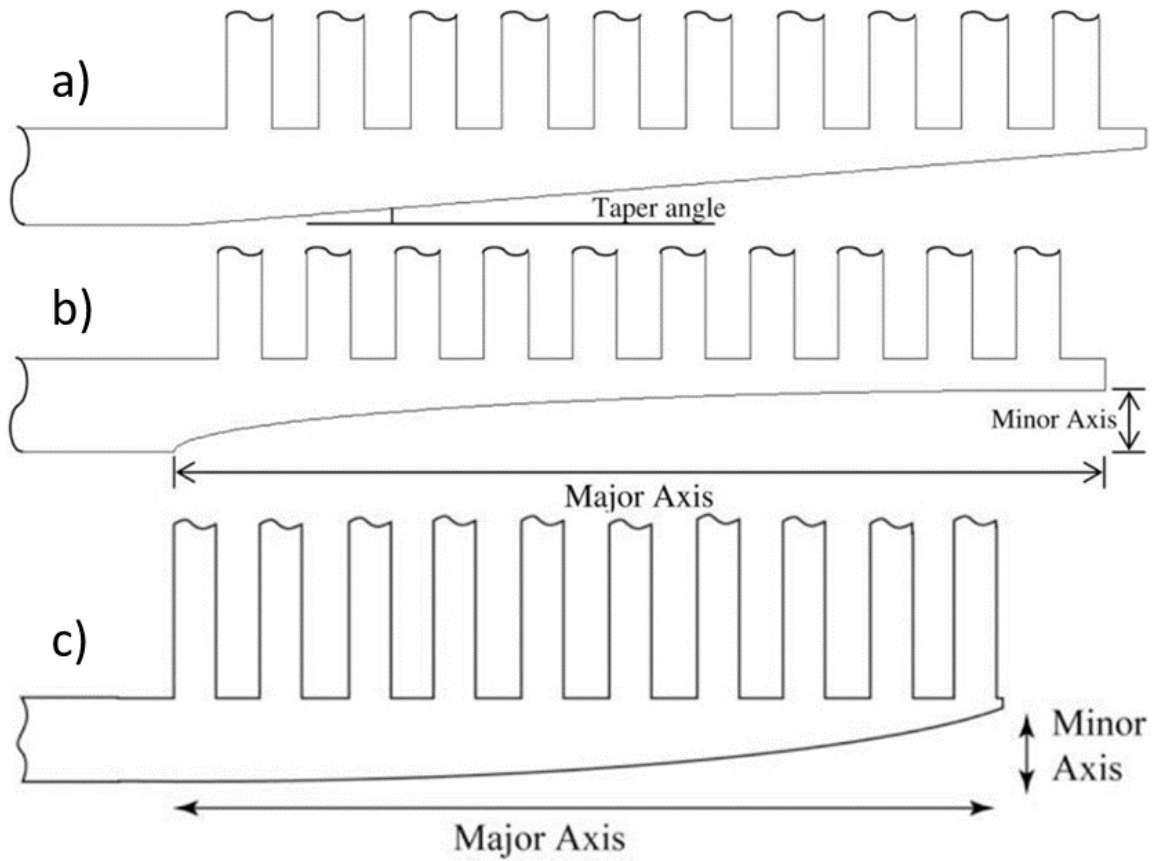


Figure 2.9. The three manifold designs considered by Tong et al. [83].

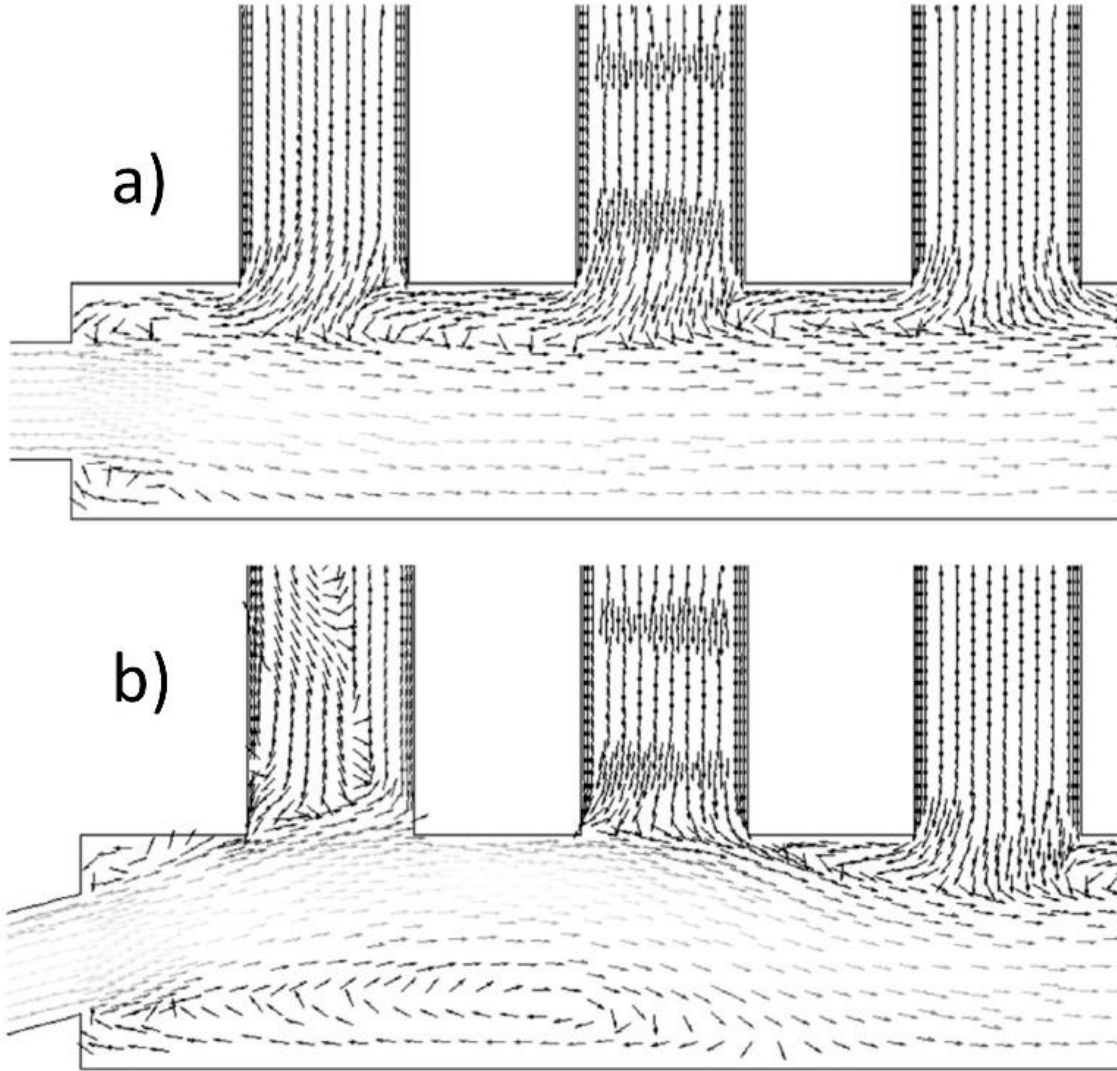


Figure 2.10. Layouts showing a) smaller inlet than the manifold leading to reverse flow in first channel, b) angled inlet, showing recirculation by Tong et al. [83]

The overall pressure drop in the heat exchanger was studied by Miura et al. [84], with manipulation of the flow patterns within the heat exchanger. Experiments were performed on 32 different possible fluid pass patterns including the Z-type. They found the pressure loss to be linearly dependent on the number of passes while the effect of flow channel per

pass was not clear. The results obtained from the experiments were used to modify the friction factor model with the assumption of inlet velocity to be directly affecting the pressure loss. The flow types 2×1 and 1×2 were numerically modeled, and pressure drop was found in a good agreement with the predicted values. Rao et al. [85] presented their study on U- and Z-type arrangement. It was found the effect of flow maldistribution is significant on the heat exchanger performance, with Z-type having more maldistribution in comparison to U-type. Increasing number of plates reduces effectiveness while increasing manifold size reduces flow maldistribution.

Another study on overall pressure drop was carried out by Rao and Das [86], with experimental pressure drop as a consequence of non-uniform flow distribution. A comparison between U- and Z-type plate heat exchangers showed that fluid flow rate, the number of channels and their size all contribute to flow maldistribution. The U-type arrangement has better flow distribution, while higher operating temperature leads to more flow maldistribution. Finally, an industrial heat exchanger is studied showing that up to 300 plates, flow distribution is normal, but further additions would result in no flow in those following channels.

Wasewar et al. [87] studied manifold shape modification where a conventional longitudinal manifold was modified with a curved shape design as shown in Figure 2.11. It was found that the flow uniformity index reduced by 70.71% which is a significant improvement. The velocity contours in the manifold showed how the diverging manifold changes the velocity

vector direction, thus enabling better flow distribution. Gunnewiek et al. [88] presented a numerical study of turbulent air flow in combining manifold. It was found that increasing manifold length to width ratio increases the pressure loss. A higher suction velocity in the lower channel was due to buoyancy-driven flows which increase with the wider manifold, leading to better efficiency in non-uniform flow than uniform flow.

The effect of different fluids on the flow distribution in a Z-type flow arrangement was studied numerically by Mohan et al. [89]. It was found that for same flow rate, the Reynolds number is different for different gasses due to the variation in the kinematic viscosity. Hence, the Reynolds number for Hydrogen is much smaller as compared to air and oxygen. These results are in almost perfect uniformity seen for hydrogen whereas other gasses showed non-uniformity. Between air and oxygen, oxygen was more uniformly distributed as compared to air. It was also found that higher flow rates and smaller manifold size lead to a non-uniform distribution.

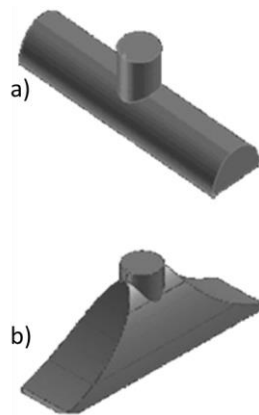


Figure 2.11. a) Conventional b) modified manifold design by Wasewar et al. [87]

Table 2.2. A summary of the literature on conservative manifold design characteristics.

Author	Type of study	Specifications	Studies conducted	Major outcomes
Gandhi et al. [63]	Numerical Turbulent flow Fluid used - Air and water	Inlet and outlet in-line with channels at middle of manifold Number of channels investigated – A (9,27), B (8,24), C (10,30,50) Reynolds number - 35,600-100,500	With and without a channel directly in line with the inlet and outlet port Effect of pitch diameter, header diameter, channel diameter, inlet outlet diameter, number of tubes inlet flow rate is discussed	<ul style="list-style-type: none"> Non-uniformity increased with <ol style="list-style-type: none"> Increase in tube diameter Increase in inlet flow rate Increase in total number of tubes C1 and C12 designs were the best configurations
Mohammadi et al. [64]	Numerical Laminar flow Fluid used - water	Triangular manifold Number of channels investigated – 20 Reynolds number - 5 to 25	The size of manifold Angle of manifold	<ul style="list-style-type: none"> Long narrow channels better Optimum corner angle for each manifold width Overall pressure loss minimum for biggest manifold with smallest corner angle
Minqiang et al. [66]	Numerical Laminar flow Fluid used - water	Z-type Number of channels investigated – 20 Inlet velocity 1 mm/s	Asymmetrical design layout Length, width, depth and spacing between channels Position and radius of inlet-outlet ports Width of manifold	<ul style="list-style-type: none"> Symmetrical manifolds better than asymmetrical Corner angle significant for asymmetrical manifolds More flow uniformity with <ol style="list-style-type: none"> Larger length and depth Smaller width High aspect ratio of channels Larger manifold Larger inlet-outlet ports Thinner baffles

<p>Tomomura et al. [67]</p>	<p>Numerical</p> <p>Laminar flow</p> <p>Fluid used - Water</p>	<p>Z-type</p> <p>Number of channels investigated – 5</p> <p>Reynolds number - 10-100</p>	<p>Length of channels</p> <p>Asymmetrical size of inlet outlet manifold</p> <p>Shape of manifold</p> <p>Moved Baffles</p>	<ul style="list-style-type: none"> • More uniformity with <ol style="list-style-type: none"> a) Longer channels b) Outlet manifold width double to that of inlet manifold c) Corners opposite to inlet/outlet port chamfered to remove stagnant zone d) Moving baffles instead of chamfering corners
<p>Griffini and Gavriilidis [68]</p>	<p>Numerical</p> <p>Laminar flow</p> <p>Fluid used - Liquid</p>	<p>Z-type</p> <p>Number of channels investigated – 12</p> <p>Reynolds number - up to 50</p>	<p>Comparison between 2D and 3D</p> <p>Effect of channel length</p> <p>Plate thickness</p> <p>Design of manifold</p> <p>Different location of inlet-outlet ports</p>	<ul style="list-style-type: none"> • Critical Reynolds number 0.37 for 2D and 12.83 for 3D • Increase channel length • Increase inlet/outlet manifold size • No impact of plate thickness due to low Reynolds number • Move the inlet/outlet ports within the channel domain, instead of offset
<p>Solovitz and Jeffrey [69]</p>	<p>Analytical design with major pressure loss equalization</p> <p>Numerical results</p> <p>Laminar flow</p> <p>Fluid used - Water</p>	<p>Z type</p> <p>Number of channels investigated - 5 and 10</p> <p>Reynolds number - 5 to 500</p>	<p>Hydraulic diameter from the analytical model.</p> <p>Uniform and non-uniform manifold depth calculated from hydraulic diameter</p> <p>Four manifold configurations - narrow, wide, taper and power law manifold</p>	<ul style="list-style-type: none"> • Uniform and non-uniform manifold depth have no difference provided the hydraulic diameter remain same • Behavior becomes significantly non-uniform above Reynolds number of 20 • Power law better for flow distribution at low Reynolds number

Pan et al. [70,71]	Numerical and Frictional resistance model Laminar flow Fluid used - Liquid and gaseous water	Z-type flow arrangement	Obtuse, Right and Acute triangular shapes considered Symmetrical and asymmetrical	<ul style="list-style-type: none"> • Right angled triangular design better • Symmetrical manifolds better • For asymmetrical, rake angle significant
Vásquez-Alvarez [72]	Numerical and fabrication Fluid used – Nitrogen Laminar flow	Z-type and parallel Number of channels investigated – 19, 20, 21 Reynolds number - 60,000	Four configurations studied Obtuse, isosceles, circular with channels at extremes, circular with baffle at extremes	<ul style="list-style-type: none"> • Circular manifold with baffles at the extreme sides has the best flow distribution • This design has slightly more pressure loss • Higher flow rates increase non-uniformity • 3D modeling results in higher pressure loss as compared to 2D modeling, due to additional walls at top and bottom in 3D
Hassan et al. [73]	Experimental and Numerical Turbulent flow Fluid used - water	Distributing manifold Number of channels investigated – 5 Reynolds number - 100k, 150k, 200k	Pressure considerations in uniform and taper manifold	<ul style="list-style-type: none"> • Linear taper for circular cross-section of manifold and channels
Perlmutter [74]	Analytical Turbulent flow Fluid used – Dry Air	Distributing manifold	Inlet and outlet headers with/without friction	<ul style="list-style-type: none"> • Good agreement with experiments • Large manifold length to height ratio

				<ul style="list-style-type: none"> • Lower overall pressure drop is possible with manifold shapes manipulation
Tereda et al. [75]	<p>Experimental</p> <p>Turbulent Flow</p> <p>Fluid used - Water</p>	<p>Z and U-type flow arrangement</p> <p>Number of channels investigated – 25</p> <p>Reynolds number – 460, 644, 764 878</p>	<p>Manifold diameter variation</p> <p>Flow rate variation</p>	<ul style="list-style-type: none"> • Pressure variation due to flow branching dominant over the friction pressure drop in manifold • Flow non-uniformity increase with flow rate • Larger manifold reduces pressure drop variation pointing to better flow distribution • Effect of flow rate for larger manifold is less significant
Chen et al. [76]	<p>Numerical</p> <p>Fluid used – Air</p> <p>Turbulent flow</p>	<p>U-type flow arrangement</p> <p>Number of channels investigated - 72</p>	<p>Effect of flow rate, permeability, inlet flow rate</p>	<ul style="list-style-type: none"> • Low flow rate better distribution • Low permeability improve distribution but increase overall pressure drop • More channel resistance leads to uniform flow
Datta and Majumdar [77]	<p>Finite difference</p> <p>Fluid used - Air</p> <p>Turbulent flow</p>	<p>U and Z-type flow arrangement</p> <p>Number of channels investigated - 10-20</p>	<p>Comparison between U and Z type</p> <p>Effect of area ratio and friction parameter</p>	<ul style="list-style-type: none"> • U is better than Z • Decrease channel to manifold area ratio, better distribution • Most flow in the last channel for Z, first channel for U-type manifold • Effect of friction factor less significant
Bajura and Jones [78]	<p>Analytical</p> <p>Fluid used – Air</p>	<p>U and Z-type flow arrangement</p> <p>Number of channels investigated - 10-20</p>	<p>Verification of the analytical model</p> <p>Area ratio and lateral resistance manifold</p>	<ul style="list-style-type: none"> • U-type better than Z-type • Decrease area ratio for better flow distribution, less than one preferably

	Turbulent flow	Reynolds number - 60k to 80k		<ul style="list-style-type: none"> • Larger lateral flow resistance is preferred, but it increases overall pressure loss • For smaller manifolds, friction may be neglected, for longer manifolds static pressure changes due to channel branching may be neglected
Choi et al. [79]	Numerical Fluid used – Water Laminar flow	Z-type flow arrangement Number of channels investigated - 8 Reynolds number – 5, 50 and 250	Ratio between channel area and manifold area, Area ratio 4,8 and 16 studied	<ul style="list-style-type: none"> • Friction always decrease the pressure while momentum decreases pressure in combining header and increases pressure in dividing flow header • Lowest area ratio of 4 is better for uniform flow distribution, but still flow in the last channel was 2.75 time that in first
Choi et al. [80]	Numerical Laminar flow Fluid used - Water	Z-type flow arrangement Number of channels investigated - 8 Reynolds number – 5, 50 and 250	Width ratio between outlet and inlet manifold	<ul style="list-style-type: none"> • Larger width ratio 4 is the best, also less pumping power • Reynolds number effect is more significant than width ratio
Kim et al. [81]	Numerical Fluid used – Water Laminar flow	Z-type flow arrangement Number of channels investigated - 8 Reynolds number – 50, 100, 200 and 300	Manifold shapes considered <ul style="list-style-type: none"> • Trapezoid • Triangular • Rectangular 	<ul style="list-style-type: none"> • Triangular better • Higher Reynolds number decreases flow distribution • Higher Reynolds number maldistribution more significant for rectangular than triangular

Jones and Lior [82]	Analytical Turbulent flow Fluid used - Water	Number of channels investigated - 4, 8, 16 Reynolds number - 3210, 9640, 16100	Re and channel number with size of channel	<ul style="list-style-type: none"> • Channel to manifold diameter ratio is significant, more uniform smaller ratio • Fewer channels are better; non-uniformity increases with n^2 • Longer channels preferred. • Effect of distance between channels is insignificant
Tong et al. [83]	Numerical Laminar flow	Z-type modified to parallel Number of channels investigated – 10 Reynolds number - 35 to 1,400	Manifold width Linear and non-linear taper for both inlet and outlet header, Variable channels widths Shape of inlet Three non-linear tapers considered, concave down, concave up and combination of concave-down followed by concave-up section	<ul style="list-style-type: none"> • Bigger manifold width • Small taper angle for low Reynolds number, larger angle for higher Reynolds number • Concave down is best, but difficult fabrication offsets the benefit • Outlet manifold taper led to increasing non-uniformity • Making last channels of smaller widths than initial channels is strong parameter • Smaller inlet than manifold leads to flow reversal. The inlet and manifold size should be same • No benefit of having inlet fluid entering at an angle in the manifold • Rounding of the channel inlet corners led to increasing flow non-uniformity
Miura et al. [84]	Experimental and numerical	32 different flow arrangements	Effect of flow arrangement on total pressure drop	<ul style="list-style-type: none"> • Linear dependence between number of passes and the pressure drop

	Laminar flow, with some turbulent regions Fluid used - Water	Number of channels investigated up to 18		
Rao et al. [85]	Theoretical and Experimental Turbulent flow Fluid used - Water	Z and U-type flow arrangement Number of channels investigated – 19 and 33	Re 600-5500 Effect of change in manifold size and number of plates for varying Reynolds number	<ul style="list-style-type: none"> • Effect of maldistribution is significant on the heat exchanger performance • U-type is more uniform in comparison to Z-type • Z-type performance is least affected by flow distribution • Increasing plates reduces effectiveness • Increasing manifold size reduces flow maldistribution
Rao and Das [86]	Experimental Turbulent flow Fluid used - Water	Z and U-type flow arrangement Number of channels investigated – 10, 15 and 18	Re 700-7000 Effect of port to channel flow maldistribution	<ul style="list-style-type: none"> • Inlet-outlet Port size should be maximum possible • Total pressure drop -critical function of flow rate and port size • Flow more uniform in U-type arrangement
Wasewar et al. [87]	Numerical Laminar flow Fluid used – Air	Flow distribution manifold Number of channels investigated – 11	Modified manifold shape	<ul style="list-style-type: none"> • Non-uniformity decreased by 70.71%
Gunnewiek et al. [88]	Numerical	Flow combining manifold	Vertical transpired air heater	<ul style="list-style-type: none"> • Flow reversal can occur for smaller volume flux

	Turbulent flow Fluid used – Air			<ul style="list-style-type: none"> • Increasing manifold length to width ratio increases the pressure loss • Higher suction velocity in lower channel is due to buoyancy-driven flows, possible with wider manifold • Heat transfer in non-uniform flow can lead to better efficiency than uniform flow, for buoyancy driven flows
Mohan et al. [89]	Numerical Fluid used - hydrogen, oxygen, and air Laminar flow	Z-type flow arrangement Number of channels investigated – 80	Effect of different gasses Effect of flow rate Effect of manifold size	<ul style="list-style-type: none"> • Hydrogen uniform • Air and oxygen non-uniform as Reynolds number variation due to viscosity • Less uniform with higher flow rates • More uniform with larger manifold

2.1.2 Channel parameters

As with the manifold design, channel design is also an important consideration in ensuring uniform flow distribution within the heat exchanger. A summary of channel design impact on flow distribution is given in Table 2.3, while the detailed discussion is given in the following paragraphs.

A comprehensive study of flow distributing in channels from the manifold was provided by Fu et al. [90]. The study focused on utilizing two channels and characterized the flow behavior with attention to the difference between the first and second channel. They studied square manifolds with turbulent flow to explore the flow behavior in the channels. In this regard, a laser Doppler was used for experimental investigation and CFD for its numerical comparison. The effect of flow split ratio and inlet Reynolds number was investigated. It was found that these parameters significantly influencing the flow rate in the channels. The presence of secondary flow motion downstream of the channel was found to be a common phenomenon, especially if the flow split ratio is high contributing to significant pressure loss. As the flow splits into the channel, some recirculation occurs for the flow immediately after the inlet region. The fluid after turning into the channel becomes more turbulent as compared to the turbulence level in the manifold, mainly due to the recirculation region at the channel entrance, but it changes to laminar as it progresses in the channel. In the study by Koh et al. [91], It was found that gas flow in manifold was turbulent while it was laminar in channels, this is primarily due to the smaller diameter of channels as compared to the manifold. The region in manifold just before the channel has the maximum pressure, while the region of recirculation in the channel has the minimum pressure. It was found that for

the second channel, the vortex region is smaller while the flow rate is higher as compared to the first channel. Also, the fluid is more turbulent in the second channel as compared to the first channel. The overall flow pattern was found to remain same irrespective of the order of channel.

The channel width and length are also an important parameter for flow uniformity, studied with an approximate pressure drop model developed by Commenge et al. [92]. Incompressible nitrogen was used as the working fluid with inlet and outlet placed at the opposite diagonal corners of the heat exchanger. The whole heat exchanger was divided into smaller segments and then the approximate model was used to solve for the fluid velocity and pressure drop, and the results were compared with the numerical solution [51]. The comparison showed that the results from the approximate model are in good agreement with the detailed modeling and can be used to optimize the flow distribution. The channel length is found to be inversely affecting the maximum velocity difference, where longer channels lead to better distribution. The increase in channel width leads to increase in flow non-uniformity.

The channel width was also found to be dominating factor for flow distribution by Pan et al. [93] with a mathematical model for determination of fluid flow characteristics in complex shaped manifolds. The analytical model was complimented by an electrical resistance equivalent modeling. The solution validates the analytical foundation of dividing the manifold into several smaller rectangular segments. The optimization algorithm results

in an optimum channel width to be between 300 and 500 μm , while it becomes clear that the dominating factor for flow uniformity optimization is the channel width for the case under study, while channel depth has an insignificant effect.

In continuation to the above work, Pan et al. [94] developed a method to calculate the resistance due to friction in microchannels and obtained the flow distribution characteristics. The reason of flow maldistribution is due to the presence of different frictional pressure losses in various flow paths. One of their findings was that uniform flow might be attained for larger channel length and shorter manifold length with shorter channel width. It was found that microchannel parameters are more significant than manifold parameters, and high aspect ratio is resulting in more uniform distribution. Utilizing this model, it was suggested a manifold with a centro-symmetric shaped triangle.

The effect of channel friction was studied by Weitbrecht et al. [95], using the technique of Laser-Doppler-Velocimetry (LDV) to determine the channel velocities for a Z-type flow arrangement utilizing water as operating fluid. It was found that Reynolds number increases the flow maldistribution. They used an analytical model to study the effect of various controlling parameters and found that the losses in the combining manifold are larger than the losses in the dividing manifold. It was further found that the friction loss in the channel is the controlling parameter for the total pressure loss in the heat exchanger.

The impact of channel height was studied by Alm et al. [96], by the development of ceramic micro heat exchanger with regards to its design and fabrication in Z-type configuration. They studied the variation of channel height with increasing flow velocity. It was found that for nitrogen gas, the heat transfer efficiency was almost constant with larger height giving better results at a lower velocity and worst at higher. For liquid (water), the efficiency was decreasing for higher velocity, and smaller height better at intermediate velocity, while larger height better at higher and lower velocities.

This impact of channel height was also observed in a new class of heat exchangers used in heating ventilating and air-conditioning (HVAC) systems, where the membrane collapses into the channel, reducing the available flow area or completely blocking the flow. In HVAC systems, the use of liquid desiccant results in a reduction of power consumption by 26-80% in comparison to conventional systems [97]. Liquid-to-air membrane energy exchangers (LAMEE) are used in HVAC systems to simultaneously transfer heat and moisture through the semi-permeable membrane that prevents the desiccant carry over. In these heat exchangers, the membrane is keeping the two-fluid separate, which tends to deflect towards the air side owing to the pressure differential between the high-pressure liquid and low-pressure air. Abdel-Salam et al. [98] showed the deformed membrane due to the pressure differential and a support grid was introduced to increase the membrane strength and prevent deflection [99]. The membrane deflection reduced flow and contact area, increasing the velocity and pressure drop while increasing the convective heat transfer.

In addition, maldistribution was also found in hollow-fiber LAMEE where the circular fibers vibrate at higher air velocities leading to contact between the fibers and a reduction in contact surface area. It was found that as the air velocity increases, the impact of flow maldistribution becomes severe leading up to 58% reduction in latent effectiveness at flow rate of 250 m³/h for packing fraction of 0.1 [100] while at lower flow rates of around 0.5 m³/h, about 38% reduction in performance is observed [101]. These outcomes show the importance of having uniform flow distribution in LAMEE heat exchangers as the impact on performance is significant.

Abdel-Salam et al. [102] also reported a decrease in performance for increasing the standard deviation of hydraulic diameter (representing the effect of manufacturing tolerance) and decreasing the width. It was indicated that for air channel thickness of 2 mm and standard deviation variation from 1.2 mm to 1.8 mm results in a reduction of effectiveness from 49% to 37%. While for 6 mm channel, only 1.7% drop in effectiveness was observed. An optimum channel width was also observed for each standard deviation in the hydraulic diameter. In another study Abdel-Salam et al. [103] found that for a 3-fluid LAMEE, flow maldistribution can lead to performance degradation up to 7%. To reduce the flow maldistribution in LAMEE, an experimental study on pre-tensioned membrane was conducted, to prevent its deformation due to the pressure differential. The experimental membrane was operated for eight months and no significant deformation of the membrane was found, avoiding the flow non-uniformity.

Table 2.3. A summary of the literature on channel parameters, affecting flow distribution.

Author	Type of study	Specifications	Studies conducted	Major outcomes
Fu et al. [90]	Experimental Turbulent flow Fluid used - Water Dividing	Number of channels investigated – 2 Reynolds number - 60,000	Effect of flow rate	<ul style="list-style-type: none"> • Channel is more turbulent than manifold • Recirculation region at entry to channel • Flow rate more in the second channel • The second channel is more turbulent
Commenge et al. [92]	Approximate resistive network model and finite difference Laminar flow Fluid used - Nitrogen	Z-type flow arrangement Number of channels investigated - 13, 23 and 34	Approximate pressure model compared with finite-volume model Channel parameters of length and width studied	<ul style="list-style-type: none"> • Longer length leads to uniform distribution, as pressure loss in channels significant as compared to loss in manifold • Wider channels result in increase in flow non-uniformity
Pan et al. [93]	Equivalent electrical resistance network model Fluid used – General incompressible and continuum. Laminar flow	Z-type flow arrangement Reynolds number - less than 2,000	Combined optimization of Microchannel width, depth, and number of channels.	<ul style="list-style-type: none"> • Microchannel width is most significant; larger is better leading to fewer channels required • Microchannel depth has an insignificant effect.

Pan et al. [94]	Frictional resistance model Laminar flow Fluid used - water	Z-type flow arrangement	Pressure drop and friction resistance studied	<ul style="list-style-type: none"> Channel parameters more significant than manifold parameters High aspect ratio channels preferred
Weitbrecht et al. [95]	Analytical and experimental Laminar flow Fluid used – water	Z-type flow arrangement Number of channels investigated – 10 Reynolds number - 807, 1491, 2552 and 4604	Laser Doppler used to find flow in each channel. Analytical model used to study sensitivity of system to various parameters	<ul style="list-style-type: none"> Manifold may get turbulent but channels always laminar The loss coefficient for combining manifold is larger than that for dividing manifold The total loss is mainly due to friction loss in channels Higher Reynolds number increases maldistribution
Alm et al. [96]	Numerical Fluid used – Nitrogen and water	Z-type flow arrangement Number of channels investigated - 16	Heat transfer efficiency for varying channel height and constant width Smaller channel height termed geometry A Larger channel height termed Geometry B	<ul style="list-style-type: none"> Nitrogen, fairly constant efficiency for increase in velocity Lower velocity, geometry B slightly better, higher velocity geometry A better Water, efficiency decreasing for increase in velocity, Geometry B better at lower and higher velocity, Geometry A better at intermediate velocity Efficiency of liquid phase applications limited for lower temperature ranges
Abdel-Salam et al. [98]	Experimental	Flat-plate LAMEE	Effect of membrane deflection on flow uniformity	<ul style="list-style-type: none"> Deflection of membrane reduces the air side flow area, leading to flow non-uniformity and higher pressure loss

	Laminar and turbulent flow Fluid used – Air			<ul style="list-style-type: none"> • Use of support grid suggested reinforcing the membrane
Abdel-Salam et al. [102]	Numerical Laminar flow Fluid used – desiccant solution and Air	Flat-plate LAMEE Parallel channels for air and Z-Type for solution Number of channels investigated – 21 for air and 20 for solution side	Effect of the pressure differential on membrane deflection. Impact of manufacturing tolerances on performance	<ul style="list-style-type: none"> • Membrane deflection of up to 4 mm for 5 psig is observed • For 2 mm channel, increasing standard deviation in thickness of 0.6 mm results in 12% drop in effectiveness. • For 6 mm channel, only 1.7% drop in effectiveness. • For each standard deviation, an optimum width exists
Abdel-Salam et al. [103]	Experimental Fluid used – water, Air, and desiccant solution	3-fluid LAMEE Water in Z arrangement and cross flow for air and desiccant.	Effect of air channel variations on performance Impact of pre-tensioned membrane	<ul style="list-style-type: none"> • For three fluids, performance degraded by 7% for air channel standard deviation of 0.2 • Pre-tension in membrane significantly reduced the membrane deflection

2.1.3 Number and location of inlet/outlet ports

The number of inlet and outlet port and their location along with the orientation play a significant role in flow distribution. A summary of literature is given in Table 2.4, while the discussion is continued below.

Huang et al. [104] studied use of additional flow distributing manifold with application to planar solid oxide fuel cell (SOFC). It was suggested modifying the previously used Z-type design (Design I) with two inlets symmetrically placed from the central axis and one exit at the center of the manifold, as can be seen in Figure 2.12. Design II had two connected inlet manifolds, while Design III has isolated the two manifolds such that fluid only combines in the exit manifold. Design IV is a modified version of the Design II with ten baffles or guides in the manifolds to help distribute the flow in the extreme channels. Experiments were performed by mixing water and dye to allow a charge-coupled device (CCD) camera to record the flow distribution. It was found that the design IV was the best performing design with regards to flow uniformity, which removed the local hot spots and power was increased up to 11%.

Influence of multiple inlet and outlets were studied by Balaji and Lakshminarayanan [105], with a CFD based design configuration for microchannel applications. A commercial software [65] was used for the analysis of locating the outlet at corners while inlet at the center on opposite side of the channels. However, this design created a dead zone at the corners where the flow was minuscule and susceptible to hot spots. The Reynolds number

range of 5- 200 was studied while also varying the fluid density from 1 to 100 kg/m³. After studying various inlet and outlet combinations, they recommended to have two inlets and four outlets to ensure uniform flow distribution for the majority of flow conditions.

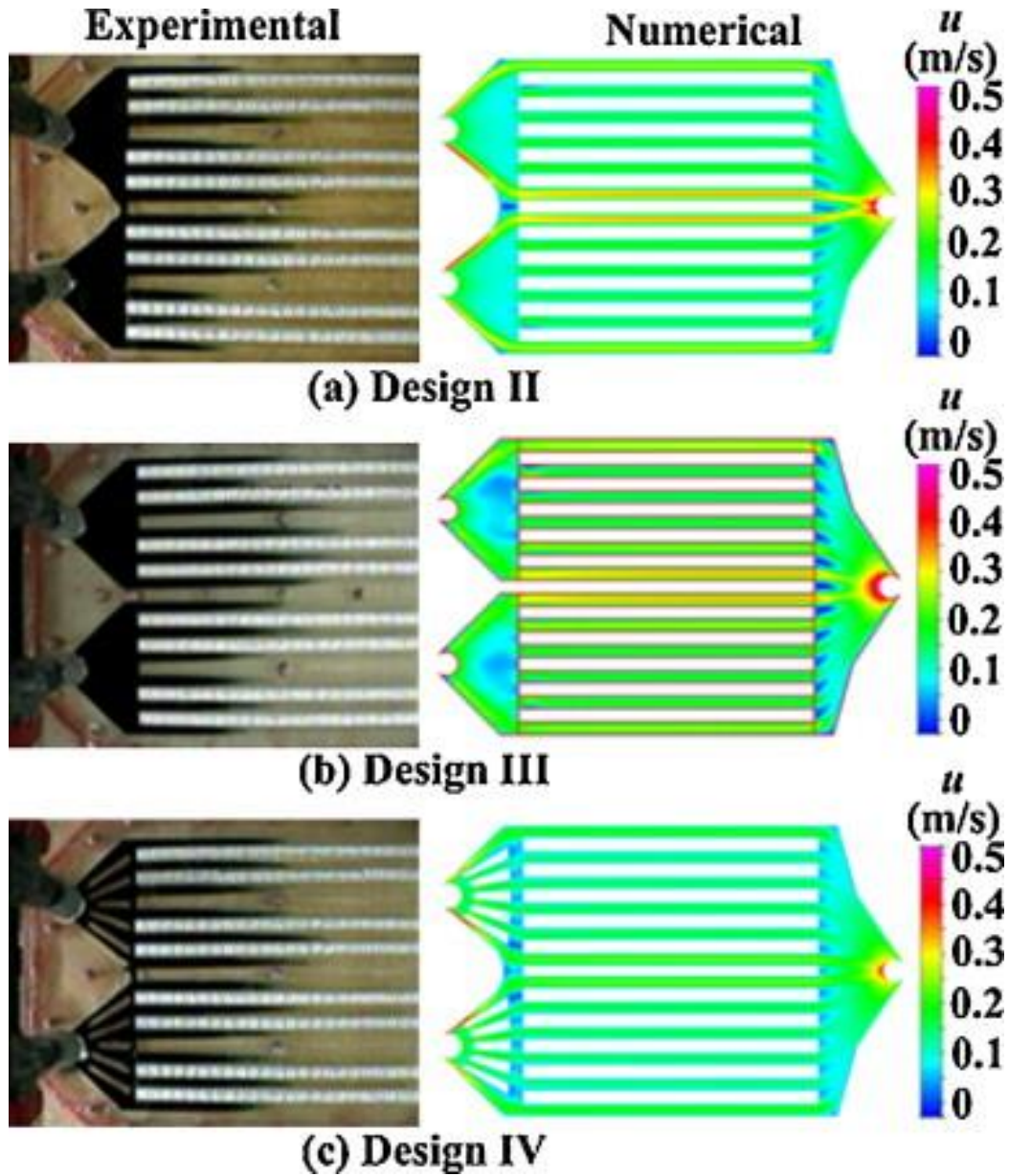


Figure 2.12. The three manifold designs considered by Huang et al. [104] for flow uniformity.

The impact of inlet and outlet size was presented by Delsman et al. [106], with a three-dimensional CFD analysis on flow distribution for microchannels using a commercial software [51]. They studied nine different arrangements for the flow distributing microchannel, out of which five main arrangements are shown in Figure 2.13. In the study, relative standard deviation was used as the quality of flow distribution, given by

$$\sigma_T = \frac{1}{\bar{m}} \sqrt{\frac{\sum_{i=1}^n (m_i - \bar{m})^2}{n-1}} \quad (2.14)$$

where, σ is relative standard deviation, m_i is flow in i^{th} channel, and \bar{m} is average flowrate per channel.

The inlet velocity was varied from 0.1 to 100 m/s ($Re=1600$) for a gas having a density of 0.68 kg/m^3 . Validation of some of the results using turbulent model was found to be within 8%. Originally 58 channels were used, then optimized to 19 by removing the solid no-flow regions. Two flow patterns were identified depending on flow velocity. Below 30 m/s, the flow rate does not affect the flow distribution while being governed by the wall friction. At higher than 30 m/s, the momentum effects become significant to affect the flow distribution. By making the inlet and outlet of double size, the relative standard deviation reduced four times while doubling the length of the flow channels reduced the standard

deviation by a factor of 1.7. The best design was having flow inlet and outlet ports parallel to the channels producing a standard deviation of 3% for the flow rate of $0.12 \text{ m}^3/\text{h}$.

The effect of variation of the inlet position for flow distribution in a parallel channel was studied by Lu and Wang [107], focusing on five configurations as shown in Figure 2.14. The variations included the channel hydraulic diameter of 1, 1.5 and 3 mm with a heat flux of 120 and 240 W. When both inlet and outlet were perpendicular to the flow channels (a), higher inlet flow rate increased the flow maldistribution while having more channels made the flow uniform. The (b) and (d) arrangements resulted in reverse flow in some of the channel making these arrangements ineffective. The (c) arrangement did not have flow recirculation and resulted in better flow distribution. Regarding pressure drop; (a) type resulted in highest pressure drop while (c) type led to the lowest pressure drop. The type (b) showed flow recirculation leading to poor performance. The types (a) and (e) had flow impinging the surface resulting in better heat transfer performance. The best thermal performance with lower pressure drop was obtained with the (c) arrangement.

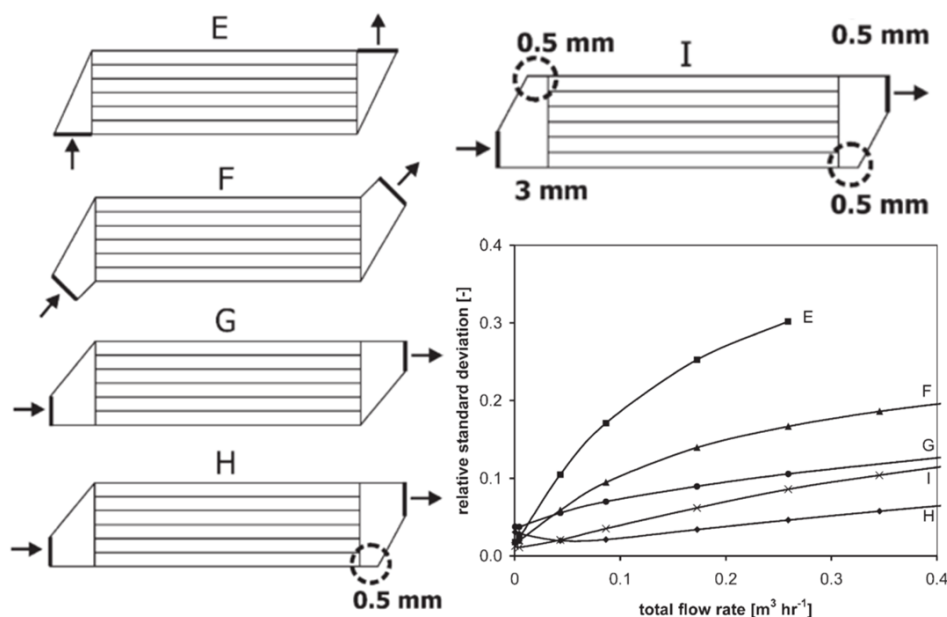


Figure 2.13. The design layouts for inlet and exit ports studied by Delsman et al. [106] and their corresponding relative standard flow deviation.

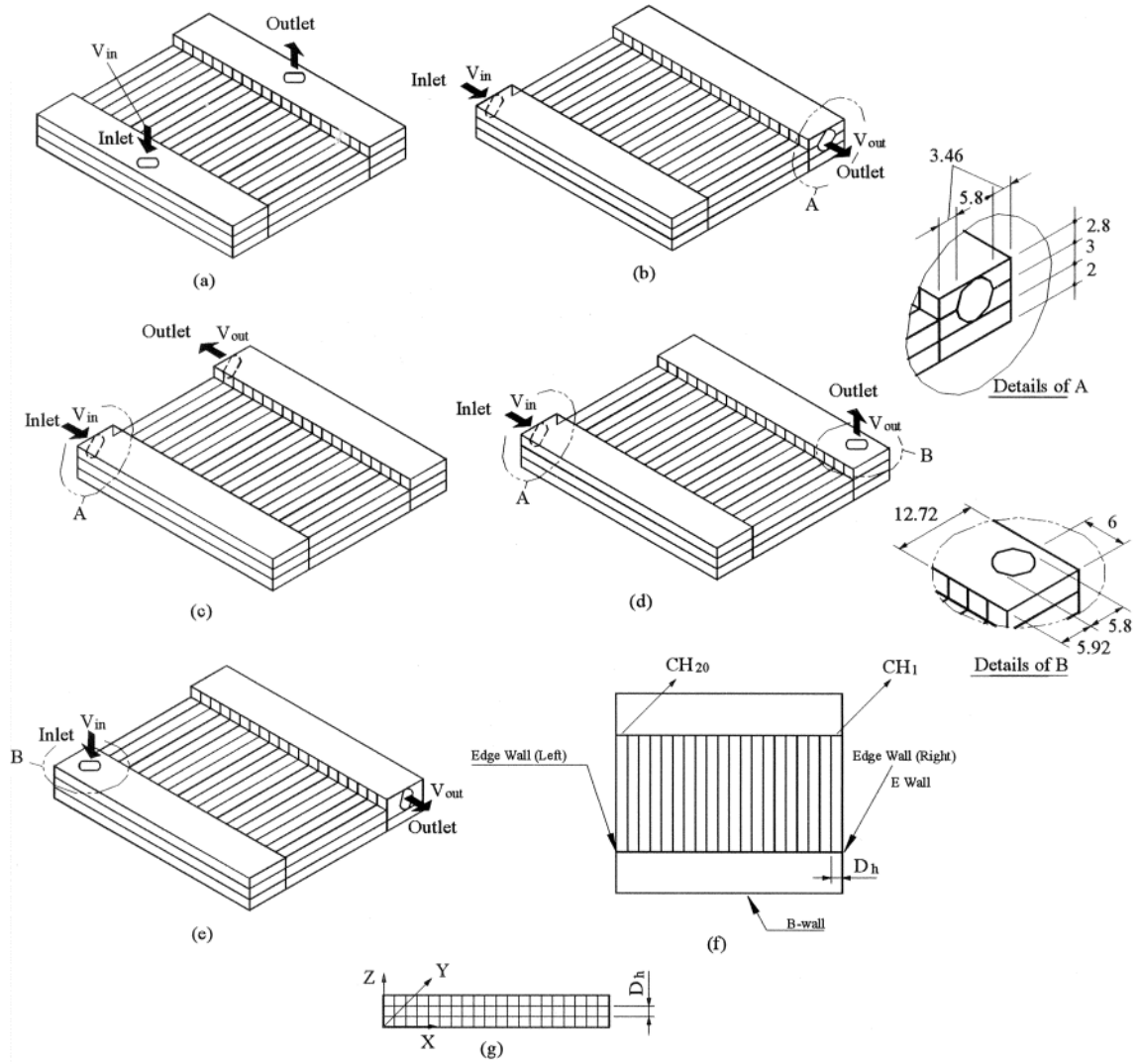


Figure 2.14. Schematic of the cold-plate, with different inlet configurations. (a) I-arrangement. (b) Z-arrangement. (c)]-arrangement. (d) L-arrangement. (e) Γ -arrangement. (f) Channel configuration of the present simulations. (g) X-Y-Z direction and D_h . Dimensions are shown in mm (Lu and Wang [107]).

Bogojevic et al. [108] studied two configurations whether the inlet/outlet manifolds are in-line with the channel domain or outside by comparing between the approximate resistance model with a numerical solution. It was found that deviations occur for higher Reynolds number and variable manifold, as additional pressure losses are ignored for the approximate solution. It was found that ports in-line with the channels result in a better distribution with an additional benefit of reduced manifold area. The effect of blocking some flow channels and studying the resulting change in flow distribution was also studied. It was found that pressure loss increased irrespective of the location of blocked channels with the significance of number of blocked channels, not their location. The location of blocked channels affects the standard deviation of flow distribution, where the blockage of middle channels results in the least deviation. The most deviation was found for blockages at the opposite side of the inlet port, with deviation for the adjacent to inlet channels to be in between the other two cases. Experimental evaluation of the heat sink revealed that the flow distribution without heat flux was uniform as fluid was a single phase, but with high heat flux, bubble formation resulted in two phase flow, leading to severe maldistribution.

Zeng et al. [109] presented a similar study with two cases, one termed right angle manifold where the inlet and outlet are in line with the channels while the oblique angle manifold has the manifold extending beyond the channels. They used a gas mixture of methanol and water in 1:1.3 molar ratio as the working fluid as it has application in steam reforming for hydrogen production. It was found that the velocity distribution was independent of the operating temperatures taken to be 400 and 450 °C and the flow distribution remained same whether the reaction was occurring or not. The results showed that more flow uniformity

could be achieved if the right-angled manifold is used. Lastly, the flow uniformity was decreasing for an increase in entrance velocity when methanol steam reforming was not taking place while if the reaction takes place an increase in entrance velocity leads to better uniformity.

A numerical investigation on the impact of asymmetrically placed inlet and outlet ports was studied with a channel parameter (G) introduced by Kim et al. [110] along with an experimental verification of two typical setups. They selected smaller channel length so that the pressure loss is occurring mainly due to the configurations of the manifold. They defined a new parameter $G = (L_{i-o}/L_m)^2 + \sqrt{W_m/L_m}$ (where L is the longer dimension and W is the shorter dimension of the manifold) and identified that the best result for flow uniformity is obtained when this parameter has a value of 0.8, while keeping the Reynolds number up to 33.2.

Table 2.4. A summary of literature on number and location of inlet/outlet ports, affecting flow distribution.

Author	Type of study	Specifications	Studies conducted	Major outcomes
Huang et al. [104]	Numerical and Experimental Fluid used – Water Laminar flow	Z-type modified to parallel with additional inlet Number of channels investigated – 12	Charge-coupled device (CCD) camera to capture flow distribution Comparison between four design layouts	<ul style="list-style-type: none"> Design IV with ten guiding vanes in manifold results in best flow distribution
Balaji and Lakshminarayanan [105]	Numerical Laminar flow	Number of channels investigated – 19 Reynolds number - 5-200	multiple inlet and outlets of circular shape location and number of inlet and outlet ports	<ul style="list-style-type: none"> Two inlets and four outlets better Results verified on low and highly density fluid.
Delsman et al. [106]	Numerical Laminar flow Fluid used - Gas	Z-type flow arrangement Number of channels investigated – 19 Reynolds number - 1600	Different angles of inlet and outlet port	<ul style="list-style-type: none"> Best layout – inlet and outlet along the channels axis Doubling inlet-outlet port size reduced standard deviation by factor of 4 Doubling channel length reduced standard deviation by 1.7 Optimal geometry depends on flow rate
Lu and Wang [107]	Numerical Fluid used – Water Laminar flow	Number of channels investigated – 20, 40 and 60 Reynolds number - 100-500 Heat flux 120-240W	Five flow arrangements Inlet velocity number of channels,	<ul style="list-style-type: none"> I arrangement highest pressure drop, J- arrangement lowest pressure drop Z-type has flow recirculation, poor performance J- arrangement, best thermal performance with lower pressure drop

Bogojevic et al. [108]	<p>Numerical and resistance network</p> <p>Fluid used - Water</p> <p>Laminar flow</p>	<p>Number of channels investigated - 40-100</p> <p>Reynolds number – 0.01-100</p> <p>Pressure losses ignored in approximate model for higher Reynolds number and variable manifold</p>	<p>Comparison approximate and numerical model</p> <p>Right angle and oblique triangle</p>	<ul style="list-style-type: none"> • Approximate model only reliable at lower Reynolds number • Better flow distribution for inlet/outlet port within the channel domain also results in smaller manifold • Pressure loss increased for blocked channels irrespective of location • Channels blocked opposite to inlet side causes most maldistribution, Middle least • Bubbling disrupts flow distribution
Zeng et al. [109]	<p>Numerical</p> <p>Fluid used - Gas mixture of methanol and water in 1:1.3 molar ratio</p> <p>Laminar flow</p>	<p>Z-type flow arrangement</p> <p>Number of channels investigated – 50</p> <p>Temperature 400C and 450C</p>	<p>Right angle and oblique triangle</p>	<ul style="list-style-type: none"> • Flow distribution independent of temperature • Right angle manifold better flow distribution with or without the chemical reaction occurring
Kim et al. [110]	<p>Numerical and experimental</p> <p>Fluid used - Water</p> <p>Laminar flow</p>	<p>Parallel flow</p> <p>Number of channels investigated – 10</p> <p>Reynolds number – 0.0332, 0.332, 3.32, 33.2</p>	<p>CCD camera for flow visualization</p> <p>20 cases with different dimensions</p> <p>Inlet and outlet offset</p>	<ul style="list-style-type: none"> • New parameter defined with optimum value of 0.8 for uniform flow • Longer manifold decreases uniformity • Wider manifold increase uniformity • Inlet-outlet distance increment increases uniformity up to a point then starts decreasing

2.1.4 Perforated plates for secondary flow distribution

In some application, a simple manifold may not be satisfactory enough to lead to a uniform flow distribution. In such cases, secondary manifolds incorporating baffle plate with openings/holes are utilized. The flow splits first in the primary manifold, then further distributes in the secondary manifold. This leads to an increased pressure drop, with improved performance due to uniform flow. A summary of literature is given in Table 2.5, with the discussion in the following paragraphs.

Jiao et al. [111] provided experimental results for flow distribution utilizing a secondary header with five and seven openings as shown in Figure 2.15. It was found that as Reynolds number increase, flow maldistribution increases. The use of secondary flow distribution header with seven opening was found to be the best configuration. Furthermore, it was found that the flow distribution is uniform when the ratio of outlet diameter of the first header and inlet diameter of the first header is equal to the outlet diameter of the second header and inlet diameter of the second header as given by Eq. (2.15)

$$\frac{D_{1(out)}}{D_{1(in)}} = \frac{D_{2(out)}}{D_{2(in)}} \quad (2.15)$$

Zhang and Li [112] presented improvements in flow maldistribution for an existing heat exchanger with the use of CFD software [51]. The study was focused on an existing arrangement being used in the industry, which is followed by experimental verification of the simulations. They recommended two stage baffle arrangement to distribute the flow more uniformly (Figure 2.16) and provided experimental validation. It was demonstrated

that at Reynolds number of 1,000, the standard deviation of flow in channels reduced from 3.47 to 0.71. Also, the equivalent diameters should be equal to get even better flow distribution.

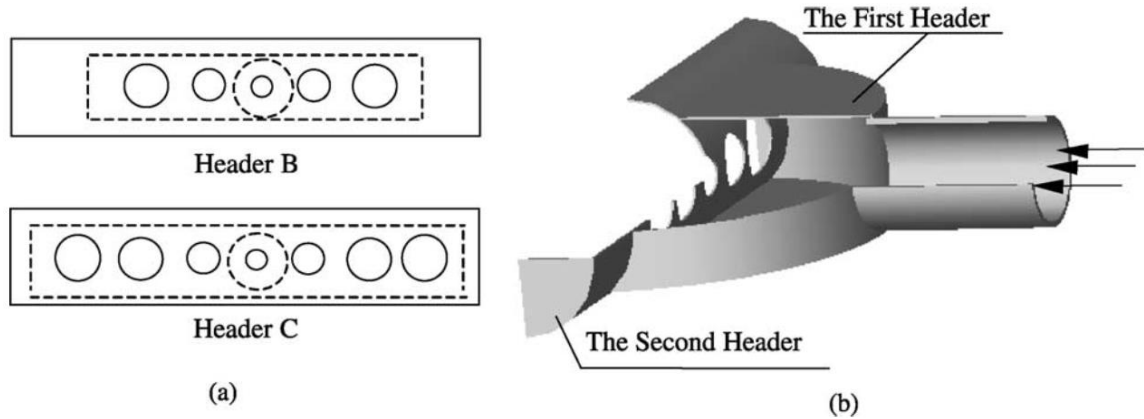


Figure 2.15. Design layout for the perforations in the secondary header. a) header B is having five while header C has seven openings, b) shows the three-dimensional layout for the secondary header arrangements. (Jiao et al. [111])

A numerical study including the impact of secondary manifold was presented by Habib et al. [113] for an air cooled heat exchange systems. The various parameters studied were including the flow velocity, a secondary distributor at the inlet, the diameter, location and geometry for the nozzle. The study showed that by reducing size of the inlet, flow maldistribution increased while doubling inlet nozzles from 2 to 4 has significantly improved the distribution by 62.5%. The presence of the second header reduces the flow

maldistribution by 50%. For this case, an insignificant effect of inlet flow velocity while slight effect of the shape of the nozzle was found on flow distribution.

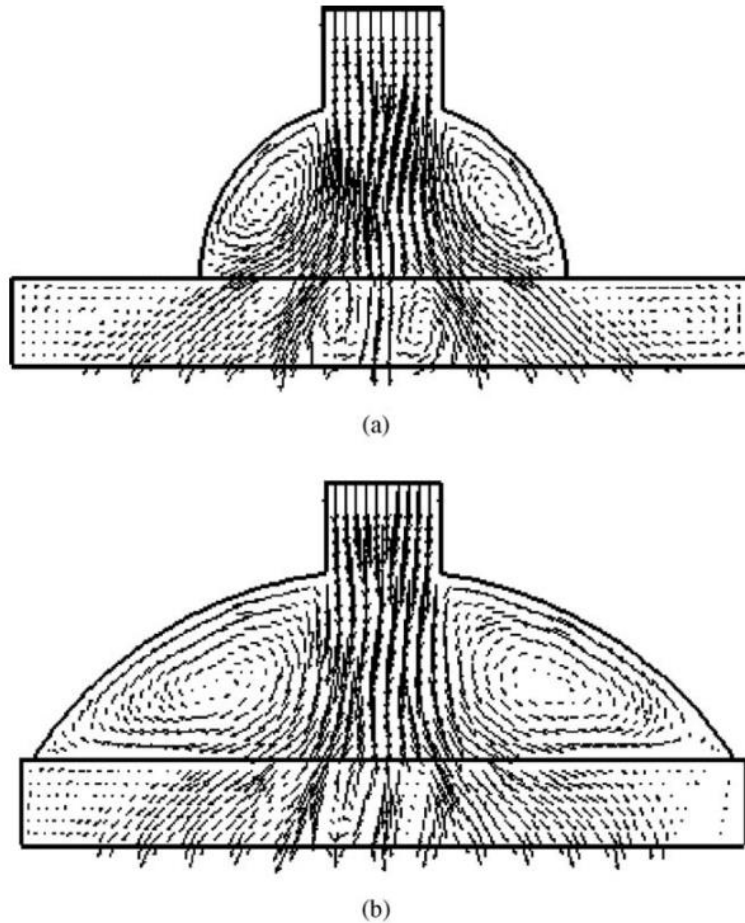


Figure 2.16. a) Type B having five holes and b) type C having seven holes in secondary distributor (Zhang and Li [112])

The utility of variable sized perforations in the baffle for secondary flow distribution was studied by Wen and Li [114]. The use of different hole diameters in a baffle was proposed, to restrict flow in some channels while allowing more flow in other channels consequently

distributing the pressure equally. The baffle consists of a single plate with holes in it to distribute the fluid evenly. This arrangement results in an increase in pressure drop leading to a reduction in mean velocities. They also studied the effect of hole distribution, baffle dimension, total area ratio, and effect of punched ratio. Later the effect of this improved design on the thermal performance was studied. It showed that the effectiveness increases with the improved layout. It was concluded that reduction of mean velocities is compensated by better flow distribution leading to enhanced overall performance.

A similar arrangement was experimentally investigated by Wen et al. [115] using the technique of Particle Image Velocimetry (PIV) to find the flow distribution behavior in a plate fin heat exchanger and the results were compared with a numerical model. They presented a base case, and two modified layouts for the holes (Figure 2.17) in the baffle placed mid-way in the manifold to distribute the flow evenly. Layout B has holes in line while layout C places the holes in a staggered arrangement. Good agreement was found between PIV and numerical results, with the layout C found to be the most efficient one in distributing the flow evenly. The punch ratio increment from the central axis resulted in lower vortices. Hence any pressure loss due to the presence of secondary baffle was compensated by the reduction in vortices. Wen et al. [116] presented a similar paper utilizing PIV to study the flow distribution in manifolds. It was concluded that the baffle is cost effective and convenient, resulting in improved flow distribution. With the use of baffle, the ratio of maximum to minimum channel velocity reduced from 23.2 to just 1.8, which is a substantial improvement.

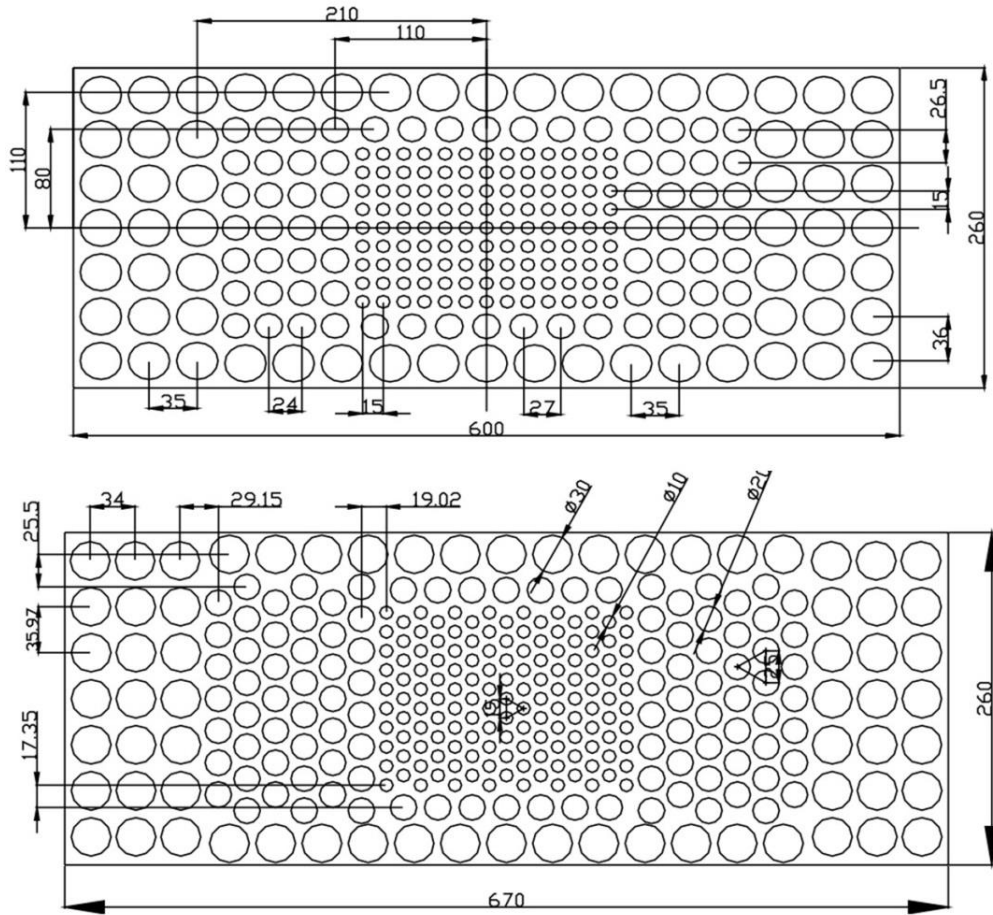


Figure 2.17. Layout B and layout C for the perforated baffles used for flow distribution by Wen et al. [115]

Lalot et al. [117] focused on an electrical heater to study the effect of flow distribution on its performance with a secondary distributor in the middle of manifold. It was found that for some cases if the inlet is not designed properly, it leads to reverse flow in some of the regions rendering them ineffective. Equation (2.16) was used to find the ratio (η) of highest velocity to the lowest velocity within the channels, utilizing the average pressure drop

across the heat exchanger and the inlet dynamic pressure (i.e. kinetic energy per unit volume).

$$\eta = \sqrt{\frac{\frac{1}{2}\rho V_0^2 + \Delta p_{av}}{\Delta p_{av}}} \quad (2.16)$$

It is evident from the equation that if the average pressure drop is larger, it will lead to better flow distribution. If the flow distribution is not uniform among the two heating elements, then the power has to be increased to achieve the same temperature. They used air as the operating fluid with Reynolds number variation from 10,000 to about 40,000 i.e. within the turbulent region. Their numerical study was performed with the use of CFD software [118], utilizing the k-epsilon turbulence model. The use of bigger manifolds has been a way to improve the flow distribution up to a certain limit. For better flow distribution, a perforated mesh is used so that the flow get distributed by the mesh/grid before entering the channels. The use of this type of grid at the middle of manifold allows the flow to be diverted along the channel axis and then flows towards the channels with axial velocity component. They applied Bernoulli's equation to two regions, first for the region between the inlet tube and channel outlets and second from the outlet channels to the outlet of the manifold where the flow exits the heater. They applied the velocity ratio parameter η to a condenser, counter flow heat exchanger, and crossflow heat exchanger and showed that as the velocity ratio decreases, the effectiveness reaches to a value of unity, thus showing the impact of proper flow distribution on the overall performance of the heat exchanger. The maximum impact was for the cross-flow heat exchanger, where flow maldistribution can lead to a decrease in effectiveness by as much as 25%.

A similar study on impact of performance with baffled secondary header was provided by Ismail et al. [119]. They used alternate large and small holes in the perforated plate similar to the design studied by Wen et al. [115]. The resulting velocity distribution is shown in Figure 2.18, with baffles case showing better flow distribution. It was found that the overall pressure drop reduced by 34% when the baffle was used, indicating the usefulness of baffle.

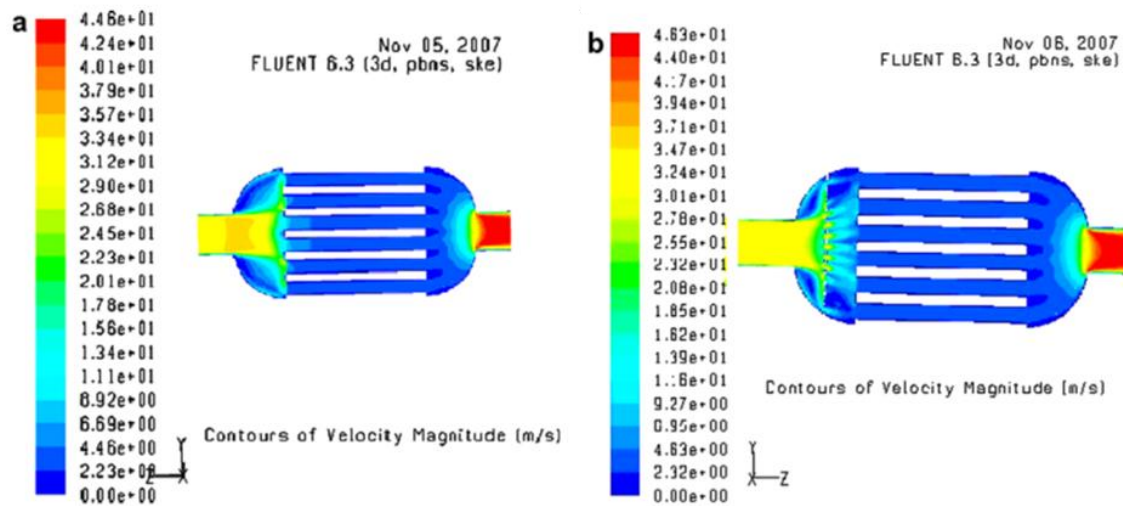


Figure 2.18. The velocity contours in a) base case and b) secondary baffle (Ismail et al. [119])

Table 2.5. A summary of literature on perforated plates for secondary flow distribution, affecting flow distribution.

Author	Type of study	Specifications	Studies conducted	Major outcomes
Jiao et al. [111]	Experimental Fluid used - Water	Two designs for secondary header by increasing the number of openings Number of channels investigated - 30 Reynolds number – 1100- to 3000	Effect of inlet pipe header, and secondary header diameter.	<ul style="list-style-type: none"> Flow maldistribution increases with Reynolds number, a correlation is presented Header C configuration is best, having seven openings Diameter ratio given for best results
Zhang and Li [112]	Numerical Laminar and turbulent flow Fluid used - Air	Number of channels investigated - 13 Reynolds number - 500-3000 Inlet at middle of manifold	Secondary flow distribution mesh in the manifold.	<ul style="list-style-type: none"> More non-uniformity at higher Reynolds number Secondary header better for flow distribution Type C with seven holes, with width of secondary header
Habib et al. [113]	Numerical Turbulent flow Fluid used - Oil	Distributing manifold, flow perpendicular to channel plane Number of channels investigated – 32 (16 in axisymmetric solution)	Inlet velocity Diameter Shape Number and location of nozzles	<ul style="list-style-type: none"> Inlet velocity has no effect on flow distribution Inlet size reduction leads to higher velocity, causing more non-uniformity. Elliptic nozzle leads to better distribution More channels result in better flow distribution as less velocity in each

				<ul style="list-style-type: none"> Increasing number of holes in secondary header increases uniformity
Wen and Li [114]	Numerical Fluid used – Nitrogen Highly turbulent flow	Number of channels investigated – 43 Reynolds number - 10k-1,000k	Effect on hole size of plate on flow distribution Plate with various sized hole distributed throughout to distribute the flow	<ul style="list-style-type: none"> Baffle with holes improve flow distribution Holes with staggered arrangement with punch ratio increasing
Wen et al. [115]	Experimental and Numerical Turbulent flow Fluid used - Water	Number of channels investigated – 21 Reynolds number - 6,000	Comparison between PIV and Numerical Effect of different layout for holes in the secondary distributor	<ul style="list-style-type: none"> Staggered arrangement of holes better than inline arrangement Punched ratio increment from the central axis reduced vortices
Lalot et al. [117]	Analytical and Numerical Turbulent flow Fluid used - Air	Number of channels investigated - 128 Reynolds number - 10k-40k	Use of perforated plate as secondary Study of heat exchanger performance and variation in effectiveness calculated depending on flow distribution	<ul style="list-style-type: none"> Better distribution with perforated plate More non-uniformity, less heat exchanger effectiveness Decrease in effectiveness 7% for condensers and counter flow 25% for crossflow
Ismail et.al. [119]	Numerical Turbulent flow Fluid used - Air	Number of channels investigated – 6 Reynolds number - 2000 to 15,000	Effect of baffle plate on flow distribution and pressure drop	<ul style="list-style-type: none"> Use of secondary baffle reduced pressure drop by 34% while improving the flow distribution

2.1.5 Flow distribution with two phase flow

Flow distribution in manifolds with the two-phase flow is a complex behavior. Very few analytical models have been developed owing to the complexity, with majority of the work focusing on experimental studies for evaluation of flow patterns and distribution behavior. A summary is given in Table 2.6, while the discussion is summarized hereafter.

Datta and Majumdar [120] developed a finite difference procedure to model the flow behavior of two-phase medium with and without the heat transfer effects. The mass and momentum equations were solved using the numerical iterative techniques, with application to three arrangements including U-type, Z-type and mixed type (Figure 2.19) by varying the boundary conditions. They validated the model, experimentally, for water and air mixture representing two-phase flow and found an excellent agreement. The results for mixed arrangement were found to follow the basic principles and logic while giving the best flow distribution among the three arrangements. Increasing in heating load led to steam formation in some channels resulting in higher maldistribution between the flow channels. Higher flow rates also result in steam formation in some channel while not in others. The moisture content was also found to be decreasing with increasing flow rate.

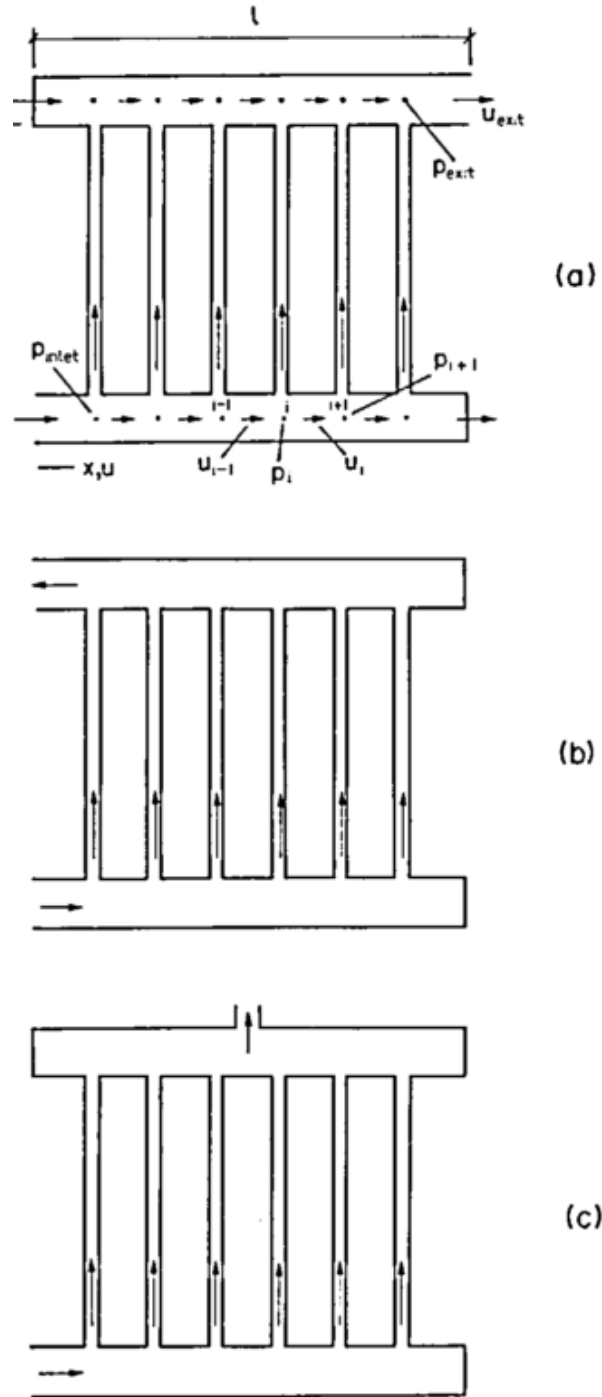


Figure 2.19. a) Parallel b) reverse and c) mixed flow manifold used by Datta and Majumdar

[120]

Balasubramanian and Kandlikar [121] studied flow distribution and pressure drop for a rectangular channel heat exchanger with hydraulic diameter of 333 μm undergoing flow boiling. Images were used to follow the movement of bubbles while measuring the temperature and pressure. A relation was established between the pressure drop variations and the associated flow patterns. The experiments revealed a liquid layer on the surface while the bubbles move through the channel as slug flow. The nucleation from the liquid film was occurring at a faster rate as compared to the channel nucleation. In addition to film boiling, there was some bubble generation from the bulk of the liquid itself. They observed the maximum velocity of the bubble to be 5.3 m/s and reported the frequency of pressure drop increased as the temperature of the surface was increased. The presence of slug flow was observed for the majority of the cases where the surface temperature was high. For particular conditions, it even led to backflow in some of the channels which resulted in increased flow maldistribution.

In contrast to boiling flows, Bobbili et al. [122] studied flow distribution keeping in view the thermal-hydraulic aspects of the design for condensing flows. A mathematical model is presented, having flow rate-based heat transfer coefficient relation. They validated their model with ε -NTU assuming pure uniform two phase flow. The parameters of flow distribution index, pressure and mass flux ratio have been studied. The cooling water temperature was found to be increasing if the NTU and pressure was increased. This led to higher heat transfer due to condensation. The mass flux ratio was also found to increase the heat transfer. The flow distribution also plays a significant role; uniform flow increases effectiveness and condensation.

Controlling of flow distribution with the use of microvalves in each channel for two-phase flow at low Reynolds number was studied by Martin et al. [123], seeded with solid or bubbly impurities. They also used a direct numerical solution technique to model the bubble as a solid particle, which is a reasonable assumption for lower Reynolds number flow and validated the results with experimental data. Microvalves were incorporated such that if any flow maldistribution is detected from exit velocities, they actuate accordingly to make the flow uniform. One application of this model is to the flow maldistribution due to fouling or clogging of sections of the channels.

A circular baffle in a circular manifold was discussed by Marchitto et al. [124], with the two-phase flow in 16 vertical channels being fed by horizontal manifold. It was found that an increase in area ratio between the manifold and total channel area resulted in an increase in liquid flow maldistribution while a decrease in gas maldistribution was found. The change in area was achieved by the placement of nozzles at the junction between the manifold and channels. They reduced the size of the inlet to the manifold by making a nozzle inlet resulting in jet formation in the manifold, this increased the gas superficial velocity and was found to be beneficial at higher gas velocities, while at intermediate velocities, a deteriorating case was observed. Hence the combined use of nozzle at manifold inlet and orifice at channels inlet would lead to a better flow distribution within the heat exchanger. Marchitto et al. [125] further mentioned that gas flow rate is the

controlling factor for flow distribution, increasing it improves gas flow distribution while reducing liquid flow distribution.

A secondary cylindrical distributor with holes was also introduced by Marchitto et al. [126], who presented upward flow in vertical channels for air and water mixture with the principal focus being the use of secondary header in the form of a cylindrical tube with inline holes on one side. It was found that the distribution was enhanced for all configuration of the tubes in comparison to its absence. Further optimization revealed that best distribution was possible by making the holes facing downwards ($\theta=180^\circ$ as shown in Figure 2.20) and by having eight openings (8hA or 8hB) instead of 16. The size of the hole was also varied, it was found that smaller hole does increase the pressure inside the manifold, but this has no effect on the flow distribution. Likewise, the flow distribution is not dependent on the header pressure drop which decreases with increase in gas velocity.

Lee and Lee [127] presented work on protruding channels in the manifolds on the two-phase flow distribution. They compared the results with the base case of no protrusion and found that an optimum protrusion depth exists for the best flow distribution. For no protrusion, more liquid was flowing in first channels, but with protruded channels, more liquid started flowing in latter channels. The protrusions increase the flow mixing, resulting in reduced effect of variation in mass quality and larger protrusion led to small localized recirculation with a distribution pattern. Finally the impact of channel shape for two phase flow distribution was studied by Premkumar and Mahesh [128], with circular and square

shapes for air and water mixture flowing in distributing manifolds. It was found that better flow distribution is obtained with square shaped manifold, with the same volume fraction. Furthermore, an increase in the air velocity results in an increase in water flow and reduction in air flow in the last channels.

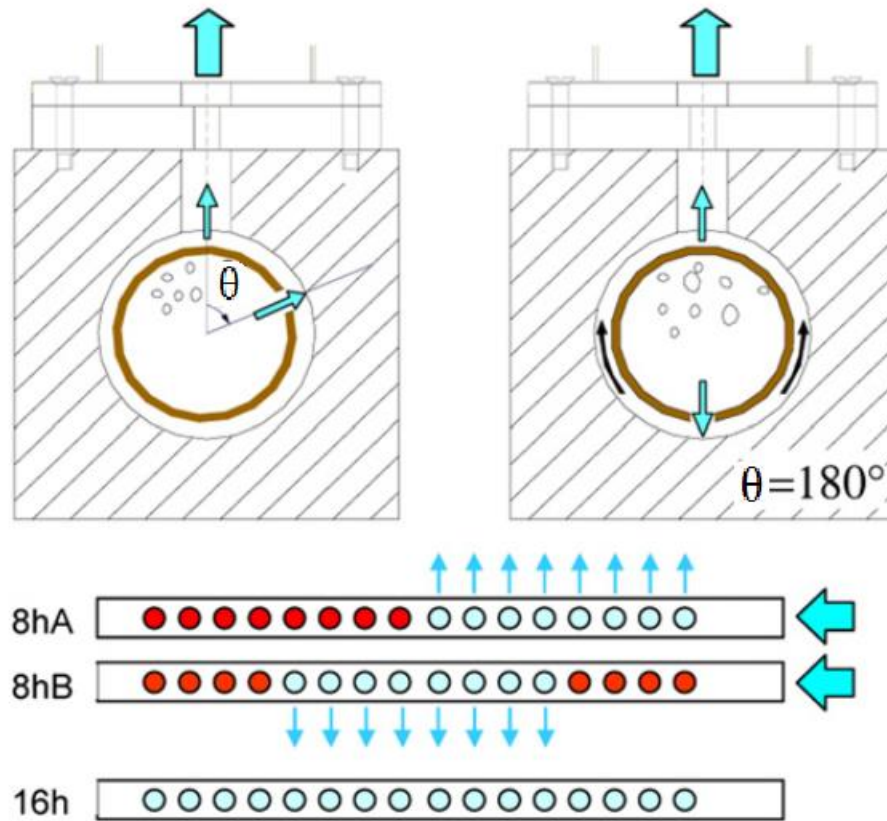


Figure 2.20. The secondary cylindrical flue shown with openings at angle θ for upwards vertical flow in channels. The arrangement of with all 16 openings and two configurations for eight opening are also shown. (Marchitto et al. [126])

Table 2.6. A summary of literature on flow distribution with two phase flow.

Author	Type of study	Specifications	Studies conducted	Major outcomes
Datta and Majumdar [120]	Finite difference Fluid used - Water and air	U and Z-type flow arrangement Heat flux studied – 50, 100, 150 and 200 kW Exit steam pressure 68.9 bar Inlet water temperature 204 °C	With and without heat transfer Steam formation depending on heat flux	<ul style="list-style-type: none"> • Mixed flow arrangement found to be best • Non-uniformity increase with heating load • Dryness fraction increases with decreasing flow rate • Higher flow rate results in steam formation in some channels while non in other
Balasubramanian and Kandlikar [121]	Experimental Fluid used – boiling water	Number of channels investigated – 6	Two-phase flow patterns and pressure drop Effect of temperature on bubbling frequency and flow rate on overall pressure drop	<ul style="list-style-type: none"> • Nucleate boiling under annular flow conditions • High interface velocity, growth reduces upon contact with wall • Pressure drop increases with increasing flow rate • Frequency of pressure drop fluctuations increases with increase in surface temperature up to 109 C. • Reverse slug flow in some channels
Bobbili et al. [122]	Analytical (Bassiouny and Martin [129])	U-type plate condenser Number of channels investigated –98	Effect of non-uniformity on thermal performance and exit vapor conditions	<ul style="list-style-type: none"> • Effectiveness and condensation rate decrease for increasing non-uniformity • Output steam quality remained virtually same

	Fluid used – Process steam		Effect of mass flow rate, flow configuration, number of channels	<ul style="list-style-type: none"> Performance and condensation deteriorated as maldistribution increases
Martin et al. [123]	Numerical, fractional-step scheme Fluid used - Water and air Laminar flow	Number of channels investigated – 3 Reynolds number – 196 and 1895	Flow maldistribution due to vapor bubbles in channels Valve activation based on flow rate, utilized to actively remove bubbles in channels	<ul style="list-style-type: none"> Numerically simulated results match with experimental Use of valves actively reduced flow maldistribution
Marchitto et al. [124]	Experimental Fluid used - Water and air	Distributing manifold for upwards vertical flow in channels Number of channels investigated – 16	Effect of area ratio Nozzle at inlet to manifold to create jet	<ul style="list-style-type: none"> Increase area ratio, gas distribution improved but liquid distribution decreased Nozzle improved liquid flow distribution at higher gas superficial velocities, but worsening effect for intermediate velocities
Marchitto et al. [125]	Experimental Fluid used - Water and air	Distributing manifold for upwards vertical flow in channels Number of channels investigated – 16	Effect of liquid and gas superficial velocities	<ul style="list-style-type: none"> Gas flow rate more important for flow distribution than liquid flow rate Increase in gas flow rate improves its distribution while reducing liquid distribution Secondary distributor found to be better for uniform flow distribution
Marchitto et al. [126]	Experimental	Distributing manifold for upwards vertical flow in channels	Impact on cylindrical distributor with 8 or 16 in-	<ul style="list-style-type: none"> Improvement with the secondary distributor, best when hole opposite to channel flow (holes

	Fluid used - Water and air	Number of channels investigated – 8	line holes as secondary distributor	<p>facing down for upwards flow in channels $\beta=180^\circ$)</p> <ul style="list-style-type: none"> • Eight holes instead of 16 yields better distribution • Smaller hole size does lead to higher pressure in manifold, but no effect on flow distribution • Header pressure drop decreases with increasing gas velocity; flow distribution is not dependent on it
Lee and Lee [127]	<p>Experimental</p> <p>Fluid used - Water and air</p>	<p>Distributing manifold</p> <p>Number of channels investigated – 4</p>	Effect of channels protruding into manifold studied	<ul style="list-style-type: none"> • For zero protrusion, more liquid flow into initial channels and then decreasing to the last channels • For protruded channels, less liquid flow in first channels and increasing towards the last channels • Optimum 3 mm protrusion found. • Larger protrusion reduces the size of recirculation • Effect of mass quality diminishes as protrusion increases, due to increased mixing
Premkumar and Mahesh [128]	<p>Numerical</p> <p>Fluid used - Water and air</p>	<p>Distributing manifold</p> <p>Number of channels investigated – 10</p>	Effect of shape of manifold, circular or square	<ul style="list-style-type: none"> • Square shape has better flow distribution than circular; volume fraction remains same • Increasing air velocity forces more water in the last channels

2.2 Analytical modelling

Analytical models are based on fundamental mathematical formulations representing the physical behavior. The momentum balance in the manifold is used to account for flow branching, while the flow is modelled by mass and momentum conservation equations. A summary of the analytical models developed for flow distribution manifolds is given in Table 2.7 while the forthcoming text provides a detailed discussion.

Acrivos et al. [130] presented work on distributing and combining manifolds where they assumed that downstream conditions have no effect on the upstream flow. They came up with an iterative method to solve the governing set of equations and found that the larger area of manifold results in better flow distribution. They also pointed that as the flow leaves the manifold, there is some increase in pressure termed as pressure recovery due to decrease in velocity along the manifold. It was found that non-uniformity depends on this pressure recovery and the frictional pressure drop.

Kubo and Ueda [131] presented formulae to calculate the flow rate ratio for a dividing and combining manifold, with the use of two dimensionless parameters of divided flow ' σ_D ' and confluent flow ' σ_c '. These parameters involve components like pressure recovery factor, the resistance coefficient of branch pipes and the area ratio of header to the pipe. They further presented equations and procedure to solve the flow distribution when the inlet is in line with the channels rather than perpendicular. The results were successfully validated against experiments performed using water as the working fluid.

Majumdar [132] presented an analytical model for combining and dividing the flow header for inviscid flow. The continuity, momentum, and orifice equations were applied to a control volume for both dividing and combining manifold and channels and solved using finite difference method.

The continuity equation was simplified to

$$\frac{d}{dx}(\rho V A_m) = -\frac{\dot{m}}{L_{c-c}} \quad (2.17)$$

where L_{c-c} is the distance between the two consecutive channels and the mass flow rate is given by

$$\dot{m} = \rho \left[\left(\frac{1}{\sqrt{1 + K_{eq} + (fL/D)}} \right) \sqrt{2\Delta p / \rho} \right] A_c \quad (2.18)$$

The momentum equation leads to

$$\frac{d}{dx} \left(K_L \frac{\rho V^2}{2} \right) = \frac{dp}{dx} - \frac{f \rho V^2 P}{8 A_m} \quad (2.19)$$

where K_L is the bending loss from the manifold to channel and P is the perimeter. The experimental verification was carried out for turbulent flow regime for viscous fluids. Two flow governing parameters were defined that control the flow distribution in the manifolds ($P_1 = ND_c^2 \sqrt{K_L} C_d / D_m^2$) and ($F_1 = 4fLD_m / ND_c^2$). It was demonstrated that flow uniformity can be achieved with low values of both parameters.

Pigford et al. [133] presented a model for an analytical solution for turbulent flow distributing manifolds. The experimental setup was needed to evaluate some flow coefficients, later used in the analytical model which is based on momentum balance and Bernoulli's equation. The governing equation that was derived, can be expressed as

$$u'u'' - 2\left(\frac{km_{out} - km_{in}}{h_c}\right)uu' - \frac{km_{out}s(s-1)}{h_c}u' - \frac{h_m}{2h_c}\left[u^2 + s\left(\frac{1-s}{2} + u\right)^2\right] = 0 \quad (2.20)$$

where k_m is momentum recovery factor that quantifies the portion of initial momentum that is conserved as fluid crosses the control volume and s is +1 for U-type and -1 for Z-type of flow field. h_c and h_m are friction parameters for channels and manifold, respectively. The resulting flow distribution was validated by experimental results with a good agreement, eventually applied to the two design configurations of U and Z-type. It was concluded that larger manifolds are better while for larger channels, the impact of the smaller header is more tolerable.

Bassiouny and Martin [129] presented the first analytical approach in understanding the flow distribution in a plate heat exchanger. Their model was useful in calculating the velocity and pressure distribution in the manifolds as well as the flow distribution among different channels along with the total pressure drop in the heat exchanger. The procedure started with the mass balance and momentum balance and then utilized Bernoulli's equation to formulate the basic fundamental flow distribution equation. For the distributing type manifold, the governing equation was simplified to

$$\frac{1}{\rho} \frac{dP}{dx} + \frac{f}{2D} U^2 + (2 - \beta) U \frac{dU}{dx} = 0 \quad (2.21)$$

Similarly, for the combining type manifold, the governing equation can be expressed as

$$\frac{1}{\rho} \frac{dP^*}{dx} - \frac{f^*}{2D^*} U^{*2} + (2 - \beta^*) U^* \frac{dU^*}{dx} = 0 \quad (2.22)$$

where β is the ratio of axial velocity component to total velocity in the manifold and ‘*’ is used for the parameters of the outlet manifold. A parameter “m” was defined whose value is based on the type of flow if the flow rate is decreasing in distributing manifold m^2 will be positive while it would be negative for flow gathering manifold. It is expressed as,

$$m^2 = \left[\left(\frac{2 - \beta^*}{2 - \beta} \right) \left(\frac{A_m}{A_m^*} \right)^2 - 1 \right] \frac{2 - \beta}{\zeta_c} \left(\frac{NA_c}{A_m} \right)^2 \quad (2.23)$$

where ζ is the average total head loss coefficient for channel flow. A zero value for m^2 means purely uniform distribution. Therefore, based on this model the value of m^2 should be kept below 0.1 to ensure uniform distribution. The results for U-type heat exchanger suggested that there exists an area ratio of inlet to outlet manifold, which would lead to uniform flow. Hence by varying the area ratio, uniform flow can be obtained for almost all heat exchangers. In continuation to the analytical modeling of flow distribution in U-type heat exchanger, Bassiouny and Martin [134] presented analytically modeling for the Z-type of flow arrangement. It was concluded that the difference occurs only when the m^2 value is negative, otherwise the results for U and Z-type are identical.

Shen [135] focused on combining and dividing manifolds to study the effect of friction on flow distribution. They used the analytical model of governing equations to determine the flow distribution in the channels and noted that as the fluid velocity varies, friction factor also varies accordingly. Thus, a constant friction factor assumption may not be applicable for lower Reynolds number. However, in the turbulent region, friction factor variation follows the 1/4th power of velocity and its effect is less significant. Therefore, a constant friction factor may be a good approximation for turbulent flow regions. They introduced a new parameter λ which is a ratio of the friction loss to the turning loss. This factor is then used to observe the effect of friction on the flow maldistribution. It was found that for dividing manifolds, maldistribution may decrease or increase, based on the area ratio of the channel to the manifold while for combining manifold the friction always results in additional flow maldistribution.

Kikas [136] studied solar water heating systems using variable and constant temperature fluid at lower Reynolds number having reverse and direct circuits. The junction pressure losses were obtained from the experimental data available while modeling the flow as algebraic equations. The model revealed that the flow uniformity does not depend on the number of channels or the total flow rate in the manifold, rather the flow distribution is only a function of the location of each channel with regard to the other. The application of such model in laminar flow range can be used as an initial guidance to estimate the performance of the flow in the turbulent region. The pressure loss occurring in the branching flow needs some further investigation to be understood properly, while some

parametric studies of flow rate and non-uniform temperature have not been included in the study.

Sparrow et al. [137] studied a combining manifold while presenting a virtual analytical model on spreadsheet to predict the flow distribution. The model was validated with numerical results showing the closeness of 1% for local and 4% for global parameters. The upstream channel flow results in flow circulation while the downstream jets get deflected along the manifold channel because of the upstream manifold fluid flow. Fang et al. [138] used a similar discrete model to find the analytical evaluation of the pressure distribution within the manifold. Their work was for combining and dividing manifold sections and comparison with experimental results for the selected cases.

Maharudrayya et al. [139] provided an analytical solution, which is validated by numerical solution, for U- and Z-type of flow patterns, while studying the effect of area ratio and Reynolds number on the flow distribution. The individual channel size was reduced with increasing number of channels for the same header dimensions and found that an increase of pressure drop with better flow distribution. The U-type has monotonic flow i.e. more flow in first channels and less flow in the last channels, in contrast to Z-type which shows less flow in the middle channel and more flow in both side of the channels. It was further noticed that Z-type has flow distribution dependent on flow rate, while U-type is independent of flow rate. That is, U-type has better flow distribution as compared to Z-type for higher flow rate.

Wang [140] unified the models available for flow distribution within the manifolds. He used the momentum balance and Bernoulli's equation to present an analytical model to calculate different flow parameters within the manifold and flow channels. The momentum balance in the manifold with a branched channel, as shown in Figure 2.21, results in the following equation:

$$pA_m - \left(p + \frac{dp}{dx} \Delta x \right) A_m - \tau_w P_h \Delta x = \rho A_m \left(u_m + \frac{du_m}{dx} \Delta x \right)^2 - A_m u_m^2 + \rho A_c V_c u_c \quad (2.24)$$

where τ_w is the wall shear stress.

Using mass balance and shear stress formulation, this equation is further simplified to the following governing differential equation:

$$\frac{1}{\rho} \frac{dP}{dx} + \frac{f}{2D_m} u_m^2 + (2 - \beta) u_m \frac{du_m}{dx} = 0 \quad (2.25)$$

The Bernoulli's equation is used to incorporate the pressure losses in the manifold and channels. The bend losses are also included as:

$$P - P_c = \frac{1}{2} \rho \zeta u_c^2, \quad \zeta = \left(1 + K_L + f_c \frac{L_c}{D_c} \right) \quad (2.26)$$

Introducing the above pressure loss equation in Eq.(2.25) and introducing two coefficients to get:

$$\frac{dw}{dx} \frac{d^2w}{dx^2} + 3Q_w w \frac{dw}{dx} + 2R_w w^2 = 0 \quad (2.27)$$

Where $Q_w = \frac{(2-\beta)}{3\zeta} \left(\frac{A_c N}{A_m} \right)^2$ and $R_w = -\frac{fL}{4D_m \zeta} \left(\frac{A_c N}{A_m} \right)^2$

The solution of (2.27) yields the following equation for the flow rate in the channels [140]:

$$v_{ci+1} = \left(0.5 \exp \left(-B_i \frac{x_{i+1}}{2} \right) \right) \left(\frac{ \left(B_i \left(\sin \left(\sqrt{3} J_i \frac{1-x_{i+1}}{2} \right) \right) \right) + \left(\sqrt{(3)} J_i \left(\cos \left(\sqrt{(3)} J_i \frac{1-x_{i+1}}{2} \right) \right) \right) }{ \sin \left(\sqrt{(3)} \frac{J_i}{2} \right) } \right) \quad (2.28)$$

where J is a function of R_w and Q_w and i is the channel number.

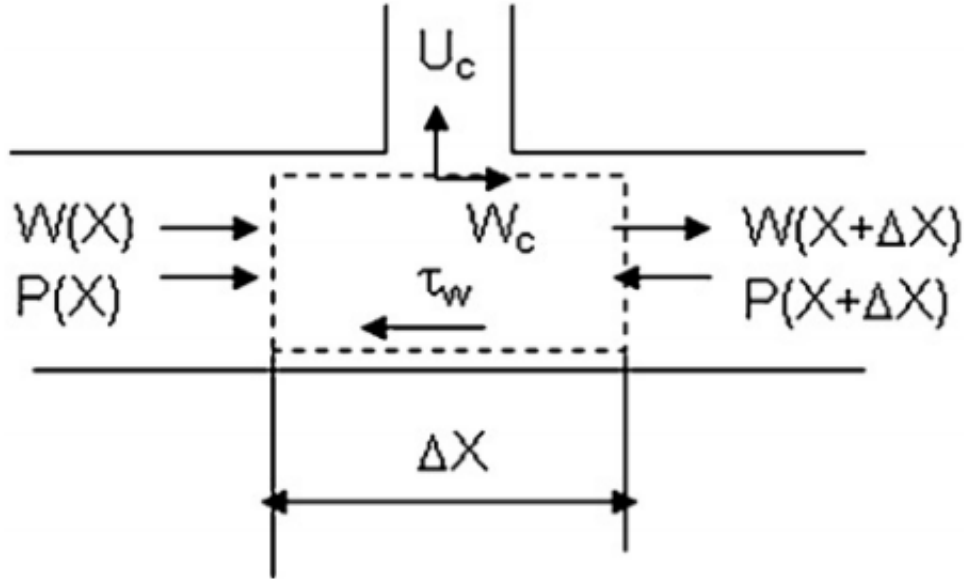


Figure 2.21. Momentum balance on the manifold with branching channel (Wang [140])

This analytical model was earlier validated in two separate articles. The application on U-type manifold was done by Wang [141]. This model includes both frictional and inertial effects on flow distribution. The effect of friction and momentum was found to be working opposite, where friction increases the pressure drop and momentum effect increases the pressure. Hence a balance of these two effects can result in uniform flow distribution. They showed that Bassiouny and Martin [129] model was neglecting friction effect while Maharudrayya et al. [139] neglected the momentum effect. The model application on Z-type was studied by Wang [142] and compared with the existing models revealing the generality of this model. He found that smaller values of channel to manifold area ratio ($M = (A_c N) / A_m$) results in better flow distribution for the Z-type flow.

Wang [140] discussed three main parameters in the current model that control the flow distribution and pressure drop, showing that better flow distribution can be obtained if the combined losses of friction and bend (ζ) are reduced by smooth surfaces and rounded bends. Furthermore, a decrease in parameter E (the length to width ratio of manifold) i.e. larger manifold width leads to better uniformity, but the impact is not as significant in comparison to the area ratio parameter M. A decrease in M value reduces the port size to force flow in initial channels.

The application of this model to design and analysis of fuel cell has been discussed by Wang and Wang [143], by providing the steps that must be followed to use the model for the solution of a particular design problem. They studied single serpentine, multiple

serpentines and straight parallel channel configurations (Figure 2.22), where a serpentine acts as single channel twisted to cover the whole area, while multiple channels reduce the individual channel lengths for the same base area. If the channel length was increased, it would result in reduction of channel number. It was found that for a decrease in channel number, pressure drop, and flow uniformity increases. A balance between the number of channels and channel length is needed to result in the lowest pressure drop with acceptable flow distribution for application to fuel cell.

Wang [144] further reviewed the flow field distributions for fuel cells and discussed numerous design configurations. He concluded that the flow distribution and pressure drop could be adjusted by the five characteristic parameters,

- 1) The ratio of total loss coefficient of channels, $\zeta \left(= 1 + K_L + f_c \frac{L_c}{D_c} \right)$.
- 2) The ratio of header length to header diameter, $E (= L_m / W_m)$.
- 3) The ratio of areas of the inlet header to the outlet header, $(A_{m, in} / A_{m, out})$.
- 4) The ratio of the total flow area of channels to the cross-sectional area of the header, $M (= A_c N / A_m)$.
- 5) The pitch between channels, L_{c-c} .

Wang and Wang [145] further utilized this model to compare the effect of various design parameters on U- and Z-type flow distribution. It was found that Z-type flow is in general more sensitive to the variation of structural parameters. U-type was found to be better for

small resistance ζ and larger M , however Z-type was found better for larger ζ and smaller M . Also a decrease in E reduced the pressure drop with an increase in flow uniformity.

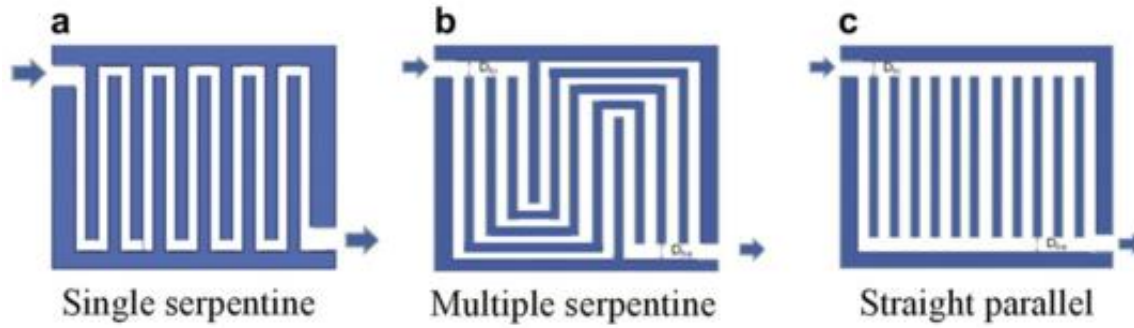


Figure 2.22. The three flow field configurations, a) single serpentine with the longest channel length, b) multiple serpentine, with four channels and comparatively smaller channel length, and c) a conventional Z-type arrangement with smaller channel length and a maximum number of channels (Wang and Wang [143]).

Table 2.7. A summary of the literature on analytical modeling for flow distributing and combining manifolds.

Analytical Modeling				
Author	Type of study	Specifications	Studies conducted	Major outcomes
Acrivos et al. [130]	Experimental and Analytical Fluid used- air	Distributing and combining manifolds Reynolds number 22,830	Flow distribution Effect of number of channels	<ul style="list-style-type: none"> • Pressure recovery and pressure drop due to friction are factors determining non-uniformity • Reducing channels enhances flow distribution until friction becomes dominant for increased channel gap
Kubo and Ueda [131]	Analytical and experimental Fluid used - water	Distributing and combining manifolds	Central inlet parallel to channels	<ul style="list-style-type: none"> • Dimensionless parameters of divided flow factor and confluent flow factor presented • Formulae are given to calculate flow rate ratio for each branch pipe • Pressure and flow rate ratio increases with the number of channels
Majumdar [132]	Analytical - Finite difference Fluid used - General	Number of channels investigated - 10	Design charts generated Two non-dimensional parameters presented	<ul style="list-style-type: none"> • Chart is given for flow imbalance and overall pressure drop for combining and dividing manifold • Can be extended to two-phase flow • Low values of F_1 and P_1 for flow uniformity
Pigford et al. [133]	Analytical	U and Z-type flow arrangement	Effect of pressure difference on flow uniformity	<ul style="list-style-type: none"> • Application of analytical model • Header should be greater than all tubes

	Turbulent flow Fluid used - Air	Number of channels investigated – 5 and 50 for U type and 10, 20 and 100 for Z type Reynolds number 53,730		<ul style="list-style-type: none"> Larger tubes allow more tolerance in header pressure changes
Bassiouny and Martin [129]	Analytical Fluid used - General	U-type flow arrangement Dimensionless distance to study presence of channels\	Velocity distribution in channels Area ratio based on new parameter m	<ul style="list-style-type: none"> More uniformity by varying the area ratio, regardless of number of channels and shape $m^2 = 0$, pure uniform flow, m^2 should be less than 0.1 for practical cases
Bassiouny and Martin [134]	Analytical Fluid used - General	Z-type flow arrangement Dimensionless distance to study presence of channels\	Velocity distribution in channels	<ul style="list-style-type: none"> Pressure drop in channels increase along the manifold direction
Shen [135]	Analytical Turbulent flow Fluid used - Air	Combining and distributing manifold Dimensionless distance to study presence of channels	Two parameters α (Area ratio) and β (L/D ratio) effect of friction on flow distribution	<ul style="list-style-type: none"> Friction most effect on the moderate area ratios Friction increases maldistribution in combining β greater than $\pi/2$, friction reduces maldistribution β less than $\pi/2$, friction increases maldistribution
Kikas [136]	Analytical Laminar flow	Z and U-type flow arrangement	Experimental pressure loss coefficients.	<ul style="list-style-type: none"> Z is better than U type Independent on channel numbers, rather position of channels

	Fluid used - Water	Number of channels investigated - 10 and 20		
Sparrow et al. [137]	Quasi-Analytical Numerical	Number of channels investigated - 20	Overall pressure drop and volumetric flow rate with flow pattern	<ul style="list-style-type: none"> Overall pressure drop increases with volume flow
Fang et al. [138]	Analytical and experimental Turbulent flow	Number of channels investigated – 15 for dividing and 8 for combining	Pressure distribution	<ul style="list-style-type: none"> The model can accommodate local disturbances in segments like T-junction Pressure distribution in manifold in good agreement with the experiments
Maharudraya et al. [139]	Analytical and numerical Laminar flow	Z and U-type configurations Number of channels investigated – 38 and 75 Reynolds number tested - 58, 233, 584 and 1871	Manifold to total channel area ratio Smaller channels width for same header areas increases channel number from 38 to 75	<ul style="list-style-type: none"> Smaller channels width increases pressure drop and enhancing flow distribution U-type has monotonic flow variation while Z-type has minimum flow in the center U-type flow distribution is independent of flow rate U-type better than Z-type for higher flow rates
Wang [140]	Analytical model	Flow distributing manifold	Three parameters of friction losses, length to diameter ratio and channel to manifold area ratio.	<ul style="list-style-type: none"> Uniformity can be achieved when <ol style="list-style-type: none"> Reduce friction losses of bend and friction ζ, Decrease $E=L/D$ ratio for manifold for better uniformity, Decrease $M=(A_{port}*n/A_{Manifold})$ ratio, it reduces the port size to force flow in initial channels

				<ul style="list-style-type: none"> • Effect of E not very significant effect as compared to M
Wang [141]	Analytical model	U type	Application of model	<ul style="list-style-type: none"> • Good agreement with previous work, more generalized model • Friction increases the pressure drop, and momentum effect increases the pressure
Wang [142]	Analytical model	Z type	Application of model	<ul style="list-style-type: none"> • Good agreement with previous work, more generalized model • Smaller values of M results in better flow distribution for the Z-type flow
Wang [143]	Analytical model	Single serpentine, multiple serpentine and Z-type arrangement.	<p>Application of the model to design of fuel cells.</p> <p>Single serpentine longest single channel, Z-type most number of smallest channels.</p>	<ul style="list-style-type: none"> • Pressure drop and flow uniformity increases, for a decrease in channel number • Balance between the number of channels and channel length for optimum design
Wang [144]	Review paper and Analytical model	Review on different flow arrangements with application to fuel cells	Two additional parameters studied after previous work (Wang [140])	<p>d) Ratio of the areas of the inlet header to the outlet header, (A/A_e)</p> <p>e) Pitch between channels, S</p>
Wang and Wang [145]	Analytical model	Z-type and U-type flow arrangements	Comparison of Z and U-type flow arrangement.	<ul style="list-style-type: none"> • Z-type flow more sensitive to structural parameters • U-type was found to better for small resistance ζ and larger M • Z-type was found better for larger ζ and smaller M • Decrease in E reduces the pressure drop with an increase in flow uniformity

2.3 Literature on split flow and manifold heating

Shell and tube heat exchangers have many industrial applications for transferring between the hot and fluid flow streams due to their ability to exchange a large amount of heat energy for low cost and easily maintainable designs. It consists of a header accepting fluid from one side and dividing the flow into the smaller tubes. The tubes from the outside are exposed to the other fluid stream normally at a lower pressure than the tube fluid. The flow should be uniformly distributed in all the tubes otherwise the performance may decrease for the heat exchanger. It is important to note that the tubes with lower flow rate would undergo an increase in temperature making them susceptible to fouling, thus degrading the thermal-hydraulic performance of the heat exchanger. Although internal fouling can be dealt with during the routine maintenance, but the external fouling is difficult to handle.

Krasnikova [146] presented five configurations for-shell-and-tube heat exchanger, including spiral and ribbing wires to increase performance. They found that for no mixing case with isolated channels, a small flow maldistribution of 5% is enough to disrupt the temperature distribution. This is handled by having mixing in one of the flow configurations, which shows no temperature variation even for 10% flow maldistribution. Furthermore, maldistribution effects are amplified as NTU increases. This can also be seen in the work of Cowans [147], who showed that NTU can be increased from 22 to 167 if an automatic balancing heat exchanger is used. He presented the idea of having converging and diverging channels or notches placed in the channels to automatically minimize the impact of flow maldistribution.

Fleming [148] studied a balanced counter flow heat exchanger, with an ideal situation of having same flow in each channels representing uniform flow condition. They found that for thermally paired channels, performance degradation becomes very severe as NTU increases. Therefore, increasing NTU would lead to an insignificant gain in performance, thus flow should be made uniform instead of increasing NTU to increase the performance. Chowdhury and Sarangi [149] studied two cases with non-uniformity either on one side or on both sides for a multi-pass heat exchanger. One of their assumptions is that the local Nusselt number is constant indicating fully developed flow throughout the tubes. They found that if the normalized flow distribution is small then the effect on performance is negligible as it implies uniform flow. The effect of flow distribution is more pronounced for higher NTU as compared to lower NTU heat exchangers.

Ambrose and Knudsen [150] studied the local heat transfer coefficient variation on the shell side for tubular heat exchangers. They used a constant flow rate of air and found that the average heat transfer coefficient varied by the six-tenths power of the mass velocity. The number of baffles increases both the pressure drop and Nusselt number with similar rate while decreasing tube spacing decrease the average heat transfer rate. In the eddy zone, a decrease of 15% in heat transfer coefficient was found. In an another study, Lee and Knudsen [151] provided empirical relations to determine the shell side heat transfer coefficient and an average value for the annular clearance between tube and orifice which showed increasing clearance reduced the heat transfer rate. The decrease in baffle space caused an increase in heat transfer; however, they found that the local heat transfer coefficient is constant at the tube cross-section. Zeng and Zhang [152] investigated the

local and local mean Nusselt number in addition to overall performance and the pressure drop. They found the Nusselt number variation for a standard case and then utilized fluid flow distributor, improving the heat transfer performance by about 10%.

Li and Kottke [153] studied the local heat transfer coefficient on the surface of tubes in a staggered arrangement for a shell and tube heat exchanger. The fully developed condition is assumed for calculation of local mass transfer coefficients while heat transfer coefficient is found by using similarity between mass and heat transfer coefficients. They found that the non-axisymmetric trend of heat transfer coefficient with the circumferential difference being greater than the axial difference. In an experimental investigation, Perez and Sparrow [154] used Naphthalene sublimation technique to find the shell-side heat transfer coefficients. They reviewed several analytical techniques for the determination of Nusselt number and compared with the new experimental technique and found good agreement for the ideal case where the leakage and bypass effects are ignored. Qu and Mudawar [11] studied a microchannel heat sink and found the Nusselt number variation along the surfaces, they found that the Nusselt number varies across the periphery, with values approaching zero near the corners.

Vásquez-Alvarez et al. [72] presented a numerical study for the design of circular manifolds with channels or baffles at outer sides of flow channels. Their study revealed that by making the manifold circular with an inlet at the center had better flow distribution, but this arrangement had slightly reduced flow in the peripheral channels. They suggested

the channel bundle diameter smaller than the manifold diameter, this resulted in uniform flow across all channels. Wasewar et al. [87] studied manifold shape modification wherein they used a conventional and a modified longitudinal design, a significant improvement in flow uniformity was observed. In addition, the velocity contours showed how the diverging manifold distributes the velocity vector direction, thus enabling better flow distribution in such systems.

It is important to note from the above discussion that the manifold may not be adiabatic in actual operating conditions, thereby resulting in degradation of thermal-hydraulic characteristics of the heat exchanger due to non-axisymmetric flow. The main goal of the present work is to investigate the performance of a heat exchanger with flow distribution from a larger tube to smaller tubes under different (manifold) operating conditions, which is, to our knowledge, scarcely addressed in the open and grey literature. In this regard, the fundamental relations for heat transfer are first verified for a standard flow system. Then we proceed with the analysis of more complicated systems.

2.4 Literature on analogies

Chilton-Colburn [155,156] presented the Colburn analogy, proposing that the friction factor coincide with the product of Stanton number and two-thirds power of Prandtl number, for turbulent flow inside tubes and flow parallel to surfaces. Colburn [155] plotted Reynolds number against the dimensionless group of Stanton number and $Pr^{2/3}$. The data included flow over a flat plate and internal turbulent flow. The analogy was found not to

be valid due to higher friction factor for cross flow over tubes. For mass transfer equipment like dehumidification, condensation, absorption, and rectification, the classic analogy was obtained [156] leading to the famous j-factor. It was found that sufficient degree of certainty is possible for design calculations, though exact values are not obtained. The analogy was also found applicable to flow inside tubes, flow over flat surfaces and flow across tube banks for heat transfer calculations and falling film absorption columns for mass transfer processes.

Webb [157] provided a critical evaluation pertaining to the Reynolds analogy and analytical solution for turbulent flow, developing a new correlation with resulting error within $\pm 2\%$ of the published data. The Reynolds number was in the range 10k - 1000k. The new Stanton number equation was derived as

$$St = \frac{\frac{C_f}{2}}{1.07 + 9\sqrt{\frac{C_f}{2}} \times \frac{(Pr-1)}{Pr^{1/4}}} \quad (2.29)$$

The combination of Prandtl-Karman equation with the above equation, resulted in improved results over the range of Prandtl number $1 < Pr < 50$. For high Prandtl number fluids in turbulent flow, Petukhov and Popov Eq. (2.30) is shown to provide better results in comparison with the Dittus-Boelter and Colburn equations.

$$St = \frac{\frac{C_f}{2}}{1.07 + 12.7\sqrt{\frac{C_f}{2}} \times (Pr^{2/3} - 1)} \quad (2.30)$$

Mahulikar and Herwig[158] studied the Reynolds analogy for temperature dependent properties of the flowing fluid in a pipe flow. It was found that the Stanton number increases with decreasing friction factor for variable properties, while both are directly proportional, for a uniform properties case. They further verified that the Sieder-Tate's Nusselt number correlations are based on the theory of the Reynolds analogy. Their study showed that for the lower velocity of 0.05 m/s, the Chilton-Colburn analogy is valid but becomes invalid for velocities higher than 3.0 m/s.

Duan and He [159] extended the Reynolds analogy for slip and transition flow within micro- and nano-sized channels. The work was based on scientific hypothesis, rather than theoretical substantiation, as the heat and flow behavior in slip and transition flow is complex. The model further utilized second-order slip boundary conditions to incorporate the transition flow regime. This method provides simple and useful initial approximations for engineering applications.

Lin [160] focused on a flat plate under laminar convection to study different analogies and developed analogies for Prandtl numbers less than 0.1. He showed that the Nusselt number analogies agree for Prandtl number of unity while unsatisfactory results are obtained for other Prandtl numbers. The Colburn and numerical results match for the whole range of Prandtl numbers. He also presented Colburn analogy factor for uniform surface temperature ($j_T = 0.98$) and heat flux cases ($j_H = 0.71$).

Lin and Lin [161] presented similarity solutions for flow over wedges under laminar forced convection cases. The work includes uniform wall temperature or heat flux conditions for very small Prandtl numbers to very large ones. A new parameter was defined to introduce the appropriate similarity variable, resulting in similarity equations that are solved using Runge-Kutta [162,163] scheme. The results were compared with the exact solution and exact agreement was obtained.

Belnap et al. [164] included the effect of wall roughness in the Reynolds analogy, for rectangular cross-sectional flow channel between Reynolds number of 10,000 to 25,000. They used conduction sublayer Stanton number to accommodate the temperature reduction near rough elements. It was reported that Nusselt and Stanton numbers show differences for rough surfaces from the standard correlations. The new Reynolds analogy for rough surfaces was verified with experimental results for $Pr = 1$ at atmospheric operating conditions.

Dalkilic et al. [165] investigated the Reynolds analogy for annular condensation in laminar flow within a vertical tube. The work was based on experimental study, to obtain both friction factor and heat transfer coefficient. These values were compared with the models available in the literature and the friction factor was found to be within $\pm 30\%$ deviation, while the two-phase friction factor had $\pm 20\%$ deviation. Another experimental verification was carried out by Kulkarni et al. [166] to study the ratio of Nusselt to Sherwood number (termed 'analogy factor' in mass transfer). They used thermal boundary layer technique to study heat transfer coefficient while naphthalene sublimation technique [167] to study the

mass transfer coefficient for a range of Reynolds number in laminar and turbulent flow conditions. The thermal boundary layer technique uses Fourier's law inside the measured thermal boundary layer profile. Furthermore, the wall temperature was obtained by extrapolation of the linear temperature profile within the conduction layer to the wall surface. Their laminar experiments showed variation within $\pm 2\%$ of theoretical value (0.677) of analogy factor, while it remained constant at 0.677 for the turbulent case.

Gimbutis [168] studied turbulent flow for flow in a tube and film flowing due to gravity. For turbulent flow, the main region is near the wall that affects the flow. The developing region for the internal- and external-flow follows different phenomenon and any analogy is merely a coincidence. However, the developed or stabilized flow has analogous velocity distribution, and similar laws govern the frictional resistance for both the turbulent internal flow and film external flow. This led the authors to contemplate the possibility of similar heat transfer analogy and found that for Reynolds number higher than 2500, the heat transfer is also analogous for both the cases. Hence, same formulae can be used for practical models of such processes. The analogy does not remain valid for flow in corrugated tubes or corrugated surfaces.

The complex turbulent flow includes factors affecting the regular turbulent flow like non-isothermy, forces of gravity, electromagnetic, centrifugal, and mass transfer from the wall surface with alternating configuration. For such complex flows, Potemkin [169] showed that superimposition principle and the generalized analogy between momentum and heat

transfer provides simplified analysis for complex turbulent flow near the wall. The method was applied to the initial section of smooth pipe, porous surface with blowing velocity, and for the sudden change of the wall temperature; obtaining reliable results for each case.

Han and Goldstein [170] studied heat and mass transfer analogies for the turbine blade performance, by obtaining the Nusselt number for constant wall temperature experiment and Sherwood number from constant concentration condition. For flow over a flat plate with Prandtl number of 0.7, the ratio of Nusselt to Sherwood number (analogy factor) compares well with the value of 0.677 in laminar region, while 0.557 is suitable for turbulent flow. The same values hold true for the blade end region as well as the upper and lower wall surfaces with one exception of the high vortex region at the bottom where the value of 0.495 is found to be suitable. It is further mentioned that this study did not include the effect of secondary flows and the uncertainty in heat transfer measurements at the leading edge.

For flow in a square channel, Steeman et al. [171] studied $2.5 \text{ m} \times 2.5 \text{ m}$ domain with 0.1 m inlet and 0.2 m outlet. Considering unity Lewis number, simultaneous heat and mass transfer yielded excellent results, whereas separate heat and mass transfer was suitable only when Grashoff number was equal for both cases. For non-unity Lewis number, Chilton-Colburn analogy yielded better results. Regarding the reference conditions, it was found that the mass averaged conditions for the domain was a suitable choice.

The use of analogies for fouling analysis was presented by Wang et al. [172] where they determined the fouling deposition by mass transfer coefficient and fouling removal by fluid friction coefficients. Three analogies were used to compare the mass transfer i.e. Prandtl, Von-Karman and Chilton-Colburn analogies. The Von-Karman was found to be most suitable for cooling tower fouling, the resulting correlations developed have the potential to provide the fouling potential for actual water used in cooling towers.

For rough and irrigated surfaces, Laptev and Lapteva [173] determined the coefficients of heat and mass transfer from the classic analogy. The skin friction laws are used to determine the conservation properties and the effective velocity. The procedure utilized mean volumetric rate of energy dissipation to find the shear stress near the surface. The comparison with experimental values was within $\pm 20\%$, with sources of error being factors of actual turbulence intensity and boundary layer separation. The work showed how the fundamental analogies can be implemented for complex cases by the proper use of relevant equations and such analogies can provide engineering data for the heat and mass transfer, when the drag is known. The analogy for flow with dispersed particles was obtained by Laptev and Lapteva [174] by computing the heat and mass transfer coefficients around solid particles under laminar flow in addition to the droplet internal mass transfer coefficient. The mass extraction from spherical droplets showed good agreements, with the model extended to turbulent external flow. The use of such model is helpful for extraction devices.

Churchill [175] made a comprehensive critique on the analogies of heat and mass transfer that are based on algebraic manipulations. He found functional and numerical errors in the calculations for turbulent flow in round tubes and flat plate. The heat flux variations in the fluid, the molecular flow near the wall and in the core, are some of the neglected or misrepresented variations for the flow conditions. He found that the Reynolds analogy for circular tubes is not valid for Prandtl number of unity, rather for a value of 0.86 based on exact integral solutions. The same observation was noted for the flat-plate solution. With regards to Colburn analogy, for Prandtl 0.86 the ratio $(Nu/RePr^{1/3})$ is not valid, rather it should be Stanton number $(St = Nu/RePr)$. This is in line with his analysis that the analogy is valid for $Pr = 0.86$, not $Pr = 1.0$. Further, for large values of Prandtl number, Nu is proportional to $Re \times (C_f/2)^2$, not to $Re \times (C_f/2)$, as suggested by the Chilton-Colburn analogy. He also found that all analogies fail for Prandtl number approaching zero.

Keeping in view of the fact that there are discrepancies seen in the literature regarding the type of flows and their corresponding analogies, the current work is mainly focusing on four different flow types, to compare the applicability of the Reynolds and Chilton-Colburn analogy (with the focus only on the heat transfer analogy, j_H , and not on mass transfer analogy, j_m). The work includes four different fluids, with air ($Pr = 0.7$), modified air ($Pr = 0.86$), modified air ($Pr = 1$) and water ($Pr = 6.9$), under laminar- and turbulent-flow conditions. The results are provided in a graphical form to show the behavior of each factor in the developing and developed conditions and are also listed in tabular form table for quick comparison of difference values.

Chapter 3

GOVERNING EQUATIONS FOR NUMERICAL

ANALYSIS

This chapter deals with the numerical model used for the solution of flow distribution in the manifold. The first section presents the governing equations, second with the boundary conditions and third with the assumption used in the numerical modeling. The fourth section present the parameters used for the analysis of such systems and the fifth section presents validations for the numerical work done.

3.1 Governing equation

The phenomenon of flow and energy transfer are modelled mathematically with the use of conservation equations. These equations include mass, momentum, and energy conservation, and are represented in term of partial differential equation. The solution of the flow behavior involves dividing the domain into smaller grid. The values of relevant variables at these grid points map their complete distribution, provided the grid is fine enough to capture the details. The relevant variables include, velocity, pressure, temperature, etc.

The flow within the channels is governed using the mass, momentum, and energy conservation equations, respectively, defined as,

Continuity equation:

$$\frac{\partial}{\partial x_i}(\rho u_i) = 0 \quad (3.1)$$

Momentum equation:

$$\frac{\partial}{\partial x_j}(\rho u_i u_j) = -\frac{\partial p}{\partial x_i} + \frac{\partial}{\partial x_j} \left[(\mu + \mu_t) \frac{\partial u_i}{\partial x_j} \right] \quad (3.2)$$

Energy equation:

$$\frac{\partial}{\partial x_i}(\rho u_i T) = \frac{\partial}{\partial x_i} \left[\left(\frac{\mu}{\text{Pr}} + \frac{\mu_t}{\text{Pr}_t} \right) \frac{\partial T}{\partial x_i} \right] \quad (3.3)$$

where μ_t is the eddy viscosity specified by the turbulent model defined as

$$\mu_t = \frac{C_\mu \rho k^2}{\varepsilon} \quad (3.4)$$

where $C_\mu = 0.09$ is an empirical constant.

For turbulent flow, K- ε model is used that solves two additional equations for turbulence kinetic energy, and rate of dissipation, ε ,

$$\frac{\partial}{\partial x_i}(\rho u_i K) = \frac{\partial}{\partial x_i} \left[\left(\mu + \frac{\mu_t}{\text{Pr}_K} \right) \frac{\partial K}{\partial x_i} \right] + G_K - \rho \varepsilon \quad (3.5)$$

$$\frac{\partial}{\partial x_i}(\rho u_i \varepsilon) = \frac{\partial}{\partial x_i} \left[\left(\mu + \frac{\mu_t}{Pr_\varepsilon} \right) \frac{\partial \varepsilon}{\partial x_i} \right] + C_{\varepsilon 1} \frac{\varepsilon}{k} G_K - C_{\varepsilon 2} \rho \frac{\varepsilon^2}{k} \quad (3.6)$$

where $C_{\varepsilon 1} = 1.44$, $C_{\varepsilon 2} = 1.92$, $Pr_K = 1.0$, and $Pr_\varepsilon = 1.3$ are constants and G_K is the turbulence kinetic energy generation rate given by

$$G_K = -\overline{\rho u_i u_j} \frac{\partial u_j}{\partial x_i} \quad (3.7)$$

3.2 Boundary conditions

At the inlet, flow at constant uniform axial velocity and temperature is assumed i.e.

$$u = u_i, \quad T_i = 298 \text{ K} \quad (3.8)$$

At the exit, zero static gauge pressure is assumed so that the pressure at the inlet represents the measure of pressure losses in the domain.

$$p_e = 0 \quad (3.9)$$

At the walls, no-slip condition is used for the flow velocity,

$$u = v = w = 0 \quad (3.10)$$

while the thermal behavior at walls is either uniform temperature or uniform heat flux (Dirichlet boundary condition).

$$T_w = \text{cont} \quad \text{or} \quad q_w'' = \text{const} \quad (3.11)$$

The Fourier law is used to find the heat transfer coefficient at the wall on the fluid side

$$q'' = -k_f \left(\frac{\partial T_f}{\partial n} \right) = -k_w \left(\frac{\partial T_w}{\partial n} \right)_w \quad (3.12)$$

For isothermal boundary condition, the heat flux is calculated by

$$q'' = h_f (T_w - T_f) \quad (3.13)$$

For heat flux boundary condition, the wall temperature is calculated by

$$T_w = T_f + \frac{q''}{h_f} \quad (3.14)$$

At symmetry, the normal gradient of all variables is set to zero and there is no normal velocity.

$$\left. \frac{\partial \phi}{\partial y} \right|_{\text{At symmetry}}, v = 0 \quad (3.15)$$

where ϕ is a general variable.

3.3 Assumptions

Following are the main assumptions for the numerical model,

- (a) Steady flow behavior is modeled i.e. no variation with time.
- (b) Constant properties are assumed, i.e. no variation due to temperature.
- (c) Flow regime is laminar, unless specified to be turbulent.

- (d) No-slip wall boundary condition is used; i.e., all velocity components are same as wall velocity, (non-zero for only the top wall in Couette flow, otherwise zero for all walls).
- (e) The wall is assumed thin i.e. wall conduction is neglected.
- (f) Uniform inlet velocity and temperature is assumed.
- (g) The pressure at the outlet is zero gauge.
- (h) The wall is assumed thin i.e. wall conduction is neglected.
- (i) Uniform inlet velocity and temperature are assumed.
- (j) The viscous energy dissipation is neglected in all the flow cases.
- (k) For Couette flow, periodic boundary condition is used as there is no definite inlet or outlet, rather each axial location has identical velocity and temperature distribution. Also, the axial pressure gradient is zero.
- (l) Symmetry is assumed before the flat plate so that it models the effect of flow striking the leading edge of the flat plate

Ansys Fluent computational fluid dynamics package [51] is used for the numerical application and solution of these equations over the flow domain. The discretization is carried out by using a finite volume method. Pressure-velocity coupling is obtained using the SIMPLE scheme while the iterative method is used to reduce the residuals leading to the solution. The procedure involves an initial estimate or guess value for all the variables.

Using these initial guess, the velocities are calculated by the momentum equation, and the pressure correction is obtained by the pressure correction equation. Now the pressure and updated velocities are calculated. At this stage, all other parameters are also calculated. Now the difference between the original guessed values and new obtained values gives the residual, which are monitored for all equations, and kept to a value less than 10^{-8} for all equations.

3.4 Thermal-hydraulic parameters

The Reynolds, Nusselt and Stanton numbers, as well as the skin friction coefficient, respectively, are calculated as:

$$Re = \frac{\rho u d}{\mu} \quad (3.16)$$

$$Nu = \frac{h d}{k} \quad (3.17)$$

$$St = \frac{h}{\rho u c_p} \quad (3.18)$$

$$C_f = \frac{\tau_w}{\frac{1}{2} \rho u^2} \quad (3.19)$$

where the velocity is free stream velocity for external flow. For internal flow, there are two options. That is, either using the average velocity or the maximum velocity in the channel. Calculations based on both velocities are presented when dealing with the analogy

validation. It should be noted that for a circular tube under laminar flow condition, the fully developed Nusselt number for constant surface heat flux is 4.36 while it is 3.66 for constant surface temperature [176].

The laminar hydrodynamic entry length, thermal entry length, and friction factor are, respectively, calculated by [176],

$$\frac{x_{hydrodynamic}}{d} = 0.05 \text{ Re} \quad (3.20)$$

$$\frac{x_{thermal}}{d} = 0.05 \text{ Re Pr} \quad (3.21)$$

$$f = \frac{64}{\text{Re}} \quad (\text{laminar}) \quad (3.22)$$

$$f = \left(0.790 \ln(\text{Re}) - 1.64\right)^{-2} \quad (\text{smooth turbulent}) \quad (3.23)$$

The pressure loss for fully developed flow is calculated by,

$$\Delta p = \left(\frac{\rho f l u^2}{2d} \right) \quad (3.24)$$

The heat transfer coefficient is defined as

$$\begin{aligned} h &= \frac{q''}{(T_w - T_m)}, \quad \text{for internal flow} \\ h &= \frac{q''}{(T_w - T_\infty)}, \quad \text{for external flow} \end{aligned} \quad (3.25)$$

Here, the surface heat flux for constant wall temperature and the surface temperature for constant heat flux condition can be directly obtained from the numerical results.

For external flow, the free stream temperature is taken as reference for the calculation of heat transfer coefficient. For internal flow, the mean temperature at a cross-section is taken as the reference, defined as [176]

$$T_{m,MWA} = \frac{\int_{A_c} \rho w c_p T dA_c}{\dot{m} c_p} \quad (3.26)$$

It is important to emphasize that the mean temperature is defined as the temperature of the fluid, taken from a cross-section and allowed to mix and reach equilibrium in an adiabatic container. Mathematically it translates into the enthalpy advection integrated over the cross-section [176]. This quantity is directly obtained from the software, by using the built-in surface integral report for mass weighted average of temperature over the cross-sectional surface at each axial increment. For the non-axisymmetric cases, the length based mass weighted integral is used to find the mean temperature using MATLAB[177]. The procedure is briefly discussed in the following paragraph.

The calculation of Nusselt number was carried out by the combined use of journal files in ANSYS Fluent[51] and functions written in MATLAB[177]. In ANSYS Fluent, multiple cross-sectional planes are created. For each plane the value of temperature, heat flux, and velocity are saved for each node point along with its coordinates. This data is imported in

MATLAB to obtain the distribution of each variable for further analysis. The mean temperature is constant for axisymmetric cases, used for the calculation of peripheral or local Nusselt number. The modified procedure for the calculation of mean temperature in non-axisymmetric cases involves the identification of the minimum temperature point as axis for each cross-section and then mean temperature is calculated for each line joining the surface points to the axis using Eq. (3.27)

$$T_m = \frac{\sum_r w T dr}{\sum_r w dr} \quad (3.27)$$

Then for each surface point, the wall temperature and mean temperature for the line from surface to the axis is used to calculate the peripheral Nusselt number using eq.(3.28)

$$Nu_{peripheral} = \frac{d}{k} \left(\frac{q_s''}{(T_w - T_m)} \right) \quad (3.28)$$

For combined entry length problems with isothermal wall, the temperature independent local Nusselt number at an axial location x is given by

$$Nu = 1.86 \left(\frac{Re Pr}{x / D} \right)^{1/3} \quad (3.29)$$

For turbulent flow, the local Nusselt number can be calculated using the Dittus-Boelter equation as

$$Nu_t = 0.023 Re^{4/5} Pr^{0.4} \quad (3.30)$$

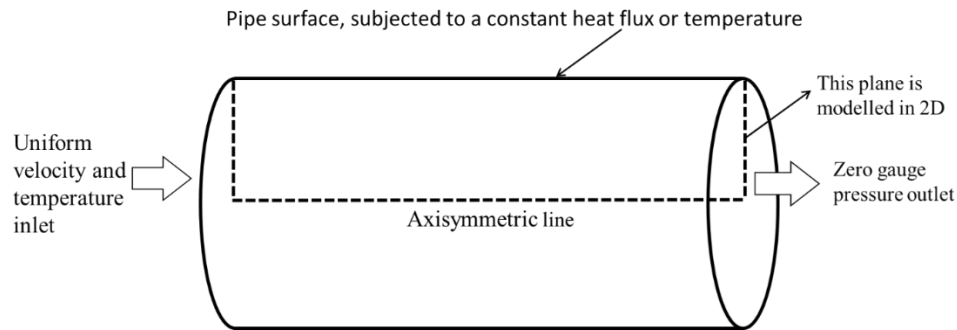
3.5 Grid independence study and validation

A simple tube with a diameter of 0.045 m is used (see Figure 3.1(a)), with an inlet velocity of 0.1 m/s (Table 3.1). The Reynolds number for these input conditions is about 300, thus flow regime is laminar. In addition, one sample case for turbulent flow is presented with inlet velocity of 3.5 m/s corresponding to Reynolds number of 12,000.

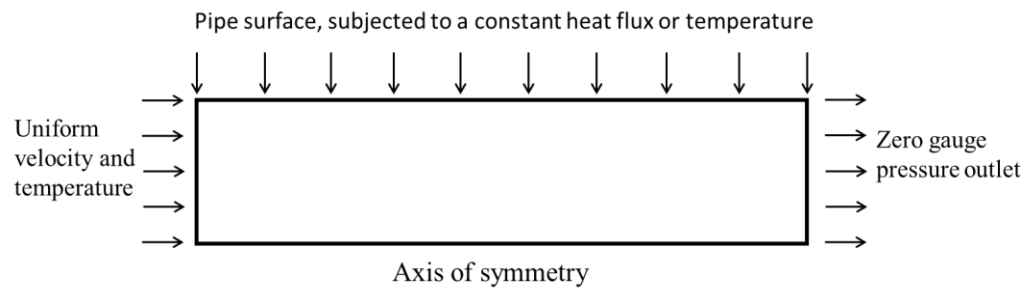
Table 3.1. The input parameters used for the validation.

Input Parameters	Value
Inlet temperature	298 K
Inlet velocity	0.1 m/s for laminar and 3.5 m/s for turbulent
Wall condition	500 K or 100 W/m ²
Tube Diameter	0.045 m

a)



b)



c)

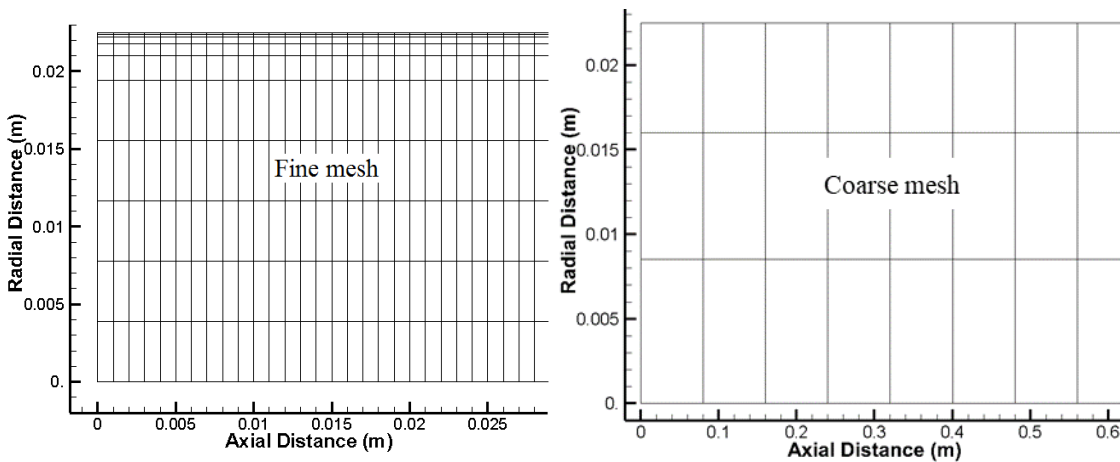


Figure 3.1. a) 3D tube flow, illustrating the corresponding boundary conditions, b) the 2D axisymmetric domain used for analysis c) the fine and coarse mesh used for axisymmetric 2D tube flow.

Four mesh densities were used to verify the mesh independency of the solution. Figure 3.1(c) shows the fine mesh used for the modeling, where the axial division is 1 mm while the radial division is considered as 4 mm, in addition a radially decreasing mesh is used for boundary layer near the wall so that the larger gradients of heat and mass flow may be captured properly. Figure 3.1(c) also shows the coarse mesh that was used for mesh independence test, with 40 mm in x axis and 4.5 mm in y direction. In addition, two coarse mesh were tested having axial divisions of 5 mm and 80 mm with radial divisions of 4 mm and 7.5 mm, respectively. These divisions resulted in a total of 4 cases with corresponding number of cells to be 75, 250, 5000 and 20000. The results for this study are presented in the next section.

The first step in finding the local Nusselt number is to verify the Nusselt number variation along the surface of a circular tube. The input parameters used for the validation are shown in Table 3.1. The input velocity leads to a Reynolds number of 300, thus the flow behavior is laminar. As flow in a tube is axisymmetric, 2D analysis from wall to the axis of symmetry as shown in Figure 3.1(b) is representative of flow and thermal behavior.

3.5.1 2D Axisymmetric Nusselt number validation

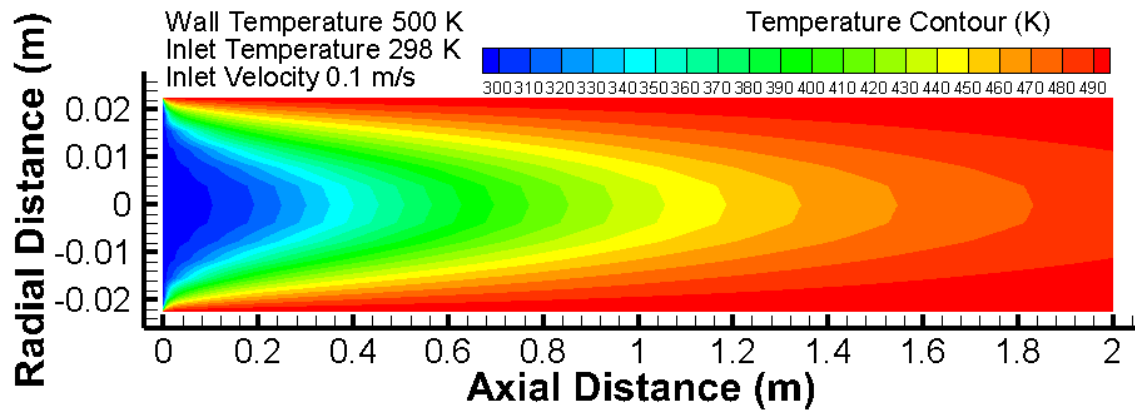
There are two types of boundary conditions that can be used for validation purpose, i.e., constant wall temperature and constant heat flux. Both are discussed in detail in the following sections.

3.5.1.1 Constant wall temperature

Figure 3.2(a) shows the temperature contours for a constant surface temperature at the wall. It should be noted that the modelling was done for the axisymmetric plane only, and the results were then mirrored to represent the whole flow cross-section. It can be seen that the sudden increase in the temperature of the fluid near the wall is possible due to high heat flux in this region. As the bulk of the fluid undergoes an increase in temperature, the rate of heat transfer decreases until the whole fluid is at the surface temperature and no further heat transfer would occur. The constant wall temperature can be maintained by having a phase change fluid outside the domain, but care should be taken in the developing region as very high energy will be absorbed by the system for maintaining the constant surface temperature.

Figure 3.2(b) shows that for the constant surface temperature condition, a very high heat flux is required in the entry region to provide enough energy to maintain the fixed temperature condition at the boundary. The heat flux is plotted on a log scale, it can be seen that an initial heat flux of about $8,000 \text{ W/m}^2$ is required which decreases in the developing region and the slope continues to decrease as the flow develops. The mean temperature can be seen increasing rapidly in the developing region owing to the high heat flux and then the rate of increase slows down as the flow becomes fully developed. This mean temperature increase would continue till all the fluid is at the wall temperature, after which no further heat transfer would occur. This behavior is in accordance with the analytical results available in literature [176].

a)



b)

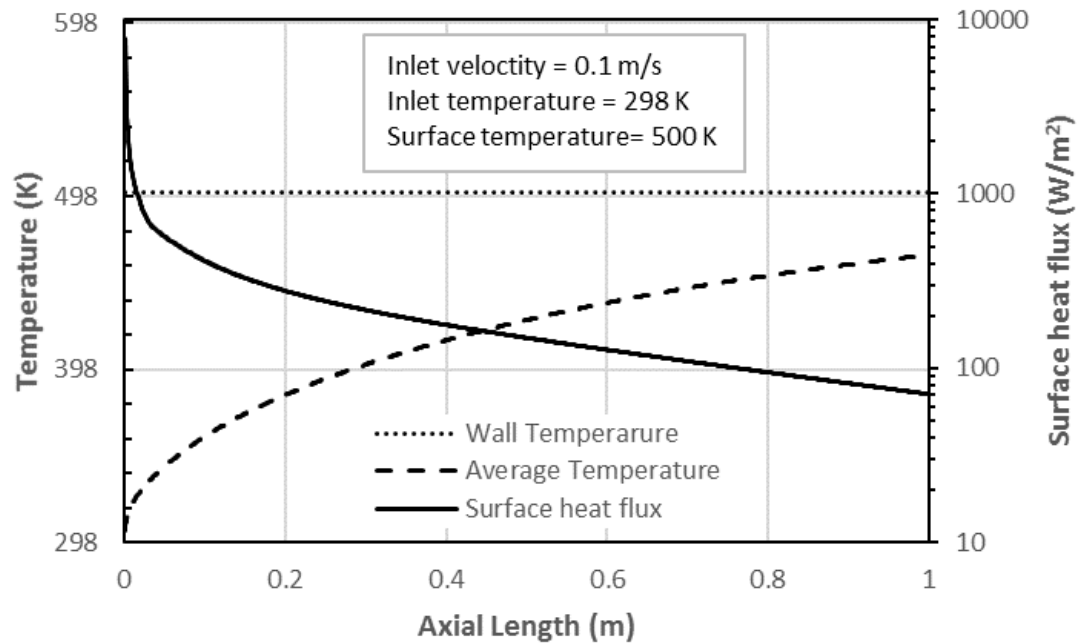


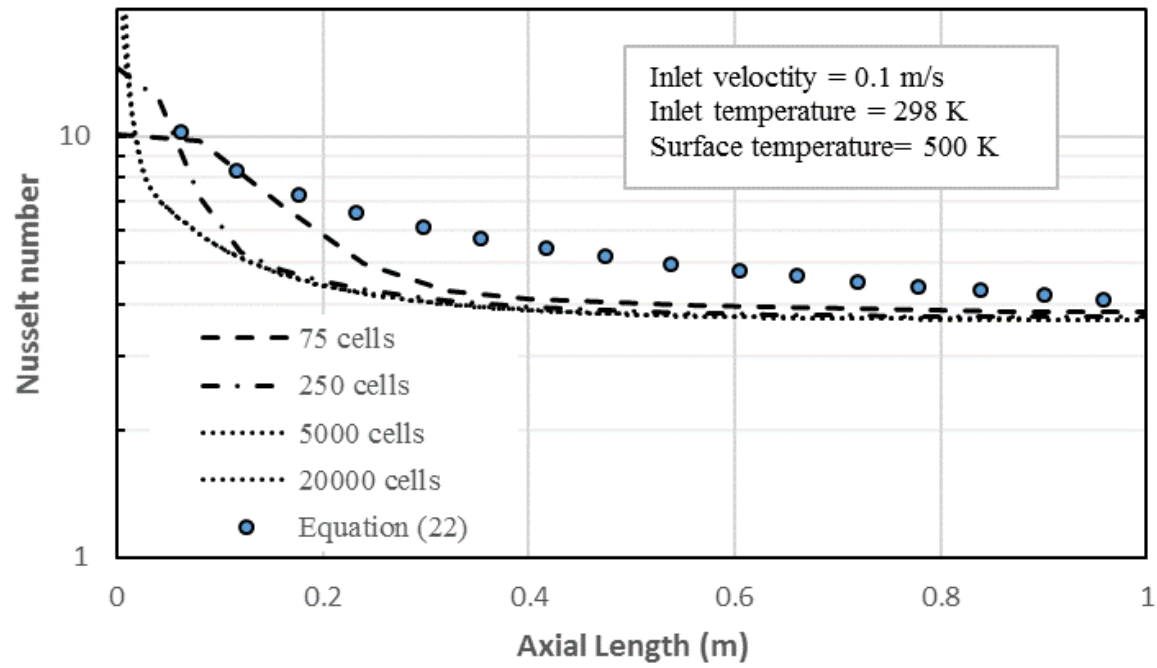
Figure 3.2. a) Temperature contours for uniform surface temperature of 500 K, b) temperature and heat flux variation for constant wall surface temperature (similar to [176]).

Figure 3.3(a) shows the mesh independence test for the case of constant surface temperature, and the results have also been compared with the correlation given by Eq.(3.29). The results are presented for the total number of cells of 75, 250, 5000 and 20000. It can be seen that results vary only for the lower number of cells, remaining invariant for the actual mesh used. In addition, the variation predicted by Eq.(3.29) is slightly overpredicting the Nusselt number, while leading to same fully developed value. The correlation is not able to predict the sudden drop in Nusselt number at entrance, while the fine mesh used in numerical modeling shows the Nusselt number drops sharply in comparison to the correlation. Figure 3.3(b) shows that similar results are obtained for the constant heat flux case and comparison with experimental values presented by Chandel et al. [178]. It is important to mention here that the numerical modeling is done at a Reynolds number of 300 while the experimental results are presented for 454. This difference in Reynolds number is resulting in higher values for the experimental data.

It can be further seen from Figure 3.3 (a) for constant surface temperature, that starting from a value above 10, the Nusselt number decreases as the thermal boundary layer develops. As the fully developed conditions are reached at around 0.7 m, the Nusselt number reaches a value of 3.66. This fully developed value matches with the iterative solution of the energy equation for circular tube under laminar fully developed condition and constant surface temperature [179].

The hydrodynamic entry length calculated from Eq. (3.20) results in a value of 0.7 m while the thermal entry length calculated from Eq. (3.21) results in thermal entry length of 0.51 m. This can be verified from Figure 3.3, where the change in Nusselt number shows less than 1% change at about 0.6 m indicating fully developed conditions has been reached. The pressure loss calculated from Eq. (3.24) equals 0.057 Pa, while the numerical solution results in pressure loss of 0.063 Pa, the difference is due to the fully developed assumption in the analytical calculation while the numerical computation takes into consideration the pressure loss in the developing region as well.

a)



b)

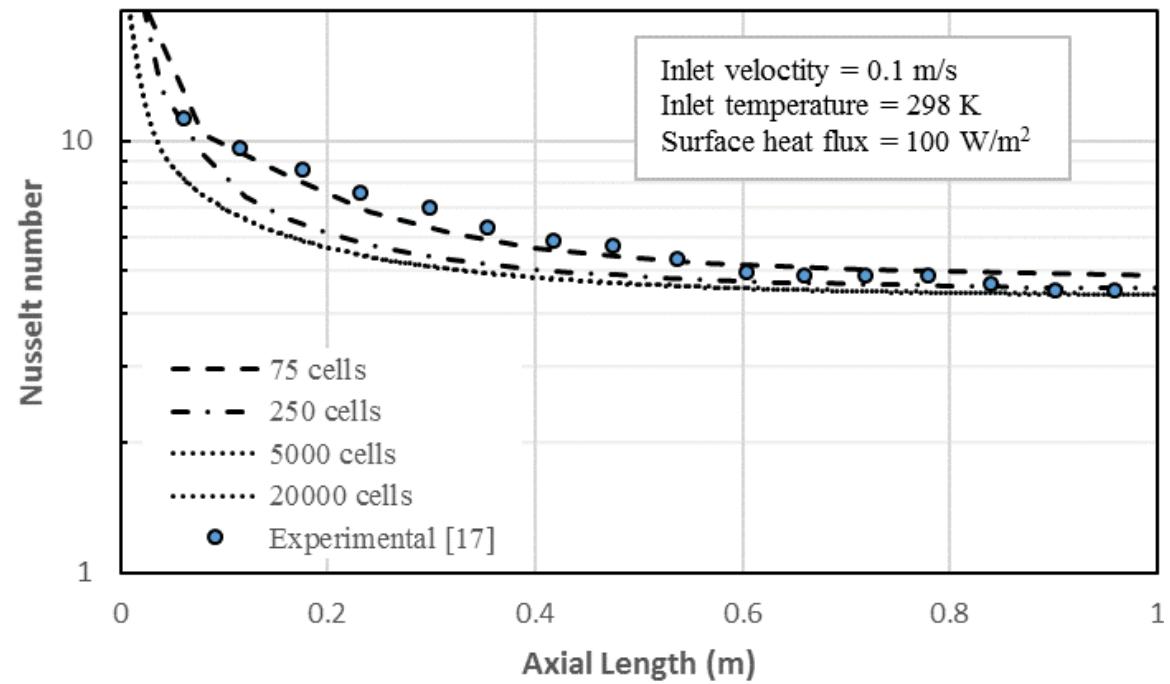


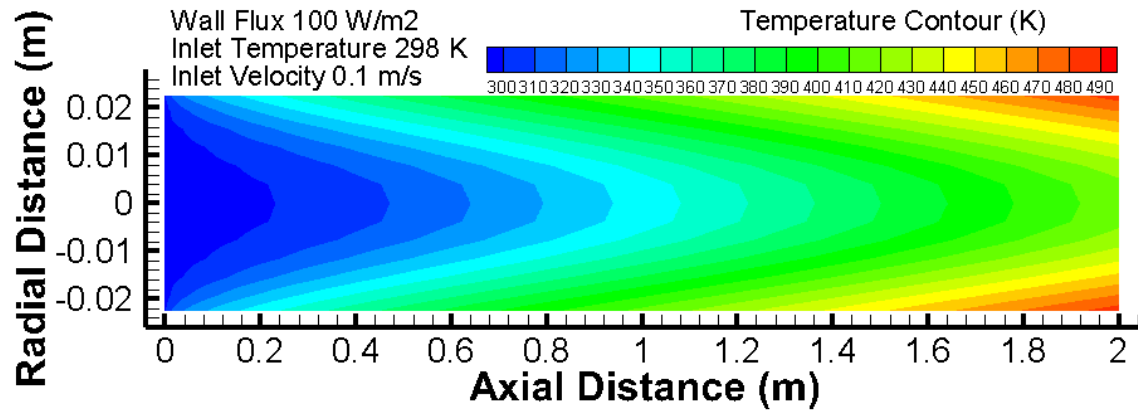
Figure 3.3. Mesh independent test of the axial variation of the Nusselt number for a) constant wall temperature and b) constant heat flux.

3.5.1.2 Constant surface heat flux

Figure 3.4(a) shows the temperature contours for the constant wall heat flux. It can be seen that the surface temperature is increasing gradually along with an increase in the mean temperature. The wall temperature does not follow the sudden increasing behavior observed for constant wall temperature (refer to Figure 3.2(a)) as the heat flux is limited in this case, leading to a gradual increase in the axial wall temperature.

Figure 3.4(b) shows the temperature variation in the tube with the constant heat flux applied on the wall. It can be seen that the mean temperature increases with a constant slope as the heat flux is constant, while the surface temperature undergoes sudden increase initially in the developing region and then the difference between the surface temperature and mean temperature becomes constant for the remaining tube length. This behavior is in accordance with the analytical results available in literature [176]

a)



b)

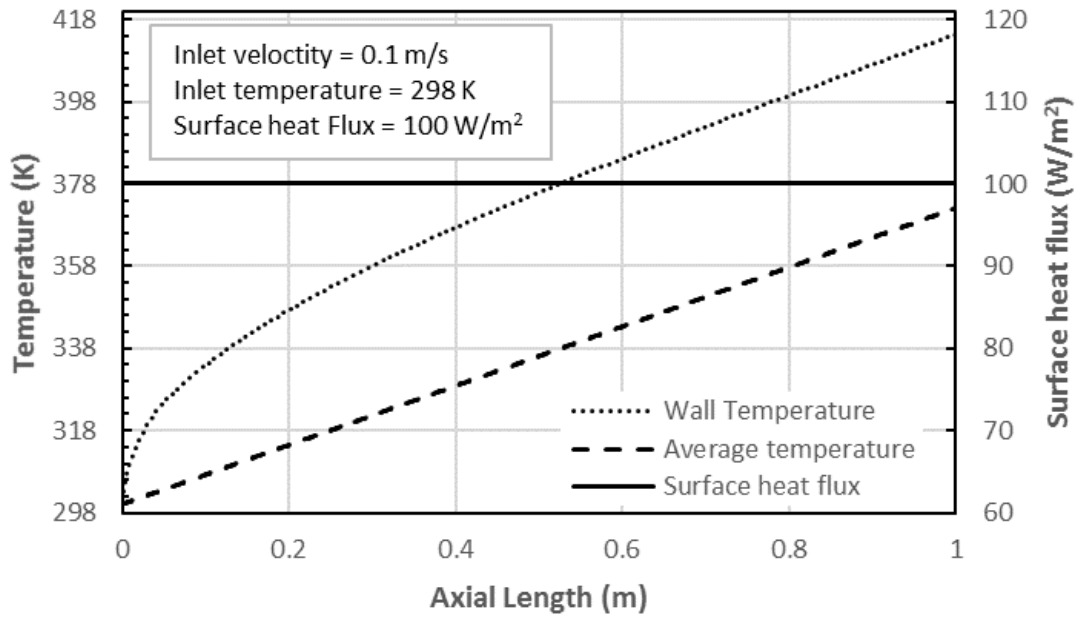


Figure 3.4. a) Temperature contours for uniform surface heat flux of 100 W/m² and b) the temperature and heat flux variation for constant wall surface heat flux.

3.5.2 Grid independence study for the flow distribution manifold

The studies for the flow distribution system involved the U- and Z- type manifolds. For both these cases, same mesh was used by just changing the outlet location. The Figure 3.5 (a) shows the layout that was used for the study. In this figure, the solid regions are not shown, but they are modelled to allow heat conduction between the channels. The details for this design are mentioned later in Chapter 7 and Chapter 6.

Figure 3.5 (b) shows the meshed domain. Constant sized mesh was used for the whole domain with mesh size of 0.001 m. For the depth (z-axis), six (even number) cells were used so that the maximum velocity in the middle can be captured. The grid independence study with mesh variations around this based case are shown in Figure 3.6 while the divisions used for each study are also listed in Table 3.2. The base case of 0.001 m size in each axis is used, and then the mesh in each axis is reduced by a factor of 10 and increased by a factor of 2. In addition, a case with mesh size of 0.75 mm, in each axis is used to verify the impact of further reduction in mesh size by a factor of about 1.33 from the base case.

It is evident from Figure 3.6 that the main mesh size is the z-axis, which shows different velocities in each channel as compared to the other cases. For all other cases, there is a slight change in the velocity of the first channel, otherwise, all the mesh sizes used result in similar velocities in each channel. Hence the choice of 0.001 for each axis is a suitable choice for studying the flow distribution in the manifold.

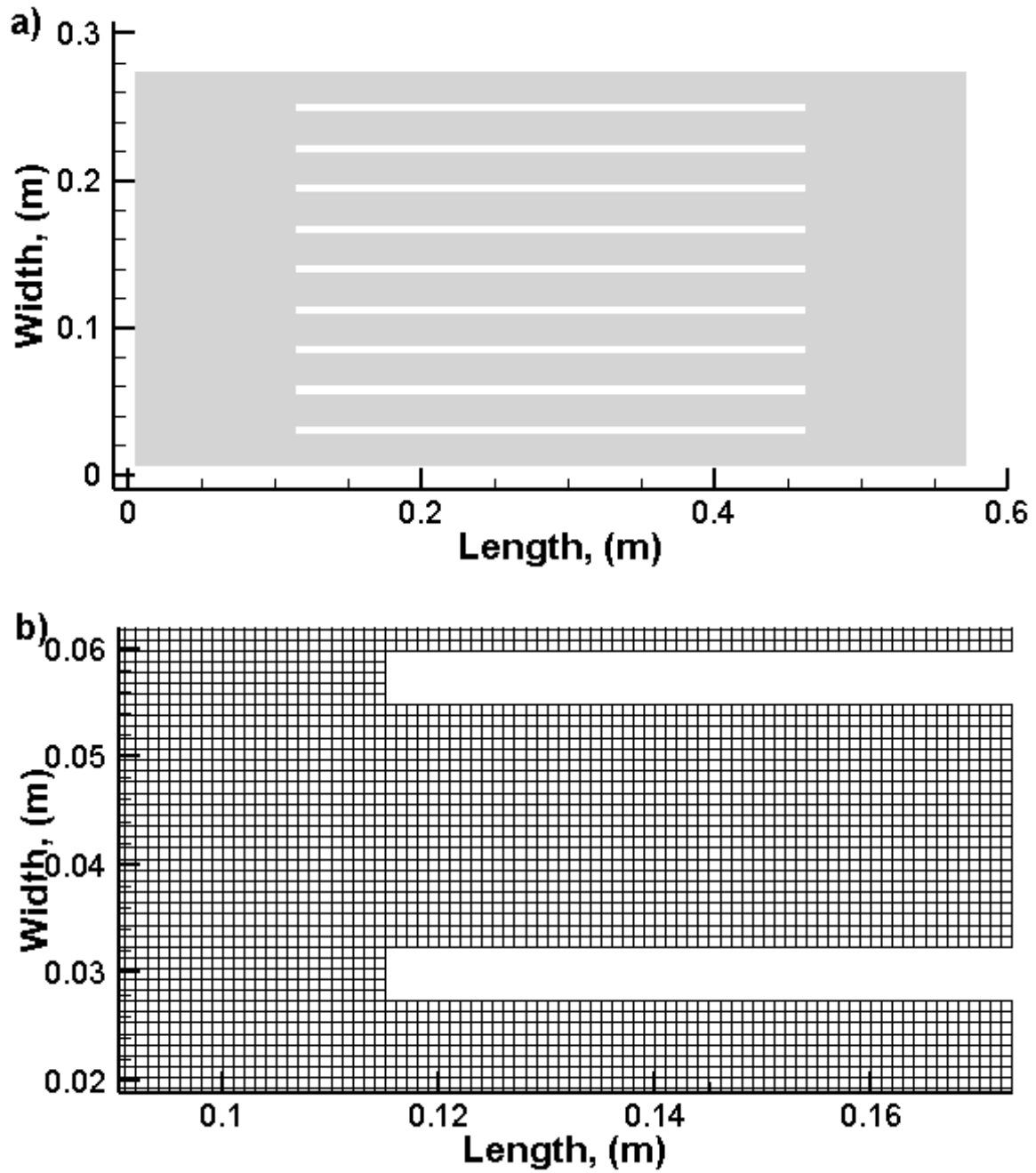


Figure 3.5. a) The layout used for the flow distribution system. b) the mesh used for the study (shown near the solid regions.)

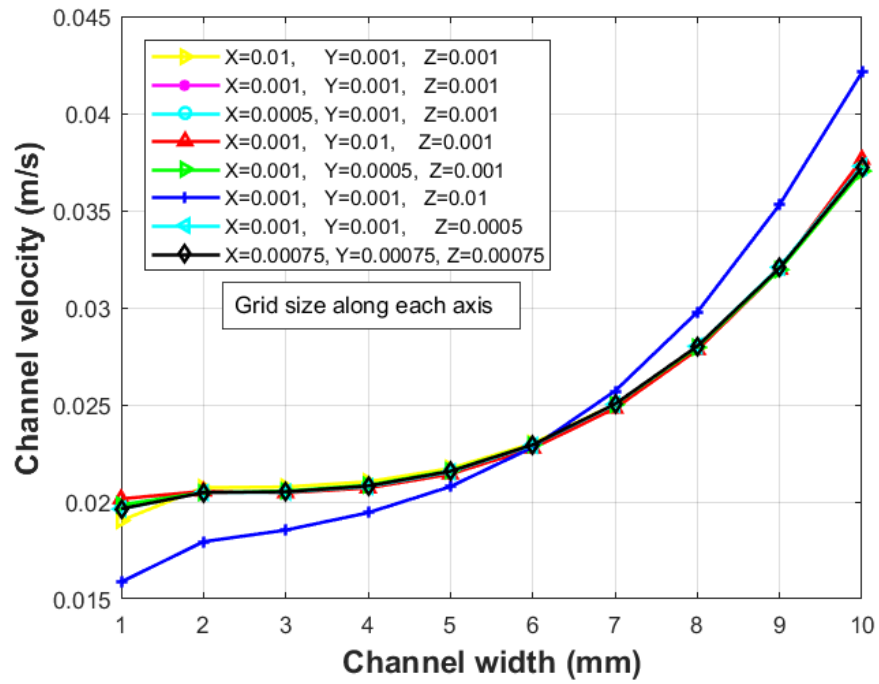


Figure 3.6. The grid independence test for the flow distribution manifold for eight different combinations.

Table 3.2. The mesh sizes in each axis used for the grid independent study for the flow distribution system

Grid size for each axis (in meter)			
	x	y	z
1	0.01	0.001	0.001
2	0.001	0.001	0.001
3	0.0005	0.001	0.001
4	0.001	0.01	0.001
6	0.001	0.0005	0.001
7	0.001	0.001	0.01
9	0.001	0.001	0.0005
10	0.00075	0.00075	0.00075

Chapter 4

SPLIT FLOW WITH MANIFOLD HEATING

This chapter consists of five sections. In first section, brief introduction is provided for the split flow cases. The results for a single 3D pipe are presented in section two. The third section deals with 4 smaller tubes and fourth section deals with 37 smaller tubes. These sections further include constant heat flux and temperature cases, in addition to impact of manifold heating for these cases. A procedure is given for calculation of mean temperature for the non-axisymmetric cases. The last section provides some comparison for the three designs, with regards to their friction and thermal performance, both uniform heating and uniform temperature cases.

4.1 Introduction

Shell and tube heat exchangers have many industrial applications for transferring between the hot and fluid flow streams due to their ability to exchange a large amount of heat energy for low cost and easily maintainable designs. It consists of a header accepting fluid from one side and dividing the flow into the smaller tubes. The tubes from the outside are exposed to the other fluid stream normally at a lower pressure than the tube fluid. The flow should be uniformly distributed in all the tubes otherwise the performance may decrease for the heat exchanger. It is important to note that the tubes with lower flow rate would

undergo an increase in temperature making them susceptible to fouling, thus degrading the thermal-hydraulic performance of the heat exchanger. Although internal fouling can be dealt with during the routine maintenance, but the external fouling is difficult to handle.

It is important to that the manifold may not be adiabatic in actual operating conditions, thereby resulting in degradation of thermal-hydraulic characteristics of the heat exchanger due to non-axisymmetric flow. The main goal of the present work is to investigate the performance of a heat exchanger with flow distribution from a larger tube to smaller tubes under different (manifold) operating conditions, which is not properly addressed in the literature. In this regard, the fundamental relations for heat transfer are first verified for a standard flow system, which is followed by the analysis of more complicated systems.

4.2 3D single tube Nusselt number calculation

The two-dimensional axisymmetric case is extended to full three-dimensional modeling in order to validate the mesh used. This validation is expected to help in modeling of the split tube system discussed later. Figure 4.1 shows the mesh used for the three-dimensional tube. The internal four circles would be extruded in the next study to represent tube flow from larger tube to four smaller tubes. At present, the whole plane is extruded and fluid flows in all the regions without any interior walls. The use of square planes inside the circular regions eliminated the mesh concentration at the center of the circle. The outside squares are used to allow proper mesh connectivity between the smaller tubes as well as the external wall of the larger tube.

Figure 4.2 show the temperature contours for both uniform wall temperature and uniform heat flux boundary conditions. These contours are similar to Figure 3.2(a) and Figure 3.4(a), validating that the use of three-dimensional modeling with the additional mesh planes inside does not affect the flow or heat transfer characteristics.

Figure 4.3 shows the surface Nusselt number variation along the axial direction. The results are again in agreement with the 2D axisymmetric cases discussed above. The coarse mesh here was of half size in comparison with the denser mesh in the axial direction. It can be seen that the results are independent of the mesh choice, except for some minor difference in the entrance region up to 0.05m section. After this distance, the results are exactly matching.

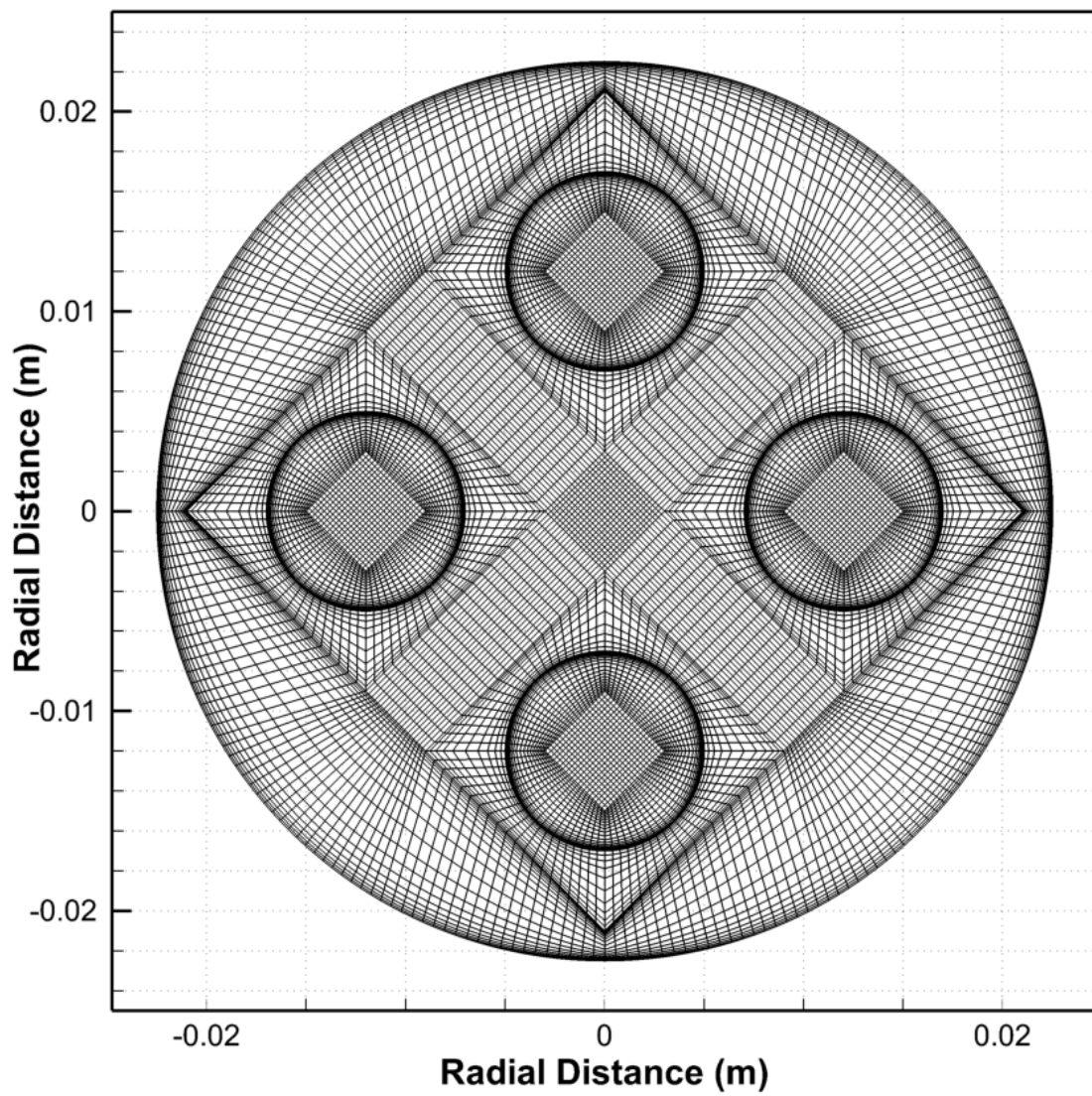
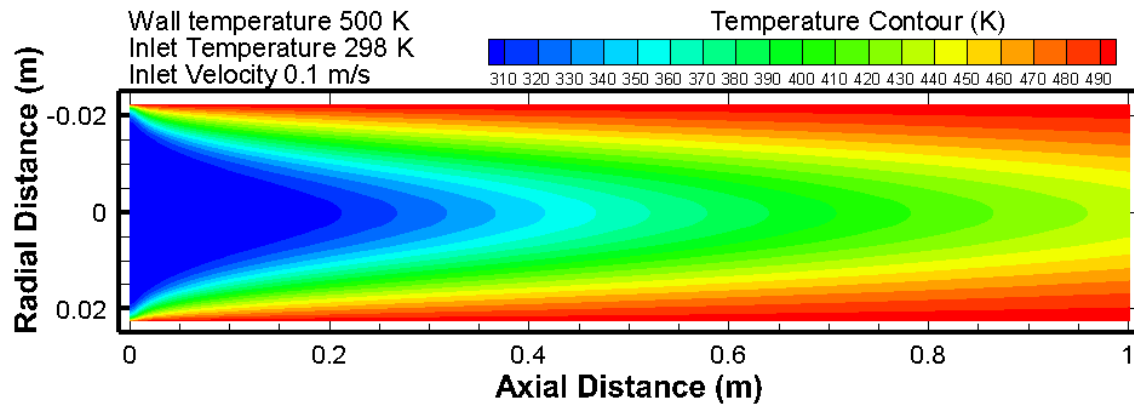


Figure 4.1. Mesh used for three-dimensional tube.

a)



b)

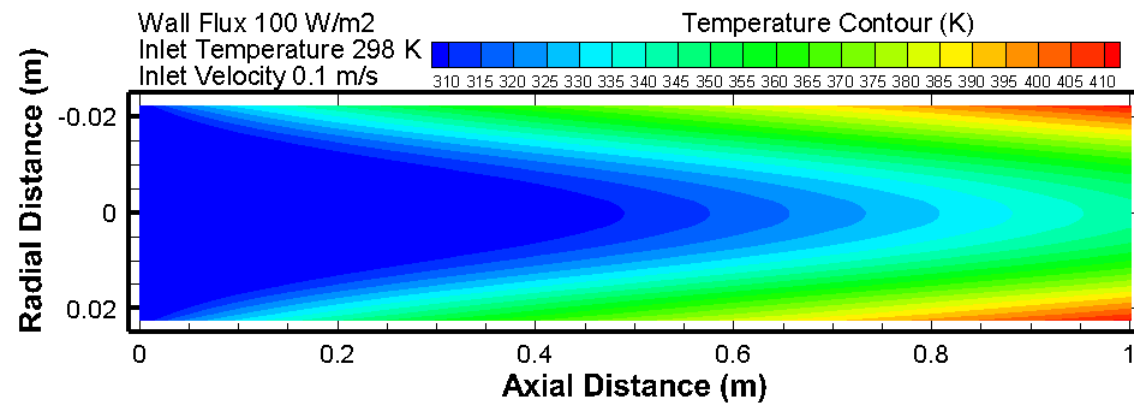


Figure 4.2. Temperature contours for a) uniform wall temperature b) uniform surface heat flux.

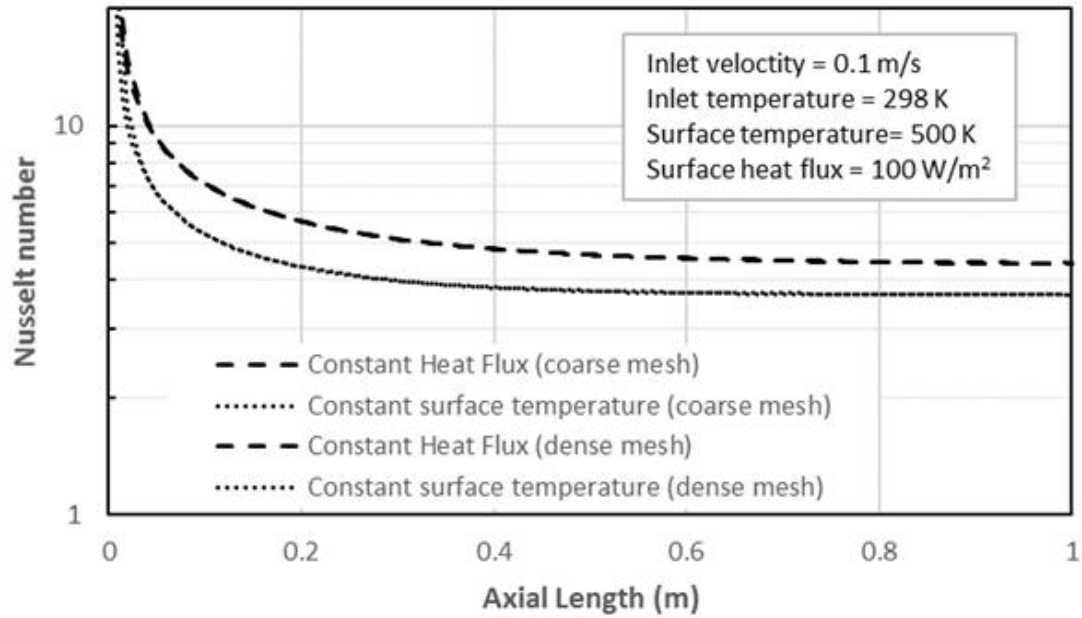


Figure 4.3. Axial Nusselt number variation for full three-dimensional tube.

Two layouts are discussed here, first with 4 tubes and second with 37 tubes. The inlet conditions and the boundary conditions are kept same in order to make a comparison between the cases.

4.3 Manifold dividing flow in four smaller tubes

Figure 4.4 shows the layout used for the manifold splitting flow in 4 smaller tubes. The smaller tubes are of diameter 1 cm while the larger manifold is 4.5 cm. The usefulness of mesh shown in Figure 4.1 for a single tube is evident in this layout, where the smaller circles are extruded to model the smaller tubes.

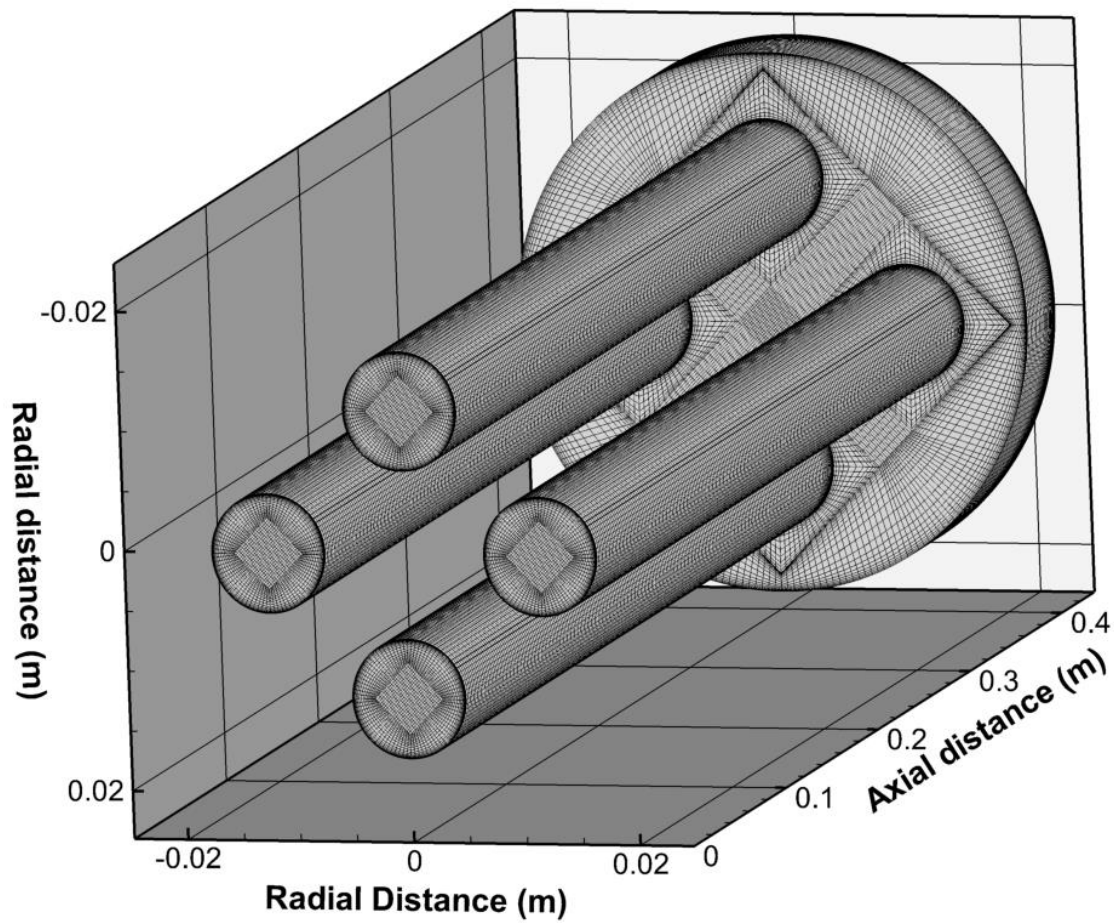


Figure 4.4. Mesh used for four tube split system.

4.3.1 Constant surface heat flux

Figure 4.5 shows the comparison of temperature distribution in the system with or without manifold heating, in addition to the constant tube heating with a uniform heat flux of 100 W/m^2 . In the first case, the use of manifold is to just distribute the flow to the smaller tubes, with no contribution to heat transfer. The thermal boundary layers develop from the tube surfaces with identical axisymmetric profiles for all four tubes.

In the second case, the manifold is also subjected to heating flux which leads to the development of boundary layer from the manifold and then progressing in the smaller tubes. It is interesting to note that the thermal characteristic of the flow inside the smaller tubes is no longer axisymmetric as the fluid heated by the manifold is flowing near the outer surface of the tube while unheated flow in the middle of manifold flows near the lower surface of the tube.

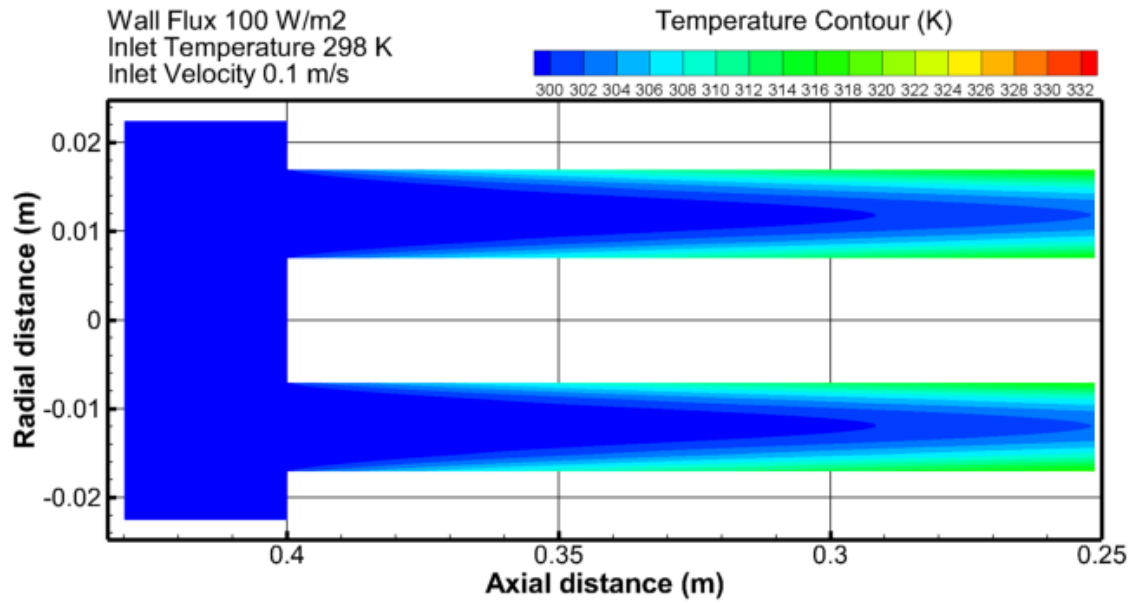
Figure 4.6 shows the top and bottom surface Nusselt number variation for the two cases. When only the tube surfaces are heated, Nusselt number begins with a high value and decreases sharply in the developing region leading to the constant value of 4.36. As the flow is axisymmetric, Nusselt number at the top and bottom surfaces undergo similar variations. For the case of heated manifold, the Nusselt number begins with high value and decreases in the developing region. At the split plane, top surface Nusselt number drops below the fully developed value due to the presence of the hot fluid region at the corner where the manifold ends and flow splits in the smaller tubes. The hot spot is the recirculation region, leading to elevated temperature as compared to remaining section where fluid is flowing without recirculation.

The impact of hot spot is visible on the Nusselt number plot, showing the reduction in heat transfer coefficient at this section. As the flow develops in the smaller tubes, the upper surface is at higher temperature leading to lower surface Nusselt number, which gradually

increases to reach the fully developed value of 4.36. The lower surface was at lower temperature, thus its Nusselt number begins from a higher value similar to standard cases and develops to the constant value of 4.36. This study shows the impact of boundary layer reducing the performance of upper surface when considering the heat transfer characteristics. Hence, in cases where the manifold cannot be isolated from the external heating, attention should be given to the reduced thermal performance of the outer surfaces.

In addition to laminar modeling, turbulent flow is also examined to determine the peripheral Nusselt number subjected to non-uniform inlet temperature. In this regard, the inlet velocity has been increased from 0.1 m/s to 3.5 m/s, resulting in Reynolds number of about 12,000 for the smaller tubes. For such conditions, Eq.(3.30) is used to find the fully developed turbulent Nusselt number to be about 37.8. Figure 4.7 shows the contour of peripheral Nusselt number, it can be seen that at inlet the flow is non-axisymmetric and the minimum value occurs at an angle of 90° which corresponds to the top side where the boundary layer from the manifold is entering. The fully developed Nusselt number from the numerical model is about 40.8, with an error of 8% which is relatively good value as the Dittus-Boelter equation can result in errors of up to 25% [176].

a)



b)

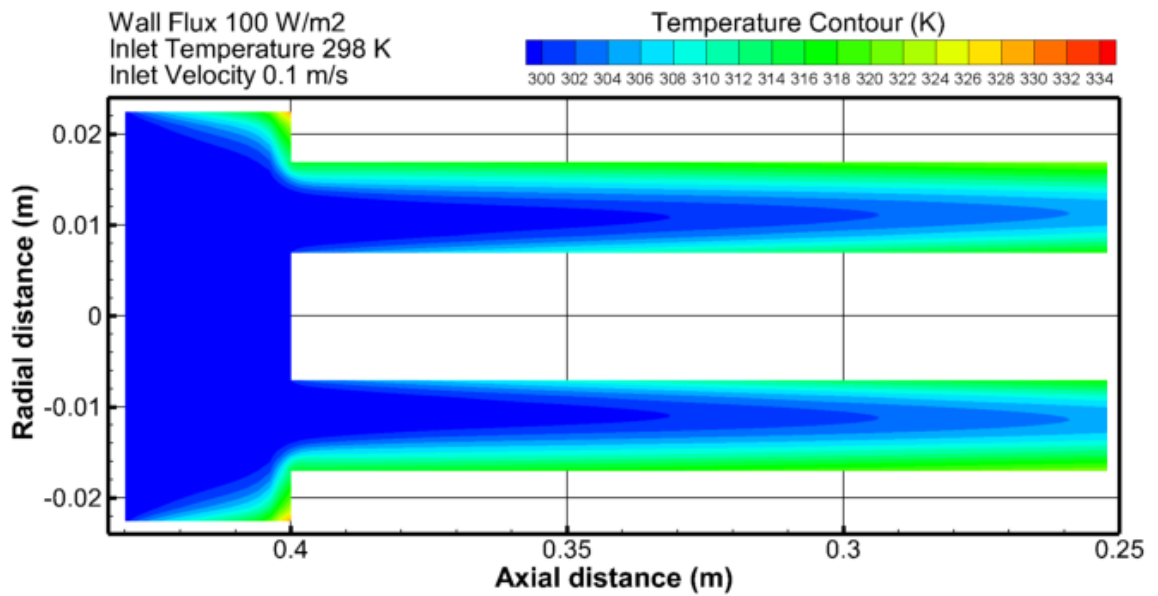


Figure 4.5. Temperature contours for four tubes subjected to constant surface heat flux a) without manifold heating b) with manifold heating.

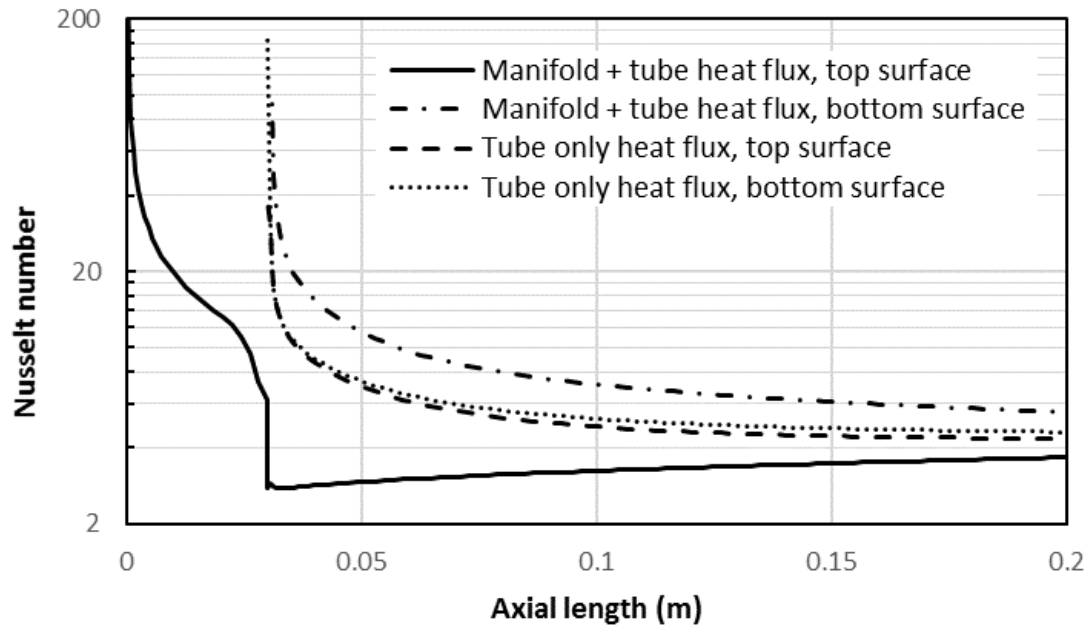


Figure 4.6. Axial Nusselt number for the tube before and after split for constant heat flux case.

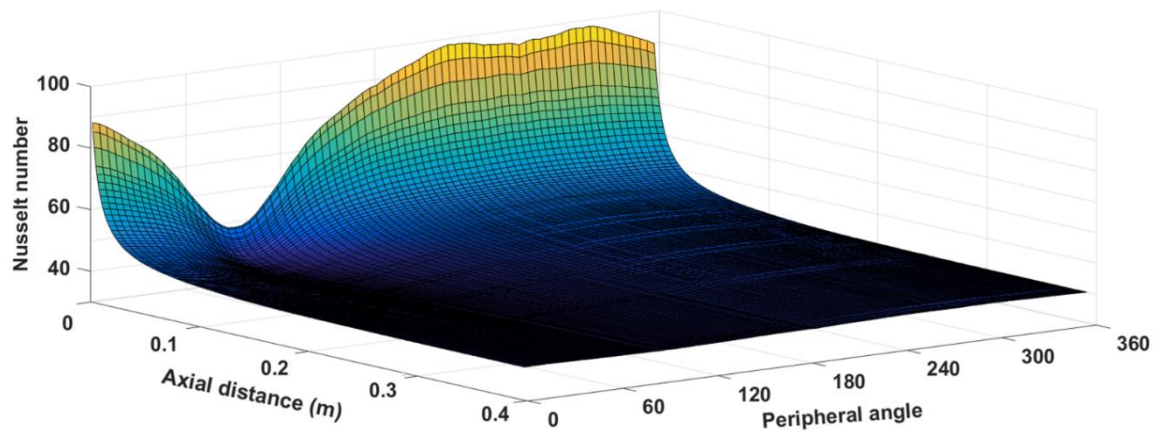


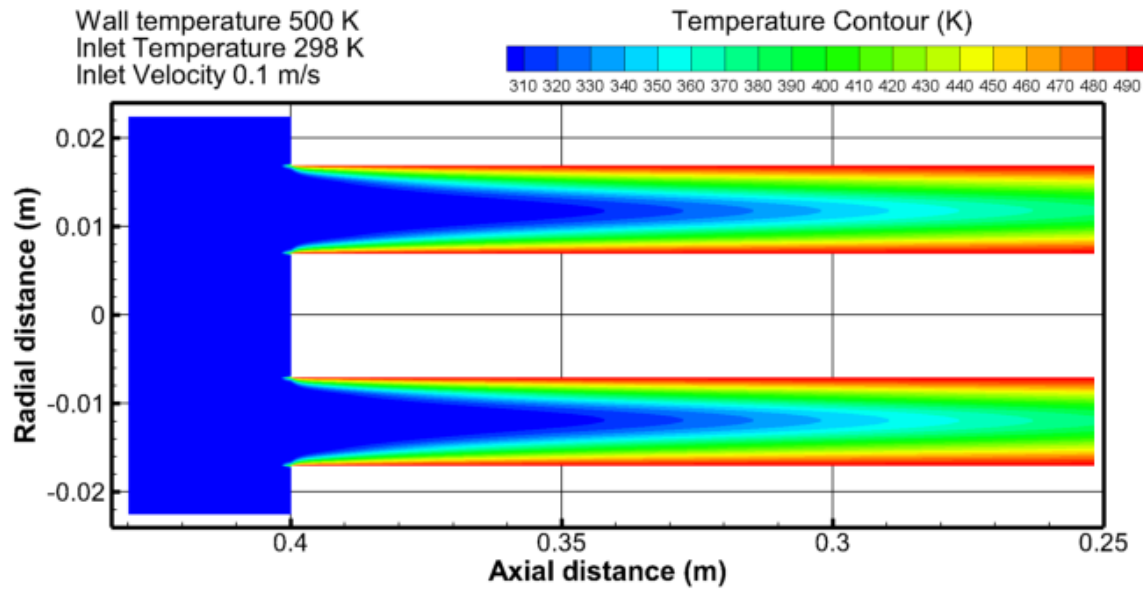
Figure 4.7. Peripheral Nusselt number variation for the turbulent flow.

4.3.2 Constant wall temperature

Figure 4.8 shows the temperature contours for constant surface temperature cases. In the first case, the boundary layer develops in the tubes axisymmetrically from all the surfaces. In the second case, the manifold boundary layer leads to a higher temperature near the upper surfaces of the tube while lower temperature near the bottom surfaces. As the surface temperature is fixed, a higher heat flux occurs at the initial sections and thereafter reducing axially. The Nusselt number variation can be seen in Figure 4.9, where the upper surface undergoes a decreasing Nusselt number in the manifold as low as 0.5 at the hot spot near the corner. Then at the entrance of smaller tube, there is a sudden increase in the Nusselt number due to the higher heat flux (owing to constant surface temperature boundary condition). It then decreases below the fully developed value with a gradual increase to the fully developed value.

This lower Nusselt number at the top surface is due to the fact that there is more heating from the lower surface as compared to the upper surface as the axis of thermal symmetry is shifted towards the lower surface owing to the effect of the boundary layer from the manifold at the top. The Nusselt number at the bottom surface of the tube follows the standard high to decreasing behavior, thus leading to a constant value of 3.66.

a)



b)

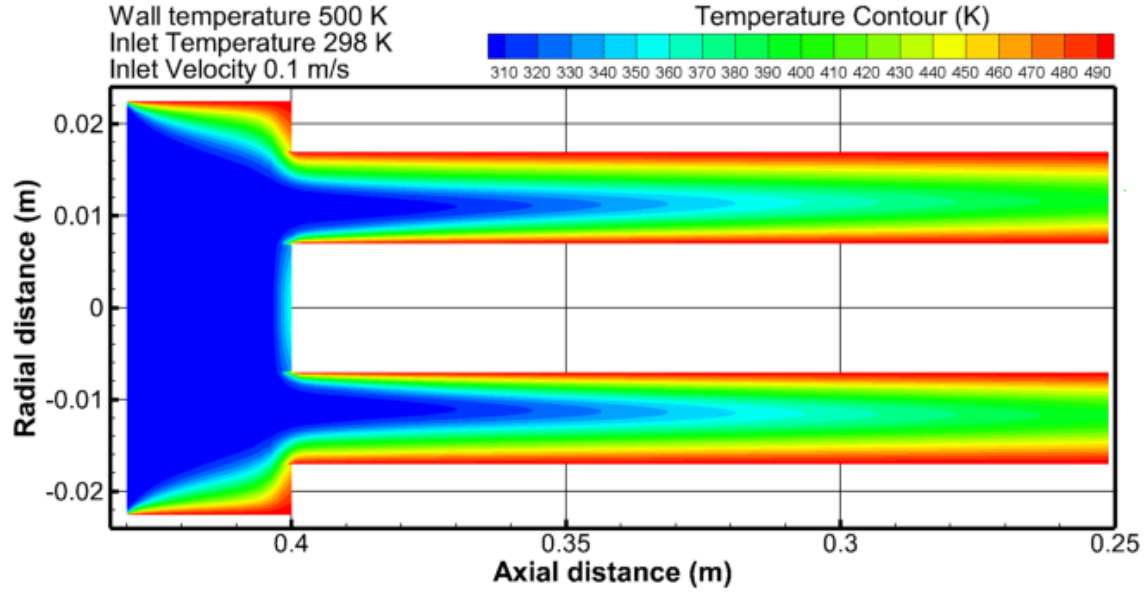


Figure 4.8. Temperature contours for four tubes subjected to constant surface temperature

a) without manifold heating b) with manifold heating.

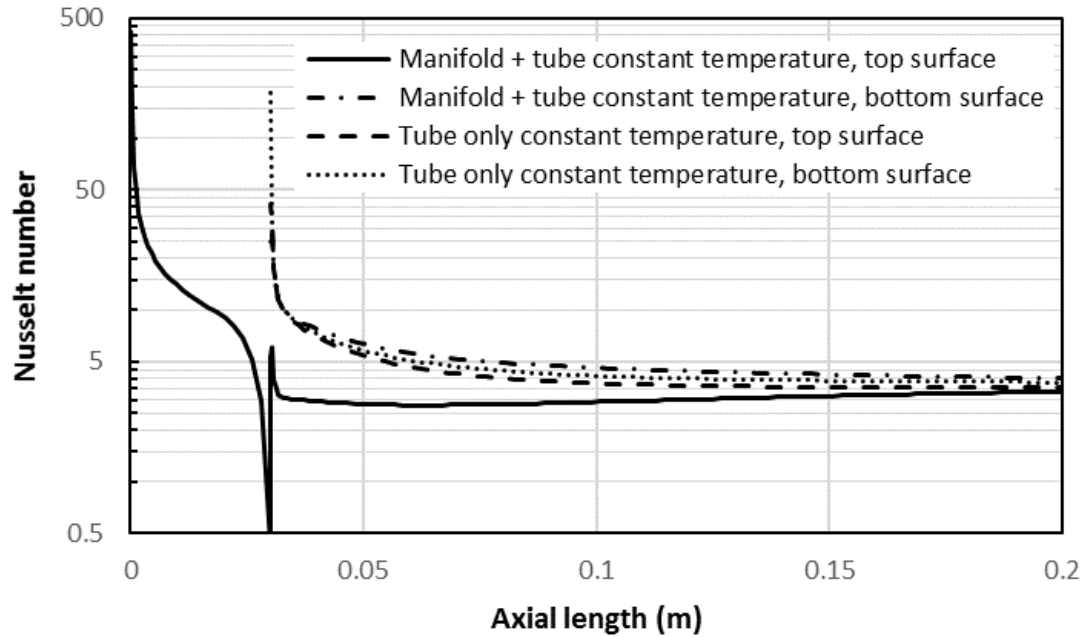


Figure 4.9. Axial Nusselt number for the tube before and after split for isothermal wall condition.

4.4 Single Manifold dividing flow in multiple smaller tubes

Figure 4.10(a) shows the mesh used for a tube system consisting of 37 tubes receiving flow from a single larger manifold. The smaller tubes are of diameter 0.3 cm while the larger manifold is 4.5 cm. The three-dimensional view is shown in Figure 4.10(b).

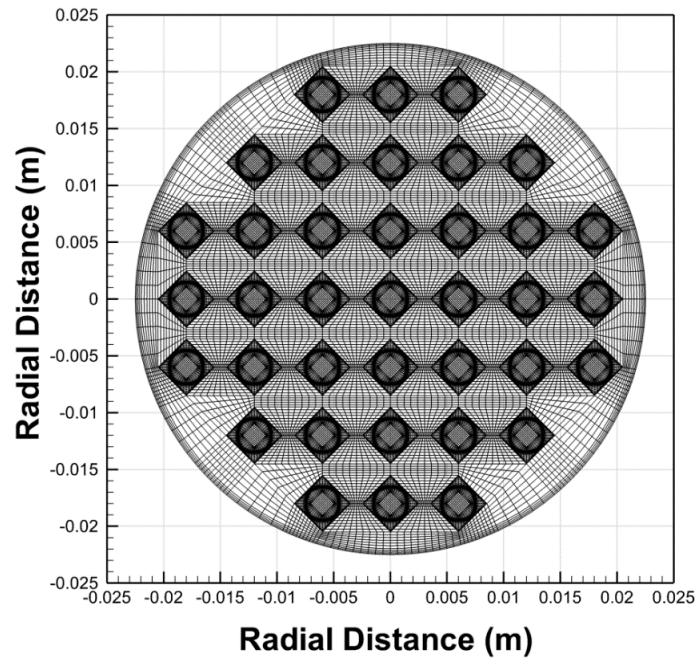
4.4.1 Constant wall temperature

Figure 4.11 shows the temperature contours for constant wall temperature case. The temperature variation in all tubes is identical when only tubes are maintained at constant temperature. For the case of manifold being subjected to same constant wall temperature

as that of the tubes, the manifold heated fluid enters the outer tubes leading to the non-axisymmetric case, with a higher mean temperature at each section of the outer tube than the interior tubes.

Figure 4.12 shows the axial variation of the Nusselt number subjected to constant wall temperature condition. Without manifold heating, all tubes have high initial Nusselt number which decreases to the fully developed value of 3.66. Whereas for manifold heating case, the Nusselt number decreases in the manifold below the fully developed value near the corner hotspot, a jump is then observed in the smaller tube due to high initial heat flux, which maintains the surface temperature with an eventual increase to reach the fully developed value. The bottom surface Nusselt number for outer tube follows the standard behavior but higher than the Nusselt number for inner tubes as the temperature is not symmetric in the outer tube in comparison with the inner tubes. All the inner tubes are axisymmetric and have the same Nusselt number variation.

a)



b)

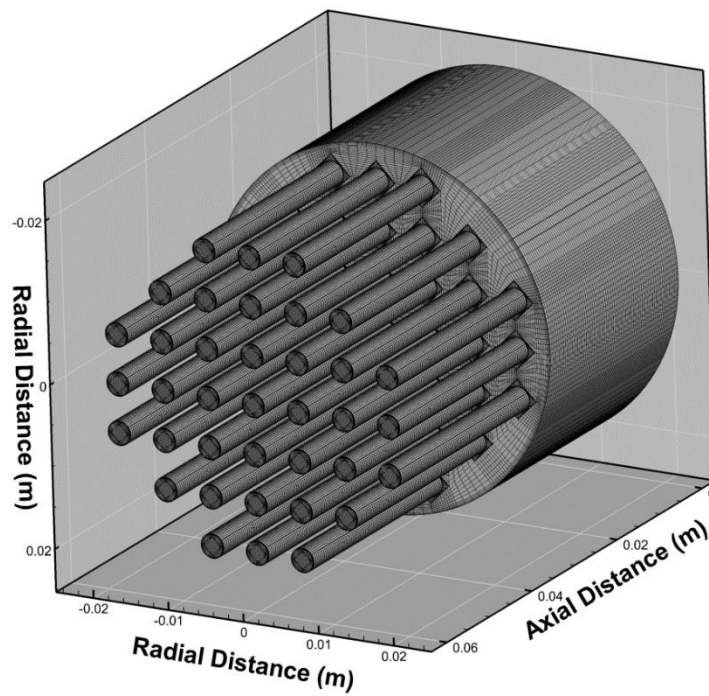
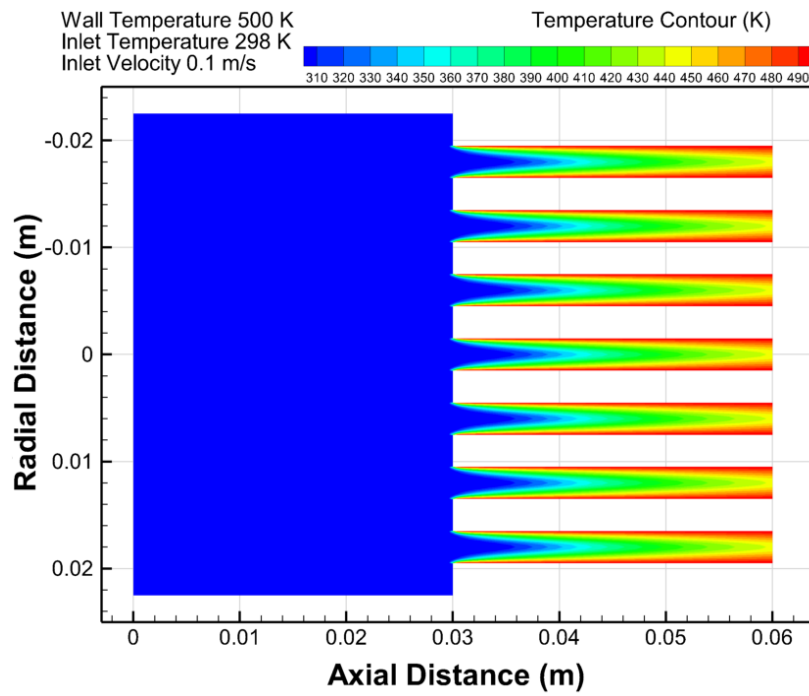


Figure 4.10. a) Crosssectional view of 37 tube split system, b) Three dimensional view of the 37 tube split system.

a)



b)

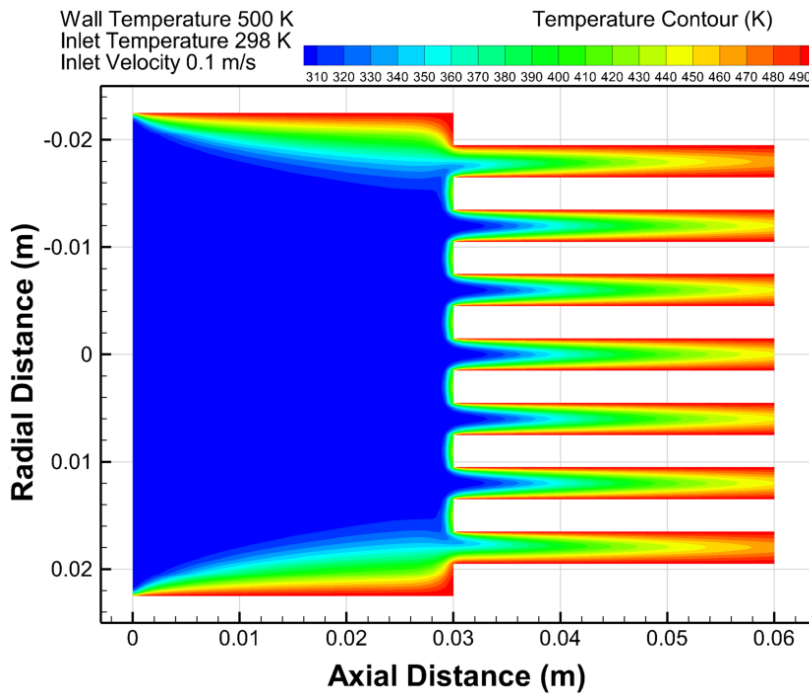
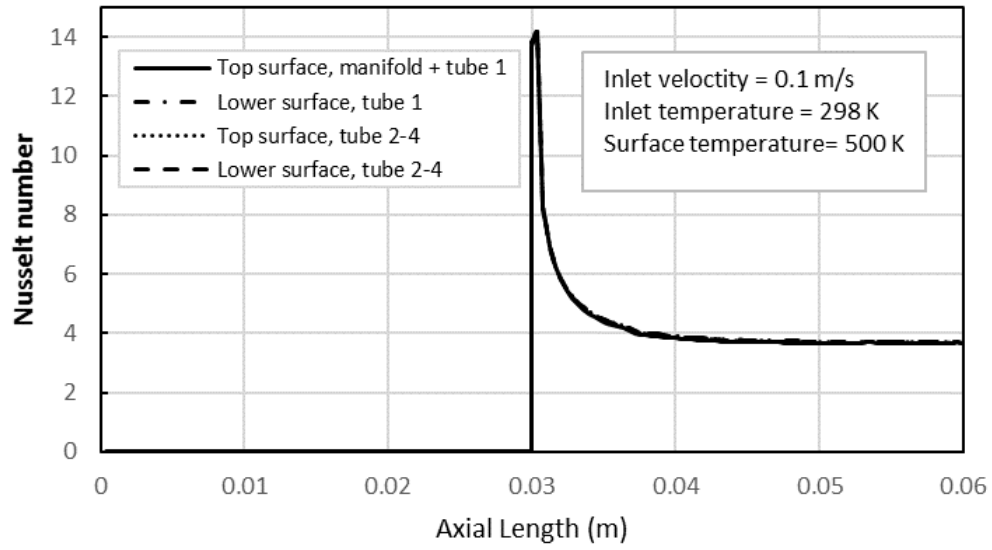


Figure 4.11. Temperature contours for a) the channel surface at 500 K with manifold adiabatic, b) all external surfaces at 500 K.

a)



b)

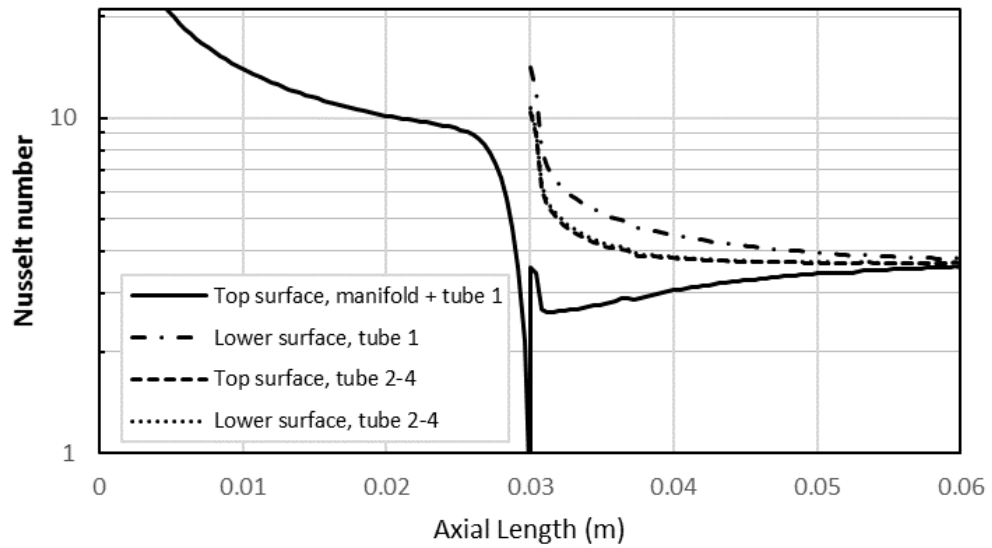


Figure 4.12. Axial Nusselt number variation for the four tubes across the cross-section of 37 tube system a) without manifold isothermal condition b) with manifold isothermal condition.

4.4.2 Constant surface heat flux

Figure 4.13 shows the temperature contours for uniform wall heat flux. The first case is with tube heat flux only while the second case is with the additional manifold heat flux. The second case shows interesting behavior where the heated flow is localized near the upper surface of the outermost tube with the lower surface at almost the inlet fluid temperature. As the heat flux is constant, the surface temperature increases slowly at the lower surface and lags behind the upper surface temperature. Now in this situation, the minimum temperature at any particular cross-section is towards the lower surface. This lowest temperature position shifts to the middle of tube cross-section as flow develops, from non-axisymmetric case to fully developed axisymmetric case.

The first part of Figure 4.14 shows the Nusselt number variation following the expected trend for the tube heated case, while the second part of the figure shows the surface Nusselt number decreasing for the manifold, then a sudden drop occurs at the split plane with the value of upper surface Nusselt number gradually increasing to the fully developed constant value within the tube. However, interestingly, the Nusselt number comes out to be negative at the lower surface of the tube at the entrance, which is not appropriate. The Nusselt number continues to decrease reaching a high negative value and then suddenly jumping to a high positive value. After that, it follows the normal decreasing behavior until the constant fully developed value is reached. It is important to note that for the calculation of Nusselt number, axisymmetric behavior is one of the main assumption which is not applicable in the current situation.

The reason behind this negative Nusselt number can be explained by Figure 4.15, which shows the variation of top and bottom wall surface temperatures along with the mean temperature at each cross-section. It is important to note that the surface temperature and mean temperature plots cross each other at the location where the Nusselt number changed from the negative to positive value. It can be seen that at the beginning of smaller tube, the mean temperature is around 303 K, the top surface temperature is around 314 K, and the bottom surface temperature is about 300 K. Hence the bottom surface is at a temperature lower than the mean temperature, and according to the definition of heat transfer coefficient (Eq. (3.25)), a negative value is obtained. Keeping in view the constant positive application of heat flux at all wall boundaries, negative Nusselt number suggest outflow of heat flux which is clearly not the case. As the difference between surface and mean temperature decreases, the heat transfer coefficient increases with negative magnitude for constant wall heat flux. As soon as the difference become positive, a high positive Nusselt number is obtained which then follows the normal trend for developing flow.

We know from the applied boundary conditions that the surface Nusselt number cannot be negative as a positive heat flux is applied at all walls, hence a modification is suggested in this paper for calculation of the peripheral Nusselt number for non-axisymmetric cases. Instead of calculating average temperature over the whole cross-sectional area of the tube, the average temperature is based on the lines joining the tube surface to the axis of the thermal boundary. The detailed method is provided in the Appendix where the analysis and calculations are done on data imported into MATLAB from ANSYS Fluent.

Figure 4.16(a) shows the results from this modification. It can be seen that now the Nusselt number is positive for both the surfaces, which should be the case based on the boundary condition of heat influx from all surface. Figure 4.16(b) shows surface plot of Nusselt number variation along the circumference of the tube with 0° angle at the right surface and increasing counter clockwise. It is clear that at the top side, Nusselt number is low initially and then increases to reach fully developed value. Whereas all other surface points have a higher Nusselt number initially and then decrease to the fully developed value.

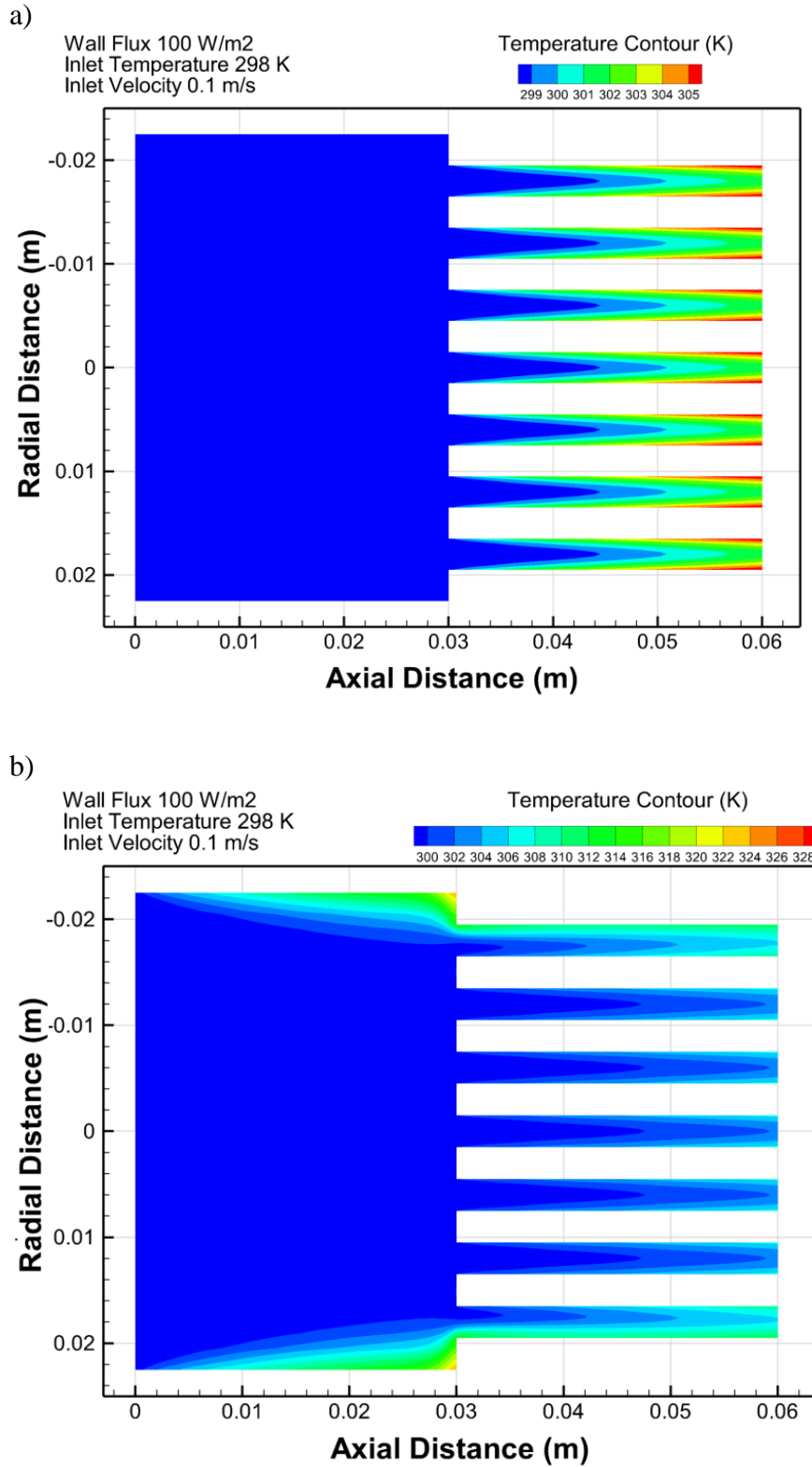
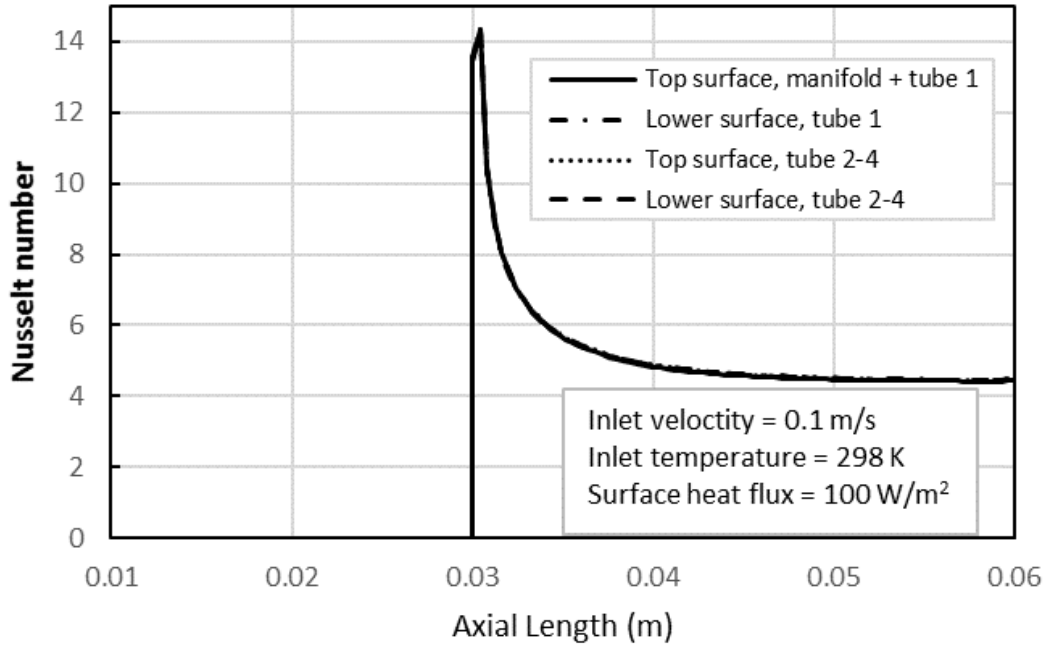


Figure 4.13. Temperature contours for a) the channel surface at constant surface heat flux with manifold adiabatic, b) all external surfaces at constant surface heat flux.

a)



b)

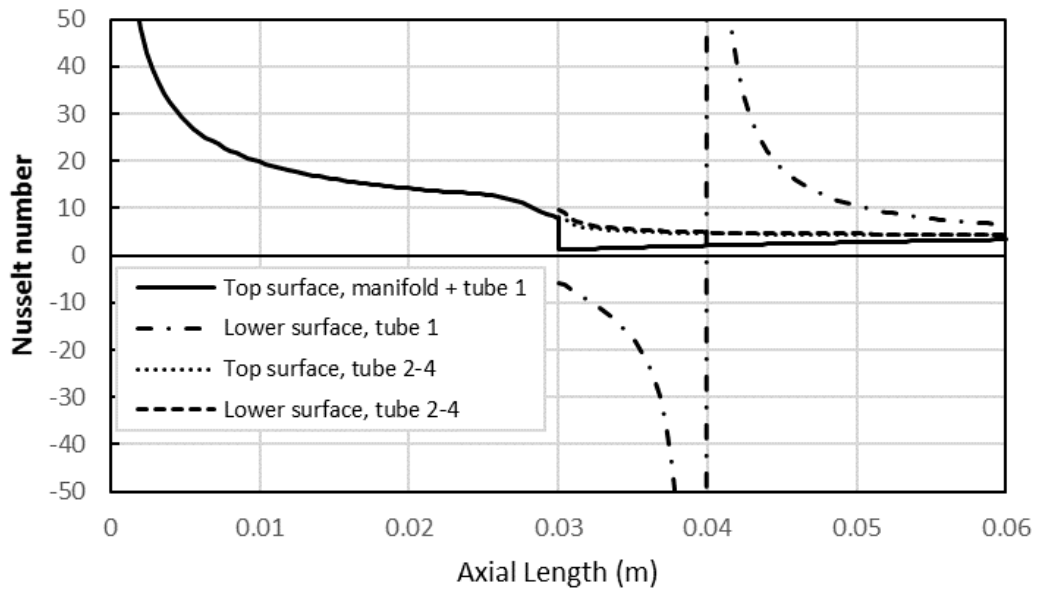


Figure 4.14. Surface Nusselt number for the four tubes across the cross-section of 37 tube system a) without manifold heating b) with manifold heating.

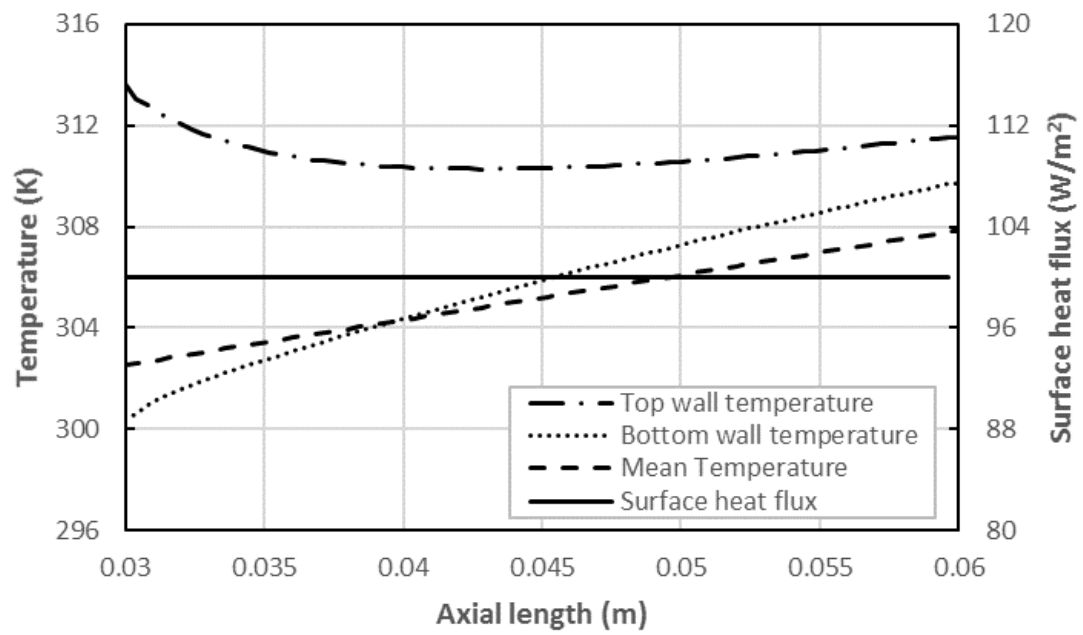
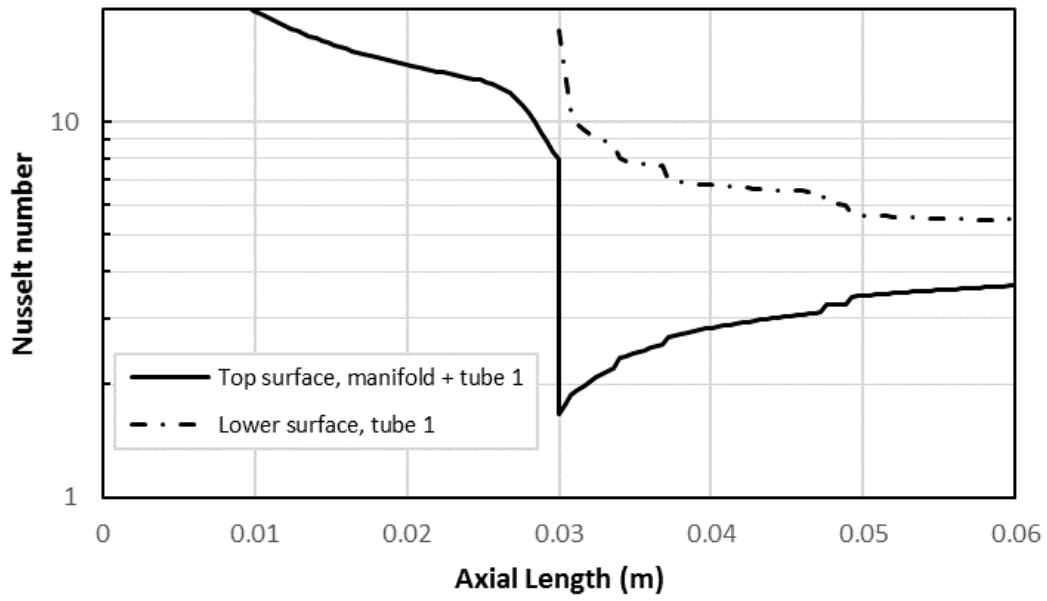


Figure 4.15. Temperature and heat flux variation for tube 1, after split from manifold.

a)



b)

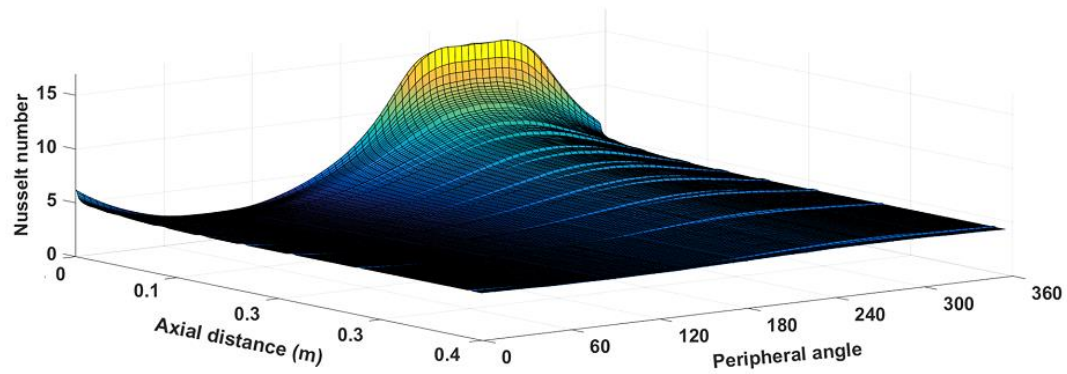


Figure 4.16. a) Axial Nusselt number variation for the first tube with modified mean temperature. b) Nusselt number variation in the top tube after split.

4.5 Performance comparison.

Three layouts have been considered with a total length of 6 cm for all cases to make a comparison between their performances with the manifold heating. The base case of the single tube is compared with 4 and 37 tube split system.

Table 4.1 provides a summary of the results, while Table 4.2 gives the ratio of results taking the single pipe as reference. Considering the single tube to be the base case, there is about a 60-fold increase in pressure loss for 4 tube system and 257-fold pressure loss for the 37-tube system. Here it is important to mention that these pressure losses are representing the losses due to the manifold to tube split flow, otherwise the same flow rate splitting into multiple similar tubes would reduce the flow in each pipe thus lowering the losses. For instance, if the same flow rate of single tube is split into 4 similar tubes, reduced flow rate would result in lower pressure loss by a factor of about 6 while for 37 tubes, about 80 times lower pressure loss would occur. For isothermal cases, 7 W of additional heat is added with 4 tube system and 25 W for the 37-tube system. Hence more heat is absorbed by the system by having more surface area exposed to the isothermal condition. The corresponding increase in exit temperature is 37 K for the 4-tube system and 131 K for the 37-tube system. These high values are due to the fact that majority of the tubes are still in the developing region and a very high heat flux occur in the constant wall temperature cases, hence a corresponding increased performance is obtained. For the constant heat flux cases, a minor increase in performance is noticed. The amount of heat transfer increased only by 0.08 W for 4 tube system and 0.7 W for the 37-tube system. This leads to a temperature increase of 0.4 K for 4 tube system and 3.8 K for the 37-tube system.

Table 4.1. Summary of results from the three main cases of split flow.

Output Parameters	Single tube		4 tubes		37 tubes	
	Isothermal	Isoflux	Isothermal	Isoflux	Isothermal	Isoflux
Pressure drop (Pa)	0.006749		0.4113		1.7349	
Outlet temperature (K)	344.201	302.305	382.068	302.713	476.188	306.149
Total heat transfer (W)	10.035	0.848	17.280	0.928	35.719	1.602

Table 4.2. Comparison of results from the three main cases, with single pipe as base case.

Output Parameters	Single tube		4 tubes		37 tubes	
	Isothermal	Isoflux	Isothermal	Isoflux	Isothermal	Isoflux
Pressure drop ratio	1		60.942		257.060	
Outlet temperature ratio	1	1	1.110	1.001	1.383	1.012
Total heat transfer ratio	1	1	1.721	1.094	3.559	1.889

Chapter 5

ASSESSMENT OF THERMO-FLUID ANALOGIES

This chapter consists of 4 sections. First section is focused on the introduction, second section is focused on the model for analogy assessment. The third section has four sub-section, each dealing with Couette flow, parallel plate flow, internal tube flow and flow over a flat plate respectively.

5.1 Introduction

Upon examination of governing differential equations for heat and mass transfer, some basic similarities are observed. The differences are reduced to dimensionless numbers, after which the equations reduce exactly to the same form. This led to the analogy between the friction and heat transfer coefficients, allowing one to be determined if other is known. The basic analogy was developed by Reynolds and then correlated by Chilton and Colburn. For Reynolds analogy, the main assumptions are that there is no pressure gradient in the axial direction and the Prandtl number is unity. This results in exact same energy and momentum equations, with the relationship between the dimensionless groups (defined earlier in section 3.4) as

$$C_f \frac{Re}{2} = Nu \quad \text{or} \quad \frac{C_f}{2} = St \quad (5.1)$$

However, Chilton-Colburn analogy included the effect of non-unity Prandtl number as

$$\frac{C_f}{2} = St Pr^{\frac{2}{3}} \quad (5.2)$$

The correlation (5.2) is valid for the range $0.6 < Pr < 60$. In the current work, these analogies are evaluated based on numerical solutions of four different flow arrangements, in order to determine the usefulness of these analogies. The work includes shear driven Couette flow, flat plate, parallel plate and pipe flow arrangements and the results are presented for developing and developed flow regions. In the study both laminar and turbulent flow regimes are also examined, so that overall applicability of these analogies may be determined for any particular case. These values can be taken as reference and better results can be achieved. The fully developed data is also presented in tabular form for quick reference purpose.

5.2 Model description

Four configurations are studied representing various flow channels, a) Couette, b) pipe, c) parallel-plate, and d) flat-plate flows. The different boundary conditions used for such flow configurations are shown in Figure 5.1. It can be seen that for the parallel plate, the top and bottom surfaces are stationary walls, while the top wall is moving for Couette flow to result in a shear driven flow. For flat plate, the top wall is symmetry, which increases the flow width so that the flow at the lower wall is not affected by the presence of top surface. For the pipe flow, two-dimensional axisymmetric modeling is done; thus, the lower axis of symmetry represents the middle of pipe section, and height representing the radius of the tube. For shear driven (periodic) flow, the width and length are taken to be 1 m. For all other cases, the channel width is taken to be 0.045 m and various laminar and turbulent

cases are considered. The length of the channel and flat plate are taken as 2 m, which is sufficient for fully developed conditions. For cases where this length is not sufficient for fully developed conditions, flow length is increased to ensure the tabular data is for fully developed conditions.

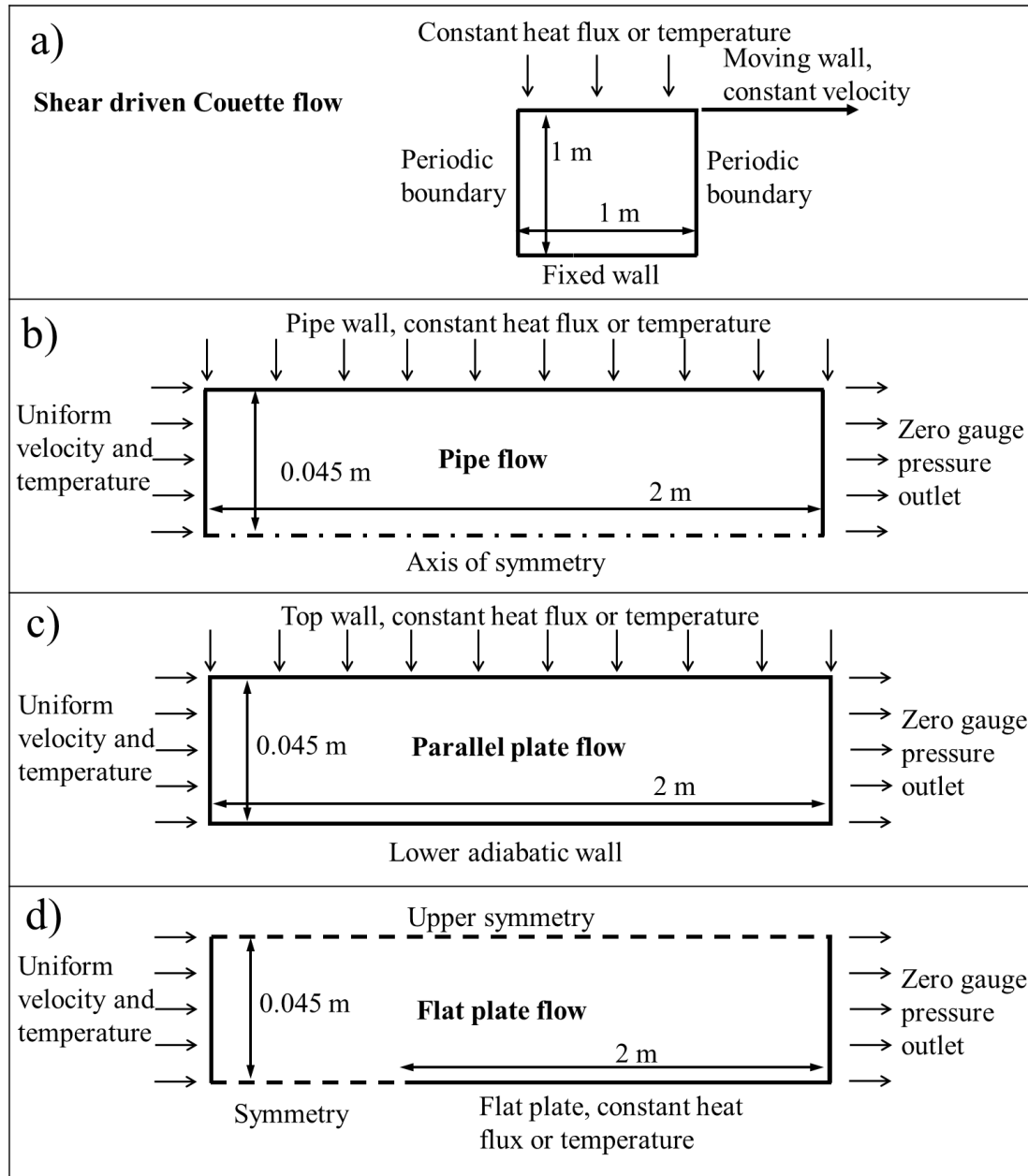


Figure 5.1. Schematic for the cases under study, a) Couette, b) pipe, c) parallel-plate and d) flat-plate configurations.

Table 5.1 shows the four fluids that are used in the present analysis, with constant properties in order to avoid secondary effects of variable properties [158]. Air and water properties are taken at normal temperature and pressure. In order to obtain Prandtl number of unity and 0.86 [175], air properties are modified to the fictitious fluids as shown in Table 5.1.

Table 5.1. List of fluids used for analogy assesment, along with their respective properties.

Fluid	Prandtl Number, Pr (-)	Density, ρ (kg m ⁻³)	Specific heat, C_p (J kg ⁻¹ K ⁻¹)	Viscosity, μ (kg m ⁻¹ s ⁻¹)	Thermal conductivity, k (W m ⁻¹ K ⁻¹)
Air	0.744	1.225	1006.43	1.79E-05	0.0242
Modified air-1	0.86	1	1032	1.00E-05	0.012
Modified air-2	1	1	1000	1.00E-05	0.01
Water	6.99	998.2	4182	1.003E-03	0.6

5.3 Validation

The validation of the current work was done against the work presented by Mahulikar and Herwig [158] on Reynolds analogy for the fluids with variable properties. Water is used as the working fluid with temperature dependent properties. It can be seen from the Table 5.2 that the values of the skin friction coefficient and Stanton number are matching well with the ones available in the literature. This validates the methods used for the calculation of these parameters from the numerical simulation.

The grid used in this study was same as used in the previous chapter. The detailed discussion is available in 3.5Chapter 3, where some additional validation studies performed using the current numerical methods, with the fundamental relations of momentum and heat transfer are discussed.

Table 5.2. Comparison of current modeling with the data published in [158].

	Current work	Literature	Percent Difference
Heat flux (W m^{-2})	50000	50000	(-)
Velocity (m s^{-1})	0.05	0.05	(-)
$C_f/2$ inlet	2.979	2.997	0.60 %
$C_f/2$ outlet	1.260	1.291	2.40 %
Stanton Number inlet	0.125	0.127	1.57 %
Stanton Number outlet	0.142	0.145	2.06 %

5.4 Results and Discussion

The following sections contain the detailed discussion about the analogy results obtained for the four flow types under study.

5.4.1 Shear Driven (Couette) Flows

For the shear driven flows (Figure 5.1(a)), the bottom surface is assumed stationary, while the upper surface is moving with a constant velocity. Four fluids are studied, as mentioned earlier, with both thermal boundary conditions of constant temperature and heat flux. Table 5.3 shows the data obtained for Reynolds number of 1,000. It should be noted that the Brinkman number ($Br = \mu u^2 / k(T_{w1} - T_{w0})$) is very small for fluids like air and water. For such fluids, the effect of viscous damping on the temperature is insignificant [180]. For such fluids undergoing Couette flow, the velocity and temperature profiles are linear, resulting in same Nusselt number and Stanton number values for both uniform temperature and uniform heat flux cases. The Nusselt number at the moving surface remains equal to six for all cases studied. Additional studies of varying height, length, and Reynolds number were performed, all resulting in same values for the Stanton number and skin friction coefficient, for same Prandtl and Reynolds number combinations, irrespective of the choice of thermal boundary condition.

The Stanton number is based on the upper moving wall velocity. For calculation of skin friction coefficient, both maximum and mean velocities are studied. With regards to the maximum velocity, we can see that as the Prandtl number increases, the ratio of Chilton-Colburn analogy changes from 3.3 to 1.5; however, for average velocity, it changes from 0.83 to 0.39. Hence, we can conclude that for lower Prandtl number, average velocity should be used, while for higher Prandtl number, maximum velocity is recommended.

Table 5.3. Data for Couette flow at Re=1000 for both constant wall temperature and heat flux.

Prandtl number, Pr	Velocity, (m s ⁻¹)		Temperature, (K)		Heat flux, (W m ⁻²)	Heat transfer coeffic ient, (W m ⁻² K ⁻¹)	Nusselt number, Nu	Stanton number, St	$St \times Pr^{2/3}$	Wall shear stress, (Pa)	$\frac{C_{f,max}}{2}$	$\frac{St \times Pr^{2/3}}{C_{f,max}/2}$	$\frac{C_{f,avg}}{2}$	$\frac{St \times Pr^{2/3}}{C_{f,avg}/2}$
	Maximum	Mean	Surface	Mean										
Constant wall temperature														
0.74	0.0075	0.00375	500.00	432.66	4.88	0.073	6.00	7.85E-03	6.45E-03	1.34E-07	1.95E-03	3.31	7.79E-03	0.83
0.86	0.005	0.0025	500.00	432.66	2.42	0.036	6.00	6.98E-03	6.31E-03	5.00E-08	2.00E-03	3.15	8.00E-03	0.79
1	0.005	0.0025	500.00	432.66	2.02	0.030	6.00	6.00E-03	6.00E-03	5.00E-08	2.00E-03	3.00	8.00E-03	0.75
6.99	0.0005	0.00025	500.00	432.66	121.2	1.800	6.00	8.62E-04	3.15E-03	5.01E-07	2.01E-03	1.57	8.04E-03	0.39
Constant wall flux														
0.74	0.0075	0.00375	711.22	573.48	10	0.073	6.00	7.85E-03	6.45E-03	1.34E-07	1.95E-03	3.31	7.79E-03	0.83
0.86	0.005	0.0025	1131.33	853.54	10	0.036	6.00	6.98E-03	6.31E-03	5.00E-08	2.00E-03	3.15	8.00E-03	0.79
1	0.005	0.0025	1298.00	964.65	10	0.030	6.00	6.00E-03	6.00E-03	5.00E-08	2.00E-03	3.00	8.00E-03	0.75
6.99	0.0005	0.00025	314.66	309.11	10	1.800	6.00	8.62E-04	3.15E-03	5.01E-07	2.01E-03	1.57	8.04E-03	0.39

5.4.2 Parallel plate flow

For parallel plates (Figure 5.1(c)), the inlet temperature is 298K with the upper wall temperature assumed to be 500K for all the fluids considered. Laminar cases for air are studied for Reynolds number of 15, 150 and 1500, while the turbulent cases are for Reynolds number of 3080, 6160 and 30800. These Reynolds number correspond to velocities of 0.005, 0.05, 0.5, 1, 2 and 10 m/s, respectively. For water, the inlet velocities studied start from 0.00035 m/s in multiples of 10 to cover the whole laminar-to-turbulent regions ($15 \leq Re \leq 1,500,000$).

Figure 5.2 shows the developing profiles for the Nusselt number, Stanton number, and skin friction coefficient. It can be seen that all cases become fully developed at a distance of about 0.6 m from the leading edge. For Reynolds number of 1500, it takes a longer distance to develop. It is also important to mention that developing region for turbulent flow is almost independent of the Reynolds number and develops faster than the higher laminar cases. The laminar Nusselt numbers converge to the fully developed value, while for turbulent flow, higher Reynolds number results in a higher Nusselt number. Figure 5.3 shows similar contours but for water ($Pr = 6.9$), it can be seen that it takes longer for water to develop in the channel (around 2 m). For Re of 1.5×10^3 , a longer length is considered to obtain the fully developed values listed in tabular form. In these figures, an important observation can be made about Stanton number that its value decreases for increasing Reynolds number in the laminar region. Then as the flow transitions from laminar to turbulent, there is an increase in the Stanton number due to sudden increase in the heat

transfer coefficient in the turbulent region. After the jump in transition region, the Stanton number again decreases for increasing the Reynolds number. A similar behavior is seen in the Moody diagram [181] for the friction coefficient, that it decreases in the laminar region, then a jump is seen in the transition region and then it reduces again in the turbulent region. This increasing behavior for the Stanton number and friction coefficient, as the flow transitions from laminar to turbulent, can also be seen in the tables (4 - 7)

Constant wall temperature: Figure 5.4 shows a comparison between different components of the analogies. It is important to emphasize that in the developing region, both factors have higher values, decreasing as the flow develops. Hence in all these figures, the flow develops from the top right corner towards opposite diagonal at the bottom left (as indicated by direction of the black arrow). In Figure 5.4 (a), the Reynolds analogy is shown with C_f based on maximum velocity. For all these cases, it is seen that Stanton number is slightly higher than the half skin friction coefficient ($St > C_f/2$). Hence, to accommodate this difference, product of St and $Pr^{2/3}$ is plotted in Figure 5.4 (b) according to the Chilton-Colburn analogy. As $Pr^{2/3}$ is less than unity, it reduces the values and the plots fall nearer to the exact values shown by the diagonal line. The lowest value of laminar flow ($Re = 15$) is the best fit, while the highest laminar flow at $Re = 1500$ shows some deviation from the exact values. In Figure 5.4 (c) and Figure 5.4 (d), it can be seen that for C_f based on average velocity, Reynolds analogy is better than Chilton-Colburn analogy for all the cases. The values all lie near the diagonal line and the modification to Chilton-Colburn analogy just increases the deviation for all the cases. Hence for laminar cases, Chilton-Colburn analogy

based on maximum velocity is suitable. For turbulent cases ($Pr = 0.74$), Reynolds analogy with average velocity is the best fit for developing as well as developed flow regions.

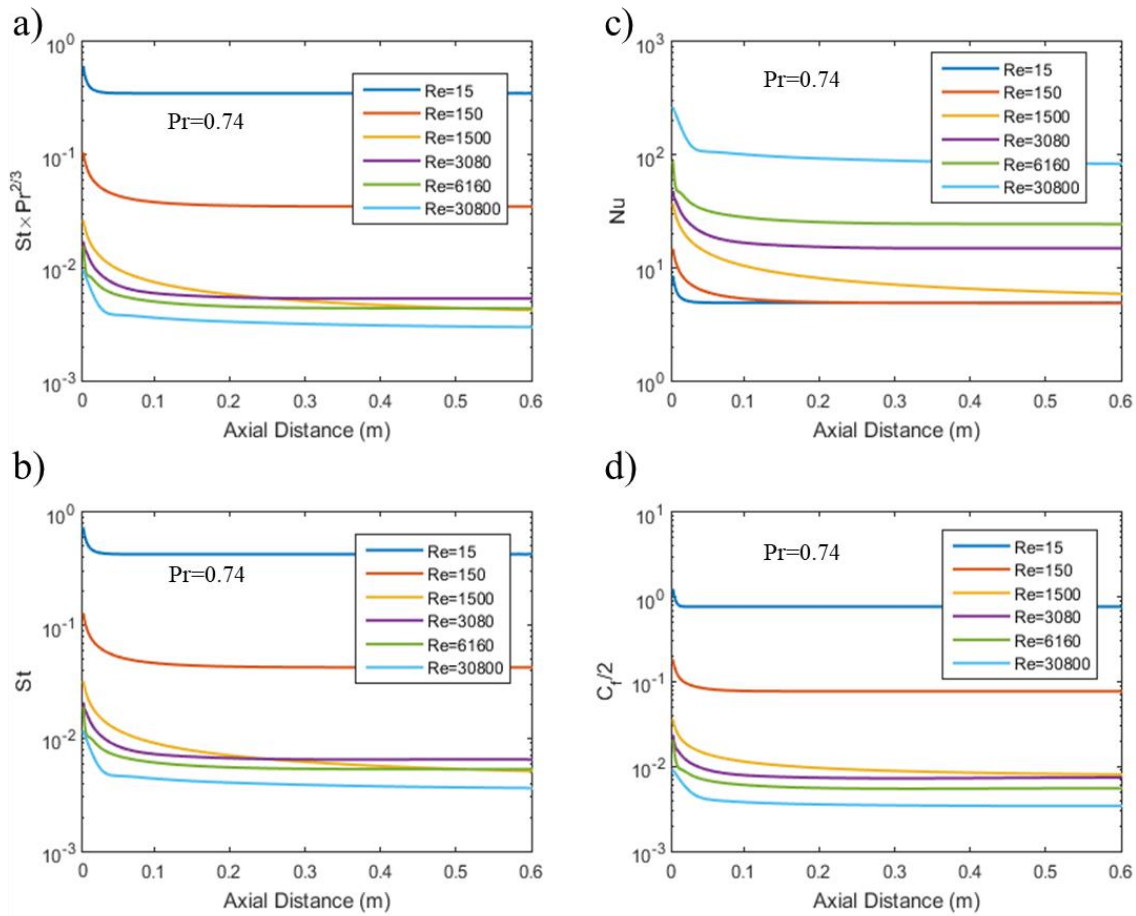


Figure 5.2. Plots for the axial development of a) $St \times Pr^{2/3}$, b) Stanton number, c) Nusselt number and d) half of skin friction coefficient. Parallel plate, $Pr=0.74$.

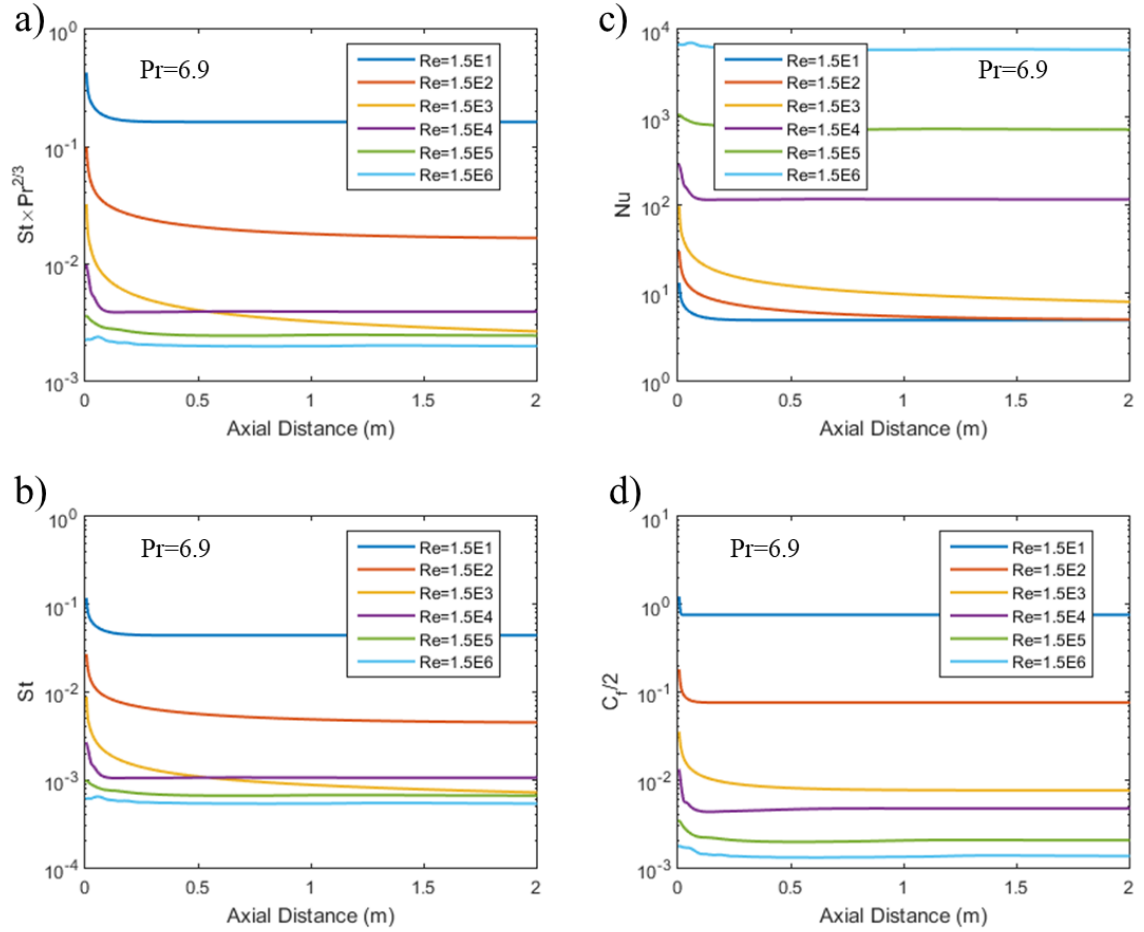


Figure 5.3. Plots for the axial development of a) $St \times Pr^{2/3}$, b) Stanton number, c) Nusselt number, and d) half of skin friction coefficient. Parallel plate, $Pr=6.9$.

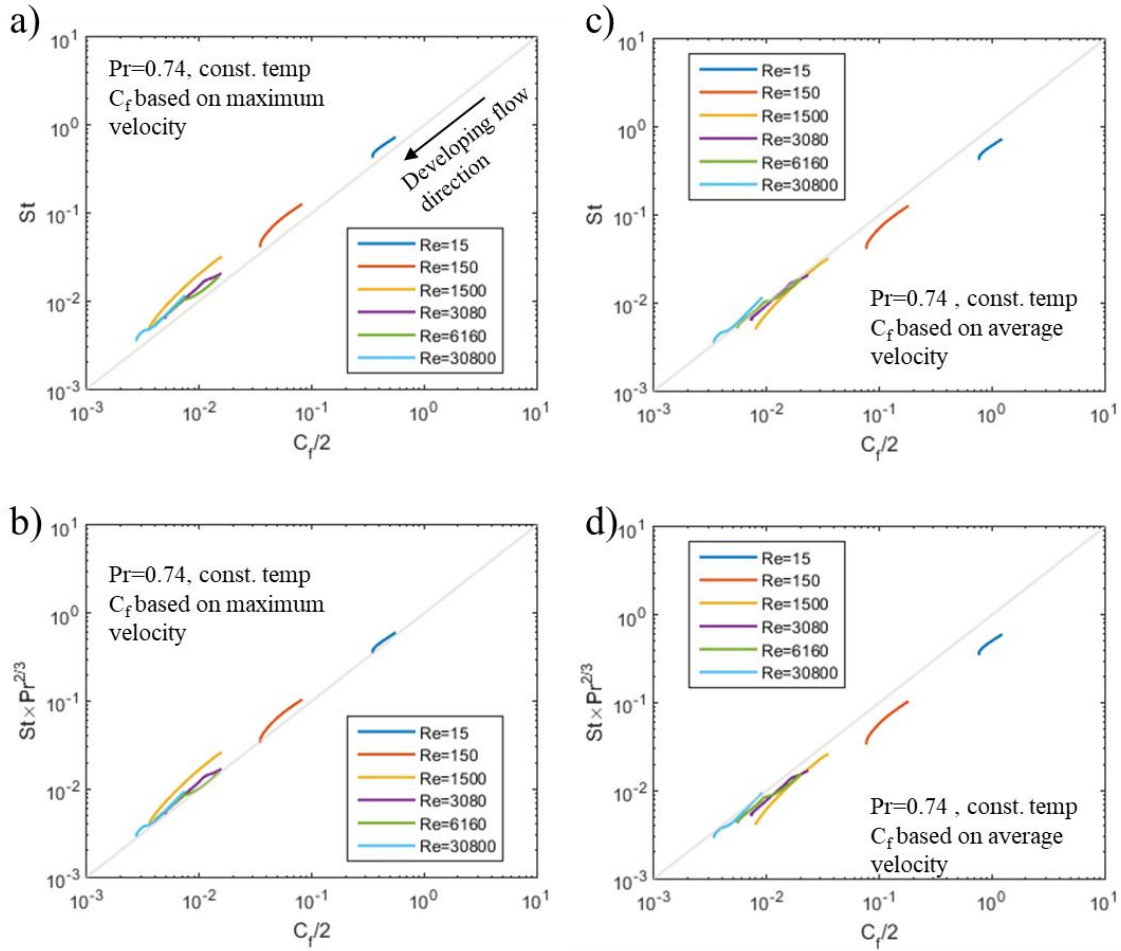


Figure 5.4. Comparison of Reynolds analogy (a, c) and Chilton-Colburn analogy (b, d) when skin friction is based on channel maximum velocity (a, b), or channel average velocity (c, d). Parallel plate, constant wall temperature, $Pr=0.74$.

Figure 5.5 shows similar contours for $Pr = 0.86$, while Figure 5.6 for $Pr = 1$. It can be seen from Figure 5.5 (a) and Figure 5.6 (a) that as the Prandtl number increases, the Reynolds analogy becomes increasingly valid for all cases, such that fully developed value lies on the diagonal line. This is in agreement with the assumption that the analogy is basically valid for $Pr = 1$. All plots in Figure 5.5 (b) and Figure 5.6 (b) don't have any difference among themselves for either laminar or turbulent cases, leading to the conclusion that for $Pr < 1$, laminar cases with Chilton-Colburn analogy should be based on maximum velocity in the channel, while for turbulent flow, Reynolds analogy should be based on average velocity. Reynolds analogy based on average velocity is good for both developing and developed regions.

Figure 5.7 shows the plots for higher $Pr = 6.9$, where we see a vertical line near the developed regions. This can be explained with the results presented in Figure 5.3, where it can be seen that for laminar flow, the skin friction coefficient develops faster than the Nusselt number, hence the friction factor remains constant for developing heat transfer coefficient. This effect is not available for the turbulent flow conditions as the development is almost similar for both heat transfer coefficient and skin friction coefficient. With regards to Reynolds analogy, it is important to note that some significant deviations are noticed (refer to Figure 5.7 (a)) for all the Reynolds number investigated, which are adjusted in Figure 5.7 (b) with the use of Chilton-Colburn analogy. For laminar flow conditions, Chilton-Colburn analogy based on maximum velocity is the best option but the fully developed values still remain away from the expected diagonal line. For $Re = 1.5 \times 10^4$, the fully developed value matches exactly with the diagonal line, but as the Reynolds

number is further increased, the developed region does show deviation from the analogy, but not as significant as for the laminar cases. In conclusion, Chilton-Colburn analogy with maximum velocity is suitable for laminar flows while average velocity is better for turbulent flow conditions.

Table 5.4 shows the raw data for all the cases studied for constant wall temperature. The ratios should have a value of 1 to result in an exact analogy. It can be seen for $Pr = 6.9$, the maximum velocity is better for laminar flow with ratio around 0.5. For a lower range of turbulent flow, the maximum velocity is better, but for higher turbulent flow, average velocity is having a better ratio of 1.45; however, these values show a significant deviation from unity. The best result is for lower turbulent flow ($Re=1.6E+4$). For cases of $Pr < 1$, the maximum velocity results in the values of ratio near unity, with improving results for decreasing Prandtl number, with an exact match for laminar and low Prandtl number cases. The Reynolds analogy shows better results for the highest Reynolds number under consideration.

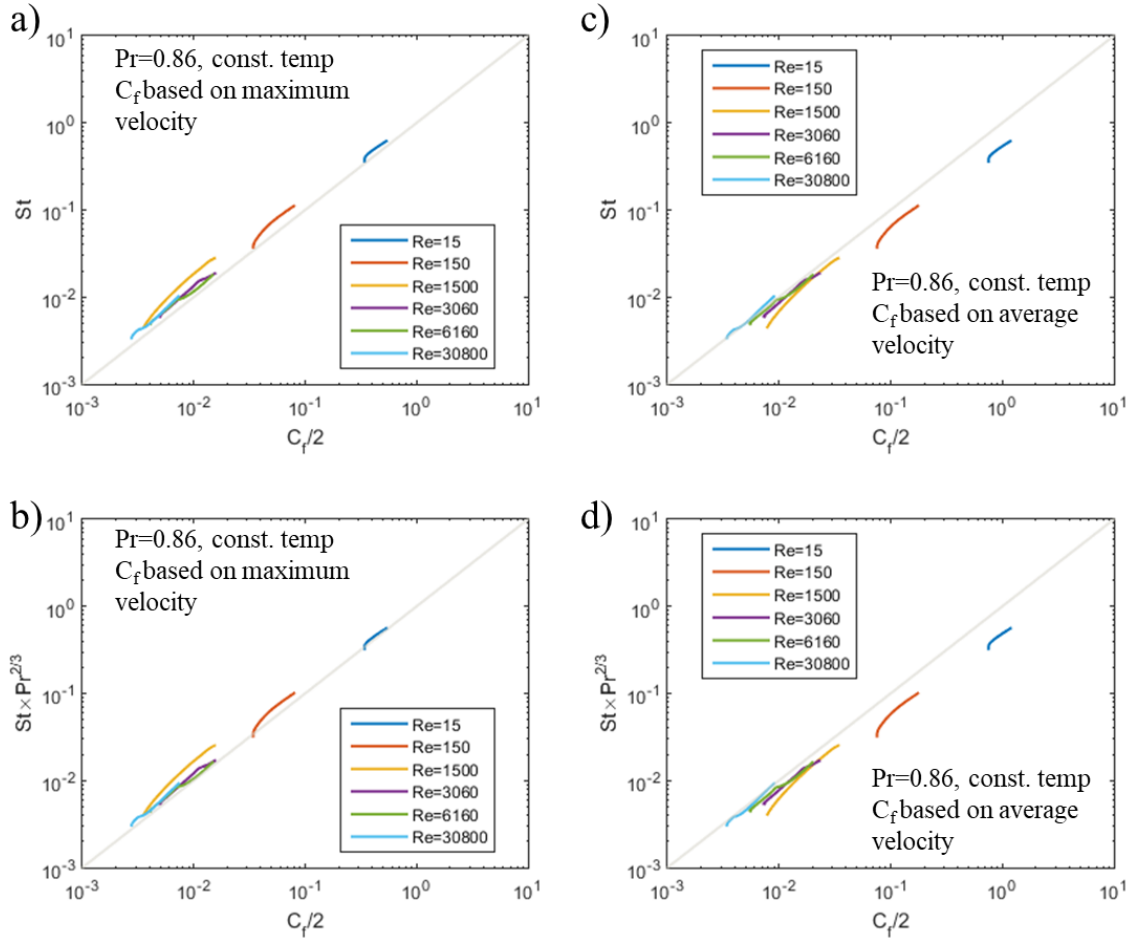


Figure 5.5. Comparison of Reynolds analogy (a, c) and Chilton-Colburn analogy (b, d) when skin friction is based on channel maximum velocity (a, b), or channel average velocity (c, d). Parallel plate, constant wall temperature, $Pr=0.86$.

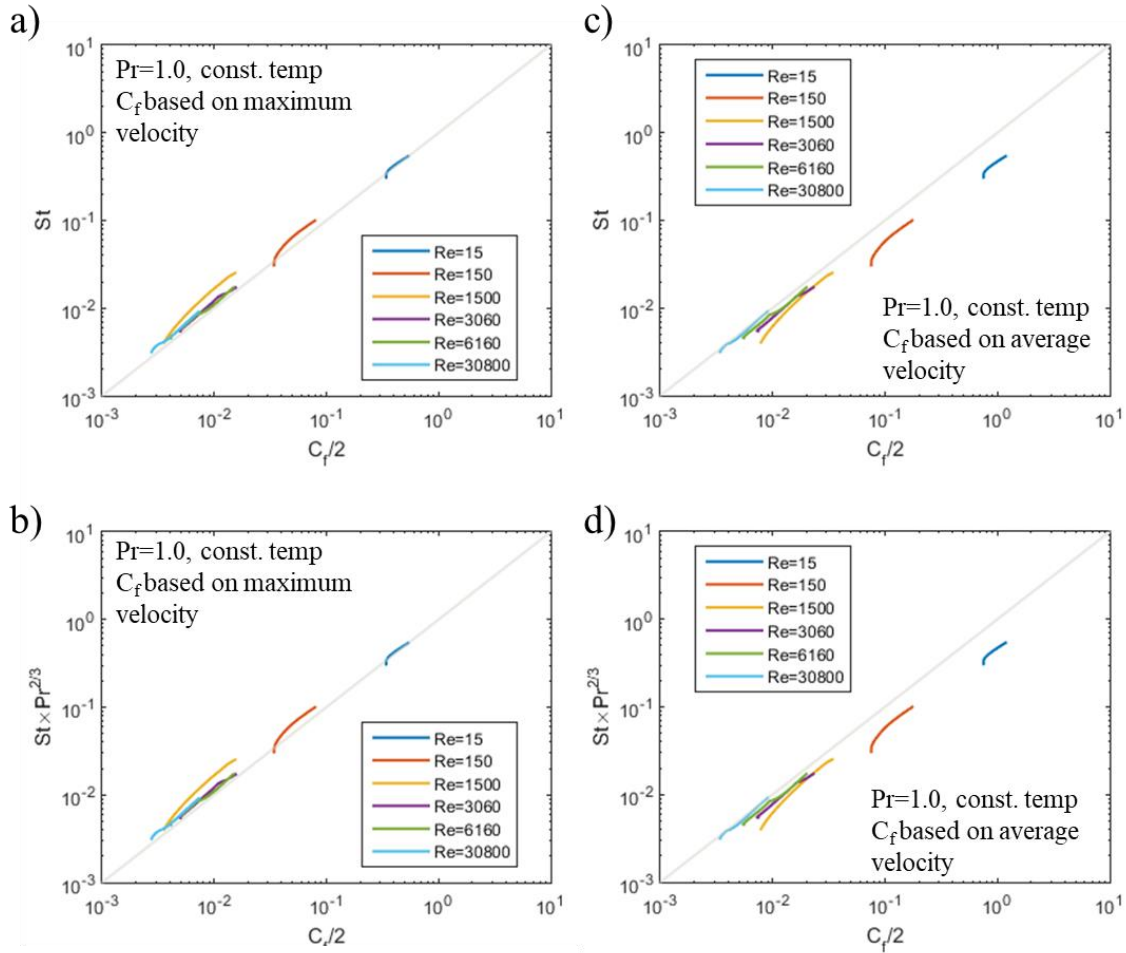


Figure 5.6. Comparison of Reynolds analogy (a, c) and Chilton-Colburn analogy (b, d) when skin friction is based on channel maximum velocity (a, b), or channel average velocity (c, d). Parallel plate, constant wall temperature, $Pr=1.0$.

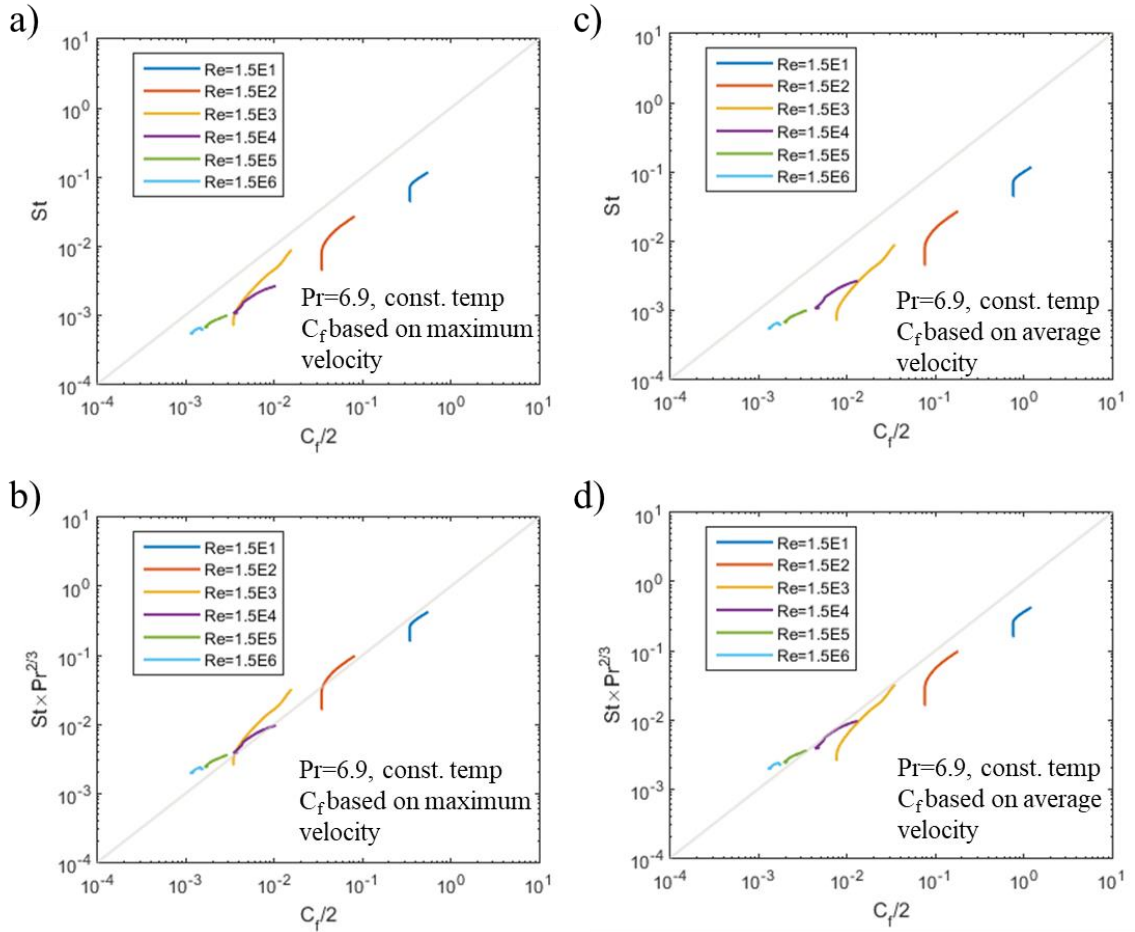


Figure 5.7. Comparison of Reynolds analogy (a, c) and Chilton-Colburn analogy (b, d) when skin friction is based on channel maximum velocity (a, b), or channel average velocity (c, d). Parallel plate, constant wall temperature, $Pr=6.9$.

Table 5.4. Data for parallel plate with constant wall temperature.

Velocity, (m s ⁻¹)		Reynolds number, Re	Wall shear stress, (Pa)	Temperature, (K)		Heat flux, (W m ⁻²)	Nusselt number, Nu	Stanton number, St	$St \times Pr^{2/3}$	$\frac{C_{f,avg}}{2}$	$\frac{St}{C_{f,avg}/2}$	$\frac{St \times Pr^{2/3}}{C_{f,avg}/2}$	$\frac{C_{f,max}}{2}$	$\frac{St}{C_{f,max}/2}$	$\frac{St \times Pr^{2/3}}{C_{f,max}/2}$
Average	Maximum			Surface	Mean										
Water Pr=6.9															
3.5E-4	5.2E-4	1.6E+1	9.3E-5	500	496.5	2.3E+2	4.86	4.4E-2	1.6E-1	7.6E-1	0.06	0.21	3.4E-1	0.13	0.47
3.5E-3	5.2E-3	1.6E+2	9.3E-4	500	377.8	8.0E+3	4.94	4.5E-3	1.6E-2	7.6E-2	0.06	0.22	3.4E-2	0.13	0.48
3.5E-2	5.2E-2	1.6E+3	9.2E-3	500	417.7	5.3E+3	4.85	4.4E-4	1.6E-3	7.6E-3	0.06	0.21	3.4E-3	0.13	0.47
3.5E-1	3.9E-1	1.6E+4	5.8E-1	500	316.4	2.8E+5	116	1.1E-3	3.9E-3	4.7E-3	0.22	0.82	3.8E-3	0.28	1.03
3.5E+0	3.8E+0	1.6E+5	2.5E+1	500	309.8	1.8E+6	723	6.6E-4	2.4E-3	2.0E-3	0.32	1.18	1.7E-3	0.38	1.40
3.5E+1	3.7E+1	1.6E+6	1.7E+3	500	307.6	1.5E+7	5880	5.4E-4	2.0E-3	1.4E-3	0.40	1.45	1.2E-3	0.45	1.66
Air Pr= 1															
3.5E-3	5.2E-3	1.6E+1	9.2E-6	500	499.9	6.9E-2	4.88	3.1E-1	3.1E-1	7.5E-1	0.41	0.41	3.4E-1	0.91	0.91
3.5E-2	5.2E-2	1.6E+2	9.2E-5	500	421.3	8.5E+1	4.86	3.1E-2	3.1E-2	7.5E-2	0.41	0.41	3.4E-2	0.90	0.90
3.5E-1	5.2E-1	1.6E+3	9.2E-4	500	362.7	1.6E+2	5.08	3.2E-3	3.2E-3	7.5E-3	0.43	0.43	3.4E-3	0.94	0.94
6.8E-1	8.3E-1	3.1E+3	3.4E-3	500	329.1	6.4E+2	16.7	5.5E-3	5.5E-3	7.4E-3	0.74	0.74	5.0E-3	1.09	1.09
1.4E+0	1.6E+0	6.2E+3	1.0E-2	500	324.0	1.1E+3	27.9	4.5E-3	4.5E-3	5.5E-3	0.82	0.82	4.1E-3	1.11	1.11
6.9E+0	7.6E+0	3.1E+4	1.6E-1	500	316.4	4.0E+3	96.9	3.1E-3	3.1E-3	3.4E-3	0.92	0.92	2.8E-3	1.14	1.14
Air Pr=0.86															
3.5E-3	5.2E-3	1.6E+1	9.2E-6	500	500.0	2.6E-2	4.88	3.6E-1	3.3E-1	7.5E-1	0.48	0.43	3.4E-1	1.05	0.95
3.5E-2	5.2E-2	1.6E+2	9.2E-5	500	431.3	8.9E+1	4.85	3.6E-2	3.2E-2	7.5E-2	0.47	0.43	3.4E-2	1.05	0.95
3.5E-1	5.2E-1	1.6E+3	9.2E-4	500	369.1	1.7E+2	5.00	3.7E-3	3.3E-3	7.5E-3	0.49	0.44	3.4E-3	1.08	0.98
6.8E-1	8.3E-1	3.1E+3	3.4E-3	500	331.7	7.1E+2	15.7	6.0E-3	5.4E-3	7.4E-3	0.80	0.73	5.0E-3	1.19	1.08
1.4E+0	1.6E+0	6.2E+3	1.0E-2	500	326.1	1.2E+3	26.0	4.9E-3	4.4E-3	5.5E-3	0.89	0.80	4.1E-3	1.20	1.08
6.9E+0	7.6E+0	3.1E+4	1.6E-1	500	317.9	4.4E+3	89.6	3.4E-3	3.1E-3	3.4E-3	0.99	0.90	2.8E-3	1.22	1.11
Air Pr=0.74															
5.0E-3	7.4E-3	1.5E+1	2.4E-5	500	500.0	1.2E-2	4.90	4.3E-1	3.5E-1	7.7E-1	0.55	0.45	3.5E-1	1.22	1.00
5.0E-2	7.4E-2	1.5E+2	2.4E-4	500	442.3	1.5E+2	4.86	4.2E-2	3.5E-2	7.7E-2	0.55	0.45	3.5E-2	1.21	1.00
5.0E-1	7.4E-1	1.5E+3	2.4E-3	500	376.8	3.3E+2	4.94	4.3E-3	3.5E-3	7.7E-3	0.56	0.46	3.5E-3	1.23	1.01
1.0E+0	1.2E+0	3.1E+3	9.1E-3	500	334.4	1.3E+3	14.8	6.5E-3	5.3E-3	7.4E-3	0.88	0.72	5.0E-3	1.30	1.07
2.0E+0	2.3E+0	6.2E+3	2.7E-2	500	328.2	2.2E+3	24.3 83.0	5.3E-3	4.4E-3	5.5E-3	0.96	0.79	4.1E-3	1.29	1.06
1.0E+1	1.1E+1	3.1E+4	4.2E-1	500	319.3	8.1E+3		3.6E-3	3.0E-3	3.4E-3	1.06	0.87	2.8E-3	1.31	1.07

Constant wall heat flux: For the constant wall heat flux case (refer to Figure 5.8), the curves are slightly rounded rather than straight lines, with the curve biased towards the Stanton number especially in the intermediate region. Hence for wall heat flux case, the Stanton number has slightly higher values as compared to the constant wall temperature cases (discussed earlier). The fully developed values remain largely similar to those for the constant wall temperature cases. Similar trends are also observed in Figure 5.9 and Figure 5.10 for $Pr = 0.86$ and $Pr = 1$, respectively. Figure 5.11 also shows that for $Pr = 6.9$, the start and end points are same; the difference being a rounded profile for the developing region. Hence, the effect of constant wall flux is only to make the curves rounded towards Stanton number, with other factors remaining almost same.

Table 5.5 shows raw data for constant wall flux cases. It can be seen that for $Pr = 6.9$, maximum velocity for laminar and average velocity for turbulent is suitable. For remaining Pr values, the maximum velocity is suitable for all flow conditions except at $Re > 1.5E5$ where average velocity starts to become suitable.

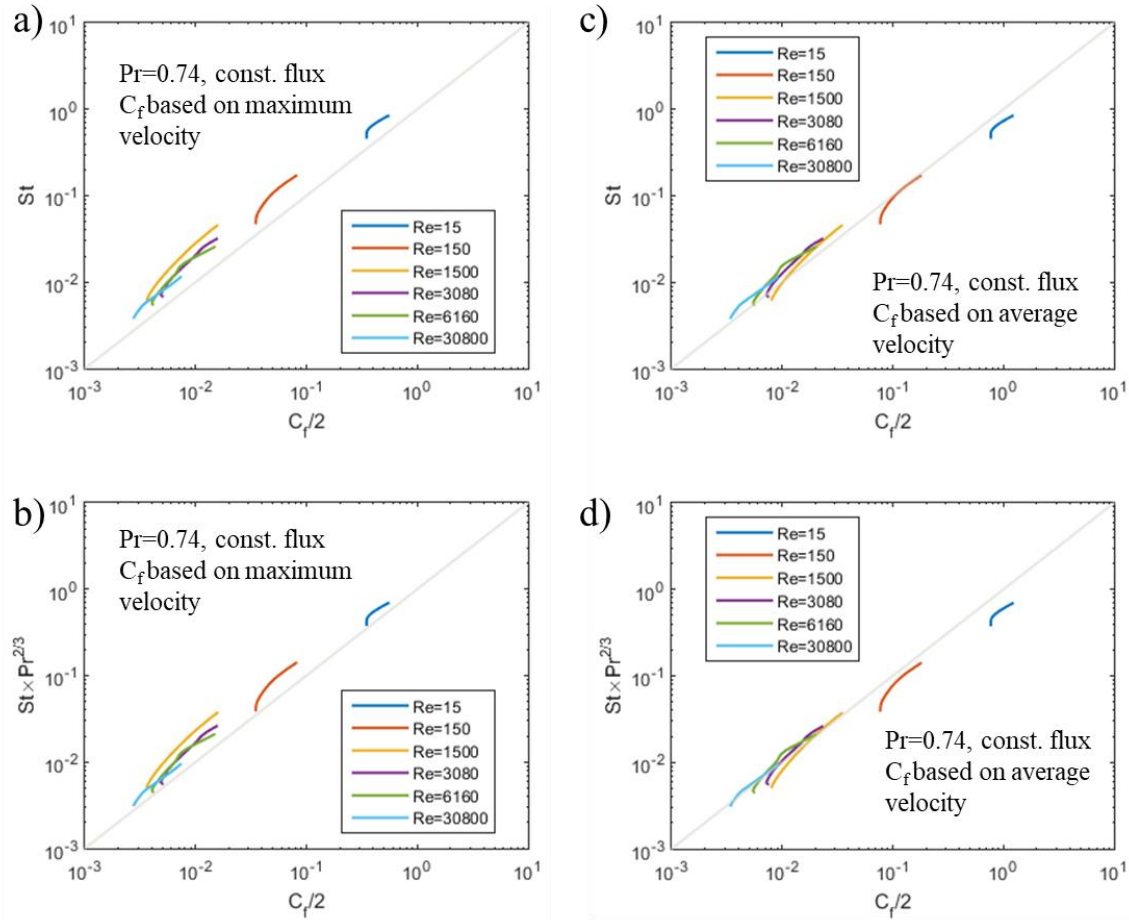


Figure 5.8. Comparison of Reynolds analogy (a, c) and Chilton-Colburn analogy (b, d) when skin friction is based on channel maximum velocity (a, b), or channel average velocity (c, d). Parallel plate, constant wall heat flux, $Pr=0.74$.

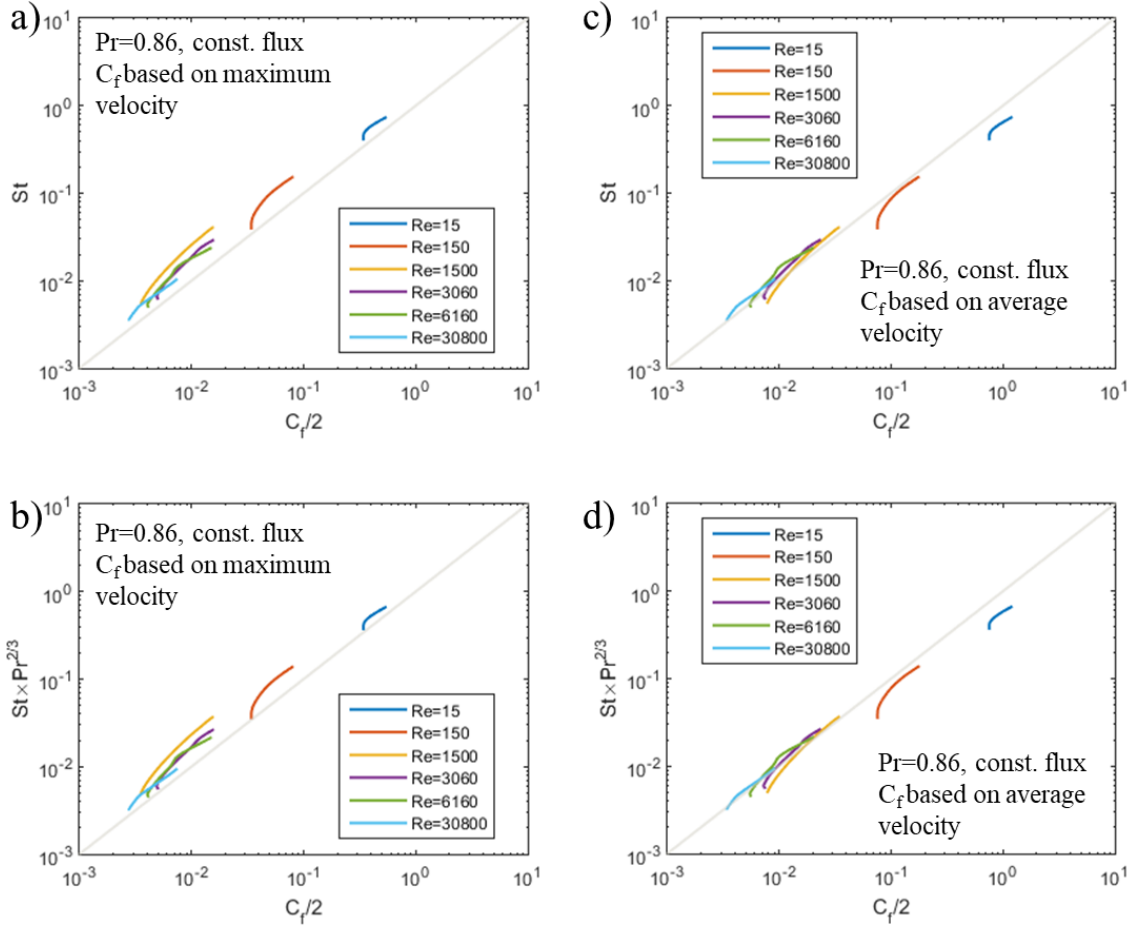


Figure 5.9. Comparison of Reynolds analogy (a, c) and Chilton-Colburn analogy (b, d) when skin friction is based on channel maximum velocity (a, b), or channel average velocity (c, d). Parallel plate, constant wall heat flux, $Pr=0.86$.

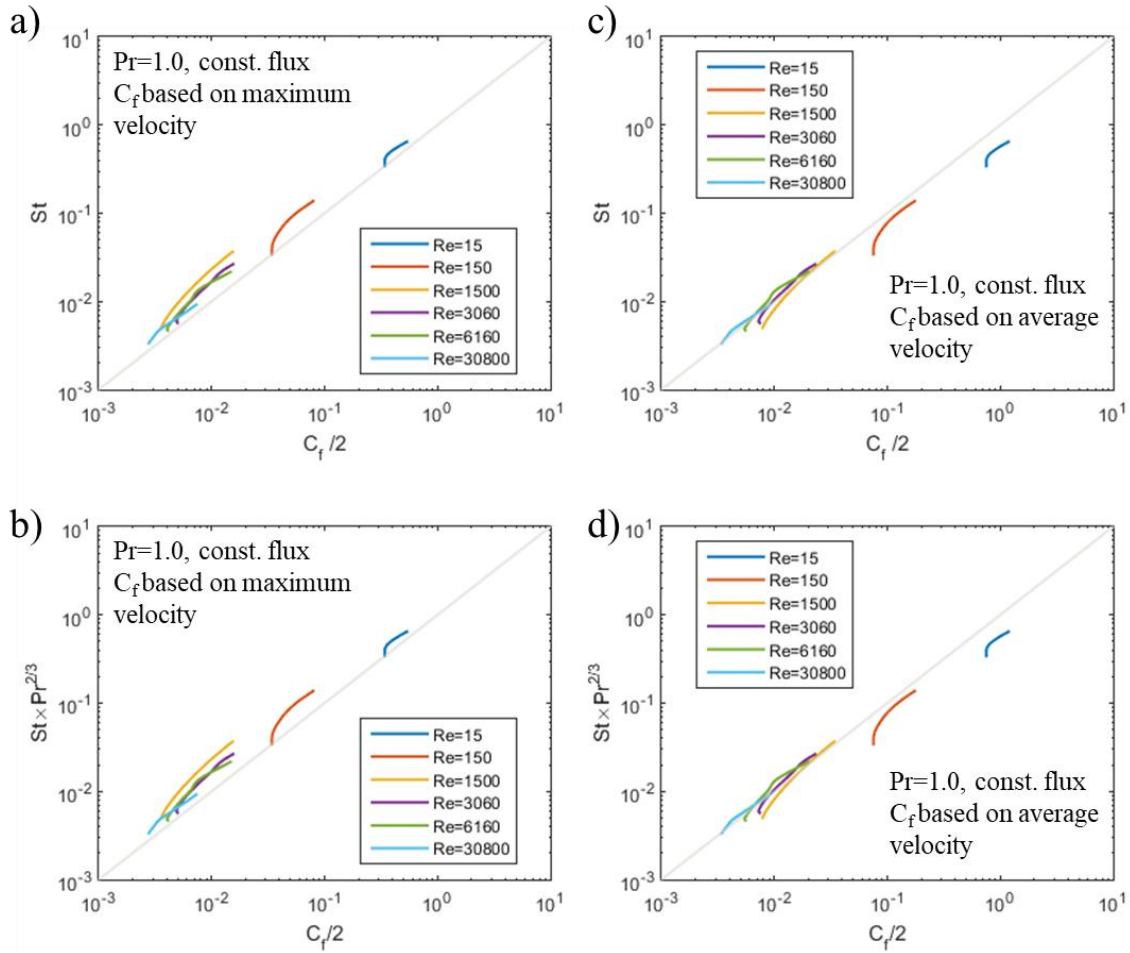


Figure 5.10. Comparison of Reynolds analogy (a, c) and Chilton-Colburn analogy (b, d) when skin friction is based on channel maximum velocity (a, b), or channel average velocity (c, d). Parallel plate, constant wall heat flux, $Pr=1.0$.

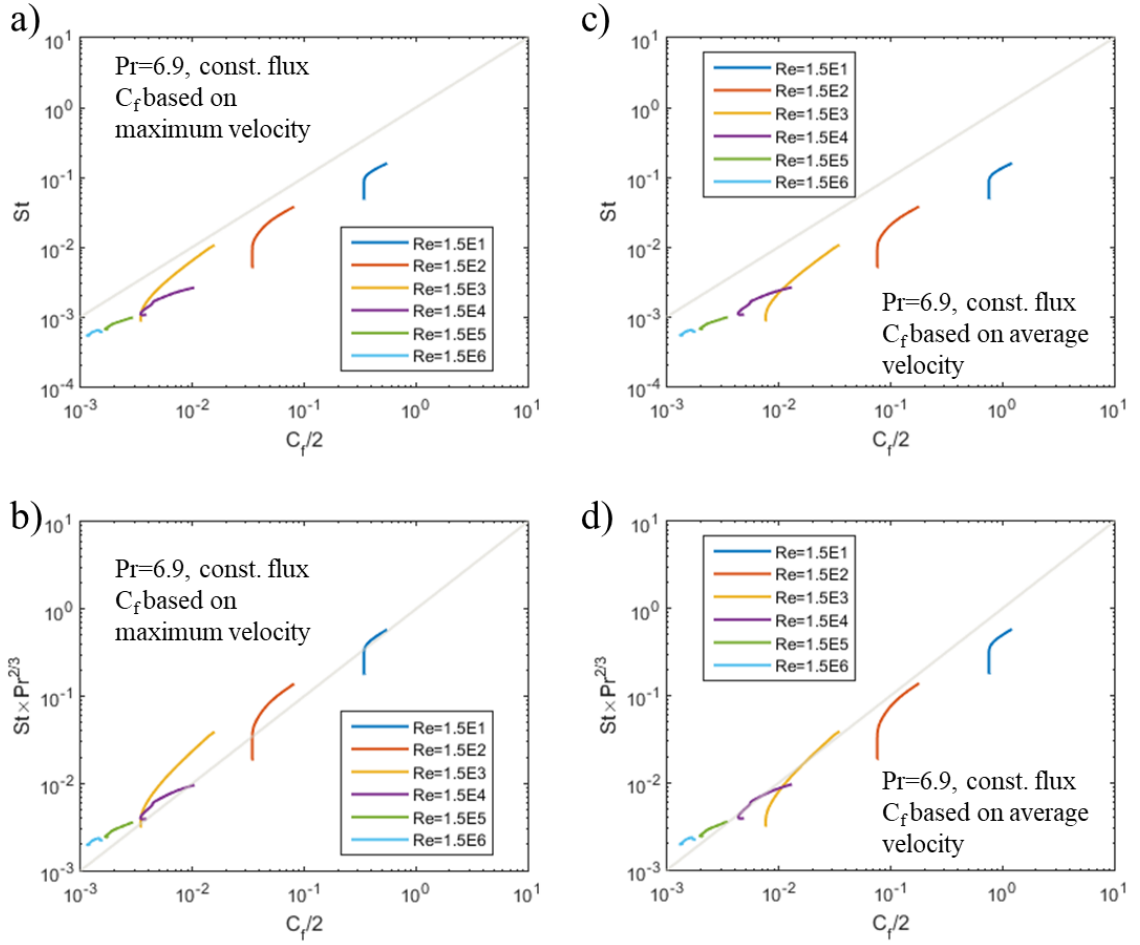


Figure 5.11. Comparison of Reynolds analogy (a, c) and Chilton-Colburn analogy (b, d) when skin friction is based on channel maximum velocity (a, b), or channel average velocity (c, d). Parallel plate, constant wall heat flux, $Pr=6.9$.

Table 5.5. Data for parallel plate with constant wall flux.

Velocity, (m s ⁻¹)		Reynolds number, Re	Wall shear stress, (Pa)	Temperature, (K)		Heat flux, (W m ⁻²)	Nusselt number, Nu	Stanton number, St	$St \times Pr^{2/3}$	$\frac{C_{f,avg}}{2}$	$\frac{St}{C_{f,avg}/2}$	$\frac{St \times Pr^{2/3}}{C_{f,avg}/2}$	$\frac{C_{f,max}}{2}$	$\frac{St}{C_{f,max}/2}$	$\frac{St \times Pr^{2/3}}{C_{f,max}/2}$
Average	Maximum			Surface	Mean										
Water Pr=6.9															
3.5E-04	5.2E-04	1.6E+01	9.3E-05	335.365	328.4	5.0E+02	5.38	4.9E-2	1.8E-1	7.6E-1	0.06	0.24	3.4E-1	0.14	0.52
3.5E-03	5.2E-03	1.6E+02	9.3E-04	394.866	328.4	5.0E+03	5.64	5.1E-3	1.9E-2	7.6E-2	0.07	0.25	3.4E-2	0.15	0.55
3.5E-02	5.2E-02	1.6E+03	9.2E-03	426.5263	358.8	5.0E+03	5.54	5.1E-4	1.8E-3	7.6E-3	0.07	0.24	3.4E-3	0.15	0.54
3.5E-01	3.9E-01	1.6E+04	5.8E-01	333.275	301.0	5.0E+04	116.33	1.1E-3	3.9E-3	4.7E-3	0.22	0.82	3.8E-3	0.28	1.03
3.5E+00	3.8E+00	1.6E+05	2.5E+01	303.469	298.3	5.0E+04	726.04	6.6E-4	2.4E-3	2.0E-3	0.32	1.18	1.7E-3	0.38	1.40
3.5E+01	3.7E+01	1.6E+06	1.7E+03	298.667	298.0	5.0E+04	5890.67	5.4E-4	2.0E-3	1.4E-3	0.40	1.45	1.2E-3	0.45	1.66
Air Pr= 1															
3.5E-03	5.2E-03	1.6E+01	9.2E-06	720.39	678.8	5.0E+01	5.41	3.4E-1	3.4E-1	7.5E-1	0.46	0.46	3.4E-1	1.01	1.01
3.5E-02	5.2E-02	1.6E+02	9.2E-05	377.811	336.1	5.0E+01	5.40	3.4E-2	3.4E-2	7.5E-2	0.45	0.45	3.4E-2	1.00	1.00
3.5E-01	5.2E-01	1.6E+03	9.2E-04	348.607	310.7	5.0E+01	5.94	3.8E-3	3.8E-3	7.5E-3	0.50	0.50	3.4E-3	1.10	1.10
6.8E-01	8.3E-01	3.1E+03	3.4E-03	312.838	300.0	5.0E+01	17.48	5.7E-3	5.7E-3	7.4E-3	0.77	0.77	5.0E-3	1.14	1.14
1.4E+00	1.6E+00	6.2E+03	1.0E-02	306.779	299.0	5.0E+01	28.83	4.7E-3	4.7E-3	5.5E-3	0.84	0.84	4.1E-3	1.14	1.14
6.9E+00	7.6E+00	3.1E+04	1.6E-01	300.454	298.2	5.0E+01	99.59	3.2E-3	3.2E-3	3.4E-3	0.95	0.95	2.8E-3	1.17	1.17
Air Pr=0.86															
3.5E-03	5.2E-03	1.6E+01	9.2E-06	701.597	667.0	5.0E+01	5.42	4.0E-1	3.6E-1	7.5E-1	0.53	0.48	3.4E-1	1.17	1.06
3.5E-02	5.2E-02	1.6E+02	9.2E-05	369.755	334.9	5.0E+01	5.38	4.0E-2	3.6E-2	7.5E-2	0.53	0.48	3.4E-2	1.16	1.05
3.5E-01	5.2E-01	1.6E+03	9.2E-04	342.646	310.3	5.0E+01	5.80	4.3E-3	3.9E-3	7.5E-3	0.57	0.51	3.4E-3	1.25	1.13
6.8E-01	8.3E-01	3.1E+03	3.4E-03	311.283	299.9	5.0E+01	16.47	6.3E-3	5.7E-3	7.4E-3	0.84	0.76	5.0E-3	1.25	1.13
1.4E+00	1.6E+00	6.2E+03	1.0E-02	305.899	298.9	5.0E+01	26.96	5.1E-3	4.6E-3	5.5E-3	0.92	0.83	4.1E-3	1.24	1.12
6.9E+00	7.6E+00	3.1E+04	1.6E-01	300.217	298.2	5.0E+01	92.45	3.5E-3	3.2E-3	3.4E-3	1.02	0.93	2.8E-3	1.26	1.14
Air Pr=0.74															
5.0E-03	7.4E-03	1.5E+01	2.4E-05	531.337	514.2	5.0E+01	5.42	4.7E-1	3.9E-1	7.7E-1	0.61	0.50	3.5E-1	1.35	1.11
5.0E-02	7.4E-02	1.5E+02	2.4E-04	336.926	319.6	5.0E+01	5.38	4.7E-2	3.9E-2	7.7E-2	0.61	0.50	3.5E-2	1.34	1.10
5.0E-01	7.4E-01	1.5E+03	2.4E-03	321.605	305.2	5.0E+01	5.67	4.9E-3	4.1E-3	7.7E-3	0.64	0.53	3.5E-3	1.42	1.16
1.0E+00	1.2E+00	3.1E+03	9.1E-03	305.029	299.1	5.0E+01	15.64	6.8E-3	5.6E-3	7.4E-3	0.92	0.76	5.0E-3	1.37	1.12
2.0E+00	2.3E+00	6.2E+03	2.7E-02	302.222	298.5	5.0E+01	25.26	5.5E-3	4.5E-3	5.5E-3	0.99	0.82	4.1E-3	1.34	1.10
1.0E+01	1.1E+01	3.1E+04	4.2E-01	299.19	298.1	5.0E+01	85.95	3.7E-3	3.1E-3	3.4E-3	1.10	0.90	2.8E-3	1.35	1.11

5.4.3 Internal tube flow

For circular tube modeling (Figure 5.1(b)), the two-dimensional axisymmetric assumption is used where the axis represents the centerline of the tube. In these figures, the flow develops from the top right corner towards opposite diagonal at the bottom left (as indicated by the direction of the black arrow in Figure 5.4(a)).

Constant wall temperature: For $Pr = 0.74$ and constant wall temperature of 500 K, it can be seen from Figure 5.12(a) that the Reynolds analogy is better for turbulent flows in comparison to the laminar flow. Plot (b) shows that Chilton-Colburn analogy brings the plots closer to the theoretical value but still with some difference that will be discussed later based on tabular data. Figure 5.12 (c), and Figure 5.12 (d) show that the use of average velocity for the calculation of skin friction coefficient leads to better results for both Reynolds analogy and Chilton-Colburn analogy. Figure 5.13 and Figure 5.14 show similar plots for $Pr = 0.86$ and $Pr = 1$. Here Figure 5.13 (a), and Figure 5.13 (b) show that for maximum velocity based calculations, the effect of Prandtl number is not significant for the parameters under consideration. However, it can be seen from Figure 5.13 (c) that for turbulent flow, Reynolds analogy is in good agreement, but for laminar flow, increasing Prandtl number from 0.7 to 1.0 results in increasing deviation from the expected values. For higher Prandtl of 6.9, Figure 5.15 shows significant deviations for majority of the cases. Therefore, for laminar flow, Chilton-Colburn analogy based on maximum velocity gives best fully developed values, while for turbulent flow average velocity seems suitable.

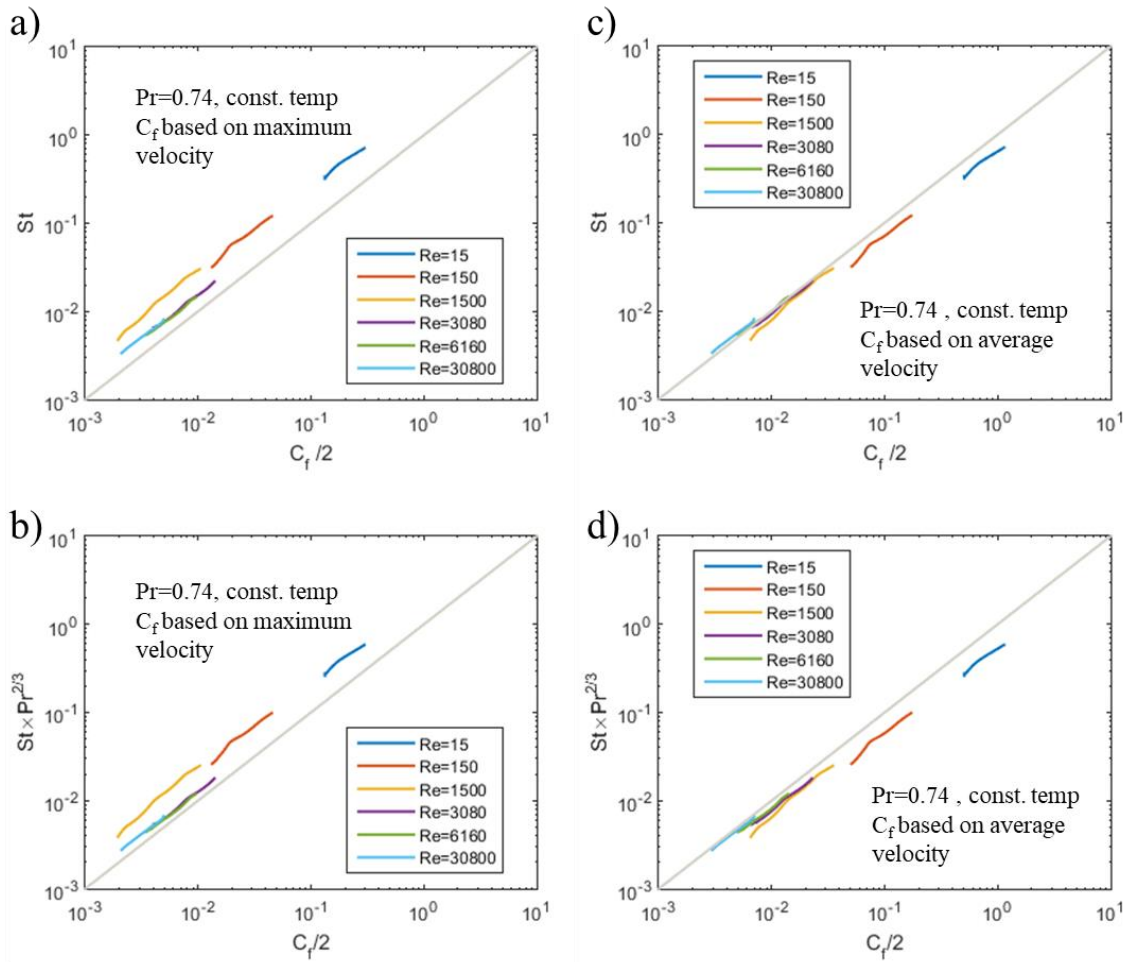


Figure 5.12. Comparison of Reynolds analogy (a, c) and Chilton-Colburn analogy (b, d) when skin friction is based on channel maximum velocity (a, b), or channel average velocity (c, d). Tube flow, constant wall temperature, $Pr=0.74$.

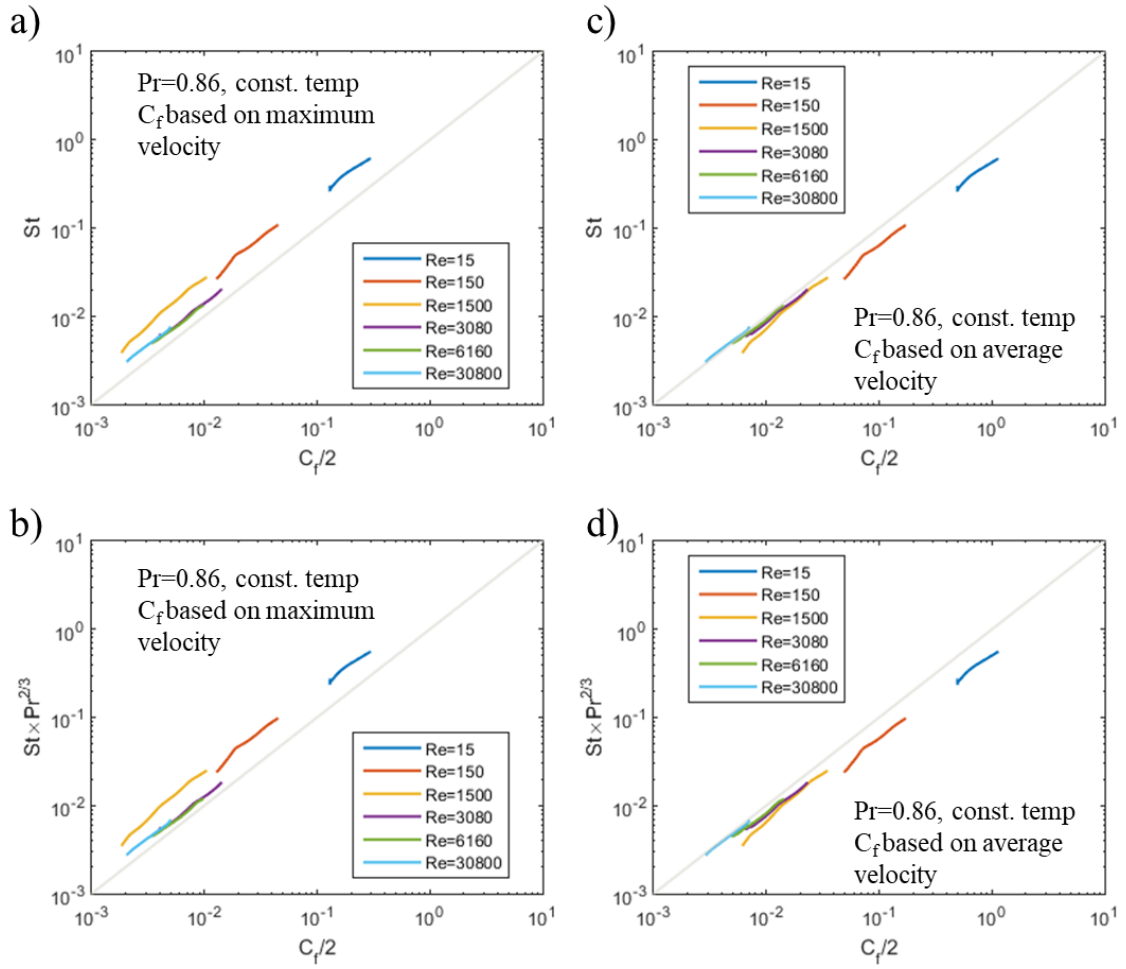


Figure 5.13. Comparison of Reynolds analogy (a, c) and Chilton-Colburn analogy (b, d) when skin friction is based on channel maximum velocity (a, b), or channel average velocity (c, d). Tube flow, constant wall temperature, $Pr=0.86$.

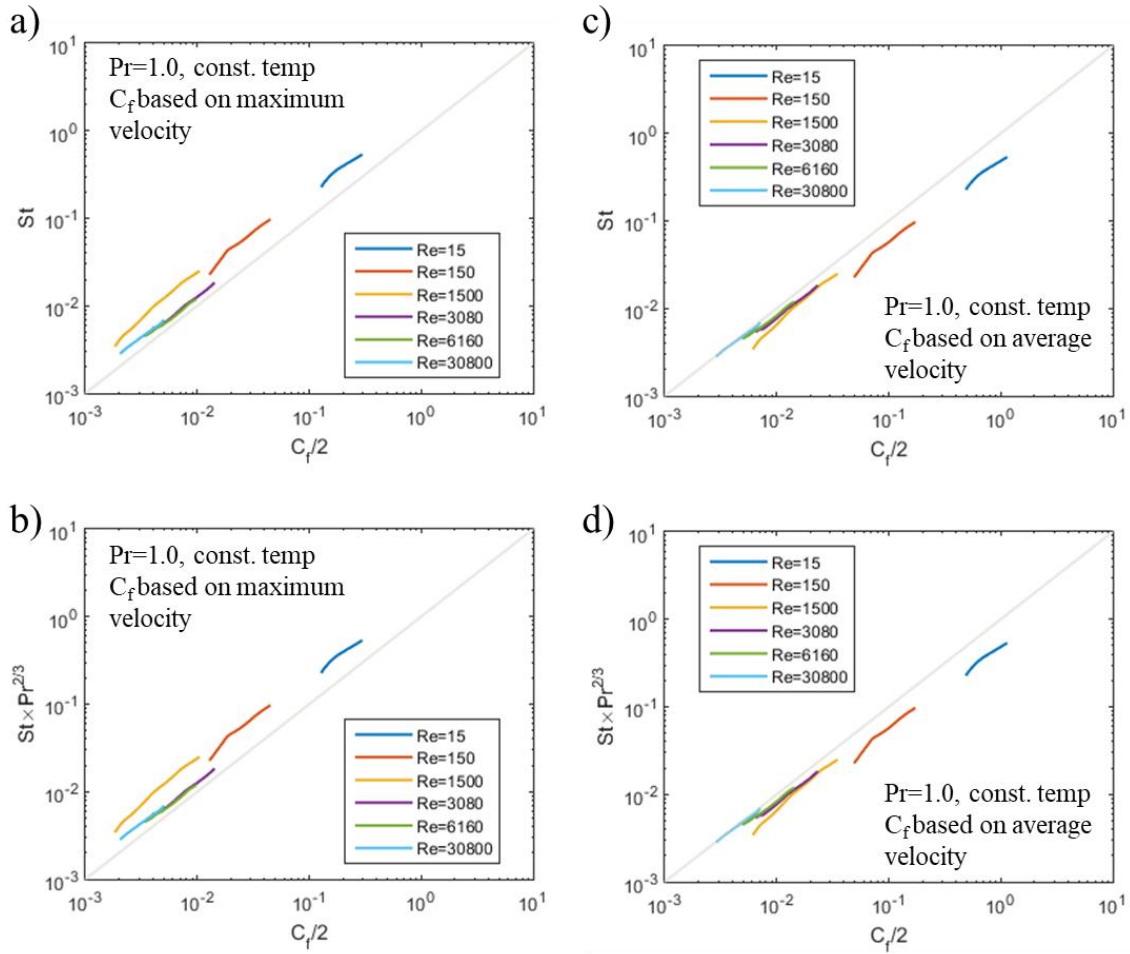


Figure 5.14. Comparison of Reynolds analogy (a, c) and Chilton-Colburn analogy (b, d) when skin friction is based on channel maximum velocity (a, b), or channel average velocity (c, d). Tube flow, constant wall temperature, $Pr=1.0$.

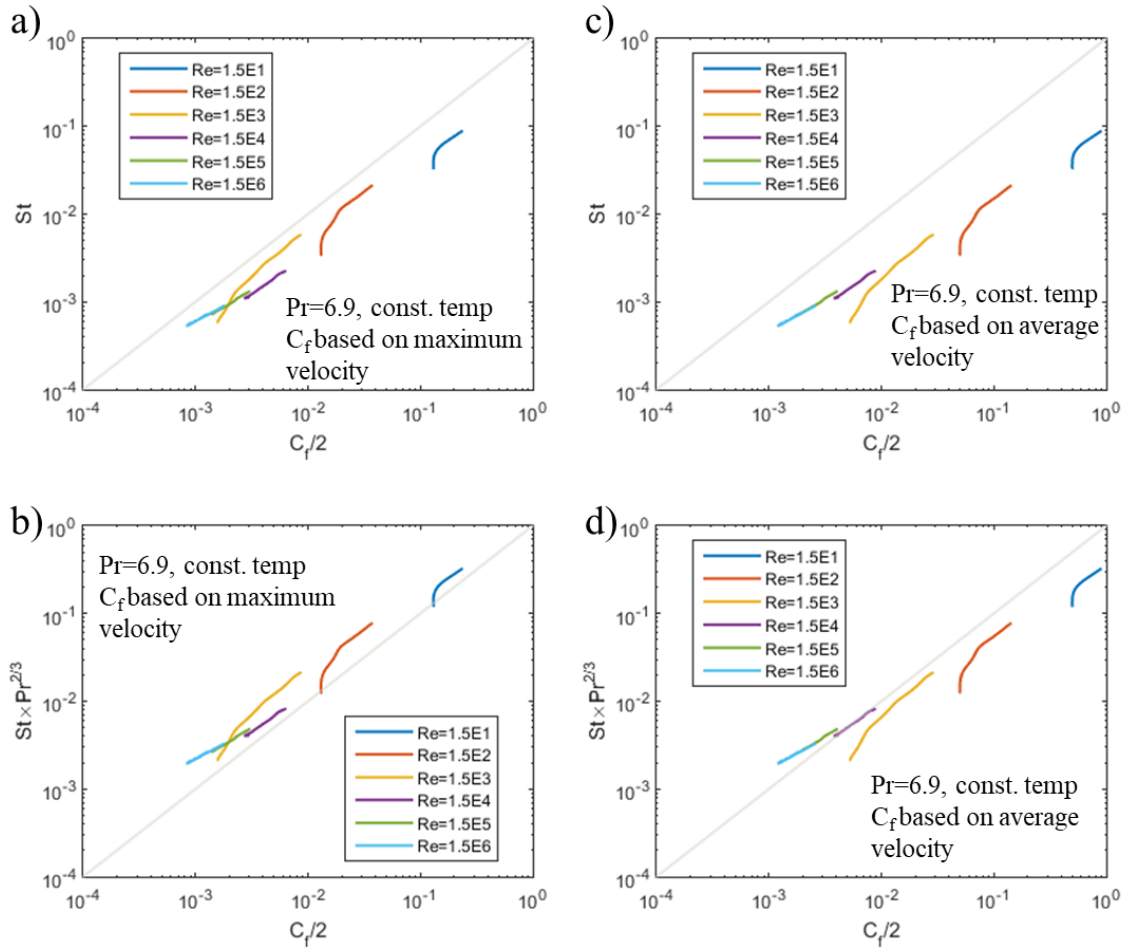


Figure 5.15. Comparison of Reynolds analogy (a, c) and Chilton-Colburn analogy (b, d) when skin friction is based on channel maximum velocity (a, b), or channel average velocity (c, d). Tube flow, constant wall temperature, $Pr=6.9$.

Constant wall heat flux: Figure 5.16 shows for $Pr = 0.74$, that the choice of maximum velocity is not recommended for any Reynolds number. The best fit for turbulent flow is obtained for Chilton-Colburn analogy with the average velocity, while for laminar flow, Reynolds analogy with average velocity is providing better agreement. As the Prandtl number is increased, for example, $Pr = 0.86$ (refer to Figure 5.17) and $= 1$ (refer Figure 5.18), there is a good agreement for turbulent flow, while the deviations are apparent for laminar flow conditions. Figure 5.19 shows that for $Pr = 6.9$, the maximum velocity with Reynolds analogy is better for developing flow, while Chilton-Colburn analogy gives good fully developed values. For turbulent flow, Chilton-Colburn analogy with average velocity is recommended as it is closer to the predicted values.

Table 5.6 shows fully developed values for the constant wall temperature case. For $Pr = 6.9$ and maximum velocity for Chilton-Colburn analogy results in a ratio of about 0.94, while for turbulent flow, average velocity is better but the ratio is still about 1.6. For $Pr < 1$, average velocity is better, especially for turbulent flows. Similarly, Table 5.7 for constant wall flux shows the same trend for $Pr < 1$, with the average velocity better for Chilton-Colburn analogy. Furthermore, for $Pr = 6.9$, maximum velocity for laminar and average velocity for turbulent flow seems to be a good choice.

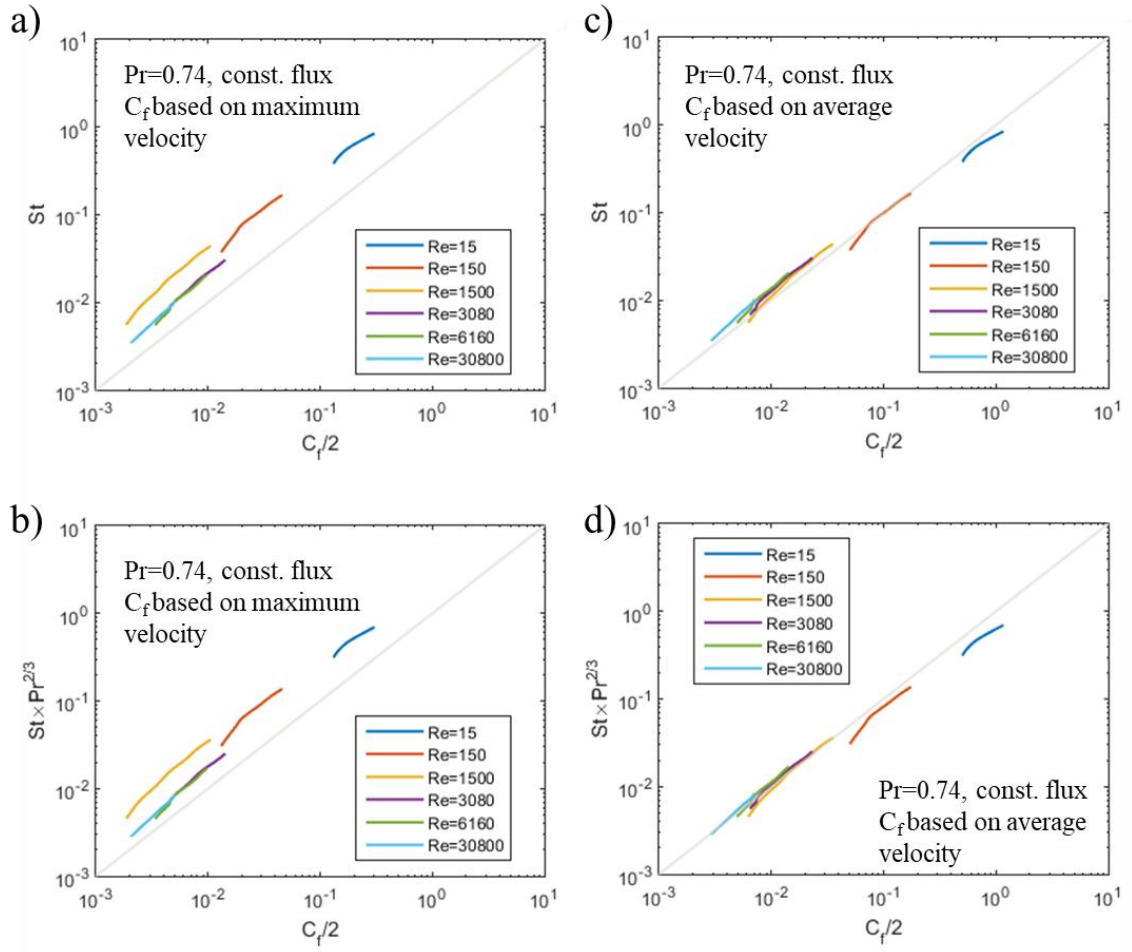


Figure 5.16. Comparison of Reynolds analogy (a, c) and Chilton-Colburn analogy (b, d) when skin friction is based on channel maximum velocity (a, b), or channel average velocity (c, d). Tube flow, constant wall heat flux, $Pr=0.74$.

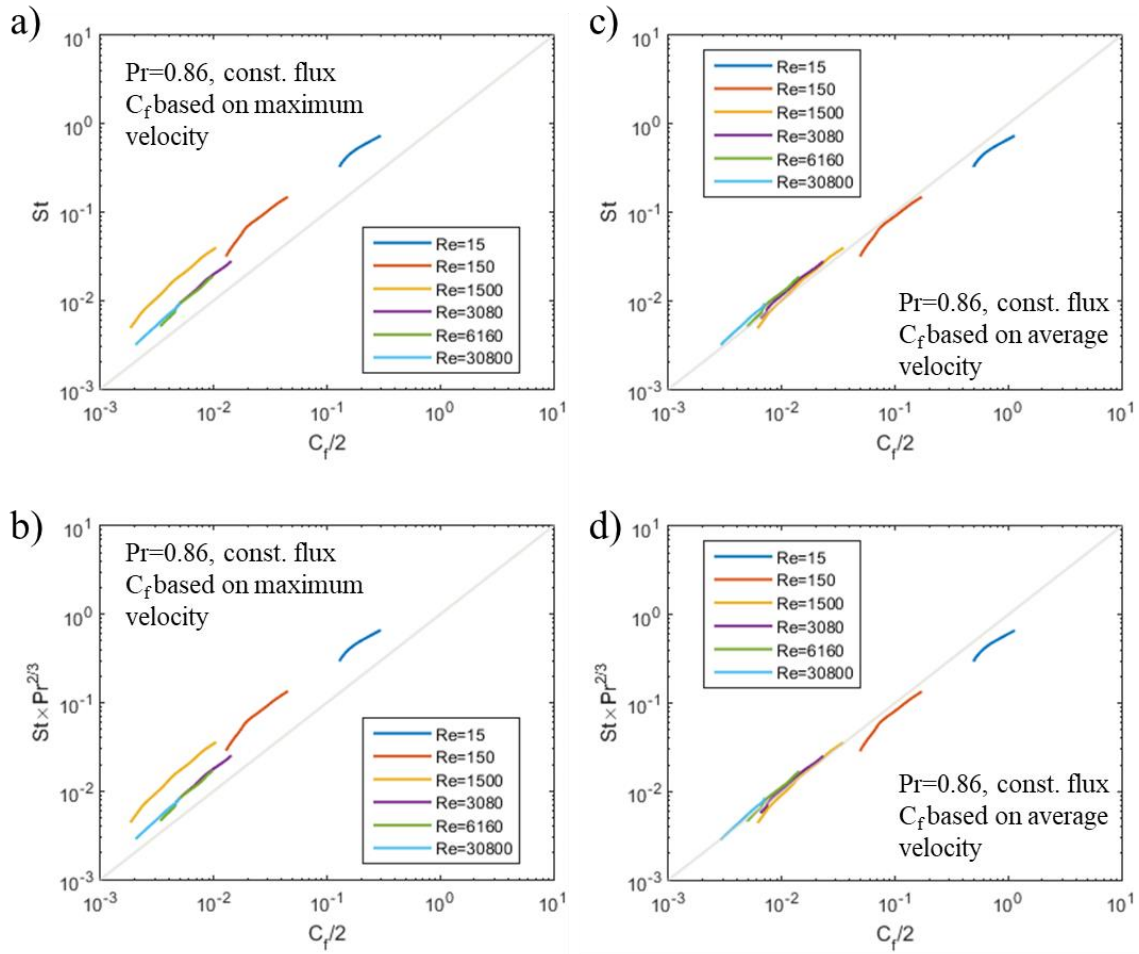


Figure 5.17. Comparison of Reynolds analogy (a, c) and Chilton-Colburn analogy (b, d) when skin friction is based on channel maximum velocity (a, b), or channel average velocity (c, d). Tube flow, constant wall heat flux, $Pr=0.86$.

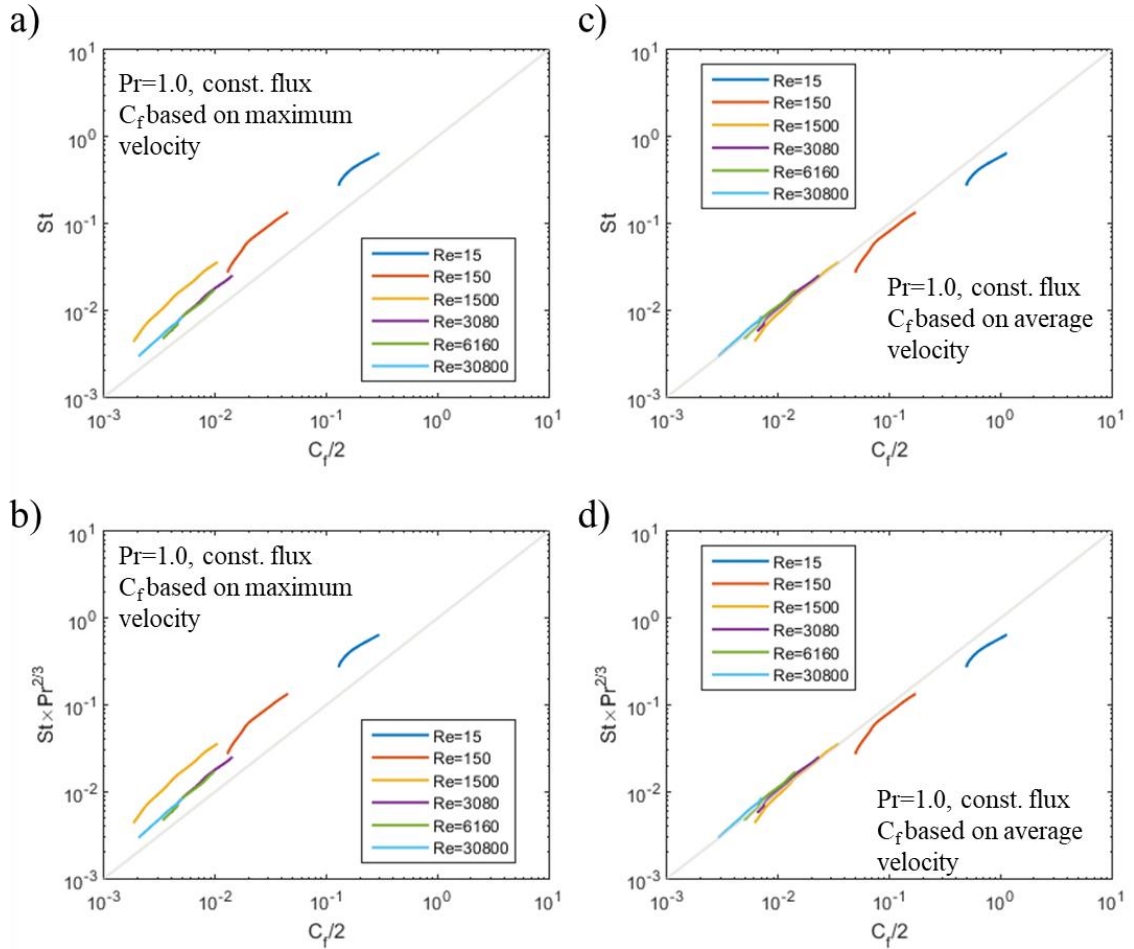


Figure 5.18. Comparison of Reynolds analogy (a, c) and Chilton-Colburn analogy (b, d) when skin friction is based on channel maximum velocity (a, b), or channel average velocity (c, d). Tube flow, constant wall heat flux, $Pr=1.0$.

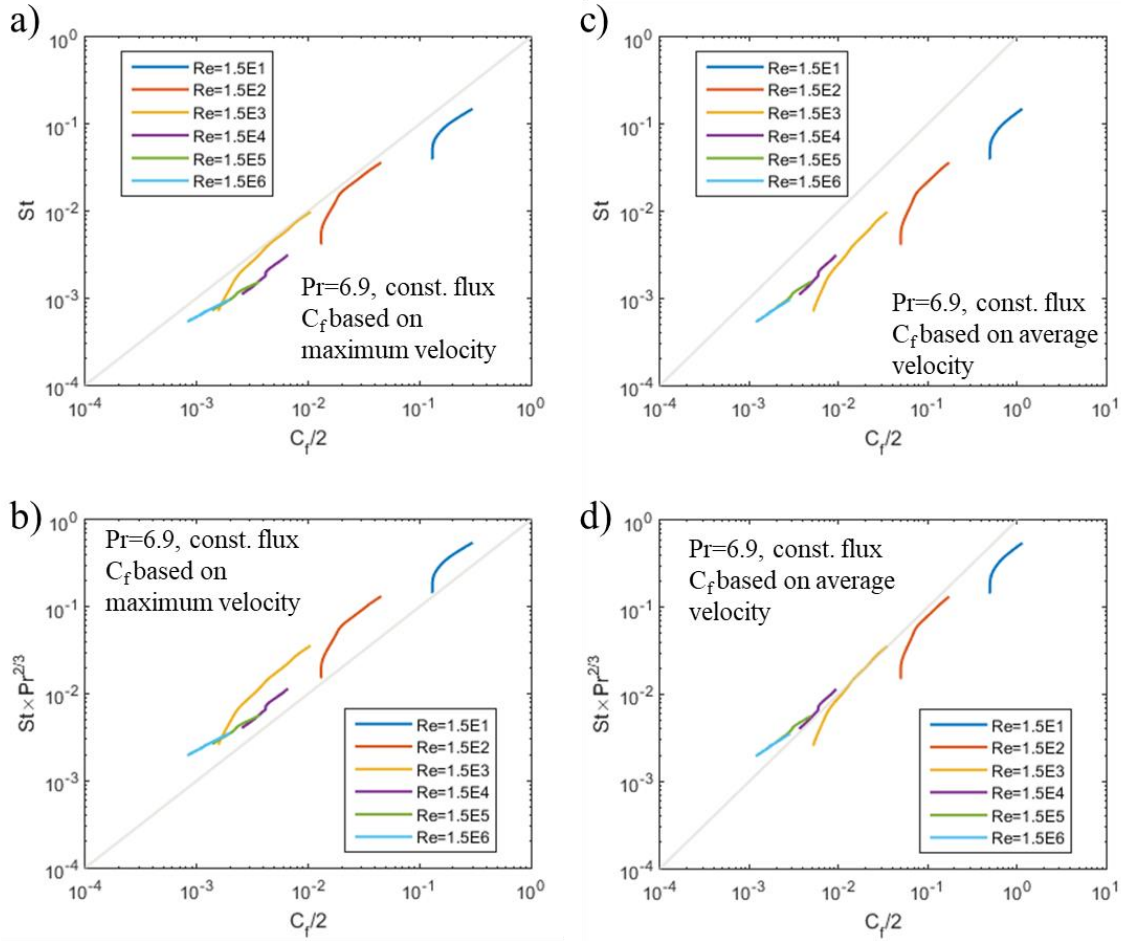


Figure 5.19. Comparison of Reynolds analogy (a, c) and Chilton-Colburn analogy (b, d) when skin friction is based on channel maximum velocity (a, b), or channel average velocity (c, d). Tube flow, constant wall heat flux, $Pr=6.9$.

Table 5.6. Data for tube flow with constant wall temperature.

Velocity, (m s ⁻¹)		Reynolds number, Re	Wall shear stress, (Pa)	Temperature, (K)		Heat flux, (W m ⁻²)	Nusselt number, Nu	Stanton number, St	$St \times Pr^{2/3}$	$\frac{C_{f,avg}}{2}$	$\frac{St}{C_{f,avg}/2}$	$\frac{St \times Pr^{2/3}}{C_{f,avg}/2}$	$\frac{C_{f,max}}{2}$	$\frac{St}{C_{f,max}/2}$	$\frac{St \times Pr^{2/3}}{C_{f,max}/2}$	
Average	Maximum			Surface	Mean											
Water Pr=6.9																
3.5E-4	6.8E-4	1.6E+1	6.1E-5	500	499.6	2.1E+1	3.66	3.3E-2	1.2E-1	5.0E-1	0.07	0.24	1.3E-1	0.26	0.94	
3.5E-3	6.8E-3	1.6E+2	6.1E-4	500	409.3	4.6E+3	3.78	3.4E-3	1.3E-2	5.0E-2	0.07	0.25	1.3E-2	0.26	0.97	
3.5E-2	6.8E-2	1.6E+3	6.1E-3	500	409.1	4.6E+3	3.77	3.4E-4	1.3E-3	5.0E-3	0.07	0.25	1.3E-3	0.26	0.97	
3.5E-1	4.1E-1	1.6E+4	5.0E-1	500	334.8	2.7E+5	123.18	1.1E-3	4.1E-3	4.1E-3	0.27	1.00	2.9E-3	0.38	1.40	
3.5E+0	4.0E+0	1.6E+5	2.3E+1	500	323.3	1.9E+6	812.61	7.4E-4	2.7E-3	1.9E-3	0.39	1.41	1.4E-3	0.52	1.89	
3.5E+1	4.2E+1	1.6E+6	1.6E+3	500	317.4	1.5E+7	6243.83	5.7E-4	2.1E-3	1.3E-3	0.44	1.62	8.9E-4	0.64	2.34	
Air Pr= 1																
3.5E-3	6.8E-3	1.6E+1	6.1E-6	500	500.0	8.0E-4	3.67	2.3E-1	2.3E-1	5.0E-1	0.47	0.47	1.3E-1	1.80	1.80	
3.5E-2	6.8E-2	1.6E+2	6.1E-5	500	455.8	3.6E+1	3.66	2.3E-2	2.3E-2	5.0E-2	0.47	0.47	1.3E-2	1.79	1.79	
3.5E-1	6.8E-1	1.6E+3	6.4E-4	500	395.7	9.3E+1	4.00	2.5E-3	2.5E-3	5.2E-3	0.49	0.49	1.6E-3	1.62	1.62	
6.8E-1	8.7E-1	3.1E+3	3.0E-3	500	354.9	5.5E+2	16.97	5.5E-3	5.5E-3	6.6E-3	0.84	0.84	4.0E-3	1.37	1.37	
1.4E+0	1.7E+0	6.2E+3	9.4E-3	500	346.1	9.7E+2	28.26	4.6E-3	4.6E-3	5.0E-3	0.91	0.91	3.4E-3	1.34	1.34	
6.9E+0	8.1E+0	3.1E+4	1.4E-1	500	331.4	3.3E+3	89.04	2.9E-3	2.9E-3	2.9E-3	0.98	0.98	2.1E-3	1.39	1.39	
Air Pr=0.86																
3.5E-3	6.8E-3	1.6E+1	6.1E-6	500	500.0	1.6E-4	4.03	3.0E-1	2.7E-1	5.0E-1	0.60	0.54	1.3E-1	2.29	2.07	
3.5E-2	6.8E-2	1.6E+2	6.1E-5	500	464.3	3.5E+1	3.66	2.7E-2	2.4E-2	5.0E-2	0.54	0.49	1.3E-2	2.08	1.88	
3.5E-1	6.4E-1	1.6E+3	6.4E-4	500	403.8	1.0E+2	3.92	2.9E-3	2.6E-3	5.2E-3	0.55	0.50	1.6E-3	1.85	1.67	
6.8E-1	8.7E-1	3.1E+3	3.0E-3	500	359.5	6.0E+2	16.03	6.1E-3	5.5E-3	6.6E-3	0.92	0.84	4.0E-3	1.50	1.36	
1.4E+0	1.7E+0	6.2E+3	9.4E-3	500	349.8	1.1E+3	26.51	5.0E-3	4.5E-3	5.0E-3	0.99	0.90	3.4E-3	1.46	1.32	
6.9E+0	8.1E+0	3.1E+4	1.4E-1	500	333.8	3.6E+3	82.12	3.1E-3	2.8E-3	2.9E-3	1.05	0.95	2.1E-3	1.49	1.35	
Air Pr=0.74																
5.0E-3	9.8E-3	1.5E+1	1.6E-5	500	500.0	5.0E-4	3.90	3.4E-1	2.8E-1	5.1E-1	0.67	0.55	1.3E-1	2.56	2.10	
5.0E-2	9.8E-2	1.5E+2	1.6E-4	500	463.9	7.1E+1	3.67	3.2E-2	2.6E-2	5.1E-2	0.63	0.52	1.3E-2	2.40	1.97	
5.0E-1	9.2E-1	1.5E+3	1.6E-3	500	413.0	1.8E+2	3.86	3.4E-3	2.8E-3	5.3E-3	0.63	0.52	1.6E-3	2.12	1.74	
1.0E+0	1.3E+0	3.1E+3	8.0E-3	500	355.8	1.2E+3	15.06	6.6E-3	5.4E-3	6.6E-3	1.00	0.82	4.0E-3	1.63	1.34	
2.0E+0	2.4E+0	6.2E+3	2.5E-2	500	346.4	2.0E+3	24.73	5.4E-3	4.4E-3	5.0E-3	1.07	0.88	3.4E-3	1.57	1.29	
1.0E+1	1.2E+1	3.1E+4	3.6E-1	500	331.2	7.0E+3	77.02	3.4E-3	2.8E-3	3.0E-3	1.13	0.93	2.1E-3	1.60	1.31	

Table 5.7. Data for tube flow with constant wall flux

Velocity, (m s-1)		Reynolds number, Re	Wall shear stress, (Pa)	Temperature, (K)		Heat flux, (W m ⁻²)	Nusselt number, Nu	Stanton number, St	$St \times Pr^{2/3}$	$\frac{C_{f,avg}}{2}$	$\frac{St}{C_{f,avg}/2}$	$\frac{St \times Pr^{2/3}}{C_{f,avg}/2}$	$\frac{C_{f,max}}{2}$	$\frac{St}{C_{f,max}/2}$	$\frac{St \times Pr^{2/3}}{C_{f,max}/2}$
Average	Maximum			Surface	Mean										
Water Pr=6.9															
3.5E-4	6.8E-4	1.6E+1	6.1E-5	367.2866	358.8	5.0E+2	4.39	4.0E-2	1.5E-1	5.0E-1	0.08	0.29	1.3E-1	0.31	1.12
3.5E-3	6.8E-3	1.6E+2	6.1E-4	312.1353	304.1	5.0E+2	4.65	4.2E-3	1.5E-2	5.0E-2	0.08	0.31	1.3E-2	0.32	1.18
3.5E-2	6.8E-2	1.6E+3	6.1E-3	318.6491	310.2	5.0E+2	4.42	4.0E-4	1.5E-3	5.0E-3	0.08	0.30	1.3E-3	0.31	1.14
3.5E-1	4.2E-1	1.6E+4	4.5E-1	334.542	304.1	5.0E+4	123.10	1.1E-3	4.1E-3	3.7E-3	0.30	1.11	2.6E-3	0.43	1.58
3.5E+0	4.0E+0	1.6E+5	2.3E+1	303.213	298.6	5.0E+4	814.32	7.4E-4	2.7E-3	1.9E-3	0.39	1.42	1.4E-3	0.52	1.89
3.5E+1	4.2E+1	1.6E+6	1.6E+3	298.66	298.1	5.0E+4	6258.24	5.7E-4	2.1E-3	1.3E-3	0.44	1.63	8.9E-4	0.64	2.34
Air Pr= 1															
3.5E-3	6.8E-3	1.6E+1	6.1E-6	1110.3	1059.4	5.0E+1	4.42	2.8E-1	2.8E-1	5.0E-1	0.57	0.57	1.3E-1	2.16	2.16
3.5E-2	6.8E-2	1.6E+2	6.1E-5	425.215	374.2	5.0E+1	4.41	2.8E-2	2.8E-2	5.0E-2	0.56	0.56	1.3E-2	2.15	2.15
3.5E-1	6.4E-1	1.6E+3	6.4E-4	368.017	323.4	5.0E+1	5.04	3.2E-3	3.2E-3	5.2E-3	0.61	0.61	1.6E-3	2.04	2.04
6.8E-1	8.7E-1	3.1E+3	3.0E-3	314.623	301.9	5.0E+1	17.72	5.8E-3	5.8E-3	6.6E-3	0.88	0.88	4.0E-3	1.43	1.43
1.4E+0	1.7E+0	6.2E+3	9.4E-3	307.667	299.9	5.0E+1	29.15	4.7E-3	4.7E-3	5.0E-3	0.94	0.94	3.4E-3	1.38	1.38
6.9E+0	8.1E+0	3.1E+4	1.4E-1	300.826	298.4	5.0E+1	92.35	3.0E-3	3.0E-3	2.9E-3	1.02	1.02	2.1E-3	1.44	1.44
Air Pr=0.86															
3.5E-3	6.8E-3	1.6E+1	6.1E-6	1078.06	1035.7	5.0E+1	4.43	3.3E-1	3.0E-1	5.0E-1	0.66	0.60	1.3E-1	2.52	2.28
3.5E-2	6.8E-2	1.6E+2	6.1E-5	414.491	371.9	5.0E+1	4.40	3.2E-2	2.9E-2	5.0E-2	0.65	0.59	1.3E-2	2.50	2.26
3.5E-1	6.4E-1	1.6E+3	6.4E-4	360.669	322.6	5.0E+1	4.93	3.6E-3	3.3E-3	5.2E-3	0.70	0.63	1.6E-3	2.32	2.10
6.8E-1	8.7E-1	3.1E+3	3.0E-3	312.968	301.8	5.0E+1	16.80	6.4E-3	5.8E-3	6.6E-3	0.97	0.88	4.0E-3	1.58	1.43
1.4E+0	1.7E+0	6.2E+3	9.4E-3	306.725	299.9	5.0E+1	27.43	5.2E-3	4.7E-3	5.0E-3	1.03	0.93	3.4E-3	1.51	1.36
6.9E+0	8.1E+0	3.1E+4	1.4E-1	300.57	298.4	5.0E+1	85.52	3.2E-3	2.9E-3	2.9E-3	1.10	0.99	2.1E-3	1.55	1.40
Air Pr=0.74															
5.0E-3	9.8E-3	1.5E+1	1.6E-5	751.168	730.2	5.0E+1	4.44	3.9E-1	3.2E-1	5.1E-1	0.76	0.63	1.3E-1	2.92	2.40
5.0E-2	9.8E-2	1.5E+2	1.6E-4	362.462	341.3	5.0E+1	4.39	3.8E-2	3.1E-2	5.1E-2	0.75	0.62	1.3E-2	2.88	2.36
5.0E-1	9.2E-1	1.5E+3	1.6E-3	331.741	312.4	5.0E+1	4.81	4.2E-3	3.4E-3	5.3E-3	0.79	0.65	1.6E-3	2.64	2.17
1.0E+0	1.3E+0	3.1E+3	8.0E-3	305.968	300.2	5.0E+1	16.02	7.0E-3	5.7E-3	6.6E-3	1.06	0.87	4.0E-3	1.73	1.42
2.0E+0	2.4E+0	6.2E+3	2.5E-2	302.681	299.1	5.0E+1	25.84	5.6E-3	4.6E-3	5.0E-3	1.12	0.92	3.4E-3	1.64	1.35
1.0E+1	1.2E+1	3.1E+4	3.6E-1	299.388	298.2	5.0E+1	79.36	3.5E-3	2.8E-3	2.9E-3	1.18	0.97	2.1E-3	1.67	1.37

5.4.4 Flow over flat plate

Constant wall temperature: For flow over a flat plate (Figure 5.1(d)) and $Pr < 1$, free stream velocity of 1 m/s is used for laminar, while 100 m/s is used for turbulent flow condition. For $Pr > 1$, free stream velocity of 0.1 m/s is used for laminar, while 10 m/s is used for turbulent flow condition. This choice of velocity is influenced by the need to keep similar laminar and turbulent regions for fluids with different properties. For turbulent cases, there does exist some laminar region in the vicinity of leading edge, but it transitions in a very short distance to turbulent flow. The resulting plots are provided in Figure 5.20, wherein Figure 5.20 (a) shows that the slope of all the cases is 1, with some slight variations due to Prandtl number.

For $Pr = 6.9$ and turbulent flow, the increase in Stanton number is at a faster rate in comparison to the skin friction coefficient, leading to a smaller slope, hence for the highest turbulent flow ($Re=2 \times 10^7$) there exists some difference as the flow develops to 2 m length of the plate used. When Chilton-Colburn analogy is used, Figure 5.20 (b) shows that all lines lie exactly on the expected horizontal line, except for the higher Prandtl number flow conditions. The Nusselt number (refer to Figure 5.20 (c)) shows increasing trend, larger at the beginning and then a slow increase. As expected, the lowest Nusselt number is for lowest Reynolds number and vice versa.

For Stanton number (refer to Figure 5.20 (d)), we see a decreasing trend despite increasing heat transfer coefficient as seen in Figure 5.20 (c). This is due to the fact that Stanton

number ($Nu/RePr$) calculation involves Reynolds number in the denominator, which itself increases continuously for flow over a flat plate. We can also see that for higher Prandtl number undergoing turbulent flow, the development of Stanton number is rather slow, which explains the non-coherent slope for the analogy plots (refer to Figure 5.20 (a) and Figure 5.20 (b)). Furthermore, Figure 5.20 (e) shows that skin friction coefficient also decreases continuously as the boundary layer develops. Table 5.8 presents the raw data for all these cases, showing that for laminar flow, the ratio for the Chilton-Colburn analogy is 0.95; however, under turbulent flow conditions, this ratio increases from 0.94 for $Pr = 0.74$ to 1.72 for $Pr = 6.9$.

Constant heat flux: Figure 5.21 shows similar plots for constant heat flux case. It can be seen from Figure 5.21 (a) that the data lines are more distributed for the Reynolds number, but with Chilton-Colburn analogy, the lines become coherent but slightly offset from the expected value. The similar shallow slope exists for higher Prandtl number and turbulent flow conditions, as seen earlier for constant wall temperature cases. The developing profiles in Figure 5.21 (c), Figure 5.21(d), and Figure 5.21(e) are also following similar trends.

Table 5.9 shows that for constant wall flux case, the ratio of analogy becomes about 1.3 for all laminar cases, while it transitions from 0.99 to 1.74 for increasing Prandtl number. For the last case of very high Reynolds number, the use of 100 Wm^{-2} resulted in very small temperature changes in the region immediate to the wall, resulting in numerical error seen

as fluctuation of calculated values. To accommodate this issue, a higher heat flux was used to magnify the values resulting in reliable results. It should be noted that constant property fluids are used in these studies, so the higher flux has no impact on the dimensionless calculations.

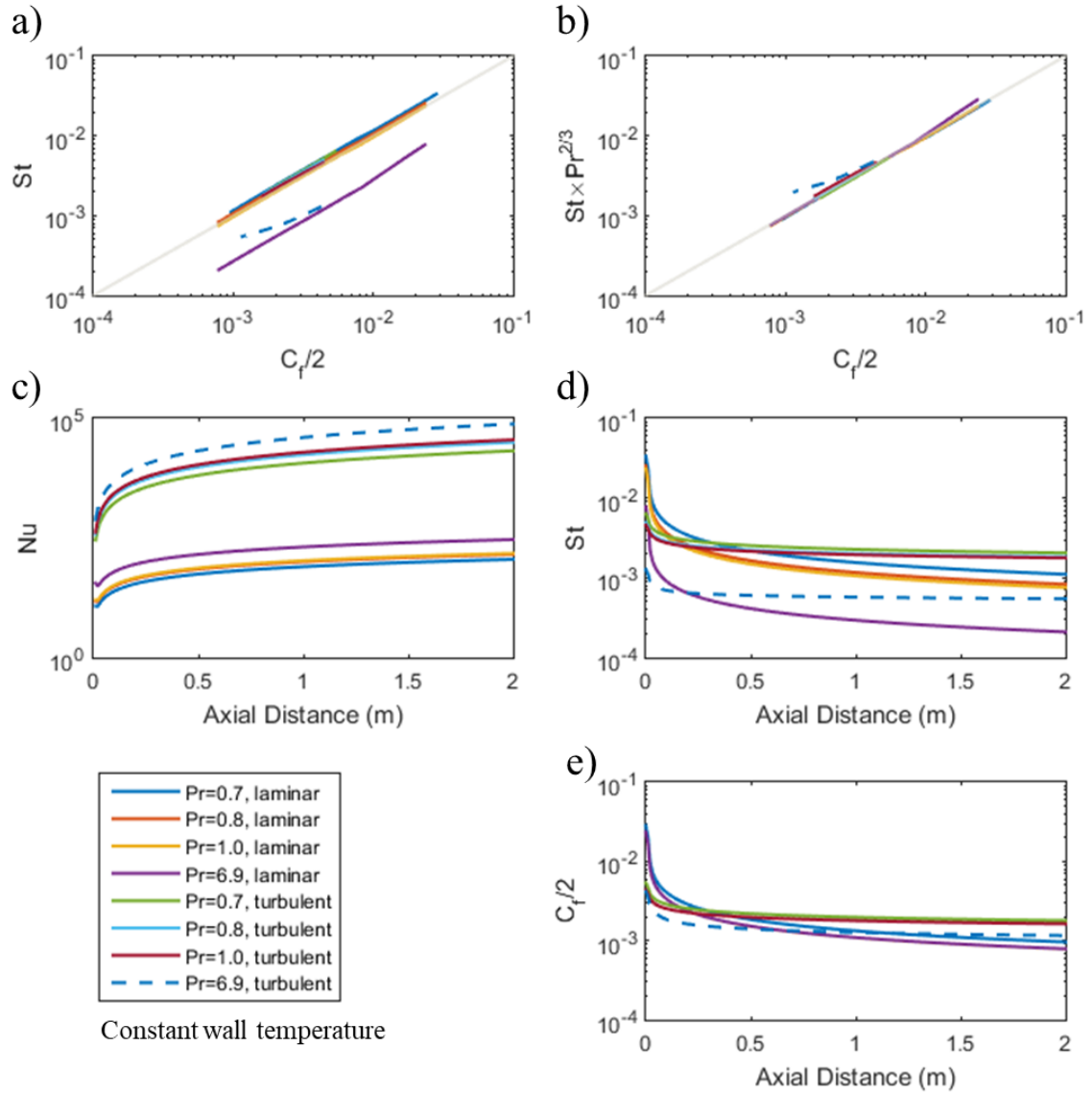


Figure 5.20. Plots of (a) the Reynolds analogy and (b) Chilton-Colburn analogy, axial development of (c) Nusselt number, (d) Stanton number, and (e) half of skin friction coefficient. Flat plate, constant wall temperature.

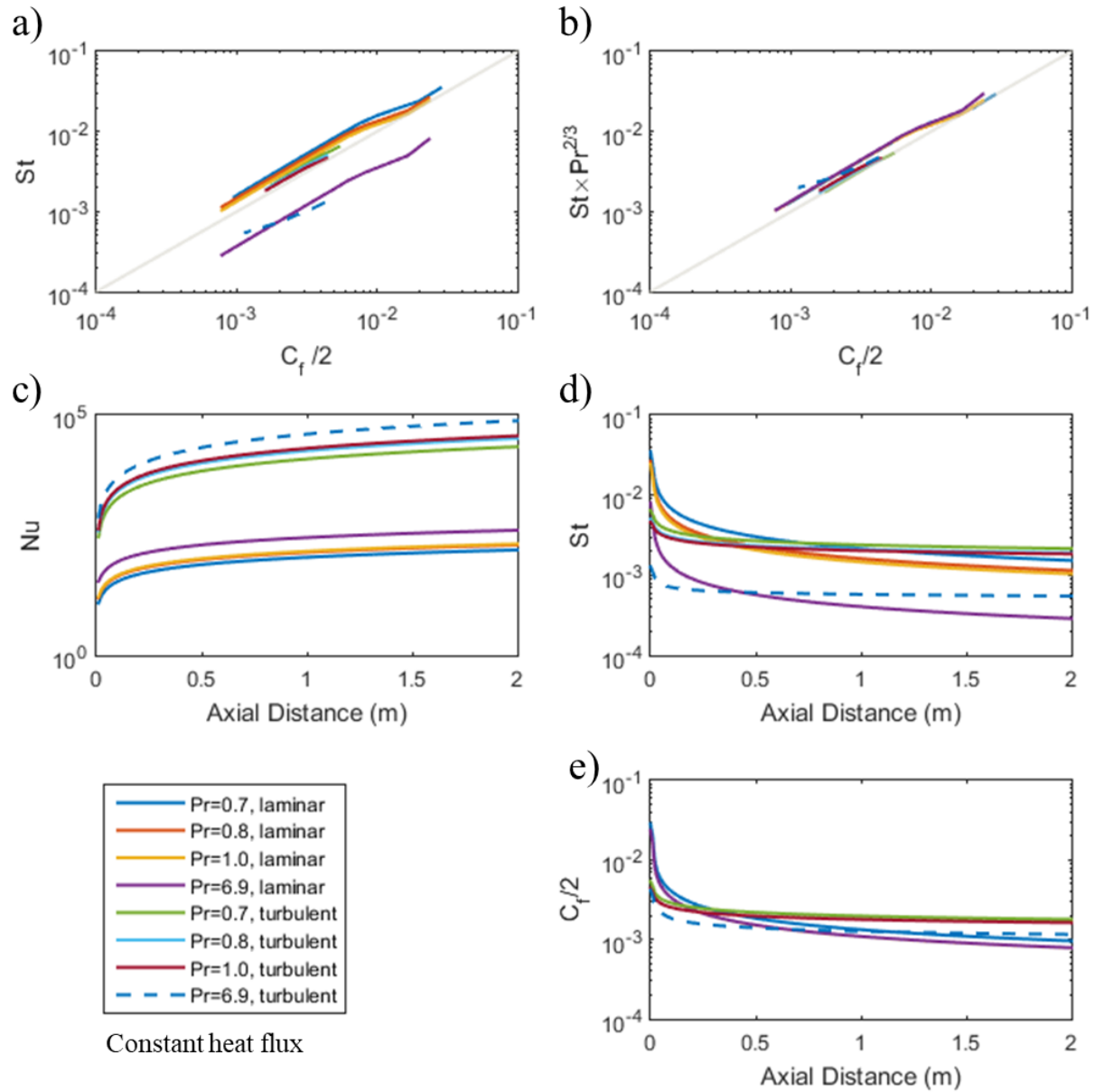


Figure 5.21. Plots of (a) the Reynolds analogy and (b) Chilton-Colburn analogy, axial development of (c) Nusselt number, (d) Stanton number, and (e) half of skin friction coefficient. Flat plate, constant wall flux.

Table 5.8. Data for flat plate with constant wall temperature (2 m from leading edge).

Prandtl number, Pr	Velocity, (m s ⁻¹)	Reynolds number, Re	Surface temperature, (K)	Heat flux, (W m ⁻²)	Nusselt number, Nu	Stanton number, St	$St \times Pr^{2/3}$	Wall shear, (Pa)	$\frac{C_f}{2}$	$\frac{St}{C_f/2}$	$\frac{St \times Pr^{2/3}}{C_f/2}$
0.74	1	1.37E+05	500	2.76E+02	1.13E+02	1.11E-03	9.09E-04	1.18E-03	9.59E-04	1.15	0.95
0.86	1	2.00E+05	500	1.73E+02	1.43E+02	8.31E-04	7.52E-04	7.85E-04	7.85E-04	1.06	0.96
1.00	1	2.00E+05	500	1.52E+02	1.51E+02	7.54E-04	7.54E-04	7.85E-04	7.85E-04	0.96	0.96
6.99	0.1	1.99E+05	500	1.77E+04	2.92E+02	2.10E-04	7.67E-04	7.85E-03	7.87E-04	0.27	0.98
0.74	100	1.37E+07	500	5.11E+04	2.09E+04	2.05E-03	1.68E-03	2.19E+01	1.79E-03	1.15	0.94
0.86	100	2.00E+07	500	3.81E+04	3.14E+04	1.83E-03	1.65E-03	1.63E+01	1.63E-03	1.12	1.02
1.00	100	2.00E+07	500	3.59E+04	3.55E+04	1.78E-03	1.78E-03	1.63E+01	1.63E-03	1.09	1.09
6.99	10	1.99E+07	500	4.60E+06	7.59E+04	5.46E-04	2.00E-03	1.15E+02	1.16E-03	0.47	1.72

Table 5.9. Data for flat plate with constant wall flux (2 m from leading edge).

Prandtl number, Pr	Velocity, (m s ⁻¹)	Reynolds number, Re	Surface temperature, (K)	Heat flux, (W m ⁻²)	Nusselt number, Nu	Stanton number, St	$St \times Pr^{2/3}$	Wall shear, (Pa)	$\frac{C_f}{2}$	$\frac{St}{C_f/2}$	$\frac{St \times Pr^{2/3}}{C_f/2}$
0.74	1	1.37E+05	351.04	100	1.56E+02	1.53E-03	1.26E-03	1.18E-03	9.59E-04	1.59	1.31
0.86	1	2.00E+05	382.42	100	1.97E+02	1.15E-03	1.04E-03	7.85E-04	7.85E-04	1.46	1.32
1.00	1	2.00E+05	394.17	100	2.08E+02	1.04E-03	1.04E-03	7.85E-04	7.85E-04	1.33	1.33
6.99	0.1	1.99E+05	298.83	100	4.01E+02	2.88E-04	1.05E-03	7.85E-03	7.87E-04	0.37	1.34
0.74	100	1.37E+07	298.38	100	2.19E+04	2.15E-03	1.77E-03	2.19E+01	1.79E-03	1.20	0.99
0.86	100	2.00E+07	298.51	100	3.27E+04	1.90E-03	1.72E-03	1.63E+01	1.63E-03	1.17	1.06
1.00	100	2.00E+07	298.54	100	3.69E+04	1.85E-03	1.85E-03	1.63E+01	1.63E-03	1.13	1.13
6.99	10	1.99E+07	298.44	10000	7.65E+04	5.49E-04	2.01E-03	1.15E+02	1.16E-03	0.47	1.74

For the comprehensive results presented regarding the analogies, it is found that Reynolds analogy is suitable for turbulent tube flow having $Pr < 1$ with both constant wall temperature and flux conditions, also for turbulent parallel plate flow with average velocity, $Pr < 1$; however, results are better for constant wall temperature as compared to constant wall flux boundary conditions. On the other hand, Chilton-Colburn analogy is suitable for laminar tube flow, parallel plate laminar flow with maximum velocity and parallel plate lower turbulent flow $Pr > 1$, and flat plate all under constant wall temperature operation, except turbulent flow and $Pr > 1$. For other cases, significant differences are present with regard to Reynolds and Chilton-Colburn analogies. Therefore, the use of these analogies for any flow configuration should be assessed carefully.

Chapter 6

FLOW DISTRIBUTION IN CHANNELS – NUMERICAL STUDY

This chapter deals with the numerical study conducted for the flow distribution system. The first section describes the model, second section presents the flow distribution for U- and Z- type manifolds. The third section presents peripheral Nusselt number and mean temperature calculation procedure. The fourth section is focused on the assessment of flow and energy analogy for the flow distribution manifold.

6.1 Model description.

Figure 6.1 shows the layout used for the study of flow distribution system. The width of the manifold is taken to be 110 mm and spacers are 5 mm wide. The depth of the channel is also taken to be 5 mm. An extended inlet allows the flow to be developed before entering the inlet manifold. The inlet temperature is taken as 298 K, with Reynolds number of 460, 980 and 1440. The top surface is subjected to uniform heat flux of 1000 W/m^2 . The exit is taken as zero-gauge pressure. Further details of the numerical modelling have been discussed earlier in Chapter 3, while the comparison of the numerical results with experimental and analytical values will be discussed in Chapter 7.

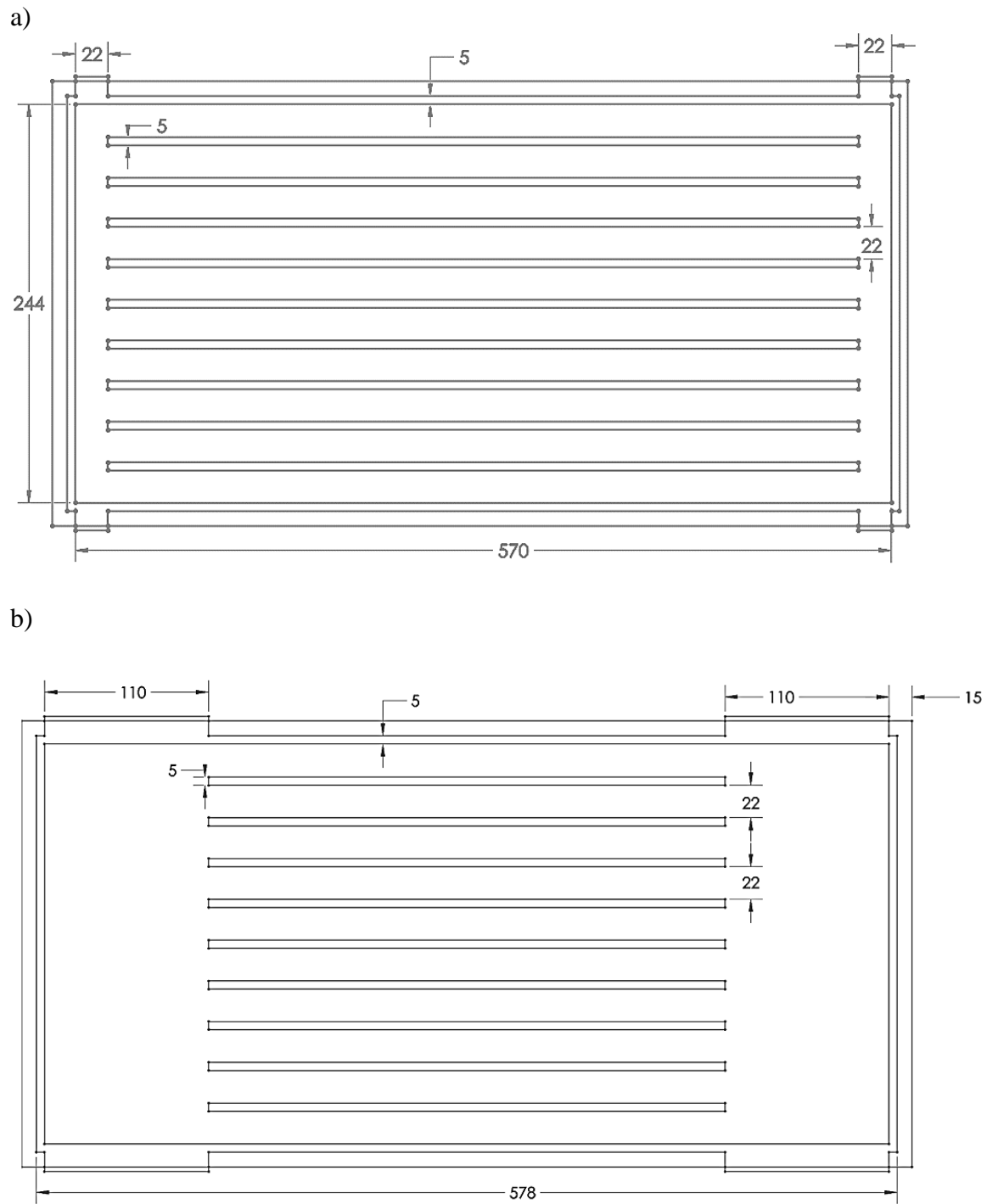


Figure 6.1. The layout used for the flow distribution manifold, a) narrow and b) wide manifold.

6.2 Flow distribution:

In this section, the velocity and flow rate distribution results are shown. The results are presented for both wide and narrow manifold designs. It should be further noted that the area of the channel and density of the fluid is constant, hence the normalized velocity distribution in each channel will be same as the normalized flow rate distribution.

6.2.1 U-type arrangement.

With the arrangement of U-type, it is expected that the channel nearest to the inlet and exit side would receive the maximum flow rate, as they will take the path of least resistance. Figure 6.2 shows a comparison of the velocity distribution in each channel for a flow rate of 100 L/hr ($Re = 480$). A decreasing behavior can be seen for the velocity, with the first channel receiving the majority of the flow rate, while the last one has the lowest one. It can be seen that the wider manifold significantly enhances the flow distribution. These velocities are normalized with the average velocity to get the normalized velocities, which are listed in Table 6.1. It can be seen for the wider manifold that the velocity in the first channel is about 1.45 while in the last channel is 0.68 of the average value, whereas these values are 3.17 and 0.19 respectively for the narrow manifold.

Figure 6.3 shows similar plots for the flow rate of 200 L/hr ($Re = 960$). It is evident that the velocities are following the same decreasing behavior, with better distribution for the wider manifold. By comparing the normalized velocities, it can be seen that the flow rate

is more uniformly distributed as compared to 100L/hr case, due to the fact that the higher flow rate increases the momentum of the fluid in the inlet section of the manifold, which forces more fluid to move into the far channels. Similar plots for the flow rate of 300 L/hr ($Re = 1440$) are shown in Figure 6.4.

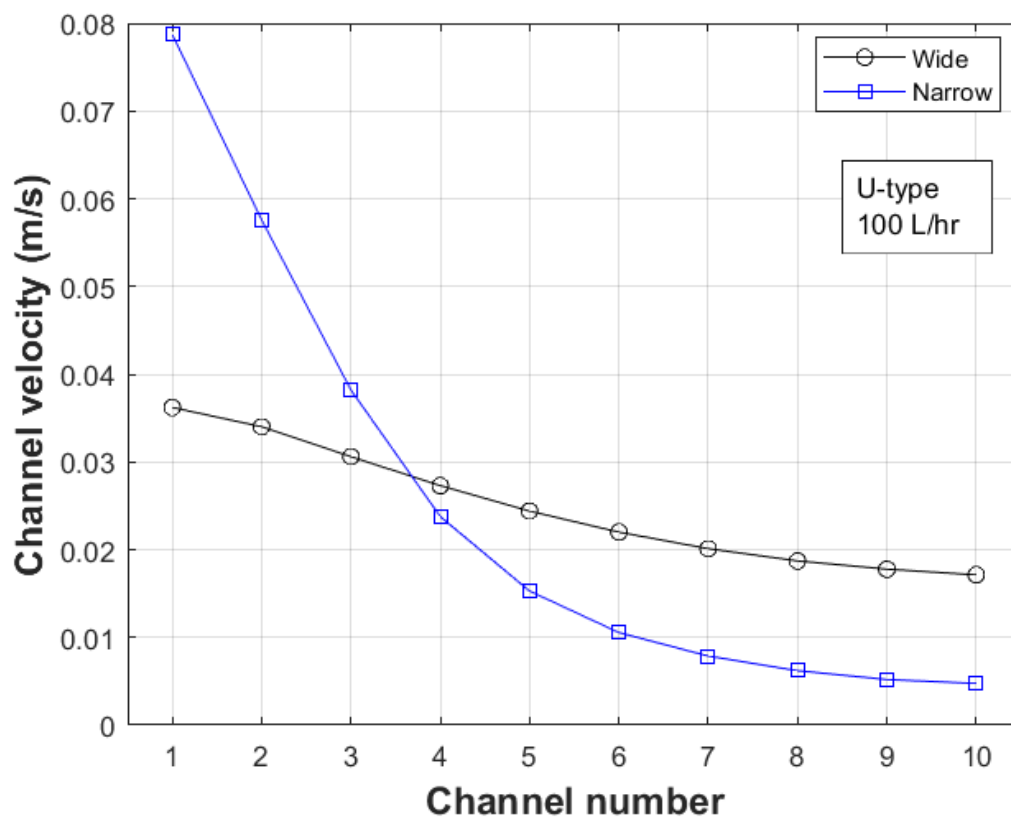


Figure 6.2. Velocity distribution comparison among channels between wide and narrow manifold. U-Type and 100 L/hr.

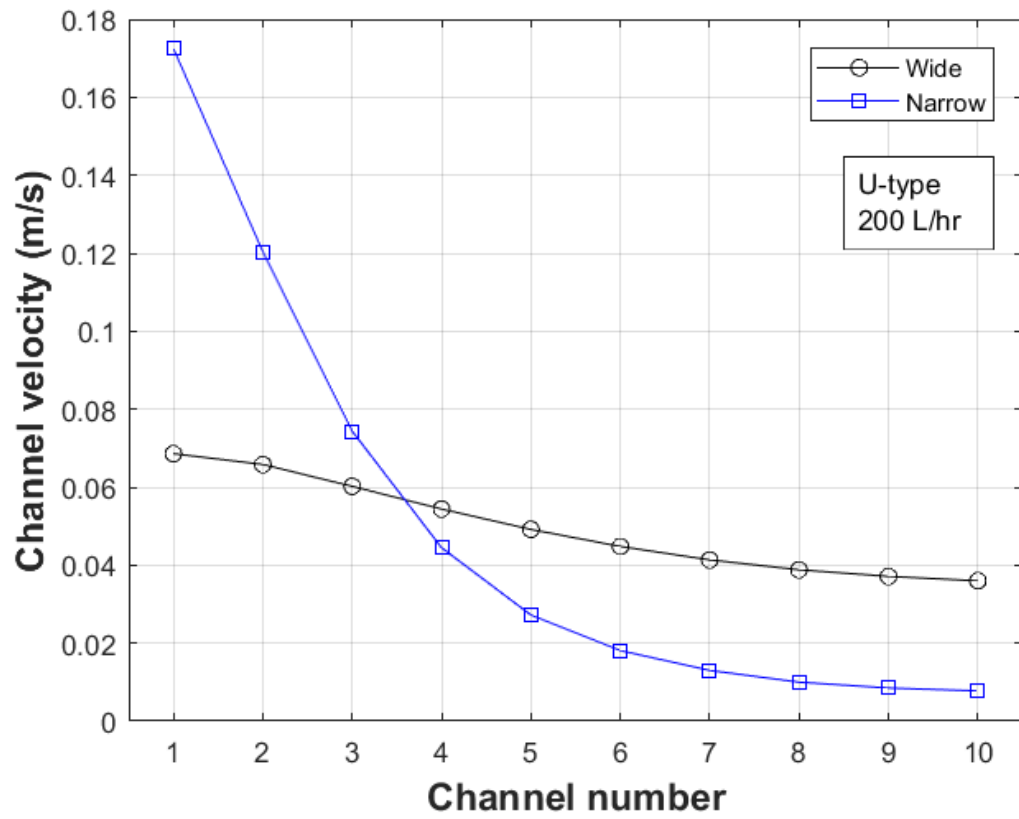


Figure 6.3. Velocity distribution comparison among channels between wide and narrow manifold. U-Type and 200 L/hr..

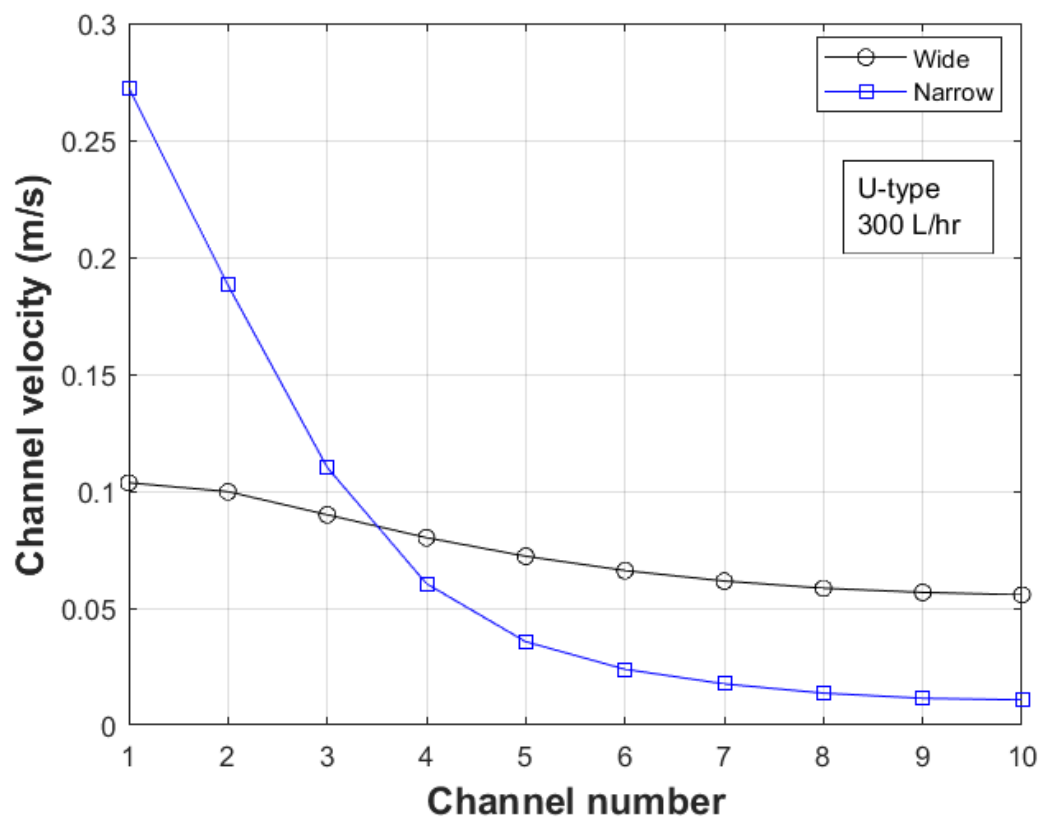


Figure 6.4. Velocity distribution comparison among channels between wide and narrow manifold. U-Type and 300 L/hr.

Table 6.1. The actual and normalized velocities for each channel. U-Type, wide and narrow manifold.

Channel Number	Wide manifold velocity		Narrow manifold velocity	
	Actual (m/s)	Normalized (-)	Actual (m/s)	Normalized (-)
100 L/hr				
1	0.0362	1.4586	0.0787	3.1727
2	0.0340	1.3700	0.0576	2.3205
3	0.0306	1.2326	0.0382	1.5394
4	0.0273	1.0996	0.0238	0.9579
5	0.0244	0.9828	0.0153	0.6158
6	0.0220	0.8861	0.0105	0.4252
7	0.0201	0.8101	0.0079	0.3174
8	0.0187	0.7541	0.0062	0.2500
9	0.0178	0.7162	0.0052	0.2096
10	0.0171	0.6899	0.0048	0.1915
200 L/hr				
1	0.0686	1.3820	0.1725	3.4760
2	0.0658	1.3264	0.1204	2.4254
3	0.0602	1.2134	0.0744	1.4985
4	0.0544	1.0961	0.0445	0.8958
5	0.0492	0.9907	0.0272	0.5485
6	0.0448	0.9027	0.0181	0.3646
7	0.0414	0.8333	0.0130	0.2621
8	0.0388	0.7821	0.0100	0.2014
9	0.0371	0.7481	0.0085	0.1712
10	0.0360	0.7250	0.0078	0.1565
300 L/hr				
1	0.1036	1.3920	0.2725	3.6609
2	0.0998	1.3409	0.1880	2.5267
3	0.0899	1.2083	0.1101	1.4798
4	0.0801	1.0767	0.0605	0.8127
5	0.0722	0.9700	0.0357	0.4791
6	0.0661	0.8879	0.0239	0.3209
7	0.0616	0.8274	0.0176	0.2368
8	0.0585	0.7862	0.0137	0.1838
9	0.0567	0.7623	0.0115	0.1542
10	0.0557	0.7483	0.0108	0.1451

6.2.2 Z-type arrangement.

For the Z-type flow rate, fluid enters from one side of the manifold and leaves from the opposite side. In this case, we can see from Figure 6.5 that the flow in the first channel is lowest, with an increasing behavior. For the narrow manifold, flow is highest for the last channel with about twice the velocity of the wide manifold. The normalized velocities are also listed in Table 6.2. In comparison with the U-Type, the first channel has only 0.8 while last channel has 1.5 flow rate of the average value. Similarly, for the narrow manifold, these values are about 0.68 and 3.5 respectively, showing significant flow maldistribution. Figure 6.6 and Figure 6.7 show similar plots for the higher flow rates of 200 L/hr and 300 L/hr, with increasing behavior for the velocity and better distribution for the case of wide manifold.

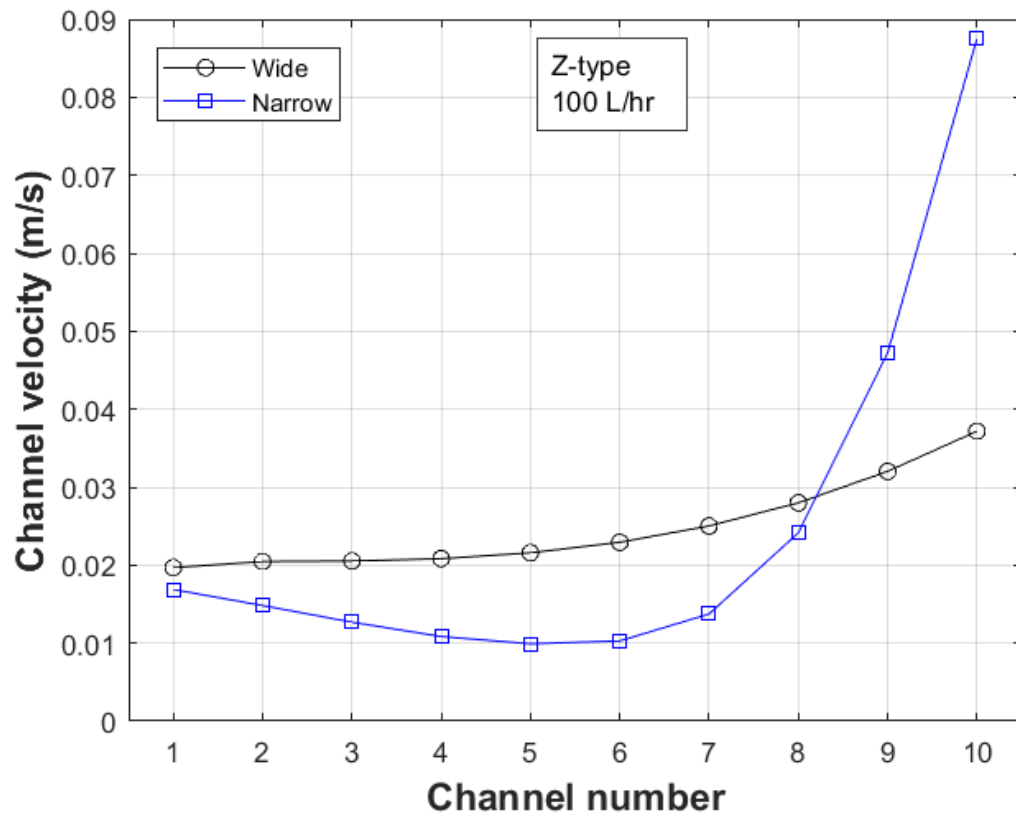


Figure 6.5. Velocity distribution comparison among channels between wide and narrow manifold. Z-Type and 100 L/hr.

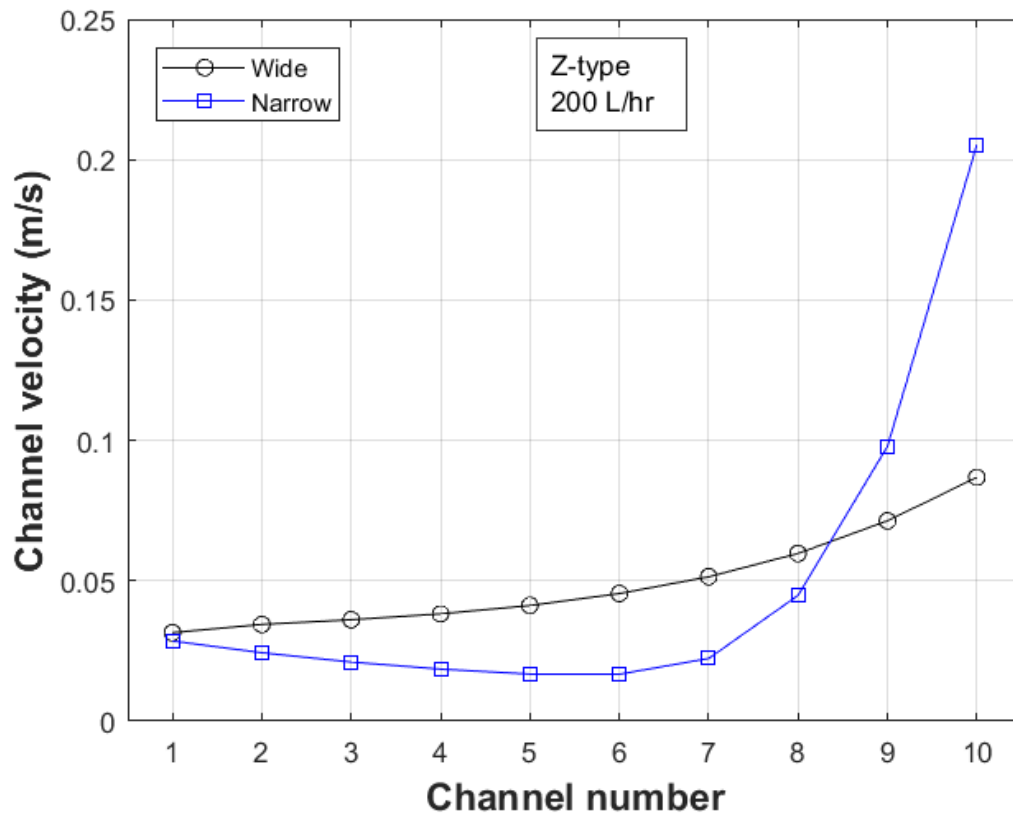


Figure 6.6. Velocity distribution comparison among channels between wide and narrow manifold. Z-Type and 200 L/hr.

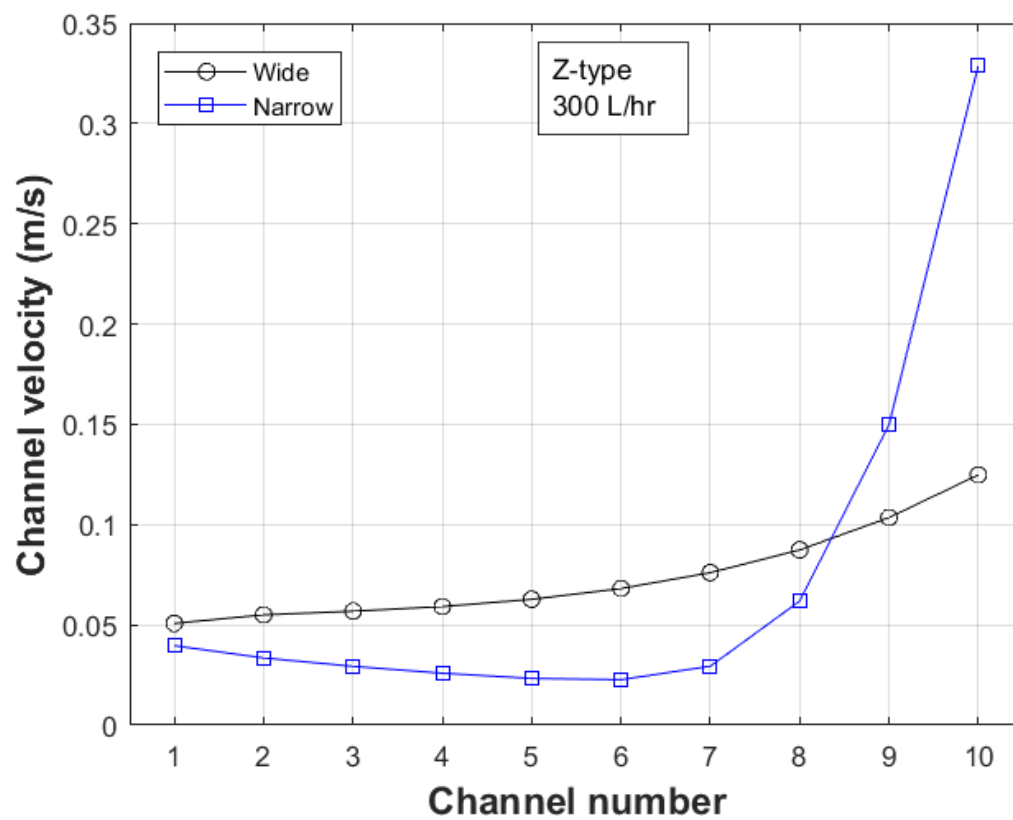


Figure 6.7. Velocity distribution comparison among channels between wide and narrow manifold. Z-Type and 300 L/hr.

Table 6.2. The actual and normalized velocities for each channel. Z-Type, wide and narrow manifold.

Channel Number	Wide manifold velocity		Narrow manifold velocity	
	Actual (m/s)	Normalized (-)	Actual (m/s)	Normalized (-)
100 L/hr				
1	0.0197	0.7928	0.0169	0.6802
2	0.0205	0.8245	0.0148	0.5975
3	0.0205	0.8269	0.0127	0.5115
4	0.0208	0.8391	0.0108	0.4371
5	0.0216	0.8694	0.0099	0.3997
6	0.0229	0.9239	0.0103	0.4145
7	0.0250	1.0080	0.0137	0.5538
8	0.0280	1.1278	0.0241	0.9732
9	0.0320	1.2901	0.0472	1.9041
10	0.0372	1.4975	0.0875	3.5284
200 L/hr				
1	0.0315	0.6350	0.0285	0.5752
2	0.0345	0.6943	0.0244	0.4909
3	0.0361	0.7279	0.0211	0.4242
4	0.0382	0.7701	0.0185	0.3734
5	0.0412	0.8299	0.0168	0.3377
6	0.0454	0.9156	0.0167	0.3369
7	0.0514	1.0360	0.0223	0.4498
8	0.0597	1.2036	0.0448	0.9028
9	0.0714	1.4379	0.0979	1.9726
10	0.0868	1.7496	0.2053	4.1364
300 L/hr				
1	0.0508	0.6820	0.0396	0.5320
2	0.0550	0.7391	0.0335	0.4502
3	0.0568	0.7632	0.0293	0.3940
4	0.0591	0.7946	0.0259	0.3479
5	0.0627	0.8429	0.0233	0.3130
6	0.0681	0.9153	0.0227	0.3044
7	0.0760	1.0215	0.0294	0.3949
8	0.0874	1.1740	0.0618	0.8309
9	0.1035	1.3907	0.1499	2.0136
10	0.1248	1.6768	0.3289	4.4192

6.3 Nusselt number and mean temperature calculations

For the calculation of Nusselt number, following equation is used.

$$Nu_p = \frac{d}{k} \left(\frac{q_s''}{(T_w - T_m)} \right) \quad (6.1)$$

It is noticed that there are three unknowns in this equation, either q or T_w , T_m and Nu . From the literature, Nusselt values are available that represent the performance of the surface. Now in order to calculate the wall temperature, a new parameter is introduced termed, Nusselt numbers star defined as

$$Nu^* = \frac{d}{k} \left(\frac{q_s''}{(T_w - T_{in})} \right) \quad (6.2)$$

In this case, the mean temperature is replaced with the inlet temperature and the Nusselt number is calculated based on the inlet temperature. This is similar to the definition of Nusselt number in open flow over surfaces, where the free stream temperature is used for the definition of Nusselt. The benefit of this is that the unknown wall temperature can be calculated, and then utilized in Eq.(6.1) to find the mean cross-sectional temperature.

6.3.1 U-type Wide manifold

100 L/hr: Figure 6.8 (a) show the velocity and temperature contours for the U-type arrangement with a flow rate of 100L/hr. The velocity is shown for the middle plane in the Z axis, while the temperature is for the top surface, to which the heat flux is directly applied.

It can be seen that due to the low flow rate, majority of the flow rate is entering the first channel and as the flow rate for the further channels is reducing. The flow inlet is assumed to be entering as fully developed by the use of an inlet section with the same cross-section of the inlet manifold. The impact of this inlet section is visible in the corner of the first section, which shows that the flow is more focused towards the channels, and less on the other side.

The impact of the above velocity distribution on the temperature distribution can be seen in Figure 6.8 (b). it can be seen that the fluid is heated uniformly in the inlet section, but the corner is having a higher temperature due to the stagnation region as visible from figure a). Based on the velocity distribution, the lowest temperature is in the location having the highest velocity.

Figure 6.9 shows the Nusselt number distribution for the inlet manifold. It can be seen that higher Nusselt number is available in the inner section and the Nusselt number values decrease in the manifold. Also, Higher Nusselt number values are visible towards the sides, due to some contribution, of the adjacent walls in heat transfer. The Figure 6.9 (b) shows the Nusselt Number star for the inlet manifold. We can see the behavior is similar for both the cases, with the only difference in the magnitudes, which are lower for Nusselt number star due to the reference temperature taken to be as the inlet section.

Figure 6.10 (a) show the Nusselt number for the exit manifold. It can be seen that large values are present for the regions where the channels are discharging the fluid. Also, the

far end of the exit manifold has a very low Nusselt number. Figure 6.10 (b) shows the Nusselt number star, where its values are lower in comparison with the Nusselt number. It is more evident from these figures that the middle of the channels is having the highest Nusselt number and the baffles are resulting in regions of low Nusselt number

Figure 6.11 (a) shows the Nusselt number distribution in the channels for the manifold. It is evident that the initial channels are having higher Nusselt number values, meaning they are more actively involved in the heat transfer, while the farther channels are having about one-third Nusselt number, mainly due to lower flowrate. Similar behavior can be seen for Nusselt number star from Figure 6.11 (b).

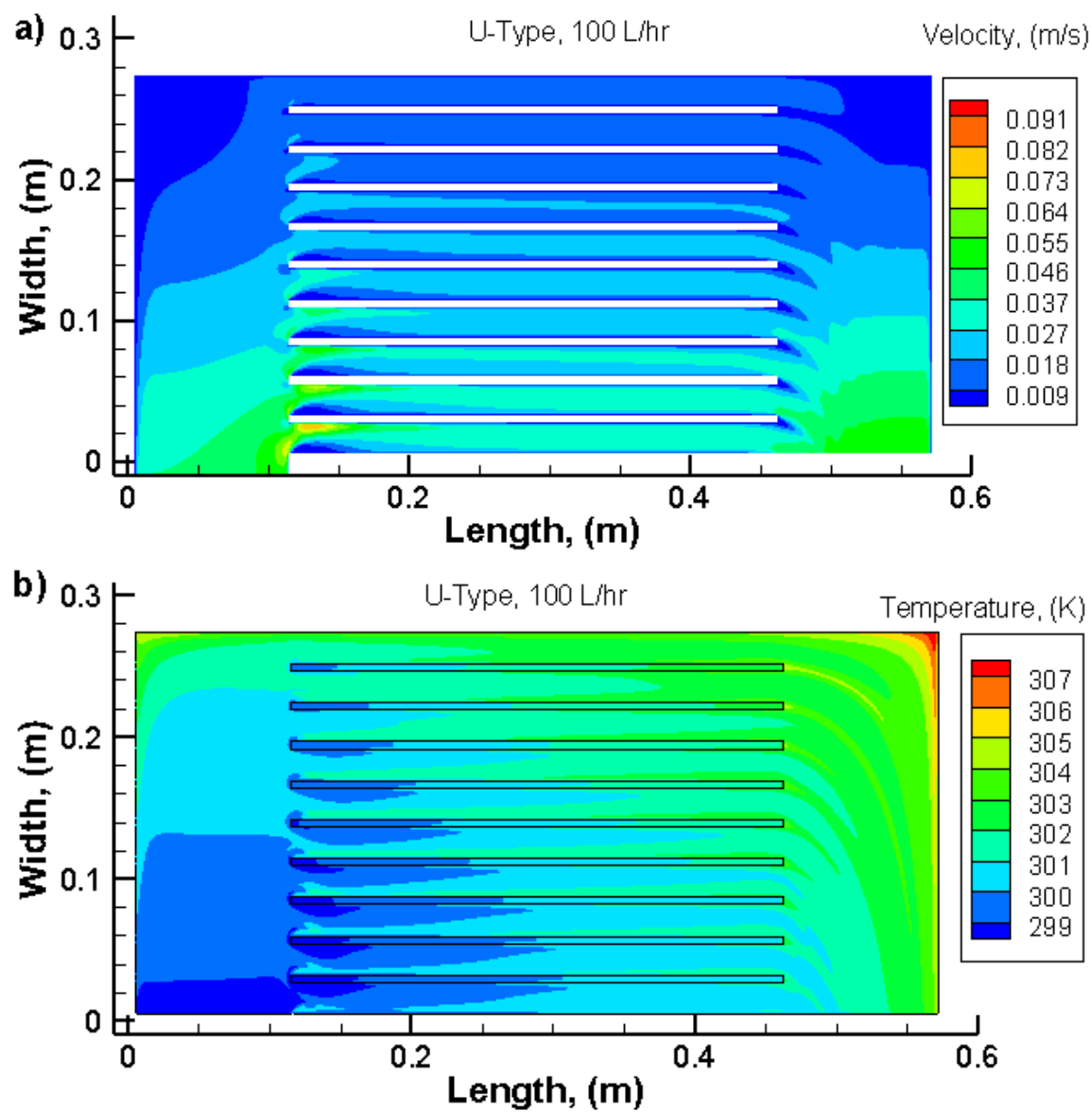


Figure 6.8. The a) velocity and b) temperature contour for the case of U-type and 100 L/hr.

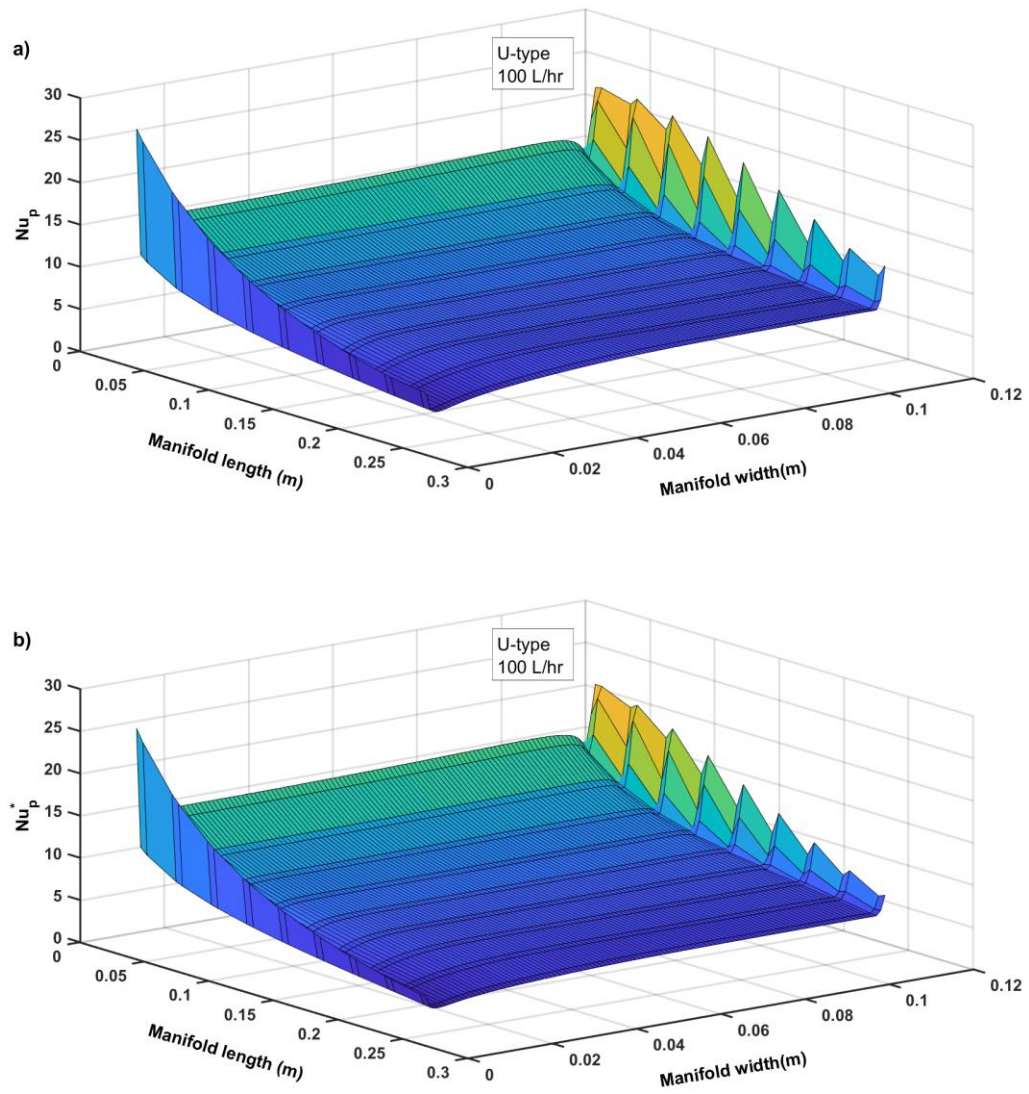


Figure 6.9. The a) Nusselt number and b) Nusselt number star for the inlet manifold. U-type and 100 L/hr.

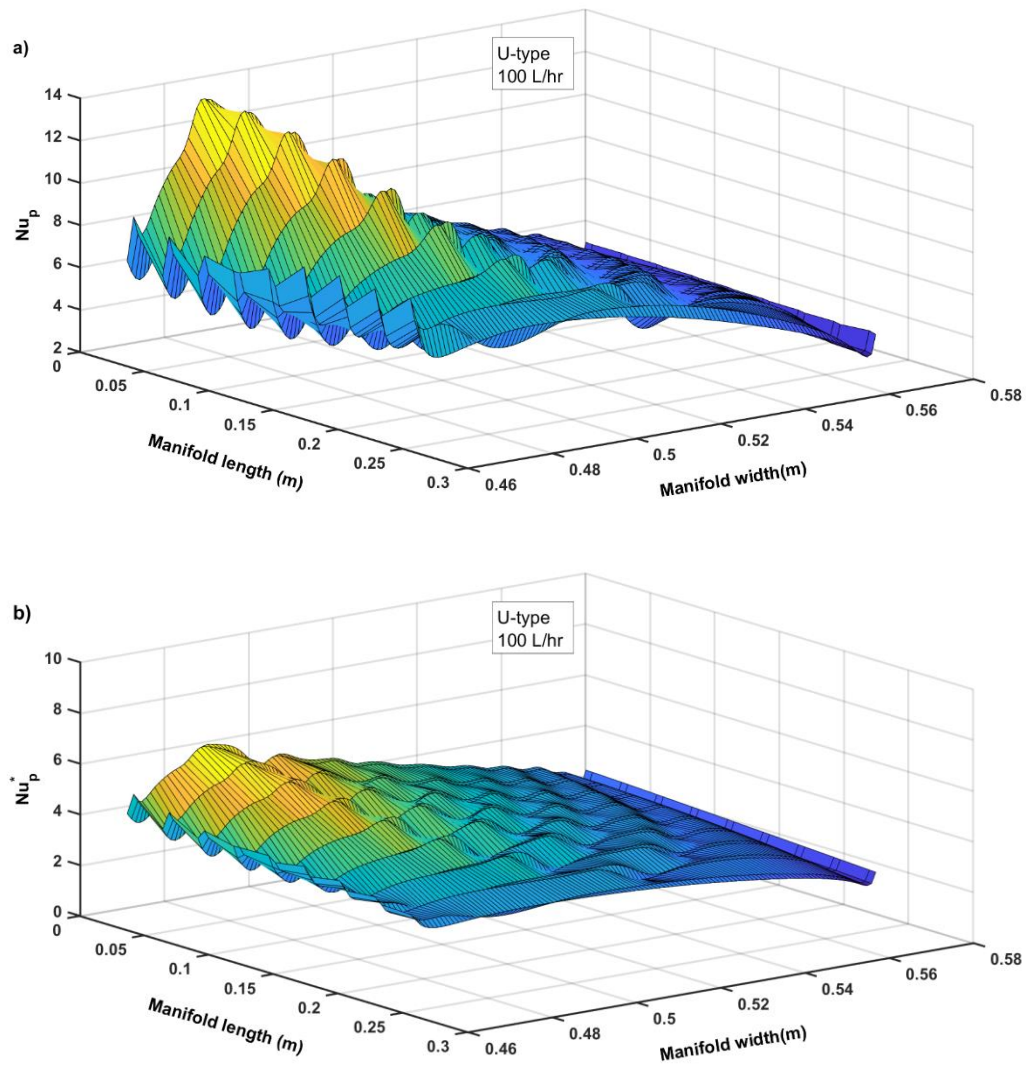


Figure 6.10. The a) Nusselt number and b) Nusselt number star for the exit manifold. U-type and 100 L/hr.

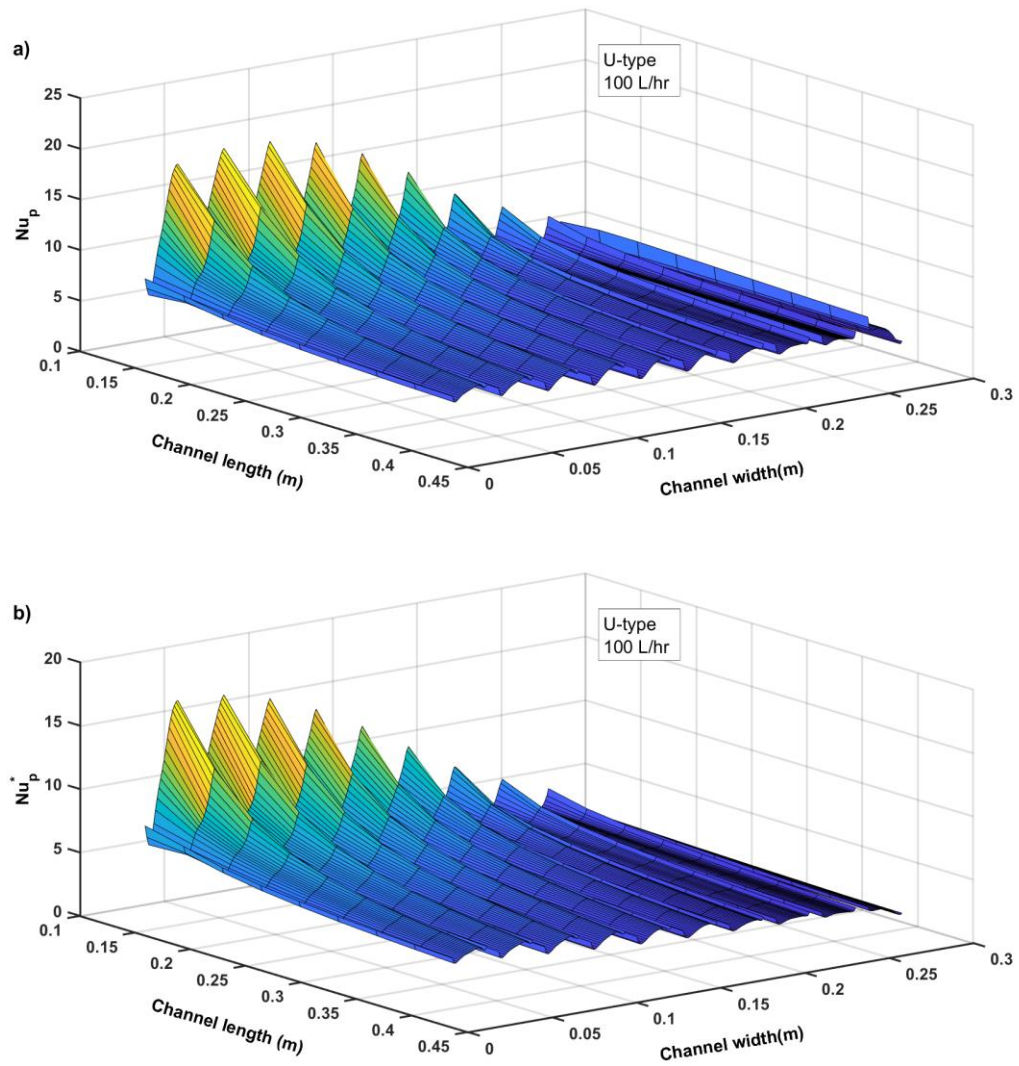


Figure 6.11. The a) Nusselt number and b) Nusselt number star for the channels. U-type and 100 L/hr.

200 L/hr: Figure 6.12 (a) shows the velocity distribution, where more velocity is seen in the later channels as compared to the flow rate of 200 L/hr. Figure 6.12 (b) shows that the temperature profiles is not like the parabolic/uniform shape as seen for the lower flow rate. Now as the flow rate is more, the fluid near the wall is having higher temperature, while more fluid is moving to the channels at higher velocity, leading to a lower temperature. We see that the profile is shifter towards the wall, with higher temperature near the wall while lower near the channels. Figure 6.13 (a) shows that effect of the hot spot zone on Nusselt numebr is more visible for the higher flow rate, as the higher velocity keeps the momentum towards the channels and leading to a larger stationary zone in the region opposite to the inlet. We can see that the Nusselt number begins with a higher value and decreases in the channels. The value remains high for the region near the channels, but almost zero values are seen for the corner. shows similar trend for the Nusselt number star, with the values being slightly lower in comparison to the Nusselt number.

Figure 6.14 shows that the Nusselt number variation in the exit section of the manifold is more uniformed in comparison for the lower flow rate. It is due to the fact that more fluid is entering the latter channels in comparison for the lower flow rates, this enable the exit section to be more filled with the fluid. We can see that as the fluid exits from the channels, higher values are obtained with decremental distribution towards the outlet. Furthermore, higher values are obtained for the Nusselt number star. Figure 6.15 shows that the Nusselt number for 200 L/hr case is almost same for all the channels, whereas it was seen that the

values were decreasing further from the inlet for the lower flow rate. This also validates that flow distribution is better than the previous case.

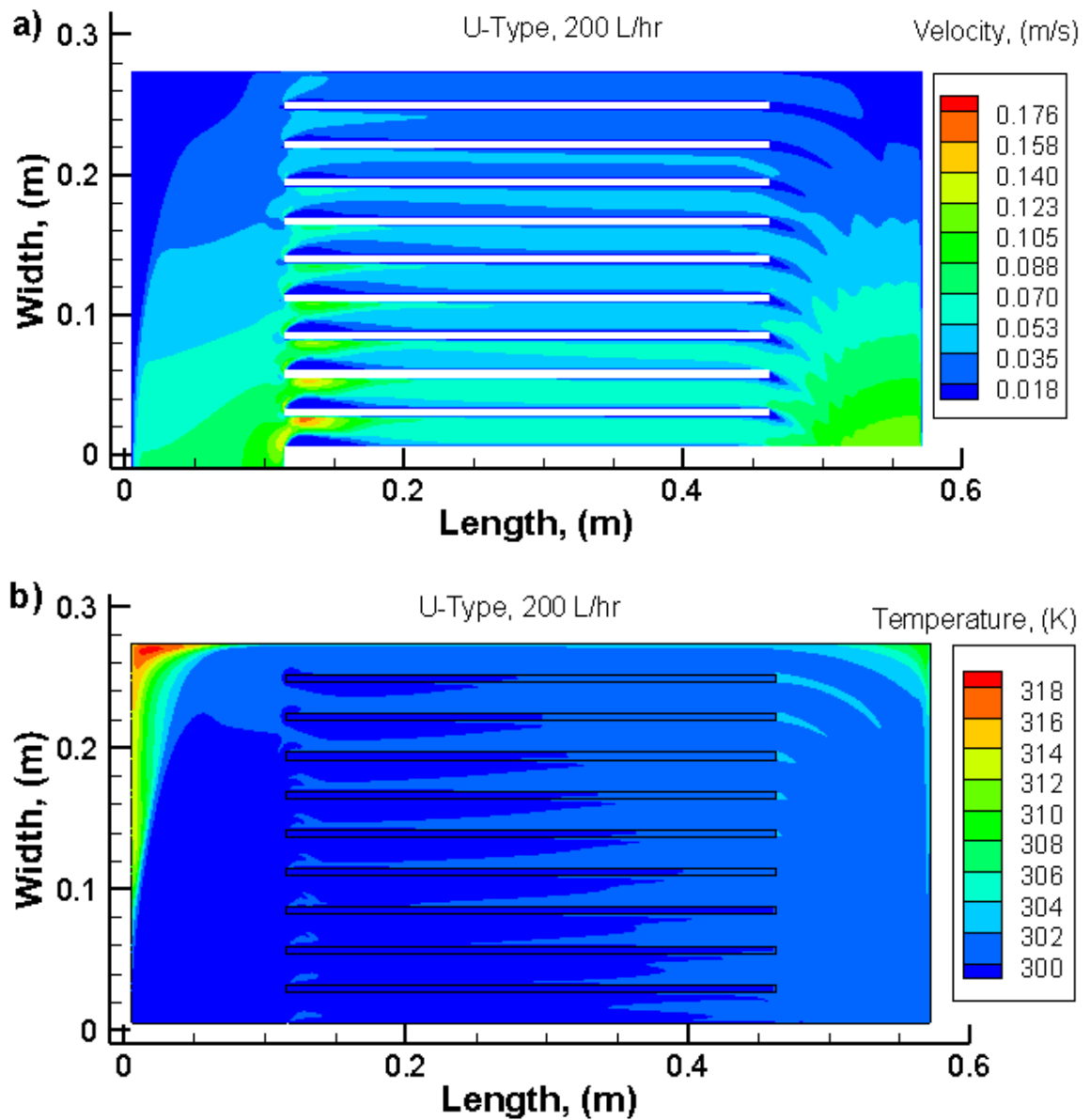


Figure 6.12. The a) velocity and b) temperature contour for the case of U-type and 200L/hr.

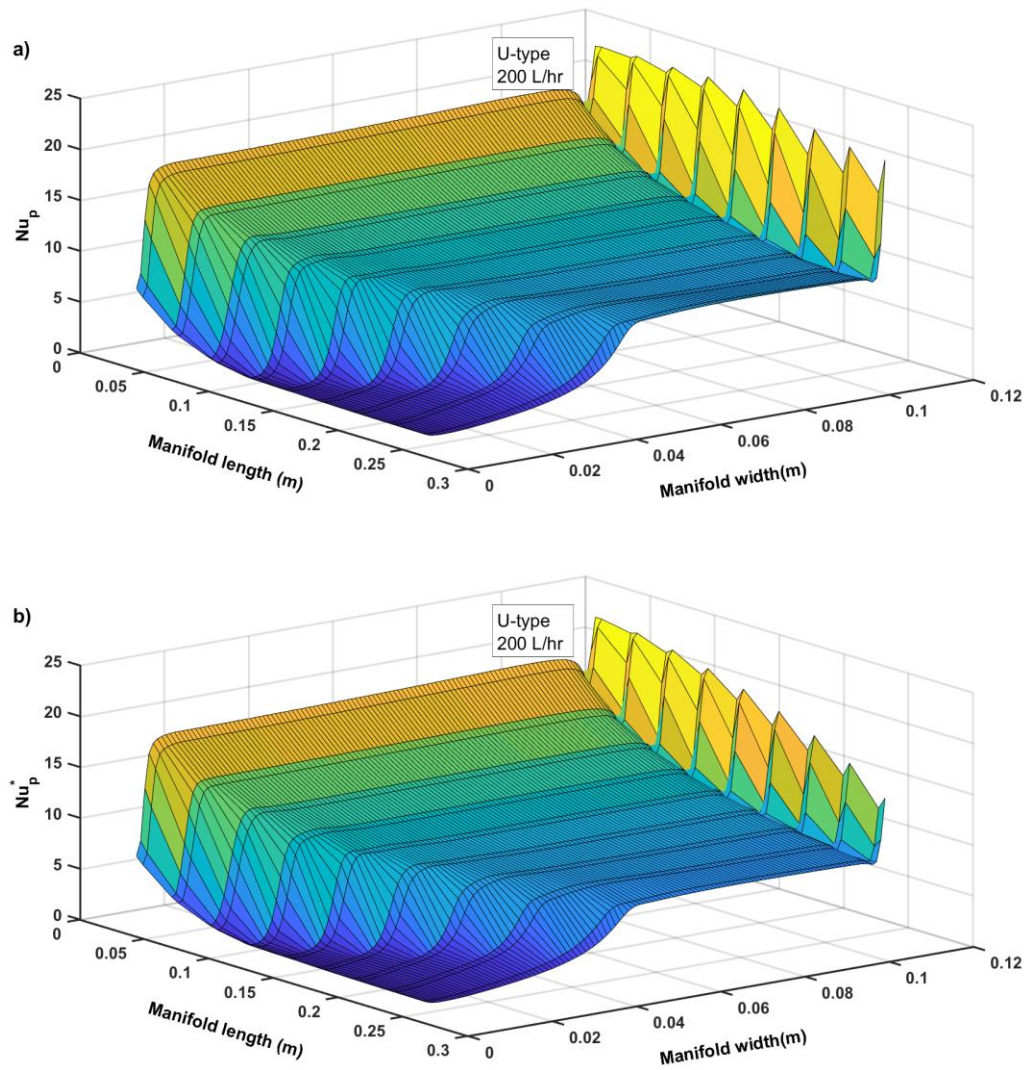


Figure 6.13. The a) Nusselt number and b) Nusselt number star for the inlet manifold. U-type and 200 L/hr.

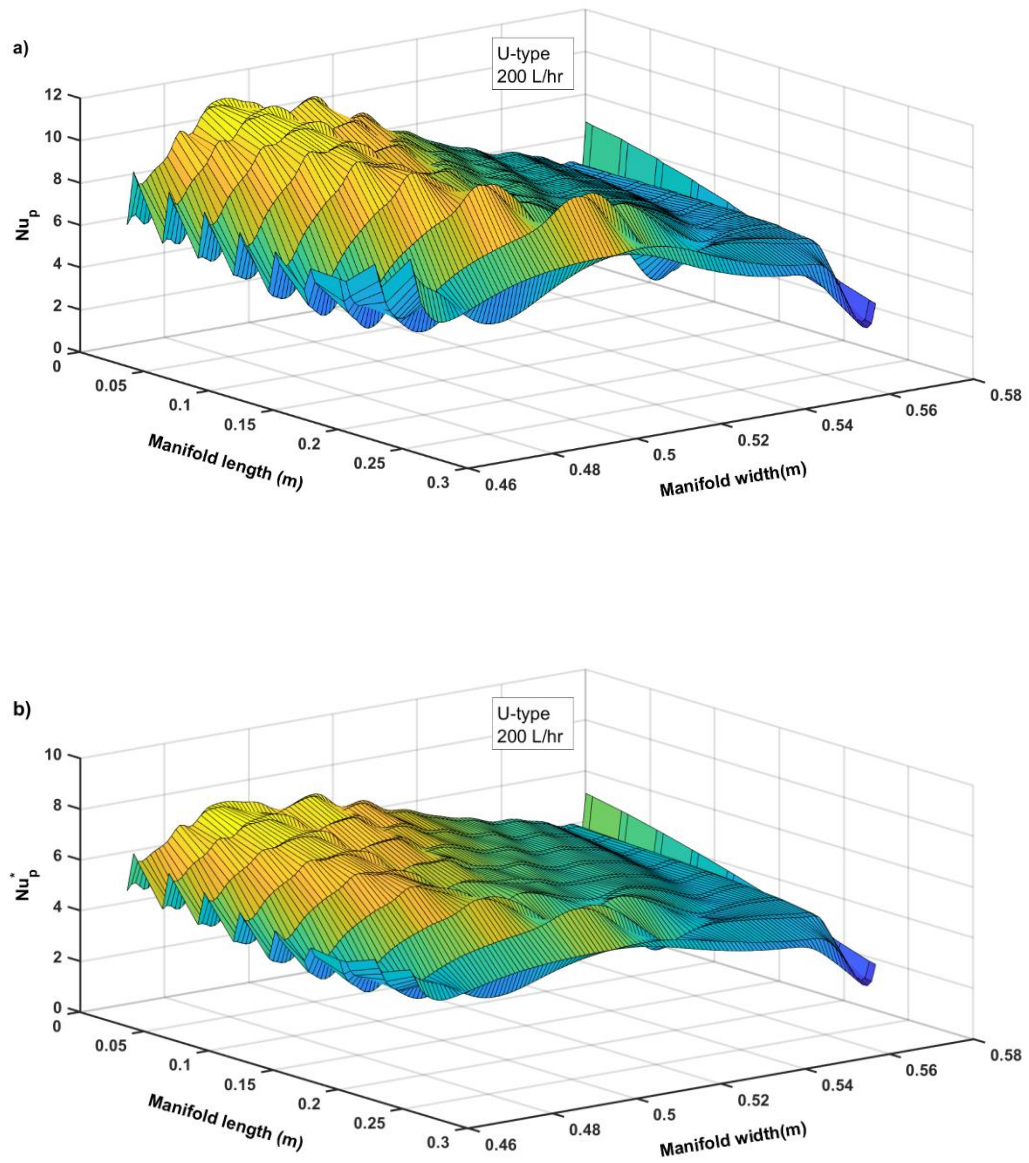


Figure 6.14. The a) Nusselt number and b) Nusselt number star for the exit manifold. U-type and 200 L/hr.

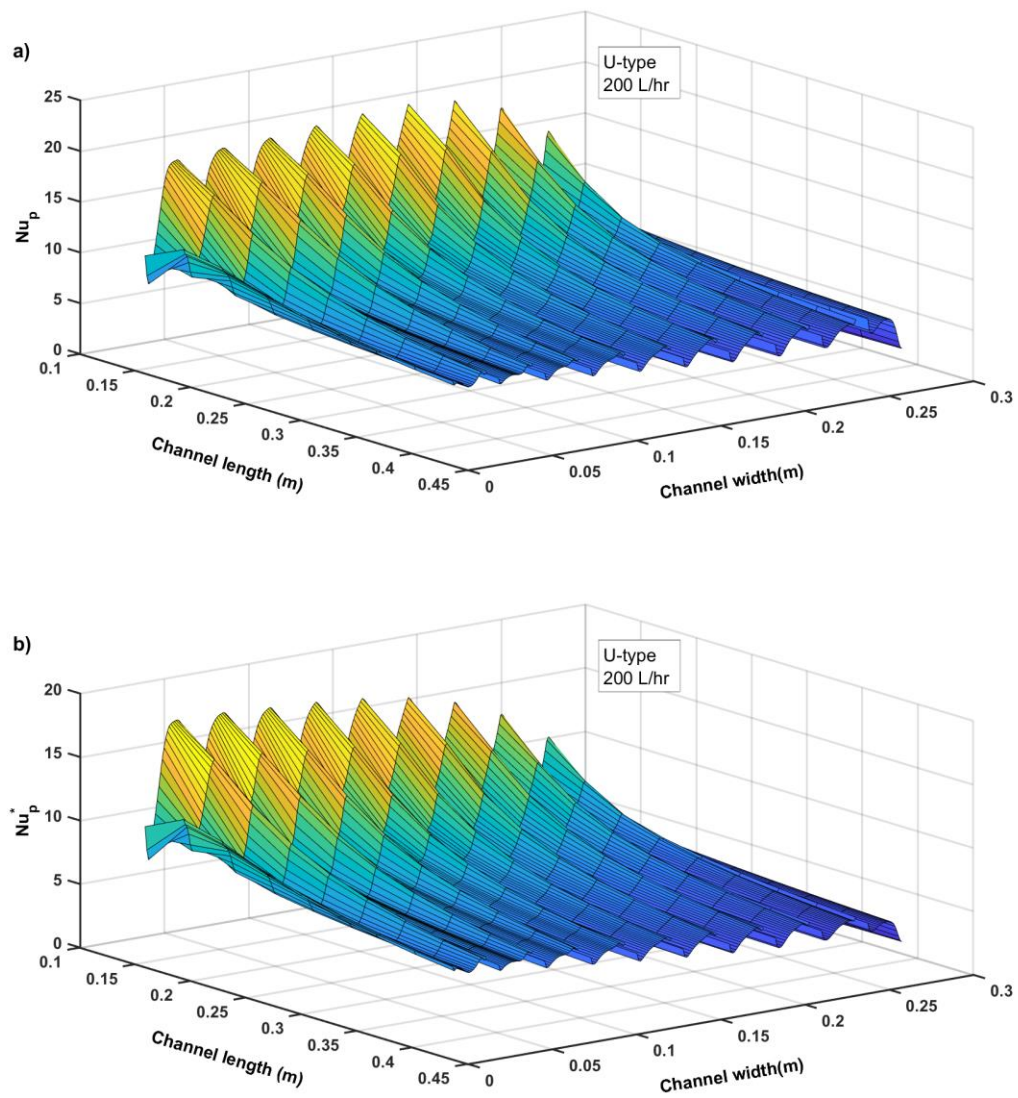


Figure 6.15. The a) Nusselt number and b) Nusselt number star for the channels. U-type and 200 L/hr.

6.3.2 Z-type Wide manifold

100 L/hr: Figure 6.16 shows the flow and temperature distribution for the Z-type arrangement. The velocity is shown for the middle plane in the Z axis, while the temperature is for the top surface, to which the heat flux is directly applied. In this case, only the location of exit is changed from the same side for U-type to the opposite diagonal side in the Z-type arrangement. It is visible that in this case, as the flow has to pass in diagonal location instead of same side, this leads to higher flow rate in the last channels and less in the initial channels. The Z-type arrangement also results in lower temperature, with slightly improved distribution in comparison to the U-type.

Figure 6.17 shows that the Nusselt number distribution in the inlet manifold is almost the same, with higher values in the beginning and decreasing towards the end. Figure 6.18 show the Nusselt number distribution for the exit section. It can be seen that the zero values are for the manifold distance of zero, which was the exit location for U-type arrangement. The Z-type has lower overall values of Nusselt number for the exit section.

Figure 6.19 shows that the Nusselt number for the flow rate of 100 L/hr is almost similar in all the channels. This was not the case for U-type at this flow rate, where the latter channel had lower values. In this case as the general flow direction is towards the diagonal, all the channels are more involved in the heat absorption.

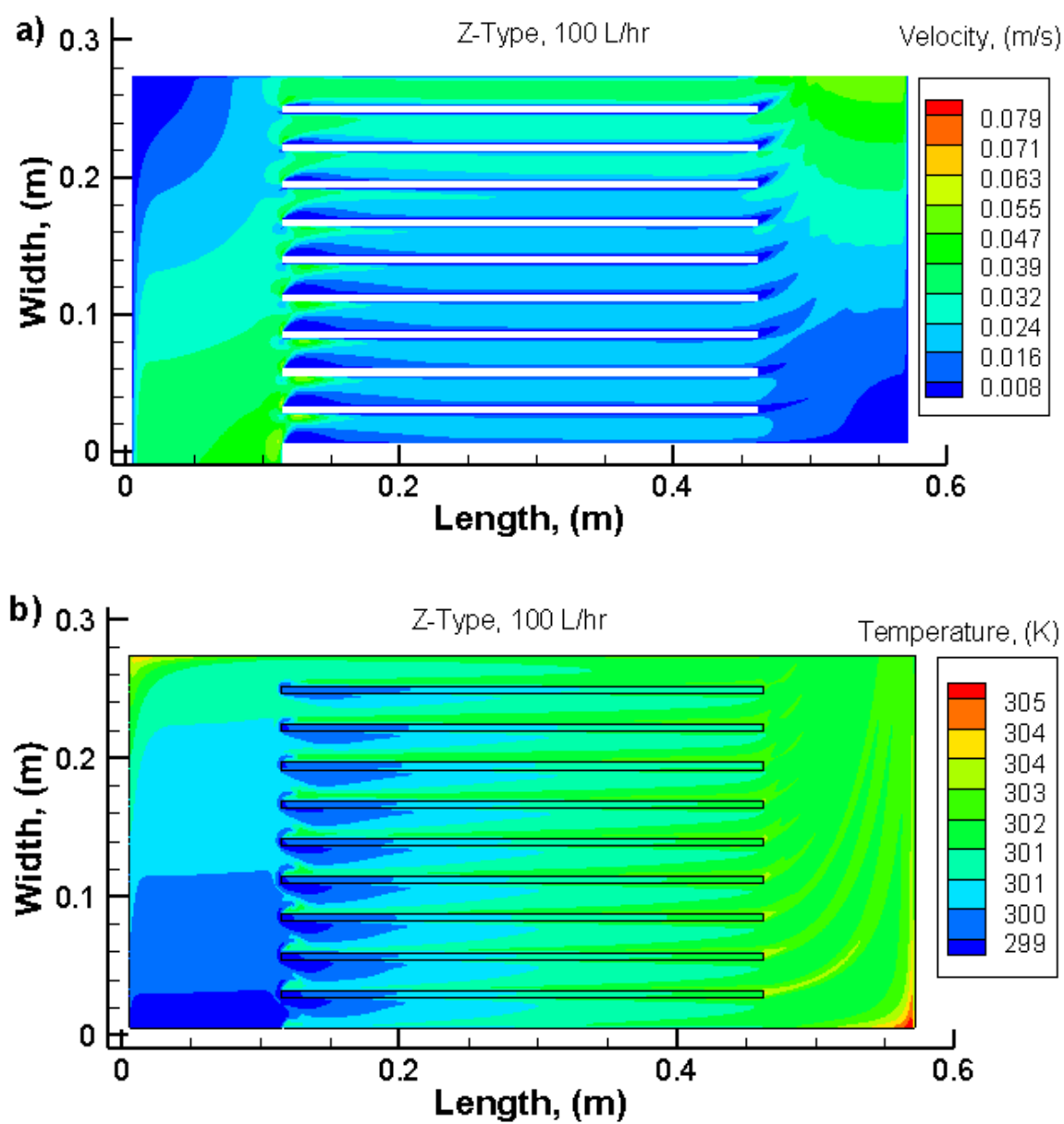


Figure 6.16. The a) velocity and b) temperature contour for the case of Z- type and 100L/hr.

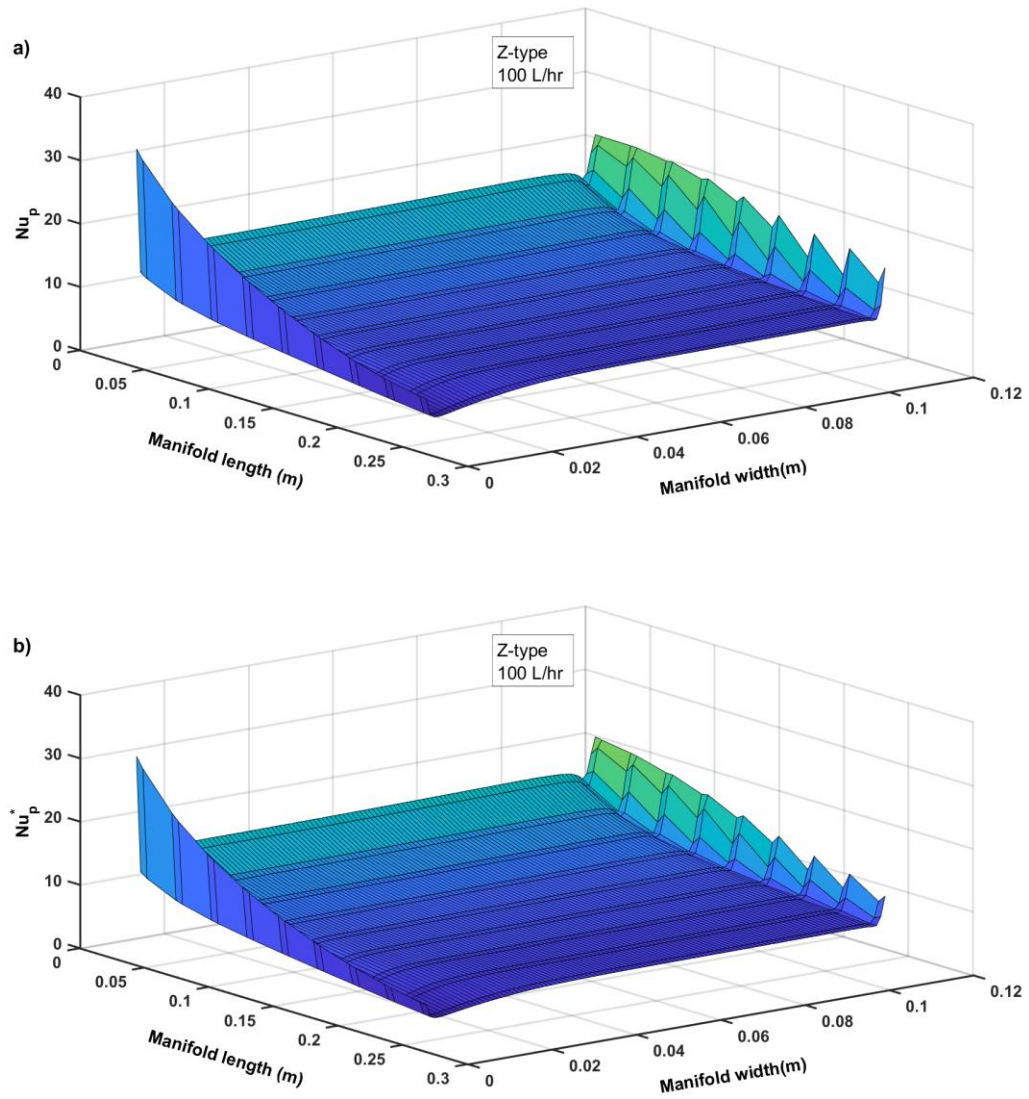


Figure 6.17. The a) Nusselt number and b) Nusselt number star for the inlet manifold.

Z- type and 100 L/hr.

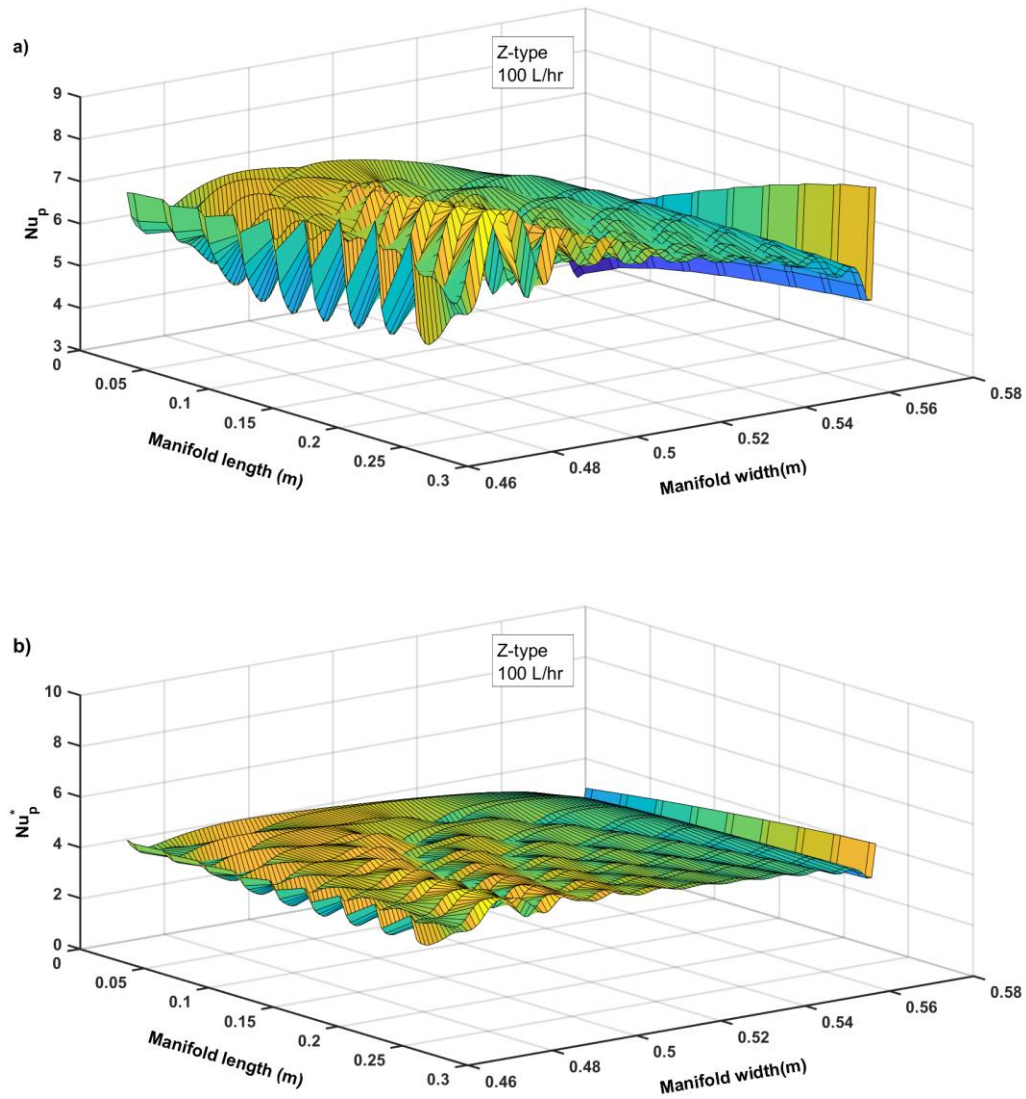


Figure 6.18. The a) Nusselt number and b) Nusselt number star for the exit manifold.

Z- type and 100 L/hr.

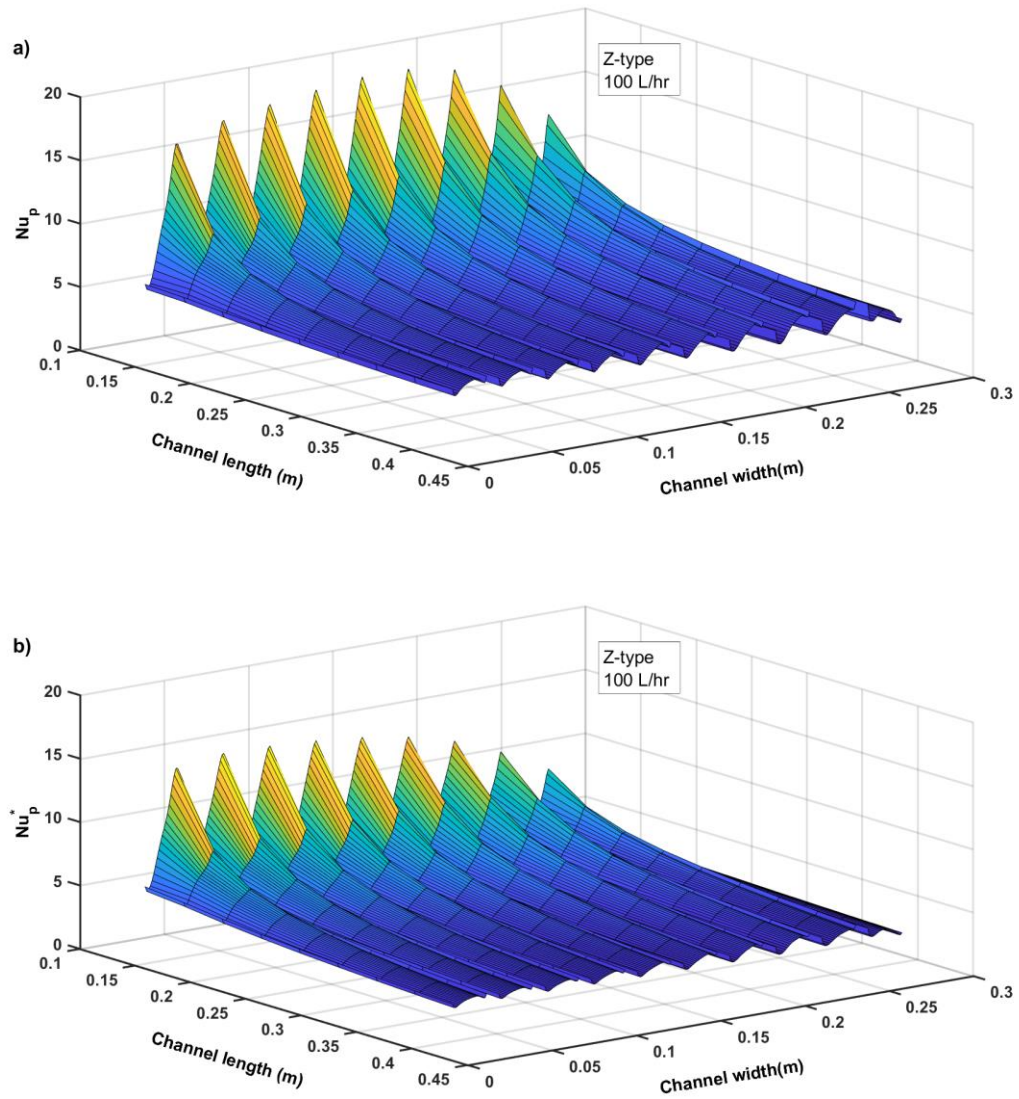


Figure 6.19. The a) Nusselt number and b) Nusselt number star for the channels. Z-type and 100 L/hr.

200 L/hr: Figure 6.20 shows the velocity and temperature contours for the higher flow rate of 200 L/hr. More flow rate is again focused in the latter channels leading to poorer flow distribution in comparison to the lower flow rate. It should be noted that the trend was opposite for the U-type, where higher flow rate was actually increasing the flow distribution.

Figure 6.21 shows the Nusselt number distribution in the inlet section, where again the hot spot is visible in the corner leading to almost zero Nusselt number. The Nusselt number values are slightly higher in comparison to the lower flow rate. Figure 6.22 shows that the Nusselt number is more uniformly distributed, showing better flow distribution in the exit section of the heat exchanger. The values are also higher for the higher flow rate. For the Nusselt number in channels, Figure 6.23 shows that the last channel has the highest Nusselt number and almost same lower values for the initial few channels.

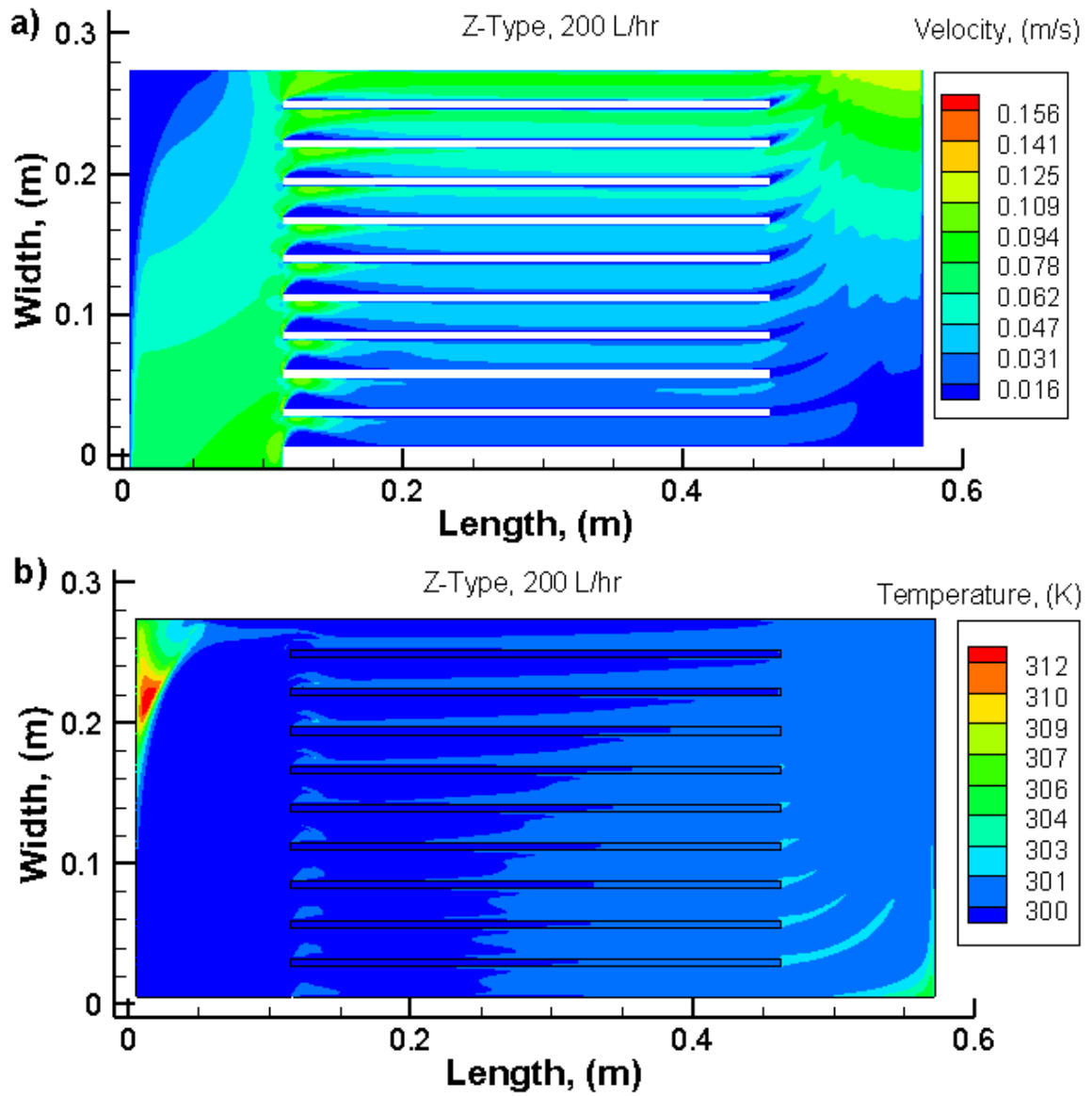


Figure 6.20. The a) velocity and b) temperature contour for the case of Z-type and 200L/hr.

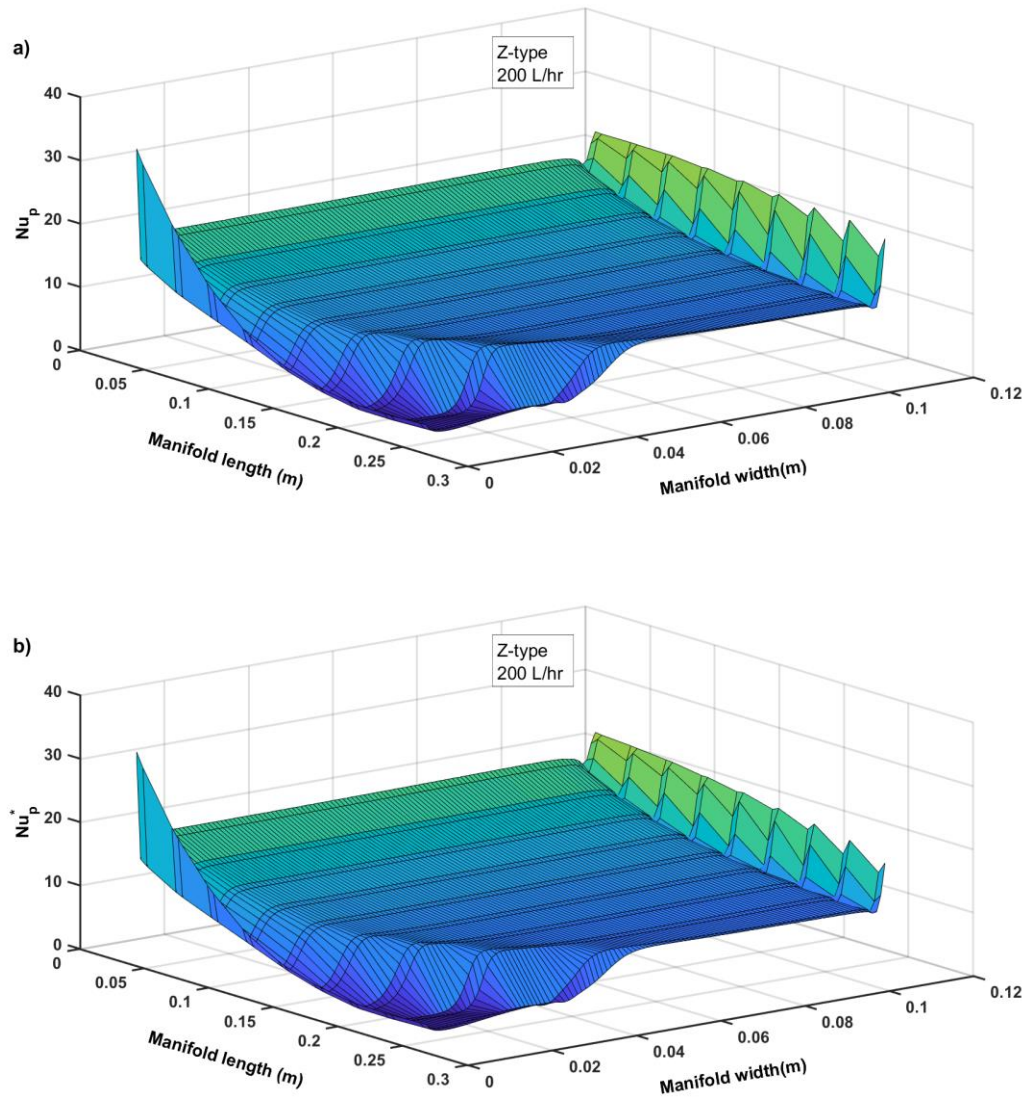


Figure 6.21. The a) Nusselt number and b) Nusselt number star for the inlet manifold.

Z- type and 200 L/hr.

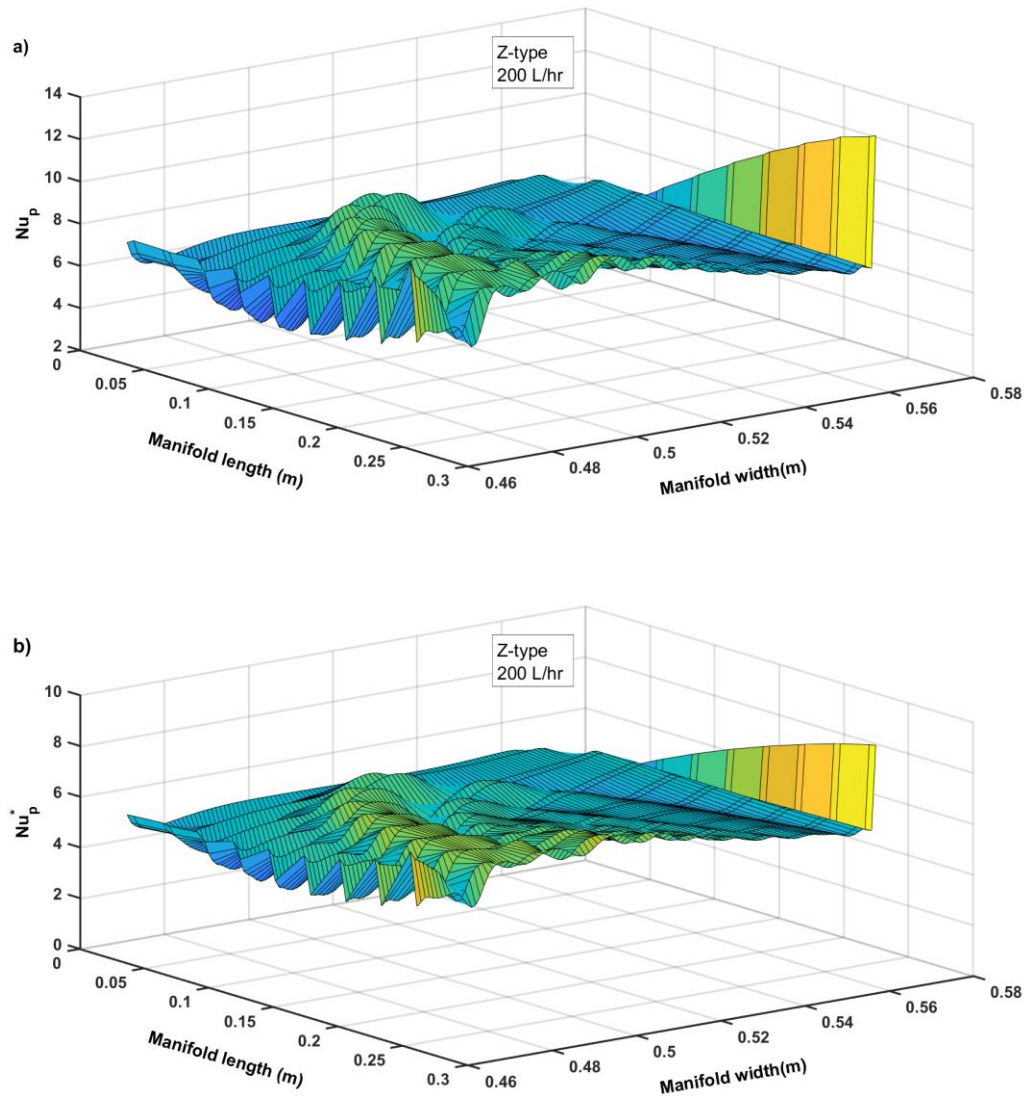


Figure 6.22. The a) Nusselt number and b) Nusselt number star for the exit manifold.

Z- type and 200 L/hr.

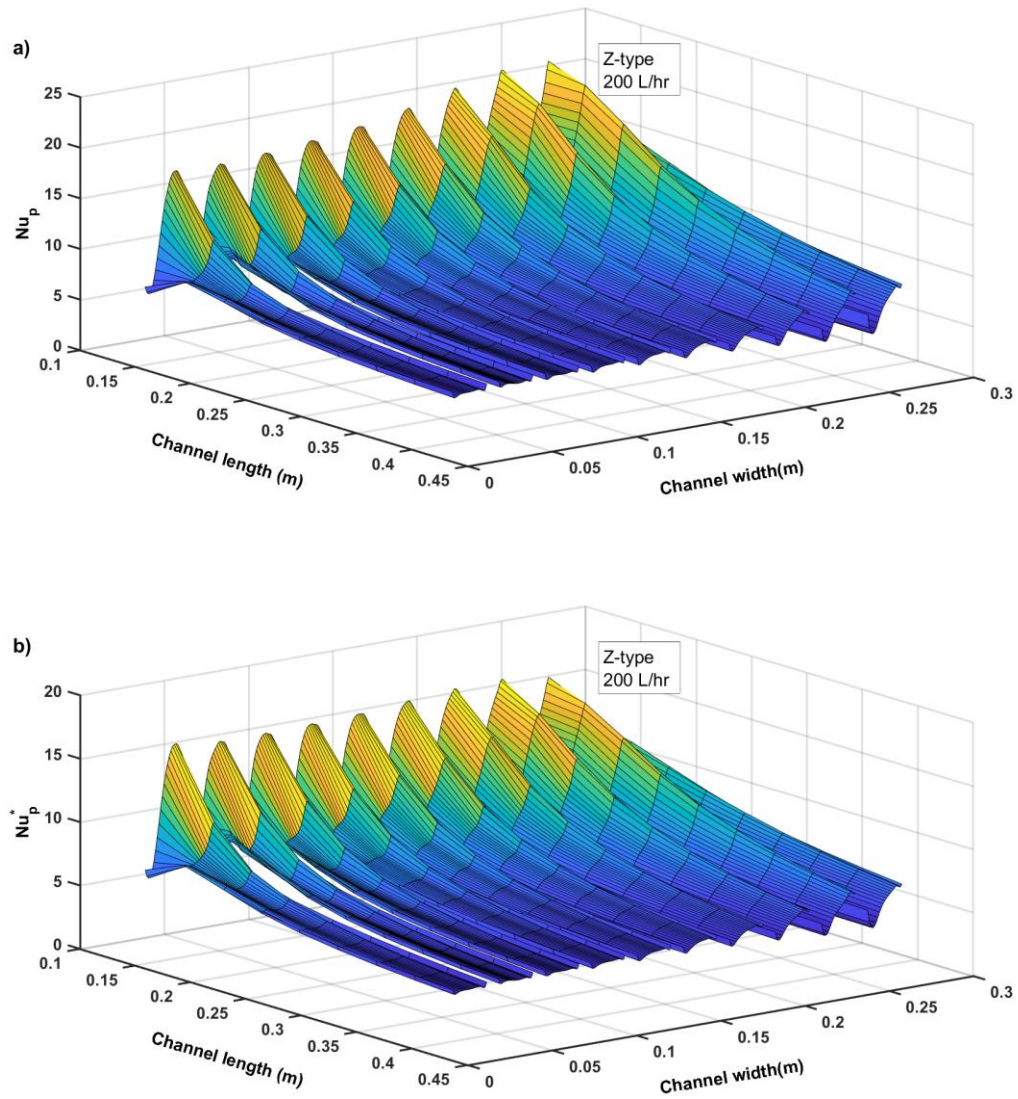


Figure 6.23. The a) Nusselt number and b) Nusselt number star for the channels. Z-type and 200 L/hr.

6.3.3 Calculation procedures of mean and surface temperatures.

To demonstrate the utility of Nusselt number and Nusselt number star, an example is presented here. The values of the surface plots in the previous sections are listed in table and a comparison is giving between the actual numerical values and the calculated values of the surface temperature and mean temperatures.

Table 6.3 shows the numerical values for the mean wall temperature and the mean cross-sectional temperature in the channels. These values are required when a heat exchanger is to be designed. To demonstrate the utility of the Nusselt number and Nusselt number star for this objective, Table 6.4 lists their numerically calculated values of these parameters.

Now based on Eq.(6.2), the wall temperature is calculated, while the mean temperature is calculated from Eq.(6.1). These calculated values are listed in Table 6.5 by comparing the values in Table 6.3 and Table 6.5, we can see that excellent calculations are possible from this method.

Table 6.3. The mean wall and cross-sectional temperature, U-type narrow manifold and 100 L/hr.

Mean Wall temperature (K)										
Channel position (m)	ch1	ch2	ch3	ch4	ch5	ch6	ch7	ch8	ch9	ch10
0.03	298.43	298.51	298.59	298.64	298.73	298.91	299.10	299.34	299.89	301.75
0.08	298.69	298.75	298.91	299.11	299.42	299.87	300.28	300.65	301.10	302.35
0.13	298.87	299.02	299.21	299.52	300.01	300.54	301.00	301.41	301.83	302.95
0.18	299.02	299.22	299.47	299.91	300.47	301.03	301.53	302.00	302.44	303.51
0.24	299.12	299.37	299.69	300.23	300.83	301.43	301.98	302.50	302.99	304.05
0.29	299.19	299.48	299.88	300.49	301.13	301.78	302.38	302.96	303.51	304.58
0.34	299.24	299.57	300.03	300.71	301.40	302.09	302.75	303.40	304.01	305.11
0.39	299.29	299.64	300.17	300.91	301.64	302.38	303.11	303.83	304.50	305.63
0.45	299.33	299.71	300.29	301.09	301.86	302.66	303.45	304.24	304.99	306.15
0.50	299.37	299.76	300.40	301.25	302.07	302.92	303.78	304.65	305.47	306.66
0.55	299.18	299.56	300.34	301.24	302.17	303.23	304.28	305.23	306.04	307.29
Mean cross-sectional temperature (K)										
0.03	298.02	298.02	298.04	298.05	298.08	298.13	298.19	298.25	298.37	299.20
0.08	298.06	298.07	298.09	298.14	298.20	298.32	298.47	298.62	298.83	299.70
0.13	298.07	298.10	298.15	298.23	298.36	298.56	298.78	299.02	299.30	300.22
0.18	298.10	298.14	298.21	298.34	298.53	298.79	299.10	299.42	299.78	300.73
0.24	298.13	298.19	298.28	298.44	298.69	299.03	299.42	299.83	300.26	301.26
0.29	298.17	298.23	298.34	298.55	298.86	299.27	299.74	300.23	300.74	301.78
0.34	298.20	298.27	298.41	298.65	299.02	299.50	300.05	300.63	301.22	302.29
0.39	298.23	298.32	298.48	298.76	299.18	299.74	300.37	301.04	301.70	302.82
0.45	298.26	298.36	298.54	298.86	299.35	299.98	300.69	301.44	302.18	303.33
0.50	298.30	298.40	298.61	298.97	299.51	300.22	301.00	301.84	302.65	303.84
0.55	298.33	298.45	298.67	299.06	299.66	300.43	301.31	302.22	303.11	304.34

Table 6.4. The Nusselt number and Nusselt number star, U-type narrow manifold and 100 L/hr.

Nusselt number										
Channel position (m)	ch1	ch2	ch3	ch4	ch5	ch6	ch7	ch8	ch9	ch10
0.03	35.22	31.13	27.66	25.59	22.52	18.64	16.34	14.10	10.29	9.46
0.08	26.53	23.67	19.34	15.61	12.20	9.55	8.10	7.26	6.57	7.13
0.13	18.85	16.26	13.95	11.44	8.92	7.35	6.53	6.04	5.74	6.23
0.18	16.34	13.84	11.74	9.36	7.54	6.49	5.91	5.57	5.40	5.84
0.24	15.05	12.59	10.45	8.26	6.85	6.05	5.61	5.36	5.25	5.67
0.29	14.35	11.86	9.62	7.60	6.43	5.78	5.43	5.23	5.15	5.54
0.34	13.95	11.42	9.07	7.16	6.14	5.60	5.31	5.15	5.09	5.45
0.39	13.72	11.14	8.69	6.85	5.95	5.49	5.25	5.12	5.08	5.42
0.45	13.56	10.94	8.41	6.62	5.81	5.40	5.20	5.09	5.05	5.38
0.50	13.47	10.80	8.20	6.44	5.70	5.35	5.17	5.09	5.06	5.39
0.55	16.55	12.76	8.45	6.49	5.59	5.05	4.81	4.75	4.84	5.05
Nusselt number star										
0.03	33.78	29.25	25.52	23.02	19.68	15.75	13.16	10.97	7.83	4.01
0.08	23.26	20.61	16.58	13.21	10.18	7.68	6.25	5.36	4.59	3.27
0.13	16.96	14.29	11.93	9.43	7.07	5.56	4.67	4.09	3.63	2.84
0.18	14.36	11.87	9.74	7.45	5.71	4.62	3.93	3.47	3.11	2.53
0.24	12.91	10.53	8.44	6.37	4.96	4.06	3.48	3.07	2.76	2.29
0.29	12.04	9.68	7.58	5.68	4.47	3.68	3.15	2.77	2.49	2.10
0.34	11.43	9.10	6.97	5.20	4.11	3.39	2.90	2.54	2.28	1.94
0.39	10.97	8.65	6.51	4.83	3.83	3.16	2.69	2.36	2.11	1.80
0.45	10.58	8.29	6.15	4.54	3.60	2.96	2.52	2.20	1.96	1.69
0.50	10.26	7.99	5.86	4.30	3.41	2.80	2.38	2.06	1.83	1.59
0.55	11.76	8.92	5.91	4.27	3.30	2.63	2.19	1.90	1.70	1.48

Table 6.5. The calculated values of mean wall and cross-sectional temperature, U-type narrow manifold and 100 L/hr.

Wall temperature computed from the Nusselt number star										
Channel position (m)	ch1	ch2	ch3	ch4	ch5	ch6	ch7	ch8	ch9	ch10
0.03	298.40	298.47	298.53	298.59	298.69	298.87	299.04	299.24	299.74	301.40
0.08	298.59	298.66	298.82	299.03	299.34	299.78	300.18	300.54	300.97	302.17
0.13	298.80	298.95	299.14	299.45	299.93	300.46	300.92	301.34	301.76	302.81
0.18	298.95	299.15	299.40	299.83	300.39	300.95	301.47	301.94	302.38	303.40
0.24	299.06	299.30	299.62	300.14	300.75	301.36	301.92	302.45	302.94	303.96
0.29	299.13	299.41	299.80	300.40	301.05	301.71	302.33	302.92	303.47	304.50
0.34	299.19	299.50	299.96	300.63	301.32	302.03	302.71	303.36	303.98	305.04
0.39	299.24	299.58	300.09	300.82	301.57	302.32	303.06	303.79	304.48	305.57
0.45	299.29	299.65	300.22	301.01	301.79	302.60	303.41	304.21	304.97	306.10
0.50	299.33	299.71	300.33	301.17	302.01	302.87	303.74	304.62	305.45	306.61
0.55	299.16	299.53	300.31	301.20	302.14	303.20	304.23	305.19	306.01	307.25
Mean cross-sectional temperature calculated from the Nusselt number										
0.03	298.02	298.03	298.04	298.06	298.09	298.13	298.20	298.28	298.42	299.96
0.08	298.07	298.09	298.12	298.16	298.22	298.35	298.50	298.66	298.90	300.25
0.13	298.08	298.12	298.17	298.26	298.40	298.60	298.83	299.08	299.38	300.61
0.18	298.12	298.16	298.24	298.37	298.58	298.85	299.16	299.49	299.86	301.06
0.24	298.15	298.21	298.31	298.49	298.76	299.10	299.49	299.90	300.35	301.55
0.29	298.18	298.26	298.38	298.61	298.93	299.35	299.81	300.31	300.82	302.04
0.34	298.22	298.31	298.45	298.72	299.10	299.59	300.14	300.71	301.30	302.54
0.39	298.25	298.35	298.52	298.83	299.27	299.84	300.46	301.13	301.79	303.05
0.45	298.28	298.40	298.59	298.94	299.44	300.08	300.78	301.53	302.27	303.56
0.50	298.32	298.44	298.66	299.06	299.61	300.32	301.11	301.94	302.75	304.08
0.55	298.34	298.46	298.70	299.10	299.70	300.50	301.40	302.32	303.20	304.55

6.4 Chilton- Colburn analogy for the heat exchanger.

The Chilton- Colburn analogy has been discussed and evaluated in the Chapter 5, where it has been seen that there can exist significant differences between the Stanton number and the half of skin friction coefficient. In this section, the same analogy is evaluated and discussed in detail for the U-type and Z-type normal manifold width for flow rate of 100 L/hr.

6.4.1 U-Type

Table 6.6 presents the listed values of the Stanton number and the half of skin friction factor, for all the 10 channels. The channel is divided with multiple cross-sections presented as channel position. It can be seen from the ratio values, that the maximum difference of 10 is observed for the middle channels and the minimum is for the last channel. Figure 6.24 shows the actual comparison for the listed data. They grey line shows the exact analogy, showing that the Stanton numbers are higher for all the cases in comparison with the half skin friction. Due to higher Prandtl number, the thermal boundary layer is expected to be 7 times that of the hydrodynamic boundary layer. This trend is visible in the figure, where most of the data is present vertically, with the change in skin friction much less in comparison to the Stanton number. It might be possible that if longer channels are used, that ensure fully developed thermal boundary layer, better comparisons may exist for the analogy.

Similarly, the inlet and exit manifolds are analyzed. By reviewing the data listed in Table 6.7, it can be seen that the inlet section ratio begins from 7 and decreases to 2.5, while for the exit section, it is higher towards the exit section as the velocity in this region increases. Figure 6.25 shows the graphical representation of the data shown in the table. It can be seen that the inlet section has a smooth profile and decreases with the minimum value of ratio being 2.5. In comparison, the exit section shows fluctuations. This is attributed to the fact that the later channels are having less velocity, while the initial channels have higher velocity. This flow when enters the exit manifold, it creates disturbance, that increase as the flow moves towards the outlet. It can be concluded that the analogies can be fitter for the inlet section and channels, but at the exit section, there is no particular trend visible.

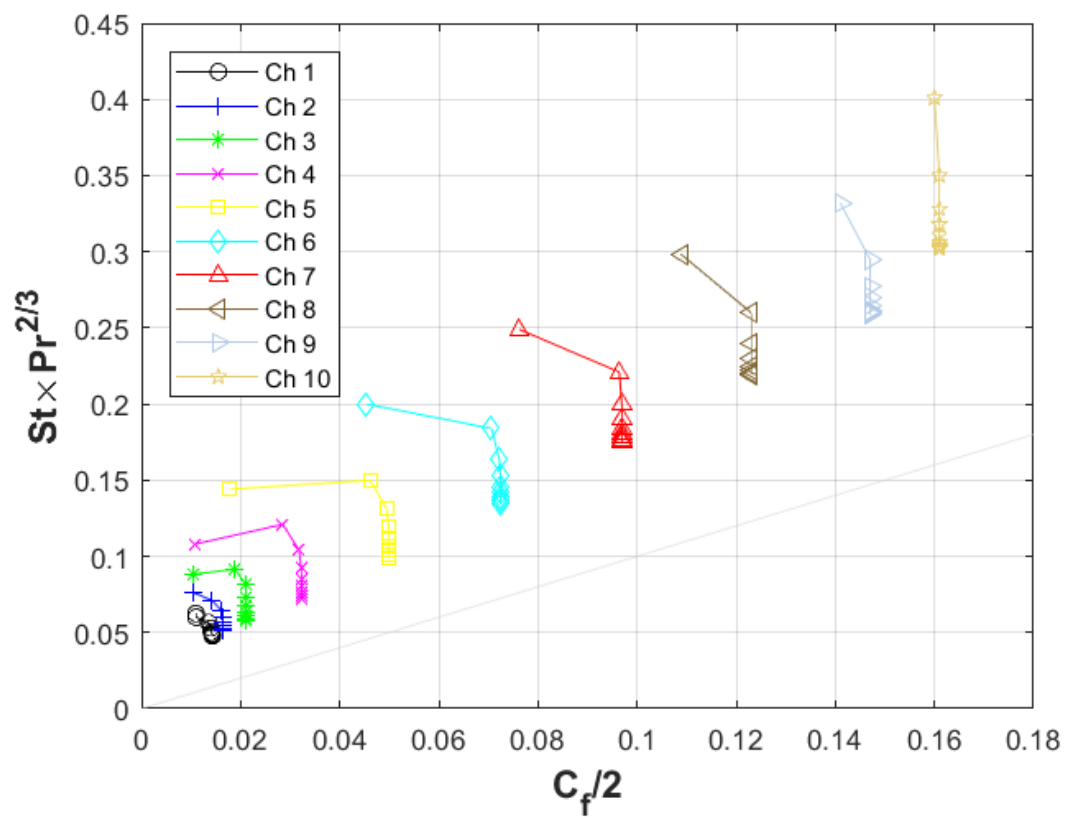


Figure 6.24. The comparison of $St \times Pr^{2/3}$ and $C_f/2$ for the channels of U-type normal manifold and 100 L/hr.

Table 6.6. The data for the assessment of Chilton-Colburn analogy for the channels in U-type narrow manifold.

$St \times Pr^{2/3}$										
Channel position (m)	ch1	ch2	ch3	ch4	ch5	ch6	ch7	ch8	ch9	ch10
0.03	2.93E-03	3.02E-03	3.21E-03	3.69E-03	4.55E-03	5.92E-03	7.83E-03	9.97E-03	1.25E-02	2.50E-02
0.08	3.38E-03	4.11E-03	4.78E-03	5.87E-03	7.78E-03	1.08E-02	1.35E-02	1.61E-02	1.80E-02	2.17E-02
0.13	3.25E-03	3.85E-03	4.95E-03	6.55E-03	8.14E-03	9.96E-03	1.19E-02	1.40E-02	1.59E-02	1.89E-02
0.18	3.05E-03	3.50E-03	4.41E-03	5.62E-03	7.08E-03	8.87E-03	1.08E-02	1.30E-02	1.50E-02	1.78E-02
0.24	2.86E-03	3.22E-03	3.96E-03	5.00E-03	6.46E-03	8.28E-03	1.03E-02	1.25E-02	1.46E-02	1.72E-02
0.29	2.74E-03	3.05E-03	3.65E-03	4.61E-03	6.07E-03	7.91E-03	9.95E-03	1.22E-02	1.43E-02	1.68E-02
0.34	2.67E-03	2.94E-03	3.44E-03	4.34E-03	5.80E-03	7.66E-03	9.74E-03	1.20E-02	1.41E-02	1.66E-02
0.39	2.63E-03	2.86E-03	3.30E-03	4.16E-03	5.62E-03	7.51E-03	9.62E-03	1.19E-02	1.41E-02	1.65E-02
0.45	2.60E-03	2.81E-03	3.19E-03	4.02E-03	5.48E-03	7.39E-03	9.53E-03	1.19E-02	1.40E-02	1.64E-02
0.50	2.58E-03	2.78E-03	3.11E-03	3.91E-03	5.38E-03	7.32E-03	9.49E-03	1.18E-02	1.40E-02	1.64E-02
0.55	2.04E-03	1.99E-03	1.92E-03	2.22E-03	2.83E-03	3.62E-03	4.72E-03	6.42E-03	9.31E-03	1.42E-02
Half skin friction factor										
0.03	1.05E-02	1.11E-02	1.29E-02	1.61E-02	2.13E-02	2.89E-02	3.35E-02	4.14E-02	6.40E-02	1.64E-01
0.08	1.10E-02	1.06E-02	1.04E-02	1.08E-02	1.78E-02	4.54E-02	7.62E-02	1.09E-01	1.41E-01	1.60E-01
0.13	1.10E-02	1.42E-02	1.88E-02	2.85E-02	4.61E-02	7.06E-02	9.64E-02	1.23E-01	1.47E-01	1.61E-01
0.18	1.35E-02	1.61E-02	2.11E-02	3.18E-02	4.95E-02	7.22E-02	9.69E-02	1.23E-01	1.47E-01	1.61E-01
0.24	1.40E-02	1.63E-02	2.12E-02	3.22E-02	4.99E-02	7.24E-02	9.69E-02	1.23E-01	1.47E-01	1.61E-01
0.29	1.41E-02	1.63E-02	2.12E-02	3.23E-02	5.00E-02	7.24E-02	9.69E-02	1.23E-01	1.47E-01	1.61E-01
0.34	1.42E-02	1.63E-02	2.11E-02	3.23E-02	5.00E-02	7.24E-02	9.69E-02	1.23E-01	1.47E-01	1.61E-01
0.39	1.43E-02	1.64E-02	2.11E-02	3.23E-02	5.00E-02	7.24E-02	9.69E-02	1.23E-01	1.47E-01	1.61E-01
0.45	1.43E-02	1.64E-02	2.11E-02	3.23E-02	5.00E-02	7.24E-02	9.69E-02	1.23E-01	1.47E-01	1.61E-01
0.50	1.43E-02	1.64E-02	2.11E-02	3.23E-02	5.00E-02	7.24E-02	9.69E-02	1.23E-01	1.47E-01	1.61E-01
0.55	1.01E-02	1.18E-02	1.58E-02	2.16E-02	2.92E-02	3.88E-02	5.13E-02	6.90E-02	9.85E-02	1.49E-01
$St \times Pr^{2/3}/C_f/2$										
0.03	5.68	7.18	8.47	10.03	8.06	4.41	3.27	2.72	2.35	2.50
0.08	5.45	5.01	4.86	4.25	3.26	2.61	2.29	2.11	2.01	2.18
0.13	4.18	4.02	3.87	3.27	2.64	2.27	2.07	1.95	1.89	2.04
0.18	3.78	3.66	3.45	2.87	2.39	2.12	1.96	1.87	1.84	1.98
0.24	3.58	3.45	3.19	2.64	2.24	2.02	1.90	1.83	1.80	1.94
0.29	3.47	3.32	3.01	2.48	2.14	1.96	1.86	1.80	1.78	1.91
0.34	3.41	3.23	2.89	2.38	2.08	1.92	1.83	1.79	1.78	1.90
0.39	3.36	3.18	2.80	2.29	2.03	1.89	1.82	1.78	1.77	1.88
0.45	3.34	3.14	2.73	2.23	1.99	1.87	1.81	1.78	1.77	1.89
0.50	5.68	7.18	8.47	10.03	8.06	4.41	3.27	2.72	2.35	2.50
0.55	5.45	5.01	4.86	4.25	3.26	2.61	2.29	2.11	2.01	2.18

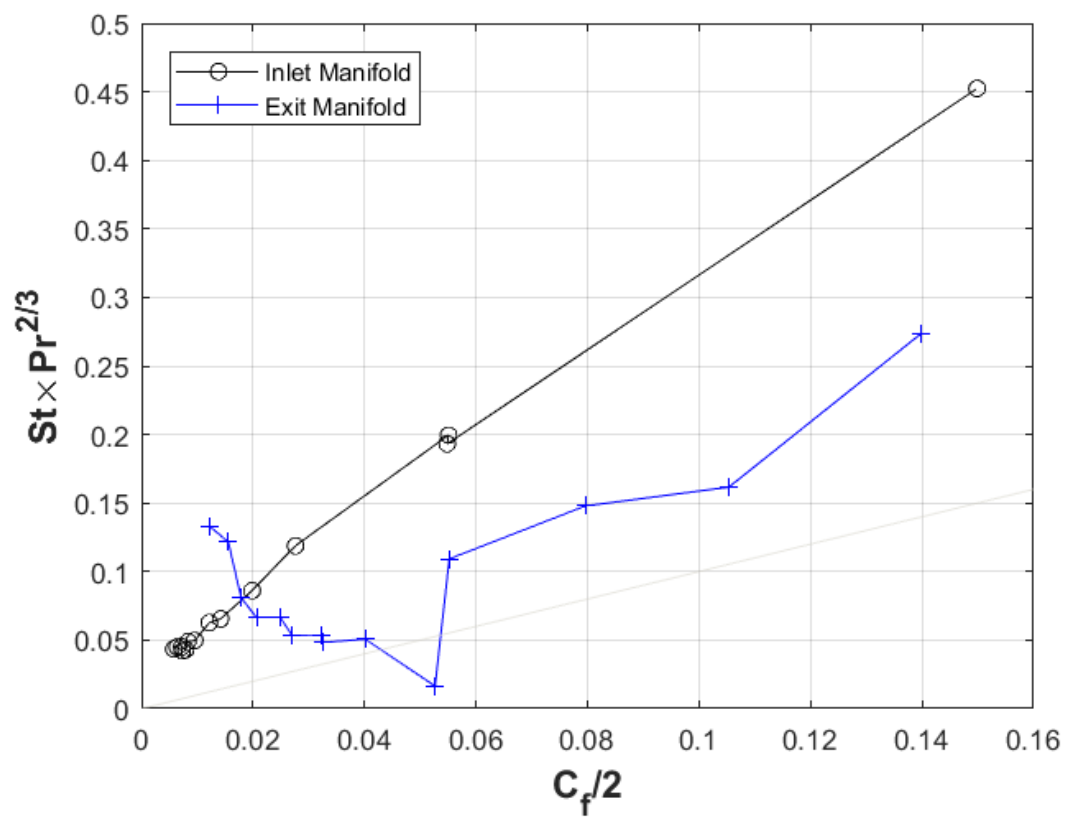


Figure 6.25. The comparison of $St \times Pr^{2/3}$ and $C_f/2$ for the inlet and exit manifold sections of the U-type narrow manifold and 100 L/hr.

Table 6.7. The data for the assessment of Chilton-Colburn analogy for the U-type narrow manifold.

Inlet manifold			Exit manifold		
$St \times Pr^{2/3}$	$C_i/2$	$\frac{St \times Pr^{2/3}}{C_f/2}$	$St \times Pr^{2/3}$	$C_i/2$	$\frac{St \times Pr^{2/3}}{C_f/2}$
4.34E-02	5.80E-03	7.50	1.33E-01	1.22E-02	10.94
4.49E-02	6.40E-03	7.01	1.21E-01	1.56E-02	7.80
4.21E-02	7.31E-03	5.76	8.10E-02	1.79E-02	4.53
4.50E-02	7.22E-03	6.23	6.63E-02	2.06E-02	3.21
4.30E-02	7.91E-03	5.44	6.70E-02	2.48E-02	2.70
4.90E-02	8.35E-03	5.87	5.36E-02	2.70E-02	1.99
4.96E-02	9.55E-03	5.20	5.29E-02	3.22E-02	1.64
6.27E-02	1.22E-02	5.15	4.84E-02	3.27E-02	1.48
6.55E-02	1.42E-02	4.62	5.07E-02	4.01E-02	1.26
8.62E-02	1.99E-02	4.34	1.64E-02	5.27E-02	0.31
1.19E-01	2.76E-02	4.30	1.09E-01	5.52E-02	1.98
2.00E-01	5.51E-02	3.62	1.48E-01	7.96E-02	1.86
1.93E-01	5.48E-02	3.52	1.62E-01	1.05E-01	1.53
4.52E-01	1.50E-01	3.02	2.74E-01	1.40E-01	1.96
3.38E-01	1.31E-01	2.58	2.72E-01	1.69E-01	1.61

6.4.2 Z-Type

Similar to the U-type arrangement, Table 6.8 presents the values of the Stanton number and half skin friction coefficient for the channels. It can be seen that for all cases, as we progress in the channels, the value of the ratio is decreasing which is in correspondence with the thermal developing profile. Near the exit the ratio is still around 2, indicating the $St \times Pr^{2/3}$ values are about double that of the $C_f/2$. Another interesting trend can be noticed that the ratio is decreasing from channel 1 to the middle channels 5-6 and then again increases. This is contrary to what was seen for the U-type. The reason for this behavior is that the velocity profiles are not the same for both types. Specially for the Z type the velocity is more in the last channels while for U-type it was more for the initial channels. Figure 6.26 shows these trends in visual form. The same observation can be seen that the middle channels have the highest ratio seen as yellow line in the figure. In addition, we can see that the expected trend of unity ratio is shown as grey color and again we see higher values for the $St \times Pr^{2/3}$ in comparison $C_f/2$. The vertical behaviors show the slow development of the thermal boundary layer in comparison the hydrodynamic boundary layer.

With regards to the inlet and exit manifold sections, it can be seen from Figure 6.27 that the Inlet section variation are much smaller in comparison to the exit manifold. The interesting point to be noted from this figure is that the analogy for the exit section is lying almost around the grey line which is the expected trend for true Chilton-Coulburn analogy. With regards to the inlet section, the difference is still large from the exact analogy. The

detailed values are listed in the Table 6.9, where it can be seen that the ratio is about 5 times for the inlet section, remaining almost constant for the whole length of the section. In addition, it can be see that the ratio for the exit section is around 1.2 for which is much closer to the other cases discussed so far.

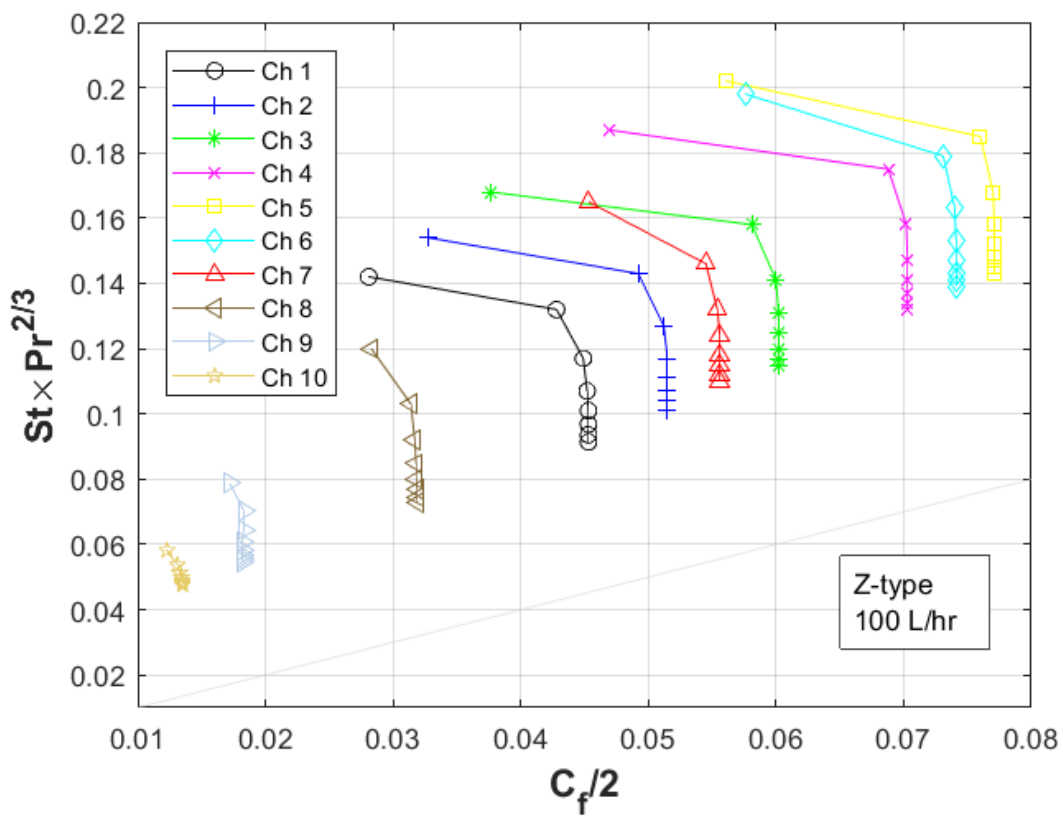


Figure 6.26. The comparison of $St \times Pr^{2/3}$ and $C_f/2$ for the channels of Z-type normal manifold and 100 L/hr.

Table 6.8. The data for the assessment of Chilton-Colburn analogy for the channels in Z-type narrow manifold.

Channel position (m)	$St \times Pr^{2/3}$									
	ch1	ch2	ch3	ch4	ch5	ch6	ch7	ch8	ch9	ch10
0.03	8.33E-02	7.83E-02	8.11E-02	8.55E-02	8.88E-02	8.68E-02	7.76E-02	6.61E-02	5.75E-02	5.75E-02
0.08	1.03E-01	1.13E-01	1.22E-01	1.32E-01	1.39E-01	1.40E-01	1.30E-01	1.07E-01	8.30E-02	6.76E-02
0.13	1.42E-01	1.54E-01	1.68E-01	1.87E-01	2.02E-01	1.98E-01	1.65E-01	1.20E-01	7.88E-02	5.82E-02
0.18	1.32E-01	1.43E-01	1.58E-01	1.75E-01	1.85E-01	1.79E-01	1.46E-01	1.03E-01	7.04E-02	5.37E-02
0.24	1.17E-01	1.27E-01	1.41E-01	1.58E-01	1.68E-01	1.63E-01	1.32E-01	9.19E-02	6.45E-02	5.13E-02
0.29	1.07E-01	1.17E-01	1.31E-01	1.47E-01	1.58E-01	1.53E-01	1.24E-01	8.48E-02	6.08E-02	4.99E-02
0.34	1.01E-01	1.11E-01	1.25E-01	1.41E-01	1.52E-01	1.47E-01	1.18E-01	8.01E-02	5.83E-02	4.89E-02
0.39	9.68E-02	1.07E-01	1.20E-01	1.37E-01	1.48E-01	1.43E-01	1.15E-01	7.69E-02	5.67E-02	4.83E-02
0.45	9.36E-02	1.04E-01	1.17E-01	1.34E-01	1.45E-01	1.41E-01	1.12E-01	7.46E-02	5.56E-02	4.79E-02
0.50	9.14E-02	1.01E-01	1.15E-01	1.32E-01	1.43E-01	1.39E-01	1.10E-01	7.28E-02	5.48E-02	4.76E-02
0.55	8.14E-02	7.01E-02	6.50E-02	6.01E-02	5.42E-02	4.76E-02	4.14E-02	3.54E-02	3.21E-02	3.26E-02
Channel position (m)	Half skin friction factor									
	ch1	ch2	ch3	ch4	ch5	ch6	ch7	ch8	ch9	ch10
0.03	2.11E-02	2.05E-02	2.22E-02	2.43E-02	2.58E-02	2.52E-02	2.18E-02	1.69E-02	1.32E-02	1.35E-02
0.08	1.31E-02	1.49E-02	1.71E-02	1.91E-02	1.97E-02	1.86E-02	1.47E-02	1.04E-02	1.05E-02	1.10E-02
0.13	2.81E-02	3.27E-02	3.76E-02	4.69E-02	5.61E-02	5.76E-02	4.53E-02	2.83E-02	1.72E-02	1.23E-02
0.18	4.28E-02	4.92E-02	5.81E-02	6.88E-02	7.60E-02	7.31E-02	5.45E-02	3.14E-02	1.83E-02	1.31E-02
0.24	4.49E-02	5.12E-02	6.00E-02	7.02E-02	7.70E-02	7.40E-02	5.54E-02	3.17E-02	1.83E-02	1.33E-02
0.29	4.52E-02	5.15E-02	6.02E-02	7.03E-02	7.71E-02	7.41E-02	5.56E-02	3.18E-02	1.82E-02	1.34E-02
0.34	4.53E-02	5.15E-02	6.02E-02	7.03E-02	7.71E-02	7.41E-02	5.56E-02	3.18E-02	1.82E-02	1.35E-02
0.39	4.53E-02	5.15E-02	6.02E-02	7.03E-02	7.71E-02	7.41E-02	5.56E-02	3.19E-02	1.82E-02	1.35E-02
0.45	4.53E-02	5.15E-02	6.02E-02	7.03E-02	7.71E-02	7.41E-02	5.56E-02	3.19E-02	1.82E-02	1.35E-02
0.50	4.53E-02	5.15E-02	6.02E-02	7.03E-02	7.71E-02	7.41E-02	5.56E-02	3.19E-02	1.82E-02	1.35E-02
0.55	4.29E-02	3.80E-02	3.33E-02	2.91E-02	2.60E-02	2.38E-02	2.11E-02	1.74E-02	1.28E-02	9.49E-03
Channel position (m)	$St \times Pr^{2/3} / C_f / 2$									
	ch1	ch2	ch3	ch4	ch5	ch6	ch7	ch8	ch9	ch10
0.03	3.95	3.82	3.65	3.52	3.44	3.45	3.57	3.91	4.35	4.24
0.08	7.91	7.56	7.15	6.93	7.07	7.52	8.79	10.26	7.87	6.17
0.13	5.06	4.70	4.46	4.00	3.61	3.44	3.64	4.25	4.57	4.75
0.18	3.09	2.90	2.72	2.55	2.44	2.44	2.67	3.29	3.85	4.11
0.24	2.61	2.48	2.36	2.25	2.18	2.20	2.38	2.89	3.53	3.85
0.29	2.37	2.28	2.18	2.10	2.05	2.07	2.23	2.66	3.33	3.71
0.34	2.23	2.15	2.07	2.00	1.97	1.99	2.13	2.52	3.20	3.63
0.39	2.13	2.07	2.00	1.94	1.91	1.94	2.06	2.42	3.11	3.58
0.45	2.06	2.01	1.95	1.90	1.88	1.90	2.02	2.34	3.05	3.55
0.50	2.01	1.97	1.91	1.88	1.86	1.88	1.98	2.28	3.00	3.53
0.55	1.90	1.84	1.95	2.07	2.08	2.00	1.96	2.04	2.51	3.44

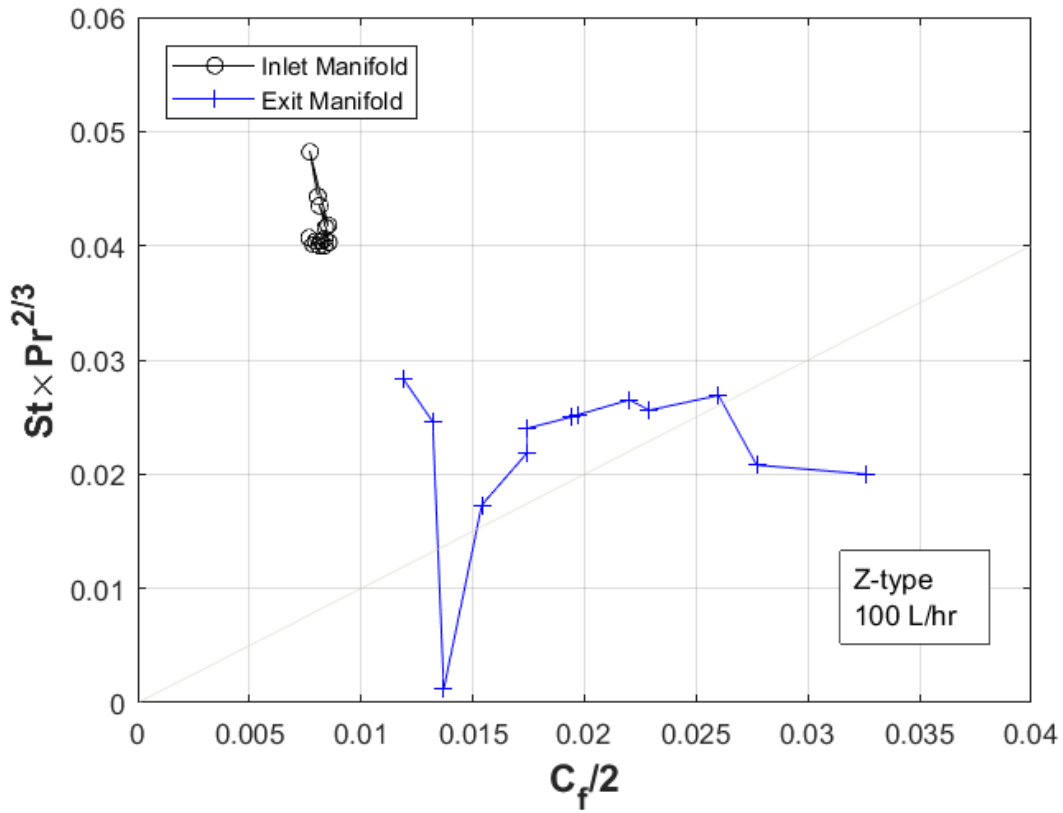


Figure 6.27. The comparison of $St \times Pr^{2/3}$ and $C_f/2$ for the inlet and exit manifold sections of the Z-type narrow manifold and 100 L/hr.

Table 6.9. The data for the assessment of Chilton-Colburn analogy for the Z-type narrow manifold.

Inlet manifold			Exit manifold		
$St \times Pr^{2/3}$	$C_f/2$	$\frac{St \times Pr^{2/3}}{C_f/2}$	$St \times Pr^{2/3}$	$C_f/2$	$\frac{St \times Pr^{2/3}}{C_f/2}$
4.07E-02	7.67E-03	5.30	2.00E-02	3.26E-02	0.61
4.01E-02	7.85E-03	5.11	2.08E-02	2.77E-02	0.75
4.04E-02	7.96E-03	5.08	2.69E-02	2.60E-02	1.03
4.00E-02	8.12E-03	4.92	2.56E-02	2.29E-02	1.12
4.04E-02	8.20E-03	4.93	2.65E-02	2.20E-02	1.21
4.00E-02	8.36E-03	4.79	2.52E-02	1.97E-02	1.28
4.06E-02	8.37E-03	4.85	2.50E-02	1.94E-02	1.29
4.03E-02	8.55E-03	4.71	2.40E-02	1.74E-02	1.38
4.16E-02	8.41E-03	4.95	2.18E-02	1.74E-02	1.26
4.35E-02	8.14E-03	5.34	1.73E-02	1.54E-02	1.13
4.18E-02	8.52E-03	4.90	1.20E-03	1.37E-02	0.09
4.82E-02	7.71E-03	6.25	2.46E-02	1.32E-02	1.86
4.43E-02	8.06E-03	5.49	2.83E-02	1.19E-02	2.39

Chapter 7

FLOW DISTRIBUTION IN CHANNELS –

EXPERIMENTAL AND ANALYTICAL STUDY

This chapter deals with the experimental modelling of the manifold design under consideration. The experiments were conducted for the wider manifold, with results available for both the U- and Z-type design of the manifold. The flow rates considered are 100 L/hr, 200 L/hr, and 300 L/hr corresponding to Reynolds number of 480, 960, and 1440 respectively. Water was used as the carrier fluid with Polyamide as seeding particles. The technique of Particle image velocimetry (PIV) was used to measure the actual velocity in each of the channel.

7.1 Introduction to Particle image velocimetry

Particle image velocimetry (PIV) is the technique, which provides the velocity of fluid in a two-dimensional plane (2D2C). The procedure involves taking snapshots of laser-illuminated suspended particle within the flowing fluid, using one CCD (charge-coupled device) or CMOS (Complementary metal–oxide–semiconductor) camera. The laser light is reflected by the particles, which is captured by the camera placed at right angle to the laser. An illustration for the complete setup for PIV is shown in Figure 7.1, where the basic components are visible. A laser light is illuminating the seeded cross-section whose

velocity is to be measured. The charge coupled camera, CCD, captures the images of particles. These images are analyzed frame by frame to make a correlation to identify their movement. This is present in form of table in numeric values or as vectors as graphical values.

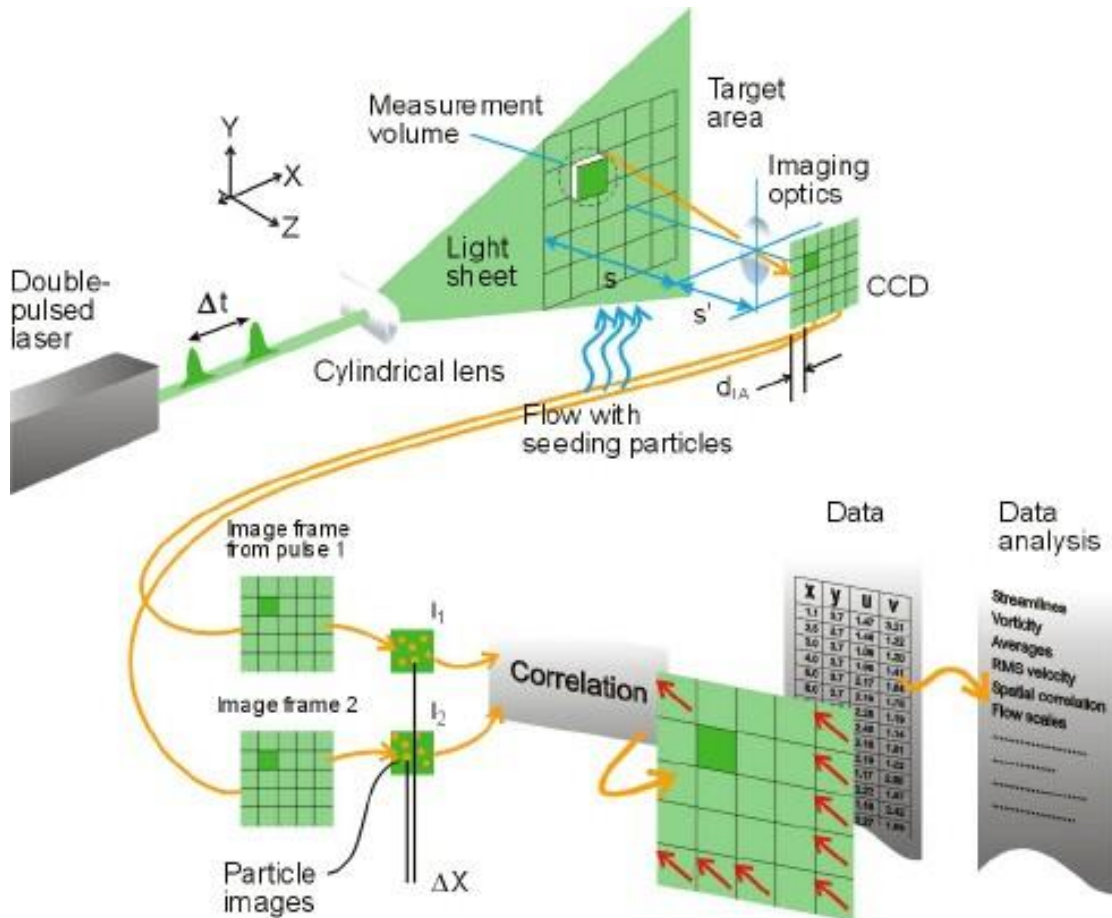


Figure 7.1. The mechanism of 2D2C PIV <https://www.dantecdynamics.com/measurement-principles-of-piv>

7.2 Experimental Setup

The setup is illustrated in Figure 7.2, while the picture of the actual setup can be seen in Figure 7.3. It consists of a submersible pump in a tank filled with particles and water mixture. The flow rate is controlled by means of valves (shown in Figure 7.4), such that any extra flow rate is diverted back to the main tank while maintaining a constant flow rate through the hydraulic circuit. A rotameter is used to measure the flowrate. The rotameter is calibrated by filling a one-liter tank and recording the time it took for each filling.

The flow from rotameter is discharged into another tank, that is elevated from the setup (shown in Figure 7.5). The purpose of this tank is to allow the manifold inlet to be of uniform profile, i.e. the flow from circular pipe is discharging in this tank while the exit is of rectangular shape according to the width and the height of the inlet manifold. This tank has an air vent valve at the top, which allow the tank to be completely filled with water, avoiding splashing and bubble entrainment in the flow. The water level in this tank is kept at a constant level, indicating same inlet and outlet mass flow rate. The vertical fluid head also ensures that the bubbles, if present, keep flowing to the top of this tank, thus ensuring the flow in the manifold is free of bubbles. The manifold itself contains ten channels, allowing the flow to be distributed and then converge in the outlet manifold. At the outlet manifold, provisions are provided such that one outlet is opened and other one sealed to represent an arrangement of Z- or U-type (as shown in Figure 7.6). The camera is installed perpendicular to the top of the domain, while the laser is parallel to the domain, such that the area illuminated by the 2D laser is captured as a 2D image by the camera. An example

is shown in Figure 7.7, where the inlet section of the manifold is illuminated by the laser light and the camera above it is used to capture the images.

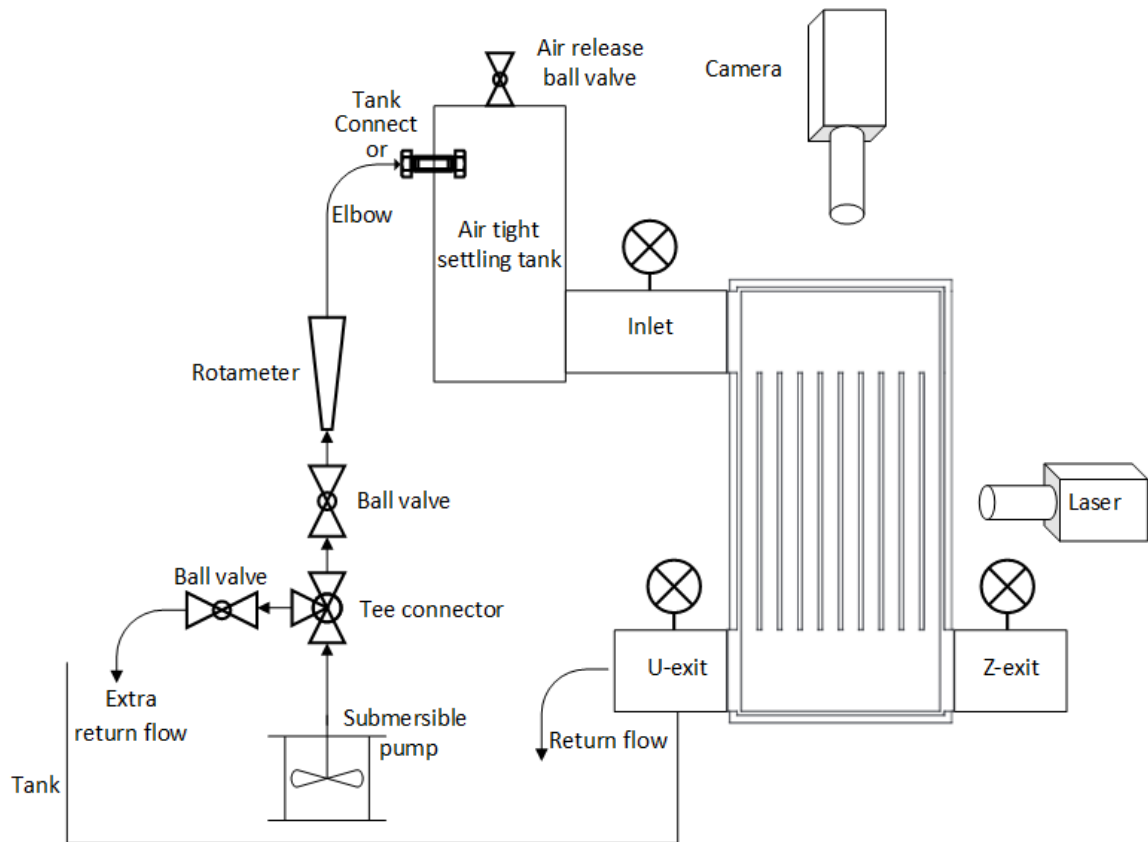


Figure 7.2. Experimental setup for flow distributing manifolds, utilizing PIV.

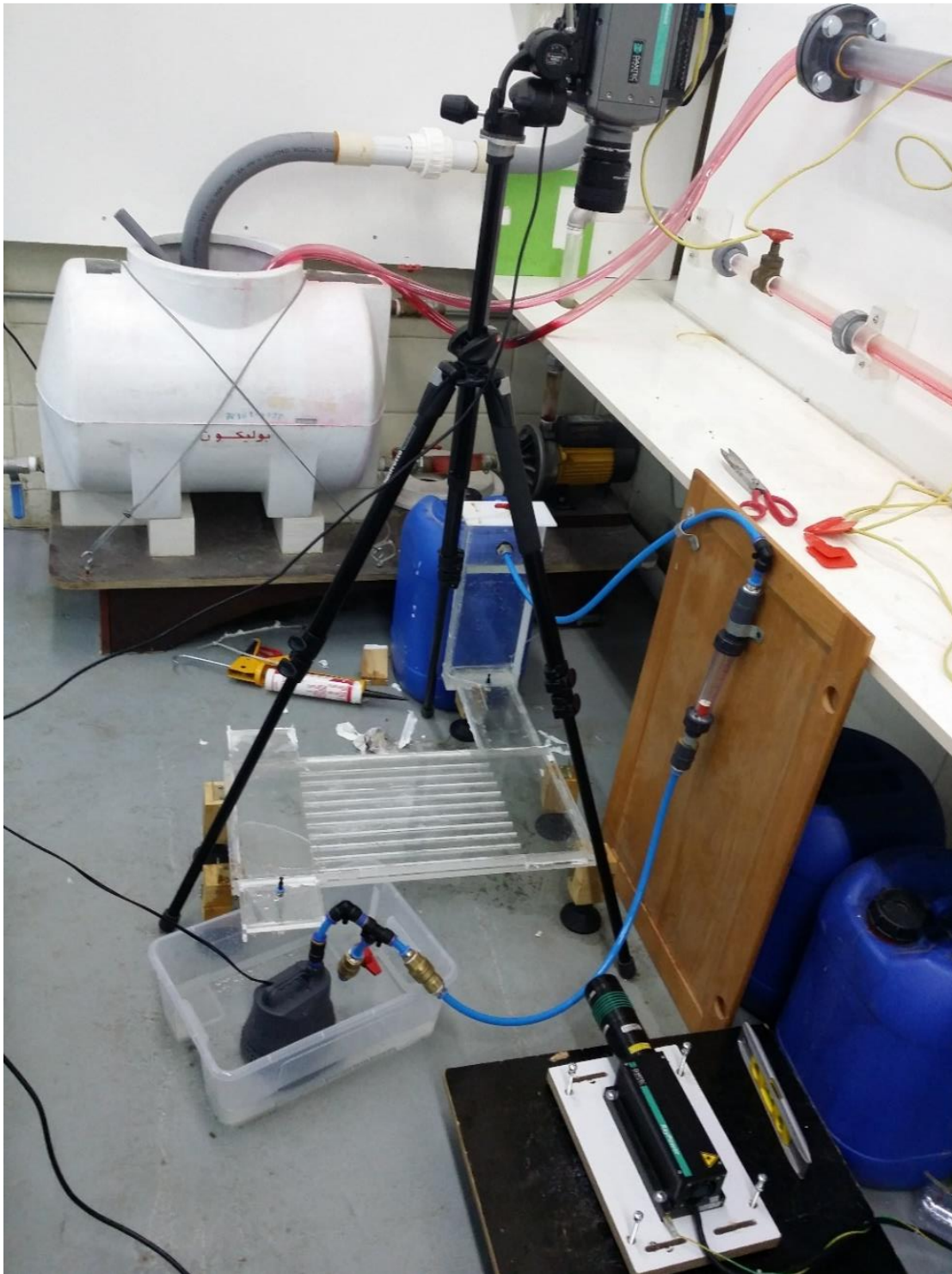


Figure 7.3. The arrangement of manifold, laser, camera, and pump.



Figure 7.4. The pump, and two valve arrangement to control the flow rate.

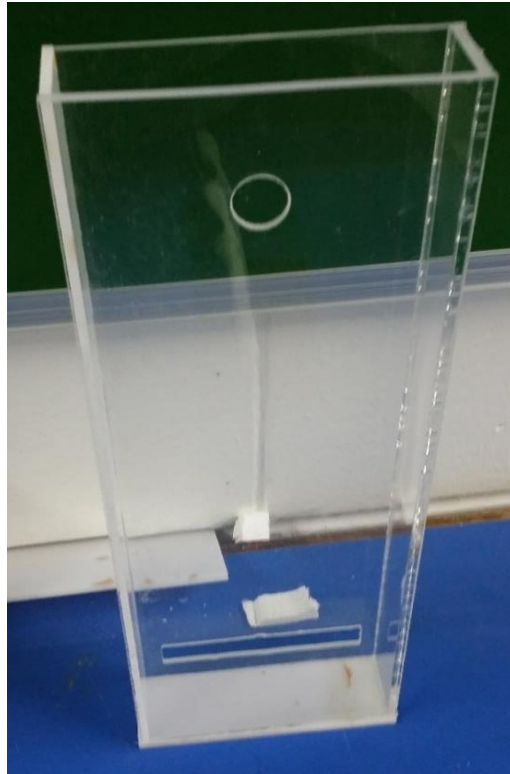


Figure 7.5. The inlet tank, designed to provide uniform inlet condition.

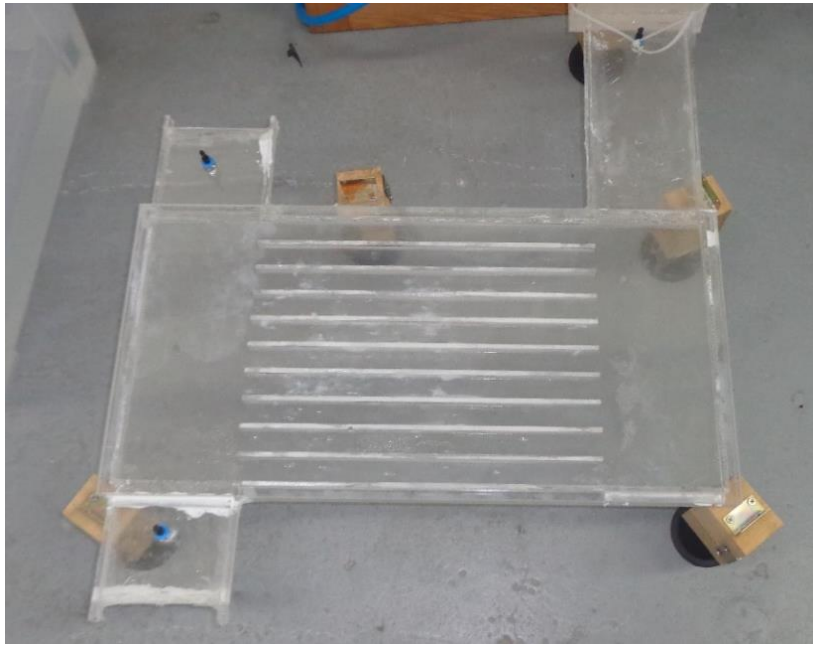


Figure 7.6. The flow distribution system, with options for both Z and U type studies



Figure 7.7. The laser illuminating the inlet section for velocity measurements

The design for the flow distribution manifolds was shown in Figure 6.1. Initially, the manifold was designed to be used in conjunction with a commercially available Photovoltaic panel. The dimension of such panel were 1.427 m by 0.61 m [182]. The manifold is to be designed to provide cooling to the panel. The fabrication was done while keeping a scaling factor of 0.4 such that the scaled down version had the dimensions of 0.570 m by 0.244 m. The velocities were also scaled down based on the principle of geometric similarities[183].

The fabrication process included designing the layout in Solid-works. The inlet is chosen to be 110 mm wide, with the height of the whole domain kept at 5 mm. the channel width is taken to be 22 mm. The design vectors were exported as vectors to Vcarve software used for the CNC machine. The CNC machine (courtesy Fablab, Dhahran) used was ShopBot 96" by 48". A 3 mm CNC tool was used for the purpose of cutting and engraving the plexiglass sheet. (attach figures). 12 mm Plexiglass sheet was used, with 5mm engraving depth. Two copies of the sheet were made to act as the upper and bottom surface, and strips of 15 mm height (5mm for top and bottom, while 5 mm for the flow channel height) were used as spacers to create the baffles or to separate the channels. The design during the CNC operation is shown in Figure 7.8. The sheet was screwed onto the base of the machine, and three passes were used, with depth of about 2 millimeters per pass. Chloroform was used to fuse/weld all the parts together, while placing 5 mm spaces on all sides to ensure the height remains constant. An inlet header was made to ensure that the flow becomes fully developed as it enters the manifold. It was cut using a laser machine and then fused

together. The outlet section was placed to allow the water some distance of travel before dropping in the tank. 5 mm Pressure taps were inserted in those inlet and outlet header to measure the differential pressure using a pressure device. The pump was a typical 220 V submersible pump, that could provide upto 400L/hr of flow rate for the current setup.

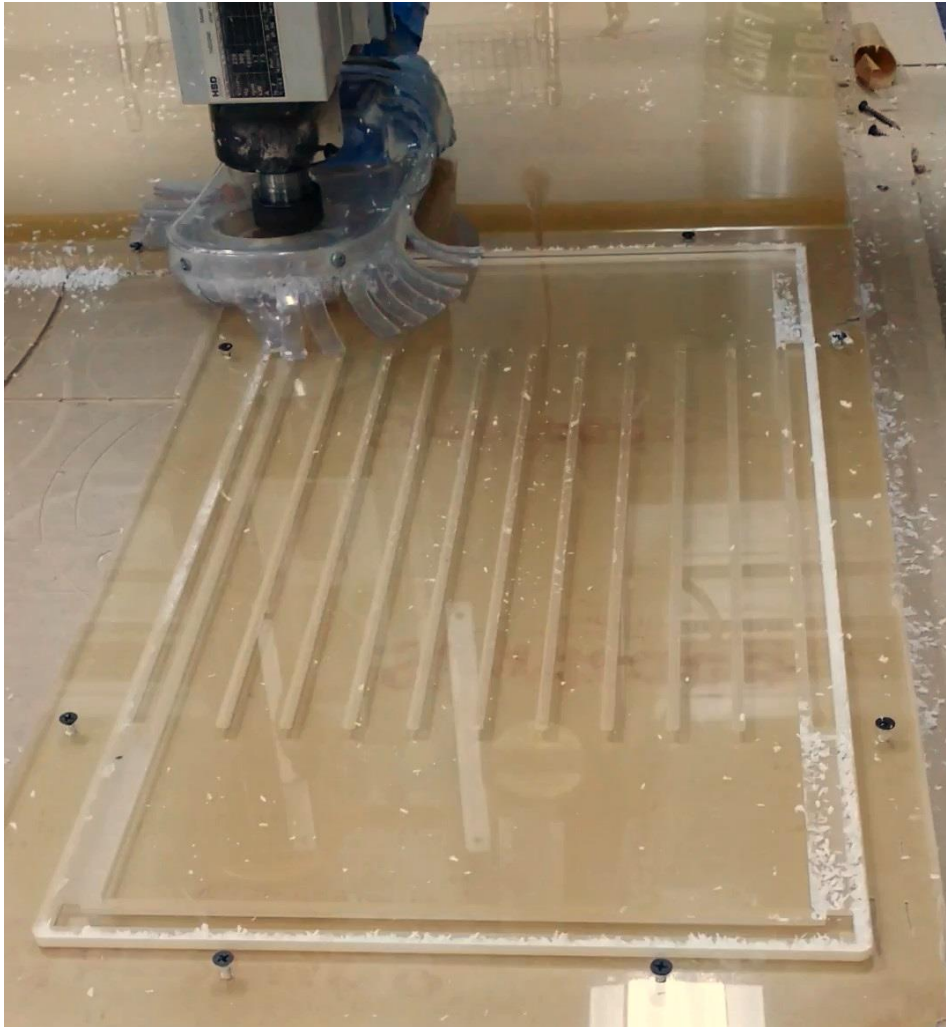


Figure 7.8. The design being cut using the CNC machine, the grooves were be fitted with spacers, to create channels.

The benefit of PIV over other velocity measuring methods is its non-intrusive nature, and there is no disturbance to the flow due to the presence of any probe for measurements. The limitation was that the design has to be made with transparent material so that laser light can pass and the camera can take picture of the flowing particles. The methods measure instantaneous velocity of each particle in view of the images taken by the camera. It is also an indirect measurement of fluid flow, as the fluid itself is not visible, rather the seeding particles are used for velocity measurements. It is important to ensure that the density of the seeding particles is close to that of water and their size is small enough to ensure they follow with the fluid,

7.3 Components of PIV system:

The components of PIV system are listed below, with more detail after the list.

1. Transparent walled fluid flow
2. Seeding particles (oil drops - $1\mu\text{m}$ to $5\mu\text{m}$) for air and hollow glass spheres, polystyrene or polyamide $5\mu\text{m}$ to $100\mu\text{m}$)
3. Two-Dimensional laser beam to illuminate the flow area
4. High speed camera to capture the movement of illuminated particles.
5. The software to analyses the images.

The PIV divides the target flow area into sub-sections, with the distance covered measured directly from the particles and the time is based on the frequency of images, such that the velocity of each individual point can be calculated as

$$u = \frac{\Delta x}{\Delta t} \quad (7.1)$$

Once two images are captured, they are divided into smaller divisions, termed as interrogation area(IA). These IA's from both images are the correlated pixel by pixel to obtain a signal peak. This peak signal, obtained from the image 1 and 2 represents the displacements, based on the pixel to pixel interpolation. The procedure is repeated for the all the interrogation areas, which provides the complete vector map for the illuminated region.

7.3.1 Seeding particles

The particles are chosen based on the fluid being used in the flowing streams. We need to make sure that the densities are similar for the fluid and particle, they should be solvable, chemical inactive, and they should not interact or stick to each other. If larger particles are used, they may settle to the bottom surfaces due to gravity. To ensure a homogeneous mixture of seeing, the setup is run with distilled water. The particles are separated mixed with a select portion of water, then introduced with the lower tank. The setup is allowed to run for some time to ensure proper distribution of the particles. The illumination from laser light also makes it possible to visually determine the distribution of the particles in the

channels. The material used for the current work is Polyamide with a density of 1.03 g/cm^3 , which is ideally suited for use with water as the flowing fluid.

7.3.2 Illumination source (Laser)

The illumination of the seeding particles is done with the use of 2D(collimated) laser. The benefit of using laser light includes, high density monochromatic light, strong brightness, with the option to focus the 2D light at varying distances, allowing for adjustments. The laser used for in the current setup is a continuous wave, which is a low power 2D light resulting in less heat generation. Other type includes solid state laser with high frequency suitable for high flow rate, or semiconductor lasers for smaller scaled flows due to their low energy. The continuous wave laser is Raypoer2000 laser by Dantec Dynamics. It has variable intensity and a focus option to make sure laser is collimated to illuminate the plane under investigation. The specifications are given in Table 7.1.

The laser is placed at the side of the middle of channels, which allows illumination of half of the channel, remaining channels are illuminated from the other side. The height of 5 mm allows the light to pass through the channels. Laser is initially set at low power to make sure it is properly aligned and focused. Then it is turned off till the camera setup is finished, at which time it is turned back on at higher power for the capture of images. Nut and bolts are installed on all 4 side of the laser to ensure it is horizontal and height is matching the channel region (shown in Figure 7.9). It is important to note that, the height of the channel

is 5mm, and setting the laser light to exact 2.5 mm location is impossible. Even if is at exact middle of channel, some particle towards the top and bottom side of the channel will also be illuminated. This will result in some particles exhibiting higher velocity, corresponding to the middle of channel, while some will have slightly lower velocity that will be offset from the center of the channel. For this reason, the video is inspected manually to ensure that the velocity of all the seeds is coherent and any off-lying seed can be neglected in the analysis. For purpose of demonstration, the channel illuminated by the laser light is shown in Figure 7.10, where it can be seen that the laser is bright enough to easily illuminate at least half of the manifold.

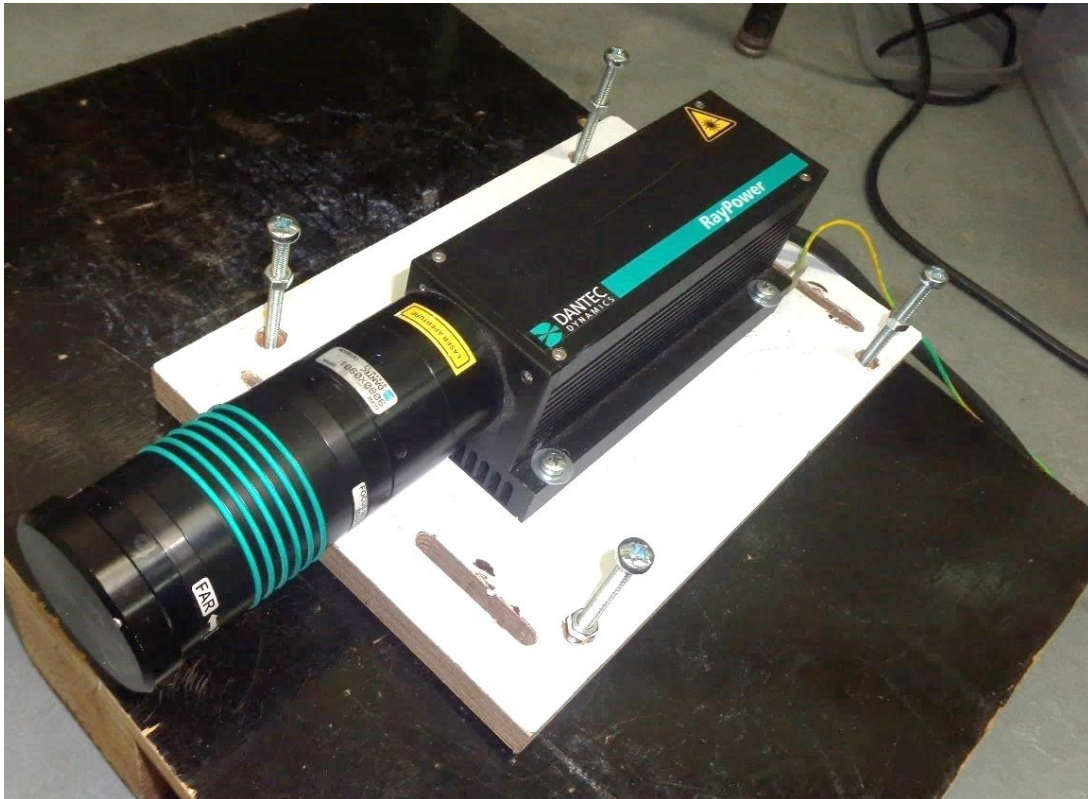


Figure 7.9. The laser light source (Raypower 2000). Specification are given in Table 7.1

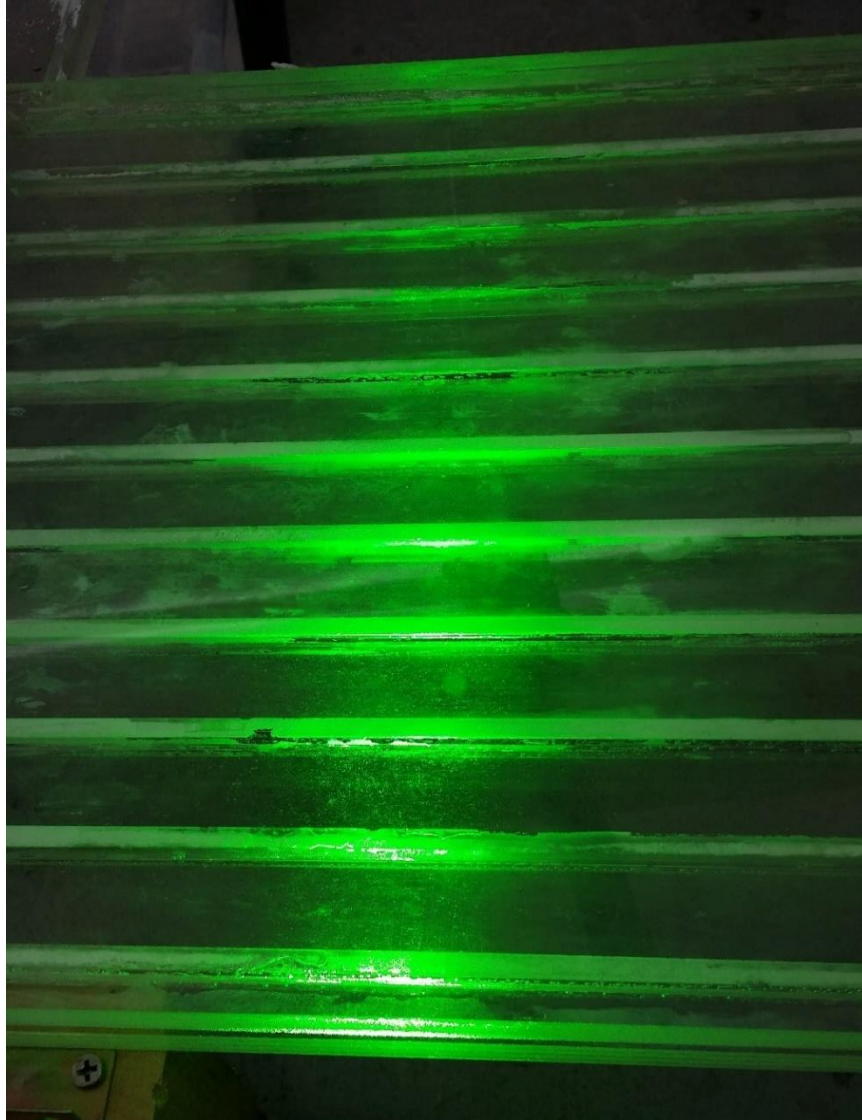


Figure 7.10. An image of the illumination provided by the laser.

7.3.3 High speed camera

The processing phase of older film based cameras is avoided with the advent of digital cameras, which have a charged couple device termed CCD arrays which converts the light directly into an electric charge that results in instant images, As the light reflected by the particles is weak, a high aperture is needed along with a high-quality lens to focus properly on the area of interest. In this regard, the camera used was a Dantec Speedsense 9040 and a Nikon 600 mm f 2.8D lens. The details about the camera are listed in Table 7.2, while that of the lens are listed in Table 7.3. A frame rate of 200 FPS was used with the exposure time of 4900 μ s for the current work. It is to be noted that FPS of 200 represents period of 0.005 s, which is used as the time in Eq.(7.1) for velocity calculations. The aperture is set to maximum to allow maximum light reaching the camera, thus ensuring the visibility of the particles

The camera is mounted on the tripod, aligned by the bubble level present on the tripod. The camera is connected via the ethernet port and the power supply. The PCC software is used to calibrate the intensity of the camera with the lens covered. After calibration, the cover is removed to view the live video from the camera. The focus is adjusted to focus on the particles within the flow, sharpening the visibility of the particles. During the experiment, a high-speed video is captured. The video is reviewed to ensure proper presence of particles, proper focus and good quality. This video is then converted into set of images to be used for further analysis in the software Dantec Dynamics.

Table 7.1. Specification of the laser used for illuminating the flow area

Model	Raypower 2000
Medium	Gas
Wavelength of laser	532± 1 nm
Transverse mode	Near TEM00
Beam diameter at the aperture	3.0nm
Polarization ratio	Greater than 100:1
Mode of operation	Continuous wave
TTL modulation frequency	maximum 10kHz
Power	2 W
Power supply	100-240 volt AC with 3A current Frequency of AC 50-60Hz
Operating temperature	10-35°C

Table 7.2. Specification of the camera used for the high-speed videos

Model	SpeedsenseCamera 9040
Resolution (pixels)	1632 × 1200
Pixel size	11.5 μm)
Depth	8,12,14 bits
Maximum exposure time	2 μs
Frames per second Fps (full frame)	1016/508 with full frame operation
Sensor type	CCD progressive scan monochrome
Chip size	18.77 × 13.8 mm

Table 7.3. Specification of the lens used with the camera

Maker	Nikon
Model	AF Micro Nikkon 60mm f/2.8D
Distance scale	0.219 m - ∞
Focal length	60 mm
f-number	2.8-32

7.3.4 Image processing

The images are converted from pixels to length unit of mm by defining the width of the channel in the image. It provides the scale factor, from pixel to mm in order to calculate the distance in mm covered by the particles for use in Eq.(7.1). The procedure followed in the Dantec Dynamics is to do image processing for find the distance covered by each particle in each from and the providing the velocity vectors.

The steps used are

1. Make double frame, to combine two images together so that the particle motion can be seen in the double frames image.
2. Image Min/Max, this is to determine the maxima and minima of the images.
The minima is used as the reference of background stationary image so that the background image can be removed and only the particles are visible.
3. Image Arithmetic, it is to subtract the Image Min obtained from the previous step from all the images, removing the background noise from the images.

4. Image Mean, an average image is generating representing the average intensity of the all the corresponding pixels, in all of the images.
5. Image Processing-Blur, it is used to blur the particle intensity.
6. Image arithmetic, to subtract the blur image from the images at step 3 to reduce intensity of each image.
7. Image processing-Gaussian filter 5×5 . It is a low pass linear filter to make the particle more visible, basing its analysis on the center of the particle instead of the edges.
8. Image min max, to find the minimum image among the output from gaussian filter.
9. Image arithmetic, it is used again to subtract the minimum image 8 from the images obtained at step 7
10. Adaptive correlation, it is used to generate the velocity vectors. It applies correlation algorithm to images at 9, obtaining the displacement vectors and time interval from time period of the images using the central difference scheme, resulting in velocity vector for the whole image.
11. Vector statistics, it is used to plot the information from the velocity vectors, It further provides the standard deviations, covariance and covariance along with the option to plot the X or Y velocity in graphs. The data can be extracted in Comma separate format for further analysis on the results.

Also include here sample vectors from Dantec and well as the sample particle image from camera, include some video in the final presentation. The process is shown in Figure 7.11 as flow chart.

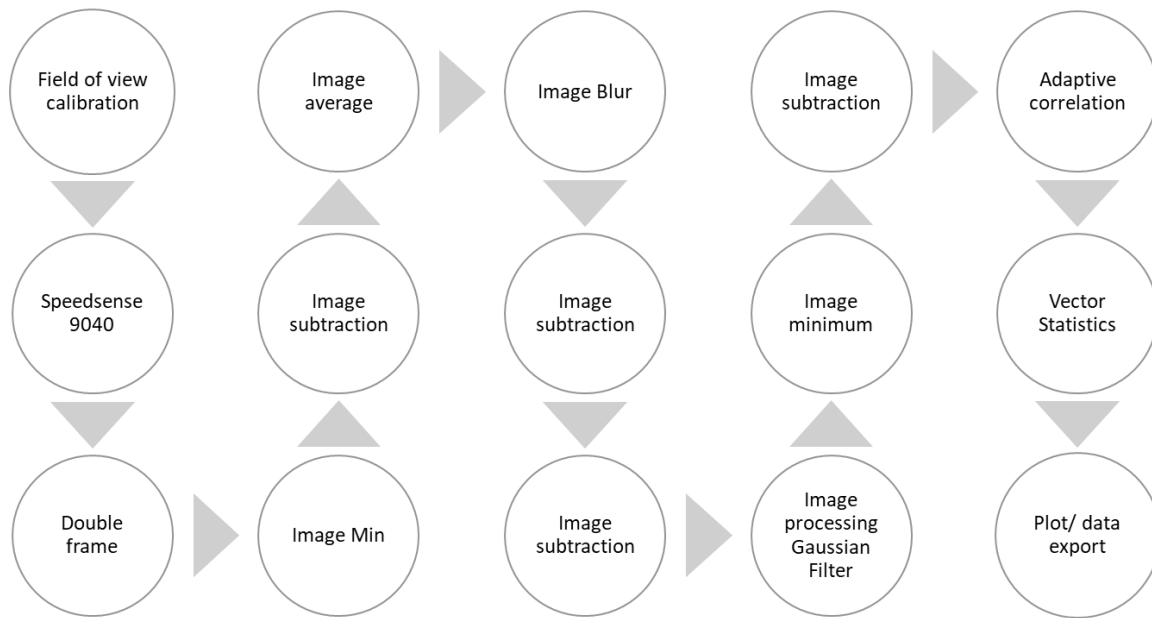


Figure 7.11. The image processing step in Dantec Dynamics

7.4 Results and discussion

The results of the present experimental investigation are discussed in terms of profile comparison in channels and the velocity comparisons among different channels. The details of the numerical study can be found in [184]. The total velocity uncertainty (which was discussed previously) is about 8.48% which is presented as $\pm 4.24\%$. This value has been added to all experimental data shown here as error bars.

7.4.1 Velocity profiles comparison

The velocities of the channels were found using the process described in the previous section. A sample case is shown here for the velocity profiles in the channels, with data for channels 9 and 10 presented here. It can be seen from Figure 7.12 (a) that the profile in the channel according to the theoretical models, where the velocity at the walls is zero and maximum in the middle. There is a limitation of the PIV system is that it is a graphic/image processing software, which will not identify the exact location of the boundaries automatically i.e. the distinction between the fluid and wall is not readily available. It does give some velocity component even at the walls which are modeled to be of 5 mm wide, although the velocity is much smaller than the actual values. Hence, the location of the walls was manually extracted and only the data of flow channel was plotted. A similar trend is visible in Figure 7.12 (b), where the same velocity profile exists for the channel. These figures validate the PIV measurements, for being accurate in finding the complete velocity variation in the channel. The average velocity is used as a representation of the channel velocity for the purpose of evaluating the flow distribution.

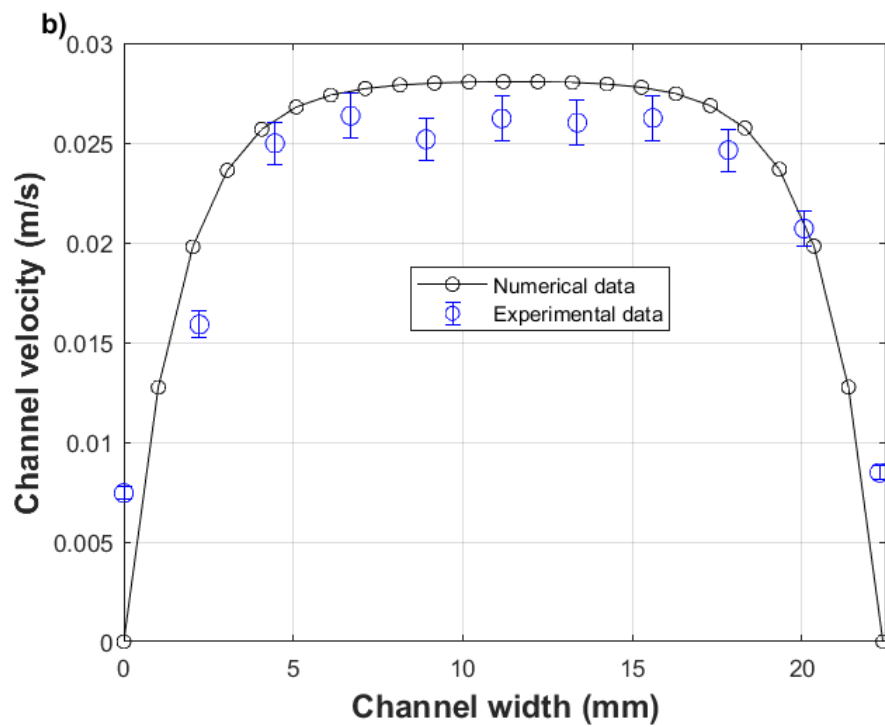
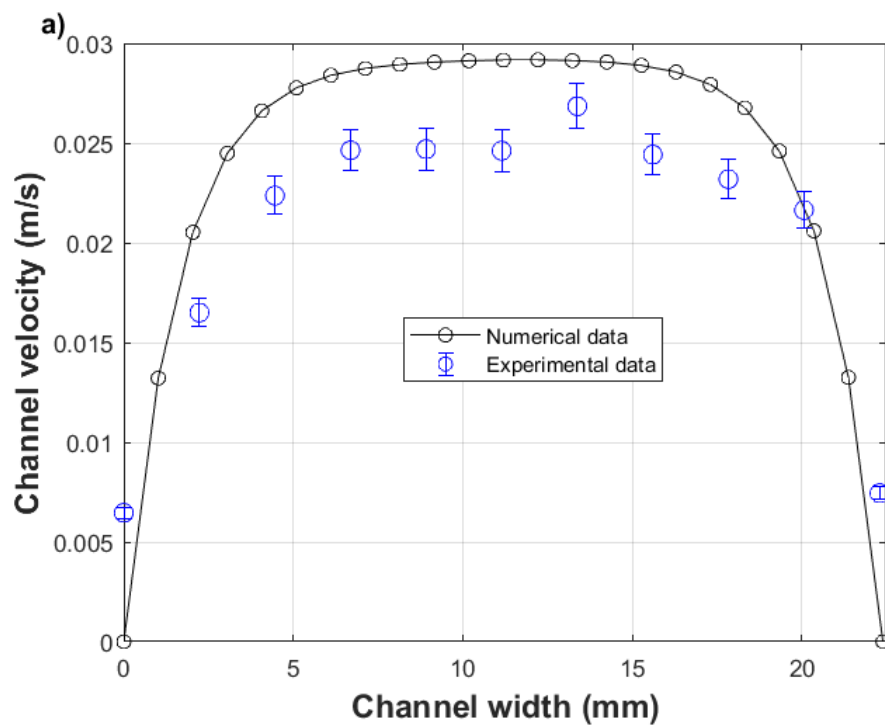


Figure 7.12. The velocity profile comparison for the numerical modelling and the experimental ones. a) for channel 10 and b) for channel 9. U- type and 100 L/hr.

7.4.2 Flow distribution:

In this section, the velocity and flow rate distribution results are shown. It should be noted that the area of the channel and density of the fluid is constant, hence the normalized velocity distribution in each channel will be same as the normalized flow rate distribution.

7.4.2.1 Comparison of four different layouts

With the arrangement of U-type, it is expected that the channel nearest to the inlet and exit side would receive the maximum flow rate, as they will take the path of least resistance. For the Z-type flow rate, fluid enters from one side of the manifold and leaves from the opposite side, hence the end channels are expected to have more flow. Regarding the error bar representation, it is important to note that error has been calculated as percentage of the actual velocity values, this makes the error bars more readily visible for higher velocities in comparison to the lower velocities.

Figure 7.13 shows the velocity in each channel of the four designs under consideration, each with constant inlet volume flow rate of 100 L/hr. It can be seen for the U-type design that the initial channels have higher velocity. For the narrow manifold design, a very high maldistribution is seen with initial channel having velocity of about 0.08 m/s while the last channel has around 0.0054 m/s. This shows that due to narrow channel, even a small fraction of the flow diversion into the channel represents a large quantity. Thus, the path of least resistance, i.e. initial channels have the highest flow rate than the other channels.

For the wide manifold, the overall behavior is similar, but with more uniform distribution. This uniform distribution is due to the wide manifold area. The fluid in the inlet section towards the channels change their direction towards the channels, and a fraction of fluid turns while the remaining continues within the manifold. Hence a wide manifold allows the flow to have a better distribution with maximum velocity of only 0.06 m/s and minimum velocity of 0.03 m/s. It can also be seen for the U-type comparisons that the slope of flow distribution is more for narrow manifold and less for the wide manifold.

Now with regards to Z-type arrangements, it is evident that the path of least resistance is through the last channels, as the fluid exits from the opposite side in relation to the inlet side. We can see that for narrow arrangement, maximum velocity of 0.11 m/s and minimum velocity of 0.02 m/s exists. In comparison to U-type design, the highest velocities are greater whereas the lower velocities are less. Regarding the wider manifold, the distribution is better.

As for the case of higher flow rate, Figure 7.14 shows the velocities for a double flow rate of 200 L/hr in comparison to Figure 7.13, it is observed that the overall distribution pattern remains similar. In addition, another increase of flow rate to 300 L/hr results in velocity distribution shown in Figure 7.15, which is again showing similar flow distribution behaviors. The values of these velocities are tabulated in Table 7.4. The comparison of

higher flow rate impact on the flow distribution is discussed in the next section, with the use of non-dimensional velocity.

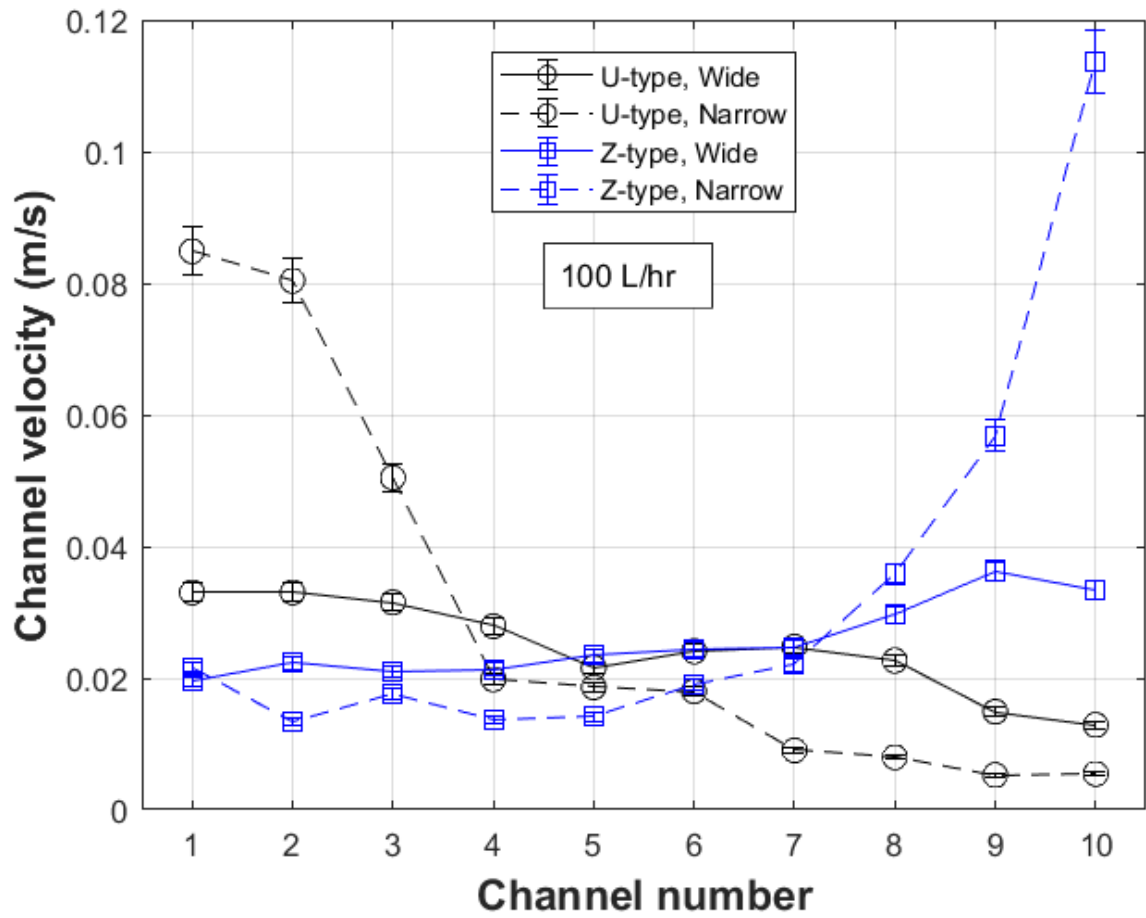


Figure 7.13. Experimental comparison of the velocity distribution between channels for flow rate of 100 L/hr and multiple configurations.

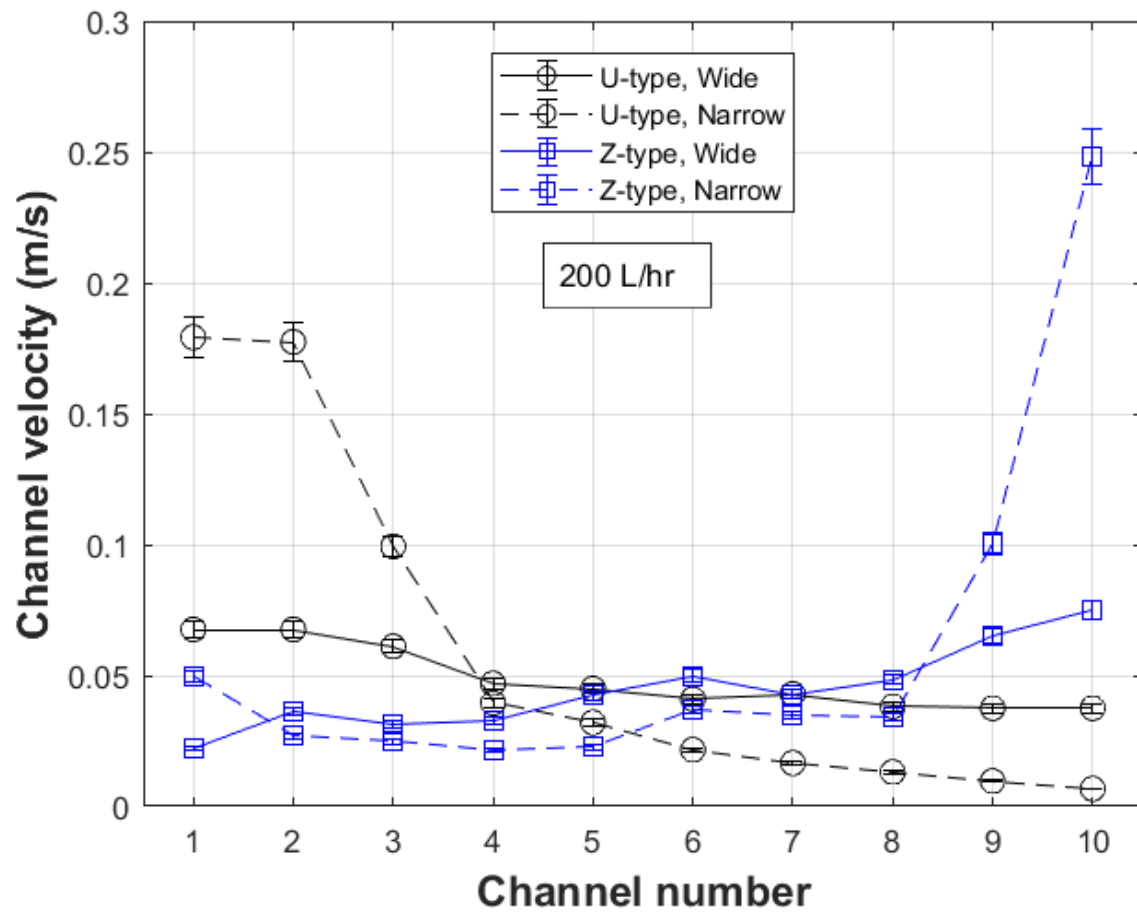


Figure 7.14. Experimental comparison of the velocity distribution between channels for flow rate of 200 L/hr and multiple configurations.

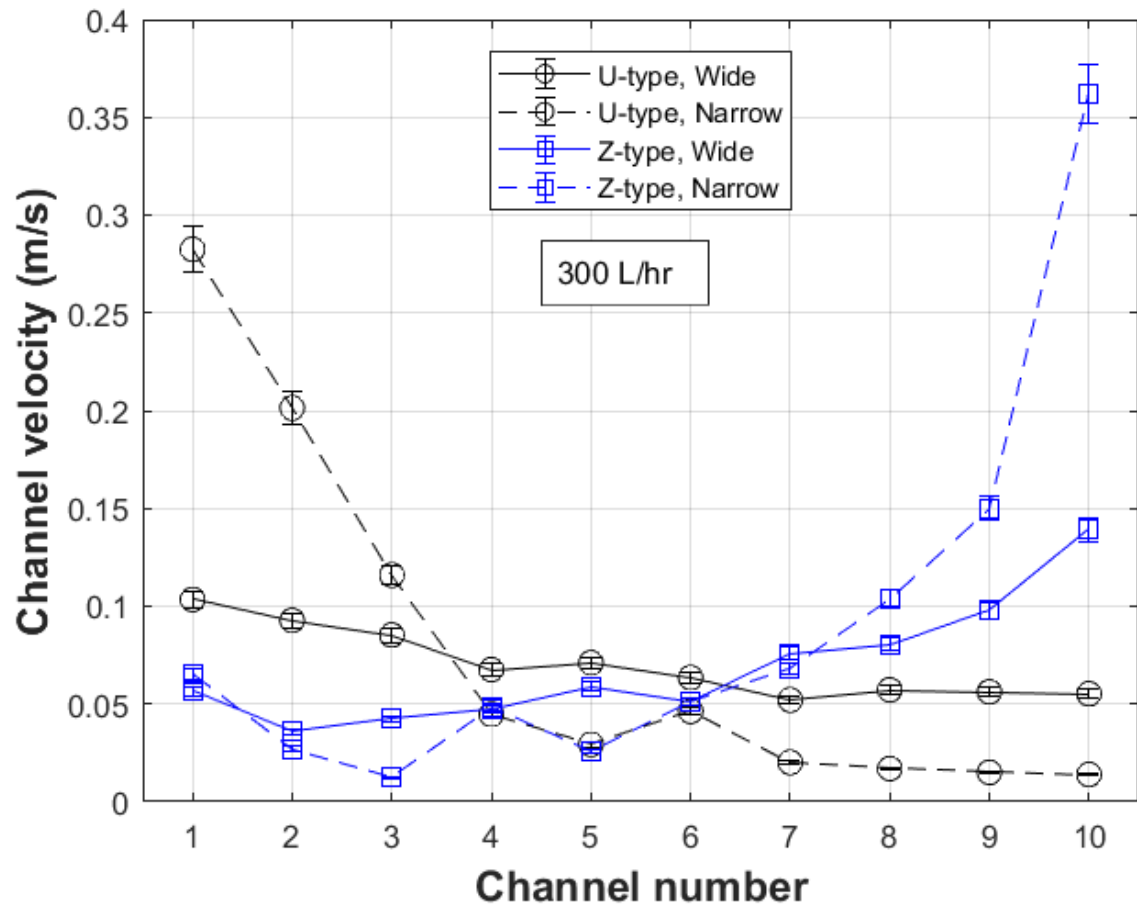


Figure 7.15. Experimental comparison of the velocity distribution between channels for flow rate of 300 L/hr and multiple configurations.

7.4.2.2 Comparison of normalized velocities

To make a comparison between these cases, non-dimensional velocities are introduced, where each velocity is normalized with the average velocity in all the channels of a particular case. i.e.

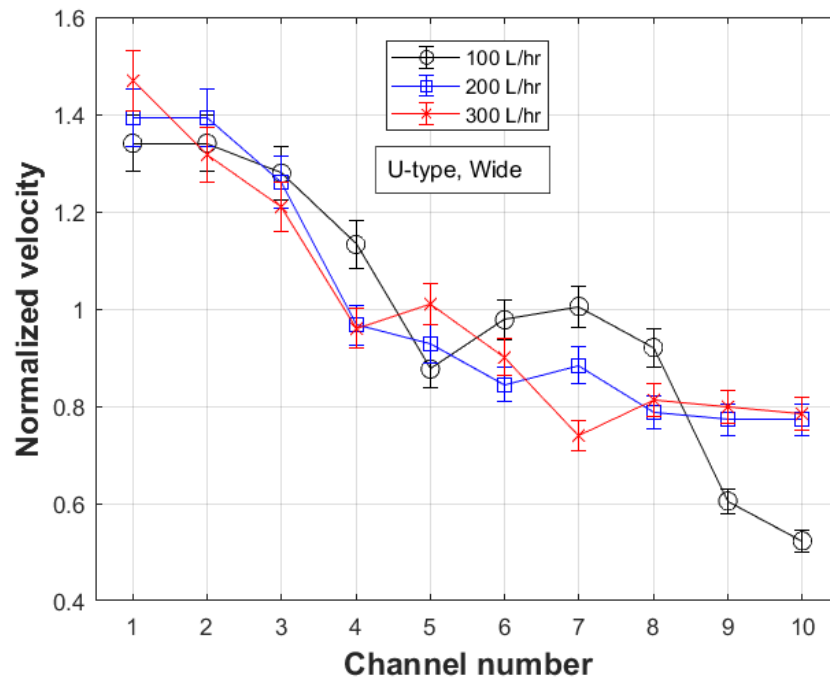
$$v_{i,\text{normalized}} = \frac{v_i}{v_{\text{average}}} \quad (11)$$

where i is the particular channel. The results are plotted in Figure 7.16 and Figure 7.17 while tabular values are listed in Table 7.4 and Table 7.5.

7.4.2.2.1 U-type

From Figure 7.16 (a), it can be seen that the higher flow rate allows more flow rate towards the last channels 9 and 10, hence the distribution is improved for U-type wide manifold. Figure 7.16 (b) shows that for the narrower manifold, there is almost no impact on velocities in the last channels. Whereas, there is increased flow in the initial channels, thus the flow distribution is decreased at higher flow rates. Similarly, a comparison can be made between wide and narrow manifold using Table 7.4. It shows that the channel 1 has velocity of 1.34 for wide and 2.8 for the narrow, which is almost double. Similarly, for the channel 10, the narrow channel has 1/3rd flow in comparison to the wide manifold. Hence, narrow manifold results in extreme values at both initial and end channels.

a)



b)

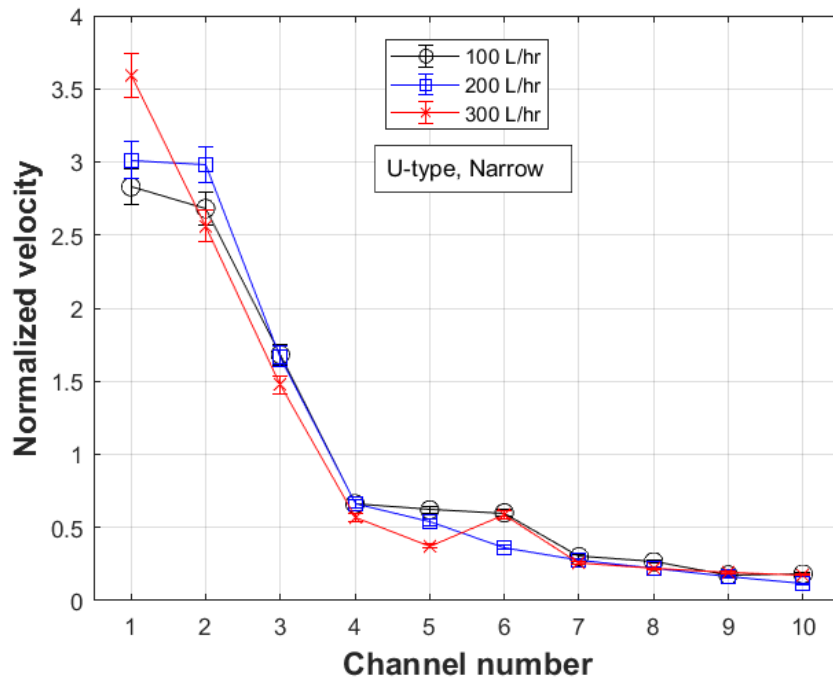


Figure 7.16. Normalized velocity comparisons for difference flow rates for a) wide and b) narrow manifold for U-type.

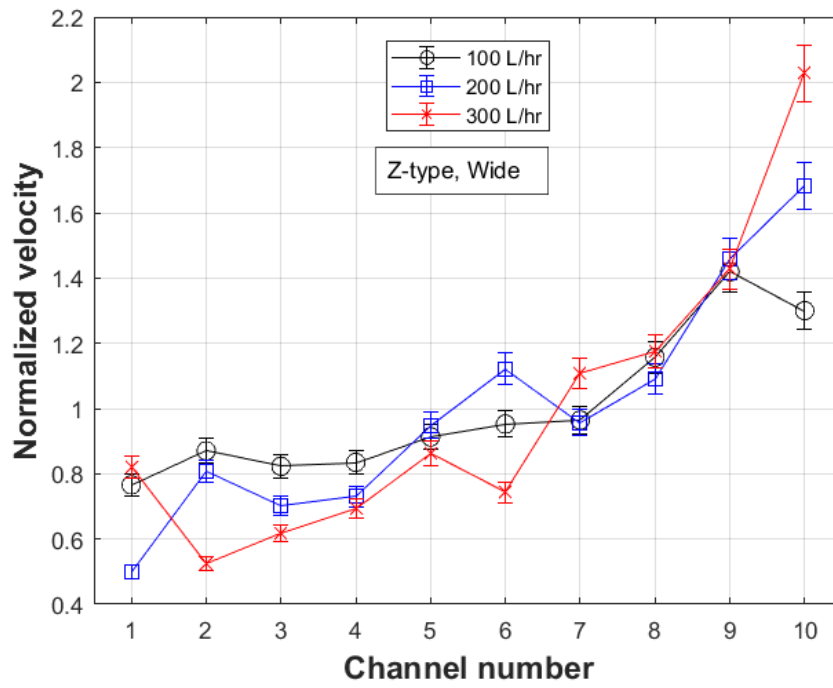
Table 7.4. The actual and normalized velocities for each channel. U-Type, wide and narrow manifold for multiple inlet flow rates.

Channel Number	Wide manifold velocity		Narrow manifold velocity	
	Actual (m/s)	Normalized (-)	Actual (m/s)	Normalized (-)
100 L/hr				
1	0.0330	1.3406	0.0848	2.8299
2	0.0330	1.3406	0.0804	2.6811
3	0.0315	1.2790	0.0504	1.6821
4	0.0279	1.1324	0.0198	0.6613
5	0.0216	0.8762	0.0186	0.6206
6	0.0241	0.9777	0.0180	0.6003
7	0.0248	1.0050	0.0090	0.3007
8	0.0227	0.9205	0.0079	0.2663
9	0.0149	0.6050	0.0052	0.1751
10	0.0129	0.5230	0.0054	0.1820
200 L/hr				
1	0.0676	1.3929	0.1792	3.0113
2	0.0676	1.3929	0.1774	2.9812
3	0.0611	1.2594	0.0993	1.6685
4	0.0469	0.9667	0.0394	0.6636
5	0.0450	0.9272	0.0320	0.5381
6	0.0410	0.8448	0.0215	0.3628
7	0.0429	0.8839	0.0165	0.2787
8	0.0382	0.7869	0.0131	0.2201
9	0.0375	0.7727	0.0096	0.1622
10	0.0375	0.7727	0.0067	0.1130
300 L/hr				
1	0.1035	1.468981	0.2824	3.5929
2	0.0928	1.317207	0.2013	2.5611
3	0.0853	1.210439	0.1159	1.4743
4	0.0676	0.959524	0.0446	0.5683
5	0.0711	1.009675	0.0294	0.3740
6	0.0635	0.900844	0.0462	0.5881
7	0.0521	0.739011	0.0201	0.2560
8	0.0572	0.812781	0.0169	0.2159
9	0.0562	0.797684	0.0150	0.1914
10	0.0552	0.783853	0.0139	0.1774

7.4.2.2.2 Z-type

Figure 7.17 is for Z-type configuration. It can be seen from Figure 7.17 (a) that lowest flow rate has the best flow distribution, whereas higher flow rates tend to decrease flow in the initial channels and increase in the latter channels, mainly due to fluid momentum. From Figure 7.17 (b) it can be seen that flow rate has almost no impact on the flow in the initial channels whereas higher flow rates tend to increase the flow in the latter channels. These trends can also be seen in Table 7.5

a)



b)

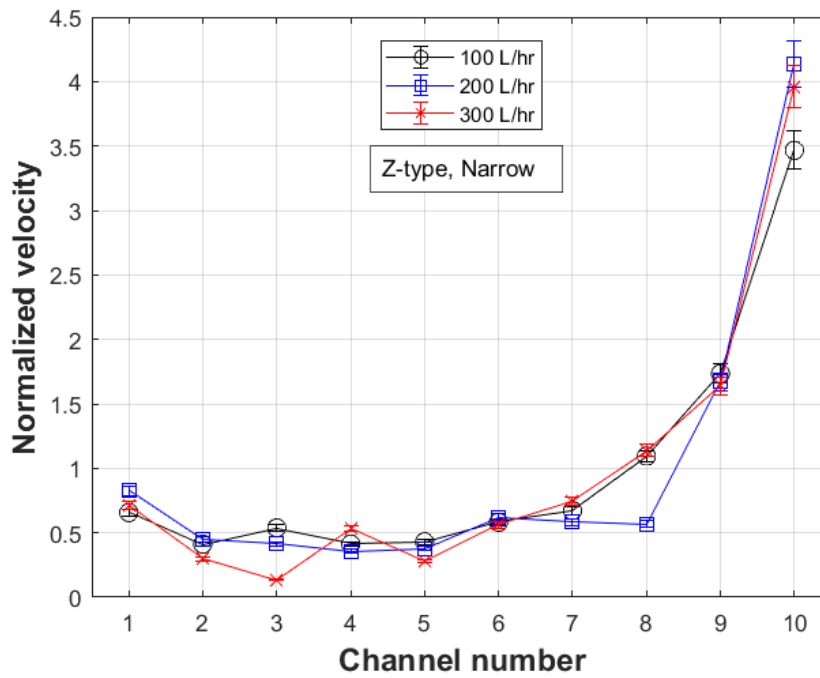


Figure 7.17. Normalized velocity comparisons for difference flow rates for a) wide and b) narrow manifold for Z-type.

Table 7.5. The actual and normalized velocities for each channel. Z-Type, wide and narrow manifold for multiple inlet flow rates.

Channel Number	Wide manifold velocity		Narrow manifold velocity	
	Actual (m/s)	Normalized (-)	Actual (m/s)	Normalized (-)
100 L/hr				
1	0.0196	0.7658	0.0215	0.6568
2	0.0223	0.8704	0.0135	0.4119
3	0.0211	0.8230	0.0176	0.5383
4	0.0214	0.8350	0.0135	0.4135
5	0.0234	0.9132	0.0140	0.4300
6	0.0244	0.9521	0.0190	0.5816
7	0.0247	0.9644	0.0220	0.6723
8	0.0296	1.1572	0.0358	1.0941
9	0.0363	1.4191	0.0568	1.7345
10	0.0333	1.2999	0.1136	3.4667
200 L/hr				
1	0.0222	0.4996	0.0496	0.8265
2	0.0360	0.8085	0.0269	0.4488
3	0.0313	0.7038	0.0247	0.4125
4	0.0325	0.7296	0.0214	0.3565
5	0.0422	0.9488	0.0226	0.3772
6	0.0505	1.1218	0.0371	0.6184
7	0.0426	0.9573	0.0350	0.5839
8	0.0485	1.0892	0.0342	0.5698
9	0.0657	1.4583	0.1003	1.6700
10	0.0755	1.6827	0.2485	4.1359
300 L/hr				
1	0.0563	0.8214	0.0650	0.7118
2	0.0360	0.5250	0.0270	0.2960
3	0.0423	0.6165	0.0124	0.1366
4	0.0476	0.6942	0.0484	0.5295
5	0.0591	0.8621	0.0258	0.2826
6	0.0514	0.7432	0.0512	0.5601
7	0.0760	1.1081	0.0680	0.7438
8	0.0806	1.1748	0.1039	1.1375
9	0.0979	1.4268	0.1500	1.6413
10	0.1391	2.0275	0.3620	3.9603

7.5 Analytical study

In this section, the analytical mode for the flow distribution manifold is studied. The models for U- and Z-type are under consideration, where the models are compared with the numerical results. The important aspect in this regard is the governing coefficient of momentum change and turn loss coefficients. The values of these coefficients are not reported in literature. In this section, the exact values are calculated from numerical modelling and then the results are presented.

7.5.1 The governing equations

The analytical modeling used here is based on the model presented by Wang [140]. The main steps are presented here, while more details can be found in the literature.

Intake manifold momentum conservation

$$\frac{1}{\rho} \frac{dP_i}{dX} + \frac{f_i}{2d_i} W_i^2 + (2 - \beta_i) W_i \frac{dW_i}{dX} = 0 \quad (7.2)$$

Intake manifold momentum conservation

$$\frac{1}{\rho} \frac{dP_e}{dX} + \frac{f_e}{2d_e} W_e^2 + (2 - \beta_e) W_e \frac{dW_e}{dX} = 0 \quad (7.3)$$

Governing equation of U type arrangement

$$\frac{1}{\rho} \frac{d(P_i - P_e)}{dX} + \left(\frac{f_i}{2D_i} + \frac{f_e}{2D_e} \left(\frac{A_i}{A_e} \right)^2 \right) W_i^2 - \left((2 - \beta_e) \left(\frac{A_i}{A_e} \right)^2 - (2 - \beta_i) \right) W_i \frac{dW_i}{dX} = 0 \quad (7.4)$$

In the above equations, the term $2 - \beta$ is defined as $2k$ to represent the momentum change from the manifold to the channels, which is calculated as

$$\beta = \frac{W_c}{W} \quad (7.5)$$

The pressure loss between the two manifolds is correlated by

$$P_i - P_e = \rho \left(1 + C_{fi} + C_{fe} + f_c \frac{l_c}{d_c} \right) \frac{u_c^2}{2} = \rho \zeta \frac{u_c^2}{2} \quad (7.6)$$

$$\zeta = \left(1 + C_{fi} + C_{fe} + f_c \frac{l_c}{d_c} \right) \quad (7.7)$$

The turn loss coefficient is calculated as

$$C_f = \frac{2(p_1 - p_2)}{\rho(v_1 - v_2)^2} \quad (7.8)$$

where, 1 represent the first plane before the turn and 2 represent the plane after the turn, for both the U- and Z-type arrangements.

The non-dimensional velocity is based on the inlet velocity

$$u_c = \frac{U_c}{W_i} \quad (7.9)$$

The normalized volume flow rate in the channels is defined as

$$C_f = \frac{n \times A_c \times u_c}{A_i} \quad (7.10)$$

where n is the total number of channels.

7.5.1.1 For the U-type.

For Z-type arrangement, the model by Wang [141] is used. The normalized velocity in the inlet manifold is

$$w_i = e^{-Bx/2} \left(\frac{\sin\left(\frac{\sqrt{3} J (1-x)}{2}\right)}{\sin\left(\frac{\sqrt{3} J}{2}\right)} \right) \quad (7.11)$$

The normalized velocity in the exit manifold is

$$w_e = \left(\frac{F_e}{F_i}\right) w_i = \left(\frac{F_e}{F_i}\right) e^{-Bx/2} \left(\frac{\sin\left(\frac{\sqrt{3} J (1-x)}{2}\right)}{\sin\left(\frac{\sqrt{3} J}{2}\right)} \right) \quad (7.12)$$

The normalized volume flow rate in channels

$$v_c = \frac{e^{-Bx/2}}{2} \left(\frac{B \sin\left(\frac{\sqrt{3} J (1-x)}{2}\right) + \sqrt{3} J \cos\left(\frac{\sqrt{3} J (1-x)}{2}\right)}{\sin\left(\frac{\sqrt{3} J}{2}\right)} \right) \quad (7.13)$$

The normalized channel velocity

$$u_c = \left(\frac{F_i}{nF_c} \right) v_c = \left(\frac{F_i}{nF_c} \right) \frac{e^{-Bx/2}}{2} \left(\frac{B \sin \left(\frac{\sqrt{3} J (1-x)}{2} \right) + \sqrt{3} J \cos \left(\frac{\sqrt{3} J (1-x)}{2} \right)}{\sin \left(\frac{\sqrt{3} J}{2} \right)} \right) \quad (7.14)$$

It is important to note here that this velocity is the average channel velocity, that is comparable to the channel area weighted average velocity, not the maximum central channel velocity. The ratio between the middle maximum line-based velocity and the area weighted average velocity is found to be 1.33. The reason for this is due to the fact that the upper and lower surfaces have zero velocity and the area based average velocity comes out to be less than the average based on the middle of the channel.

7.5.1.2 For the Z-type.

For Z-type arrangement, the model by Wang [142] is used. A new parameter ‘ ε ’ is defined for the Z-type arrangement as.

$$\varepsilon = -\frac{f_e L}{4\zeta D_e} \left(\frac{A_{cn}}{A_e} \right)^2 \quad (7.15)$$

The normalized velocity in the inlet manifold is

$$w_i = e^{-Bx/2} \left(\frac{\sin\left(\frac{\sqrt{3} J (1-x)}{2}\right)}{\sin\left(\frac{\sqrt{3} J}{2}\right)} \right) + \sqrt{\frac{\varepsilon}{2R}} \left[1 - e^{-B(x-1)/2} \frac{\sin\left(\frac{\sqrt{3} J x}{2}\right)}{\sin\left(\frac{\sqrt{3} J}{2}\right)} - e^{-Bx/2} \frac{\sin\left(\frac{\sqrt{3} J (1-x)}{2}\right)}{\sin\left(\frac{\sqrt{3} J}{2}\right)} \right] \quad (7.16)$$

The normalized volume flow rate in channels

$$v_c = \frac{e^{-Bx/2}}{2} \left(\frac{B \sin\left(\frac{\sqrt{3} J (1-x)}{2}\right) + \sqrt{3} J \cos\left(\frac{\sqrt{3} J (1-x)}{2}\right)}{\sin\left(\frac{\sqrt{3} J}{2}\right)} \right) \times \quad (7.17)$$

$$\left[\frac{B}{2} \sqrt{\frac{\varepsilon}{2R}} e^{B/2} \sin\left(\frac{\sqrt{3} J x}{2}\right) - \frac{B}{2} \left(1 - \sqrt{\frac{\varepsilon}{2R}}\right) \sin\left(\frac{\sqrt{3} J (1-x)}{2}\right) \right.$$

$$\left. - \sqrt{\frac{\varepsilon}{2R}} e^{B/2} \frac{\sqrt{3}}{2} J \cos\left(\frac{\sqrt{3} J x}{2}\right) - \left(1 - \sqrt{\frac{\varepsilon}{2R}}\right) \frac{\sqrt{3}}{2} J \cos\left(\frac{\sqrt{3} J (1-x)}{2}\right) \right]$$

The parameters k_i , k_e , C_{fe} , and C_{fi} are all calculated using the numerical model presented in the earlier chapter. The literature is empty from any calculated values of these parameters. These values are either assumed based on the best fit data or taken as an arbitrary value. The calculation of these parameters signifies the important role these values play in the results of the analytical model.

Table 7.6. The calculated coefficients of the momentum change and turn loss. U-Type.

Channel	U wide manifold				U normal manifold			
	k_i	k_e	C_{fi}	C_{fe}	k_i	k_e	C_{fi}	C_{fe}
100L/hr								
1	0.646	0.687	21.720	0.229	0.844	0.865	0.145	0.438
2	0.620	0.658	24.654	0.226	0.835	0.851	0.019	0.387
3	0.600	0.637	34.789	0.258	0.834	0.851	0.054	0.415
4	0.576	0.615	67.048	0.297	0.842	0.858	0.105	0.468
5	0.543	0.585	251.729	0.341	0.845	0.864	0.258	0.513
6	0.496	0.544	323.956	0.390	0.845	0.864	0.473	0.568
7	0.423	0.484	146.914	0.443	0.836	0.854	0.662	0.645
8	0.313	0.395	36.679	0.505	0.809	0.829	1.252	0.747
9	0.143	0.264	16.311	0.588	0.742	0.771	4.523	0.858
10	-0.071	0.128	10.704	0.814	0.521	0.589	17.247	0.797
200L/hr								
1	0.664	0.708	13.504	0.164	0.829	0.853	0.130	0.421
2	0.635	0.675	15.731	0.121	0.822	0.839	0.030	0.366
3	0.614	0.651	20.441	0.116	0.825	0.841	0.007	0.383
4	0.589	0.627	34.631	0.120	0.838	0.850	0.015	0.406
5	0.555	0.597	102.613	0.126	0.847	0.859	0.087	0.448
6	0.505	0.556	189.379	0.129	0.845	0.861	0.311	0.492
7	0.426	0.498	97.829	0.128	0.834	0.853	0.539	0.538
8	0.297	0.414	20.086	0.119	0.809	0.832	1.047	0.599
9	0.070	0.295	7.967	0.106	0.742	0.773	2.441	0.653
10	-0.368	0.181	4.395	0.148	0.506	0.599	4.743	0.544
300L/hr								
1	0.662	0.703	12.651	0.153	0.820	0.846	0.144	0.454
2	0.630	0.669	15.135	0.119	0.809	0.828	0.010	0.360
3	0.612	0.651	19.252	0.117	0.817	0.832	0.031	0.375
4	0.592	0.632	30.867	0.121	0.842	0.848	0.093	0.394
5	0.561	0.605	81.931	0.122	0.858	0.861	0.036	0.413
6	0.513	0.565	212.260	0.111	0.862	0.864	0.150	0.455
7	0.440	0.508	139.434	0.087	0.851	0.855	0.221	0.494
8	0.322	0.426	23.211	0.055	0.824	0.833	0.517	0.536
9	0.121	0.313	8.365	0.018	0.755	0.777	2.079	0.567
10	-0.245	0.199	4.368	0.031	0.503	0.577	2.796	0.431

Table 7.7. The calculated coefficients of the momentum change and turn loss. Z-Type.

Z wide manifold					Z normal manifold			
Channel	k _i	k _e	C _{fi}	C _{fe}	k _i	k _e	C _{fi}	C _{fe}
100L/hr								
1	0.806	0.080	263.831	1.466	0.967	0.605	4.788	16.118
2	0.781	0.234	408.028	2.542	0.967	0.796	7.717	269.901
3	0.760	0.389	814.980	7.058	0.969	0.873	9.520	354.507
4	0.732	0.496	932.866	33.260	0.972	0.913	14.423	562.478
5	0.691	0.567	567.620	318.471	0.973	0.933	17.635	605.901
6	0.630	0.614	99.677	103.635	0.970	0.940	17.300	555.435
7	0.535	0.644	33.833	59.940	0.959	0.932	11.092	452.677
8	0.386	0.661	24.893	46.889	0.924	0.906	4.773	389.459
9	0.146	0.670	17.661	42.245	0.827	0.871	2.976	196.470
10	-0.215	0.680	14.778	40.297	0.533	0.831	2.279	77.166
200L/hr								
1	0.844	0.117	28.560	0.531	0.971	0.618	2.482	11.801
2	0.818	0.252	99.611	0.849	0.972	0.801	5.825	75.055
3	0.795	0.390	275.192	2.298	0.975	0.874	8.019	126.397
4	0.765	0.485	832.793	8.368	0.976	0.911	11.247	206.829
5	0.722	0.549	154.686	63.537	0.978	0.933	14.732	435.952
6	0.660	0.591	40.671	155.133	0.977	0.942	16.063	529.817
7	0.565	0.618	16.932	63.793	0.969	0.934	10.347	422.326
8	0.411	0.634	8.437	29.677	0.935	0.898	3.070	396.442
9	0.142	0.641	4.616	24.457	0.841	0.855	2.032	58.712
10	-0.360	0.572	2.799	8.911	0.533	0.801	0.215	31.021
300L/hr								
1	0.833	0.141	13.319	0.131	0.973	0.625	3.650	9.791
2	0.806	0.271	13.068	0.224	0.974	0.805	4.900	78.658
3	0.784	0.402	16.140	1.052	0.976	0.874	6.549	355.718
4	0.754	0.495	23.387	5.869	0.978	0.911	9.744	437.633
5	0.713	0.560	44.426	89.680	0.979	0.933	13.240	516.305
6	0.651	0.603	122.013	188.667	0.979	0.944	15.343	448.063
7	0.557	0.630	126.069	30.621	0.973	0.938	10.644	395.691
8	0.407	0.644	75.745	17.421	0.942	0.899	2.897	242.769
9	0.152	0.649	9.457	12.295	0.846	0.846	2.565	32.934
10	-0.294	0.656	3.541	7.207	0.534	0.787	2.091	12.917

7.5.2 Results

There are two manifold designs studied. One is with the manifold width of 22 mm, while the wider one with 110 mm width. The results for both cases are discussed below.

7.5.2.1 U-Type

With regards U-type arrangement, the results are quiet in agreement with the numerical ones. Figure 7.18 shows the velocity distribution in wide manifold, when the coefficients are based on Table 7.6. It can be seen that there exists some disagreement, like the analytical model results in lower velocities for the initial channels while more flow rate is predicted for the later channels. For the higher flow rate of 200 L/hr, Figure 7.19 shows slightly closer results, except for the last channel where analytical predicts much lower flow rate. Finally, for the flow rate of 300 L/hr, we can see from Figure 7.20 that the distribution is getting slightly uniform. The trends of analytical and numerical remains similar.

For the normal or smaller manifold design, Figure 7.21 shows lower values in the initial channels while higher values for the latter channels. Furthermore, in comparison to the wider manifold, we can see that flow becomes highly non-uniform for the smaller manifold, with the difference being almost double for the first channel. Similar trends can be seen for 200 L/hr case in Figure 7.22, with the flow distribution becoming more non-uniform due to higher velocity. This trend is similar to what was seen for the case of wide

manifold. The reason, again is the fact that higher velocities increase the flow momentum and more fluid is forced to the last channels in comparison to the initial channels.

Also, for the wider manifold, the velocity magnitude itself was lower, due to more inlet cross-sectional area. This resulted in the fluid having less momentum and more flow was focused in the initial channels. With a higher flow rate, the momentum of the fluid shifted the flow distribution towards more uniform behavior. For the case of normal manifold width, the narrow cross-sectional area of inlet manifold results in higher velocities and momentum even for the flow rate of 100 L/hr. For higher flow rates, more fluid is again forced to the last channels resulting in increased flow mal-distribution. Figure 7.23 shows even increasing flow maldistribution predicted by the numerical results, while the analytical results show slightly decreasing trends.

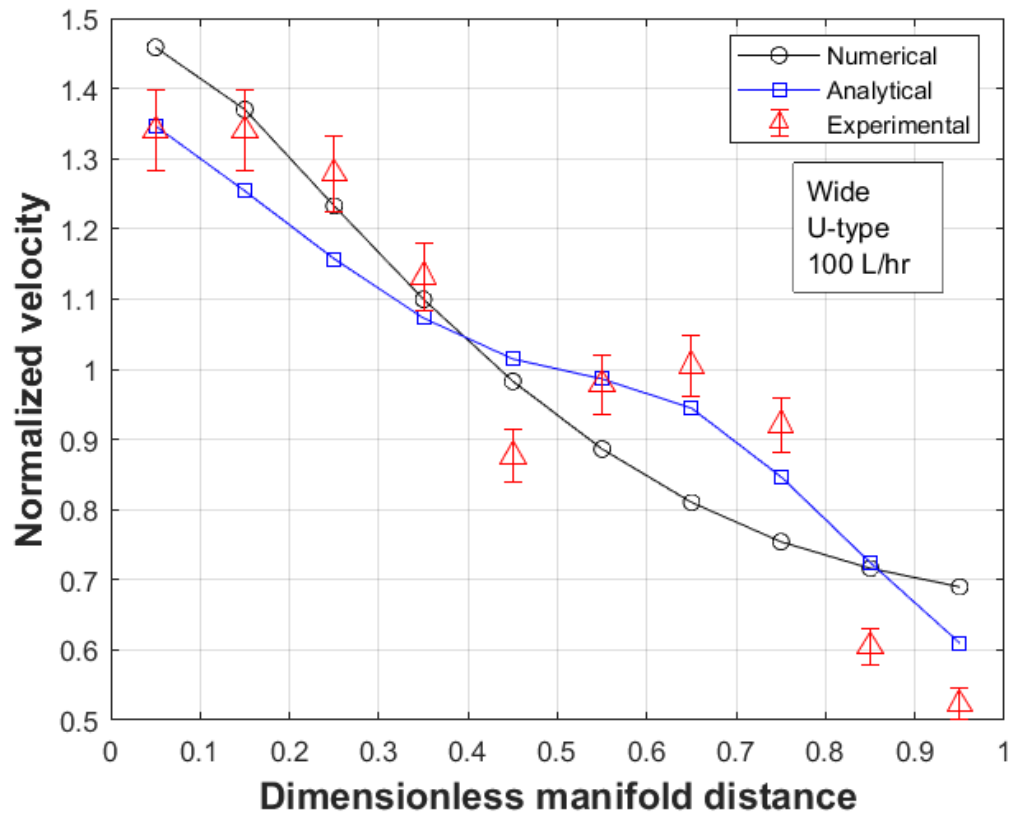


Figure 7.18 Comparison between numerical, analytical, and experimental models for the flow rate distribution in the channels.. U-type, wide manifold, 100 L/hr.

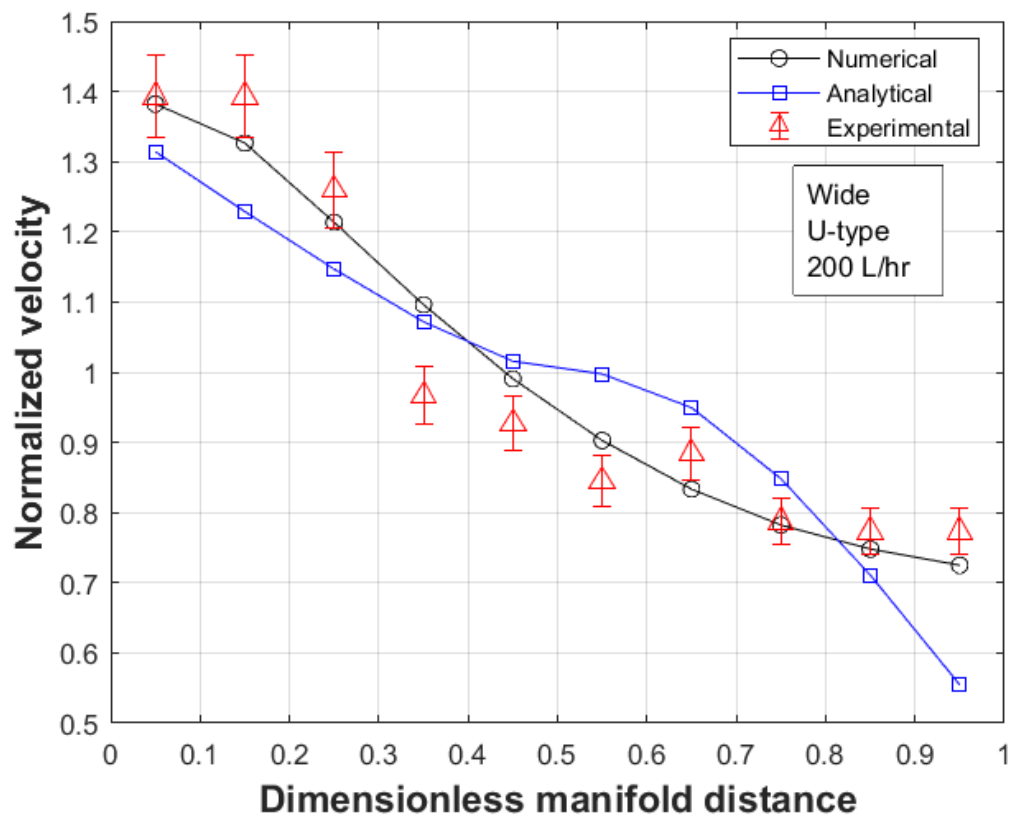


Figure 7.19. Comparison between analytical and numerical models for the flow rate distribution in the channels. U-type, wide manifold, 200 L/hr.

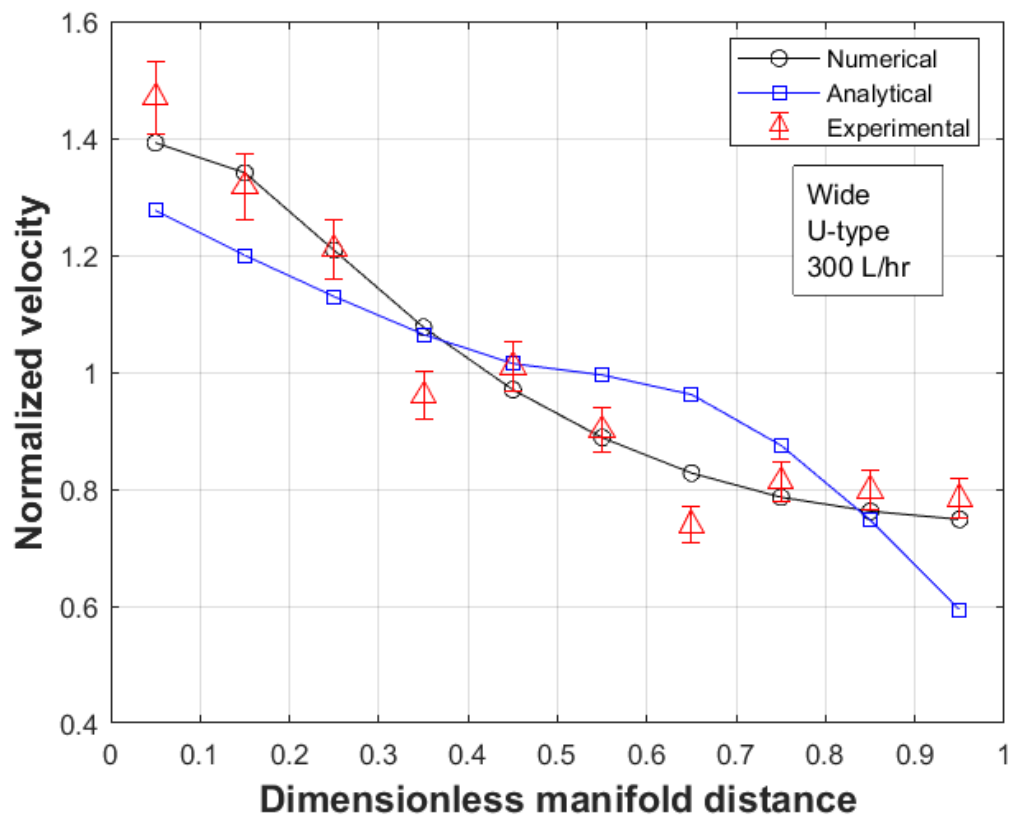


Figure 7.20. Comparison between numerical, analytical, and experimental models for the flow rate distribution in the channels. U-type, wide manifold, 300 L/hr.

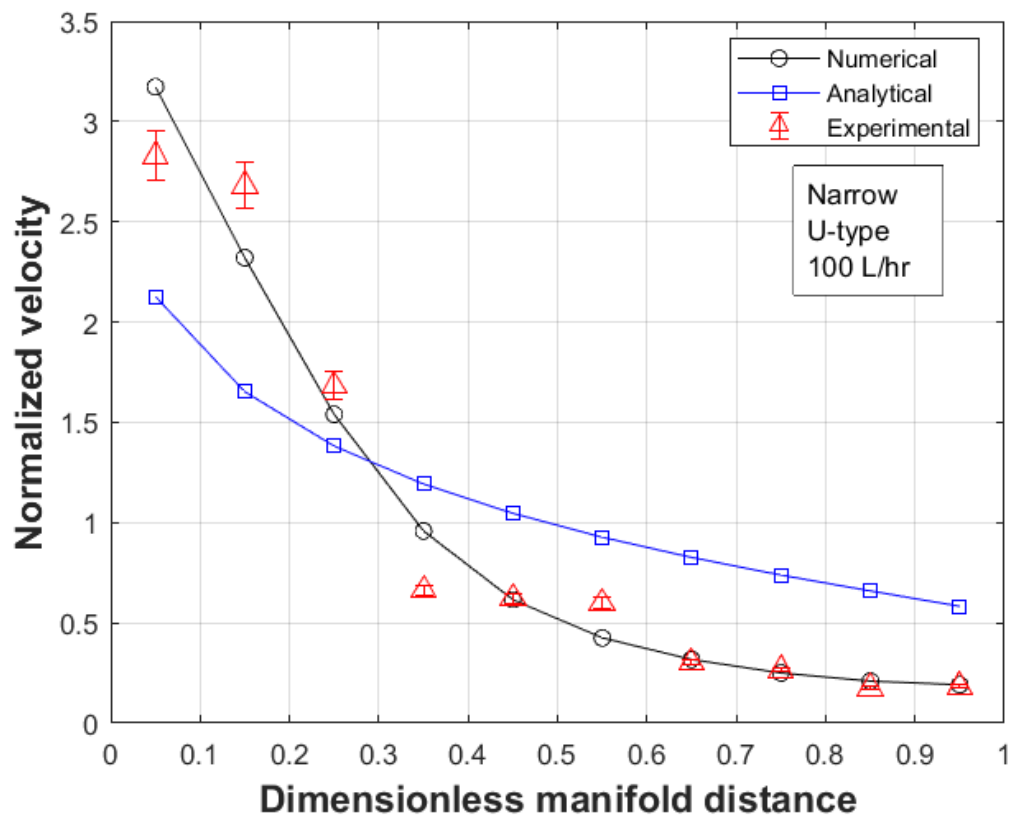


Figure 7.21. Comparison between numerical, analytical, and experimental models for the flow rate distribution in the channels. U-type, normal manifold, 100 L/hr.

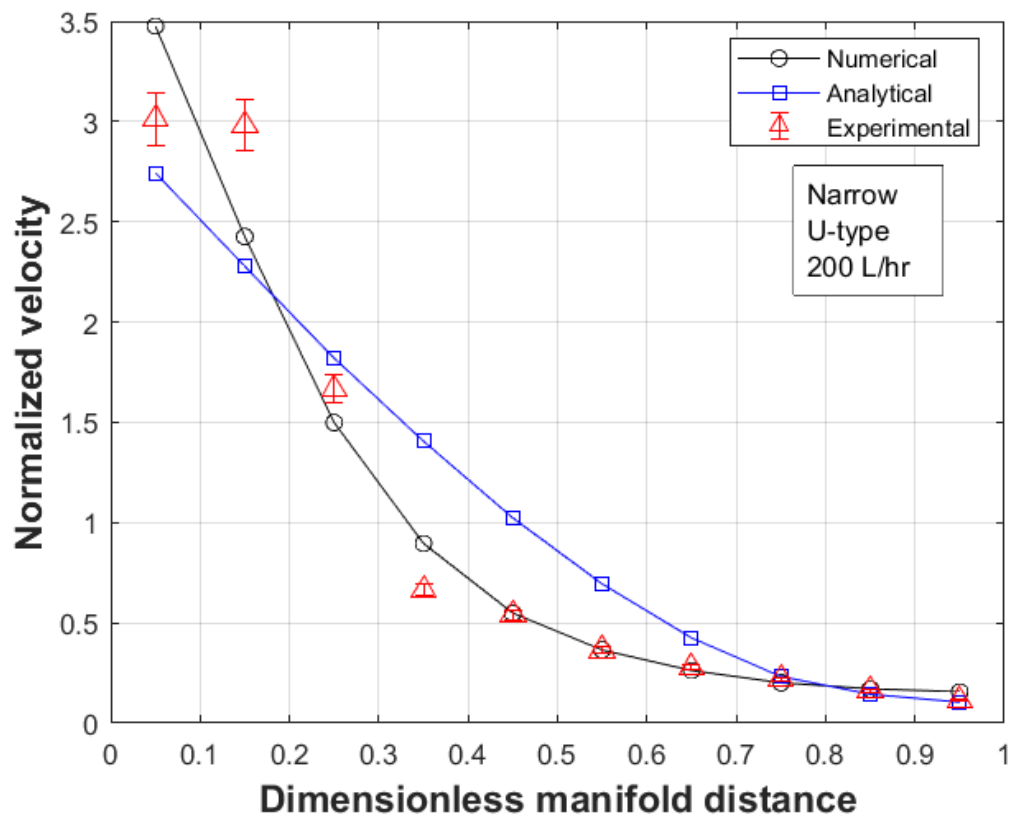


Figure 7.22. Comparison between numerical, analytical, and experimental models for the flow rate distribution in the channels. U-type, normal manifold, 200 L/hr.

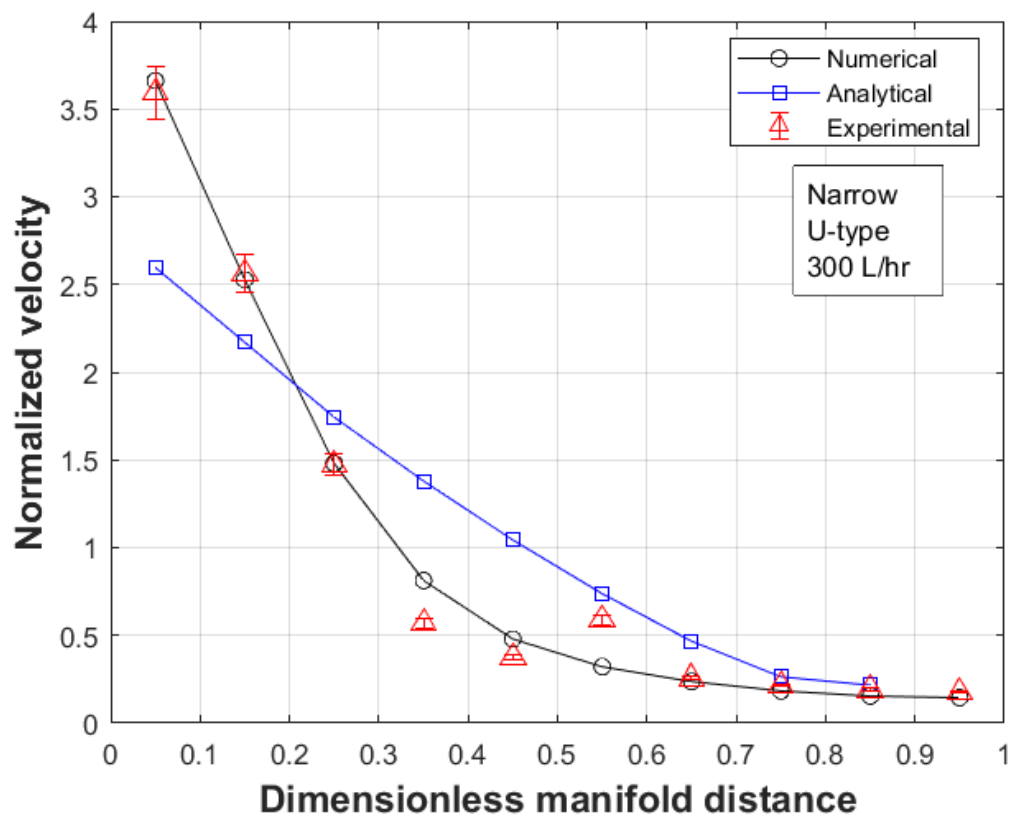


Figure 7.23. Comparison between numerical, analytical, and experimental models for the flow rate distribution in the channels. U-type, normal manifold, 300 L/hr.

7.5.2.2 Z-Type

For the Z-type design, the results are presented based on the coefficients presented in Table 7.7. Figure 7.24 shows the results for the flow rate of 100 L/hr, where it is evident, for the wide manifold, that initial channels have lower velocity with higher values for the later channels. Figure 7.25 and Figure 7.26 shows somewhat close predictions, for the higher flowrates. For the narrow manifold, Figure 7.27, Figure 7.28, and Figure 7.29 show higher predictions for the middle channels, with somewhat closer values for the side channels.

It can be concluded from these results that the analytical models are relatively useful means for flow distribution studies, but this also present the limitations of the analytical model. It has been found that the analytical models of flow distribution in manifold are significantly affected by the turn loss coefficient. It has also been demonstrated that these coefficients are not constants, rather vary significantly for each layout and between channels. They are theoretically sound, but the involvement of the experimental or numerical values for the momentum coefficient and the turn loss coefficient, strongly limit their applicability as any slight changes can results in huge differences.

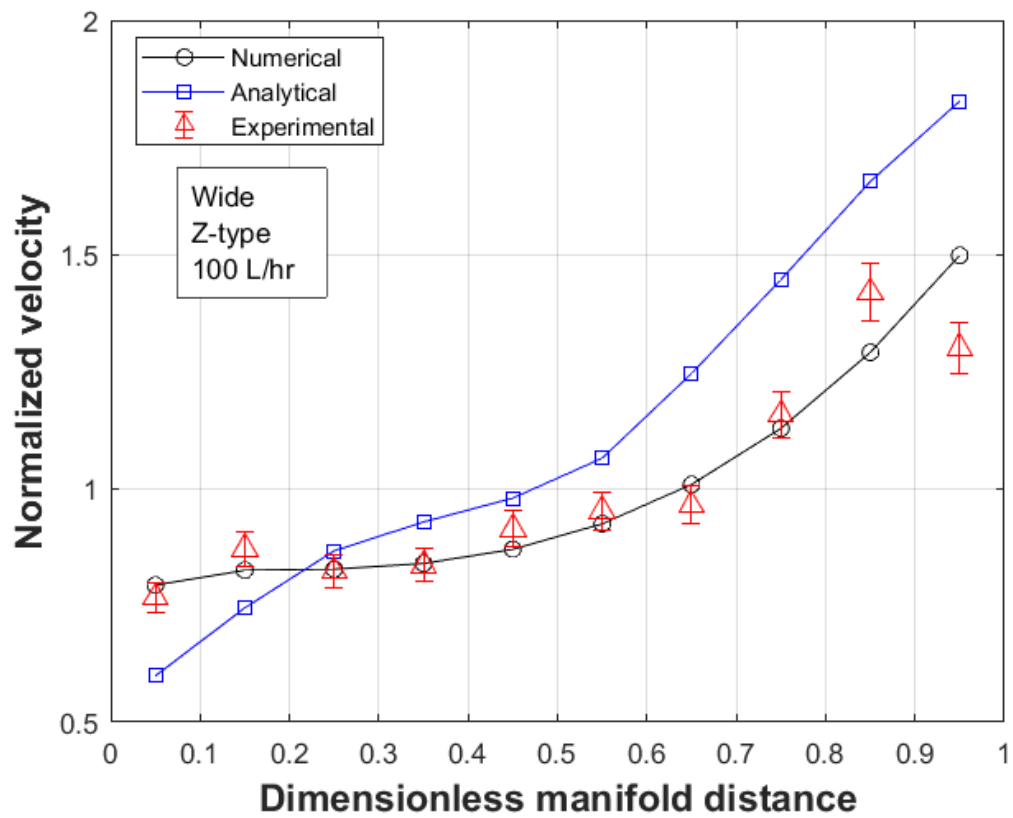


Figure 7.24. Comparison between numerical, analytical, and experimental models for the flow rate distribution in the channels. Z-type, wide manifold, 100 L/hr.

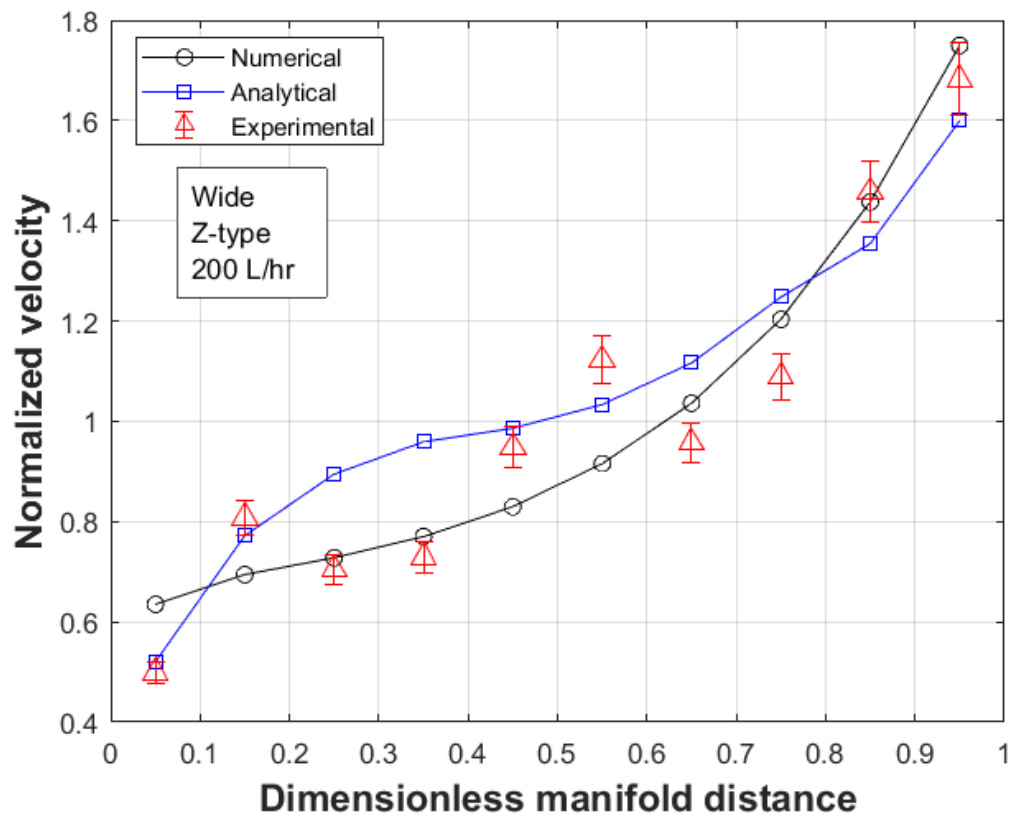


Figure 7.25. Comparison between numerical, analytical, and experimental models for the flow rate distribution in the channels. Z-type, wide manifold, 200 L/hr.

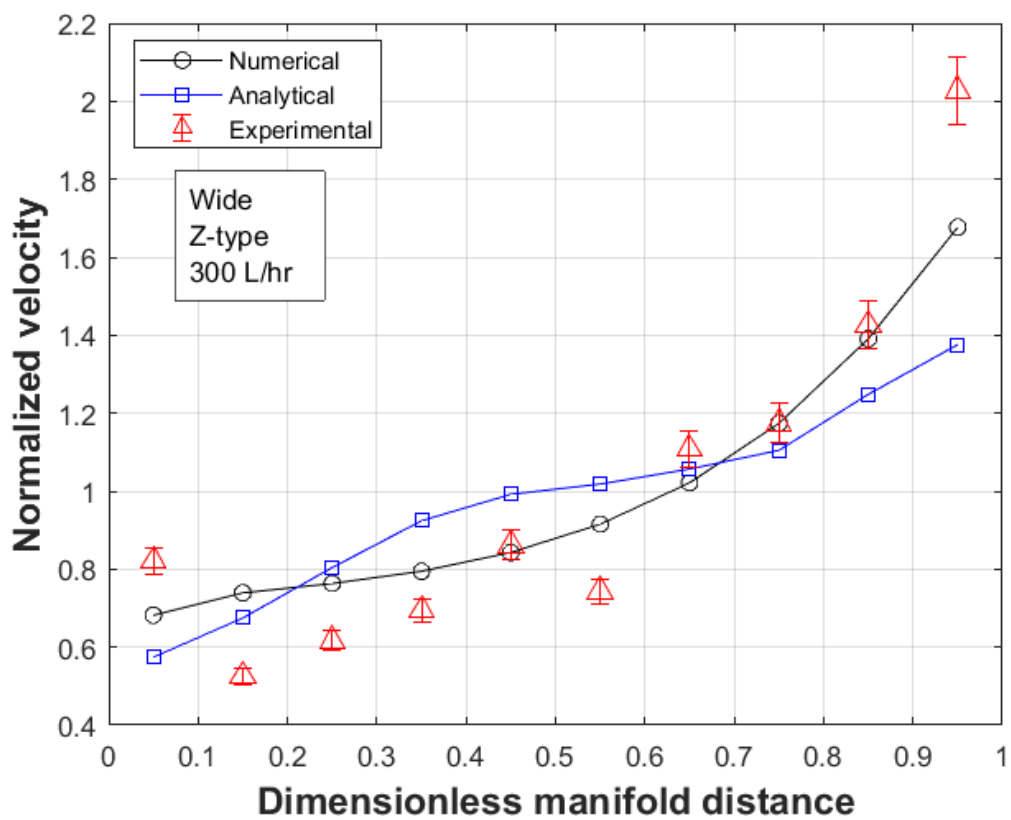


Figure 7.26. Comparison between numerical, analytical, and experimental models for the flow rate distribution in the channels. Z-type, wide manifold, 300 L/hr.

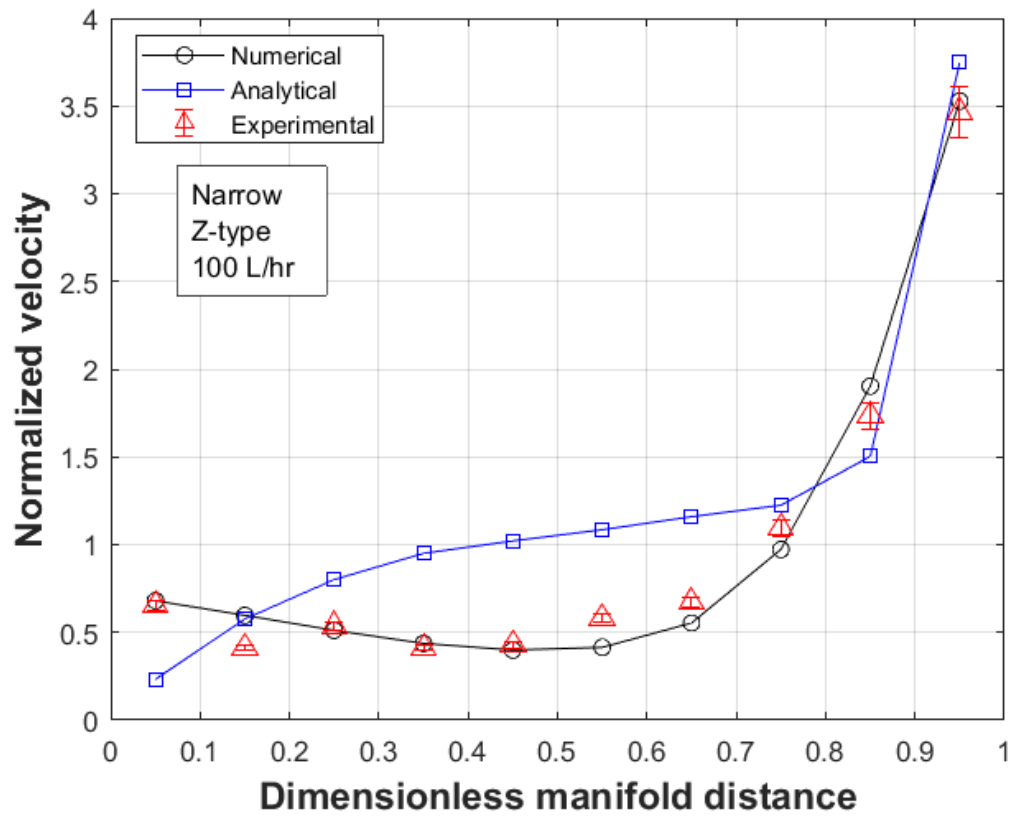


Figure 7.27. Comparison between numerical, analytical, and experimental models for the flow rate distribution in the channels. Z-type, narrow manifold, 100 L/hr.

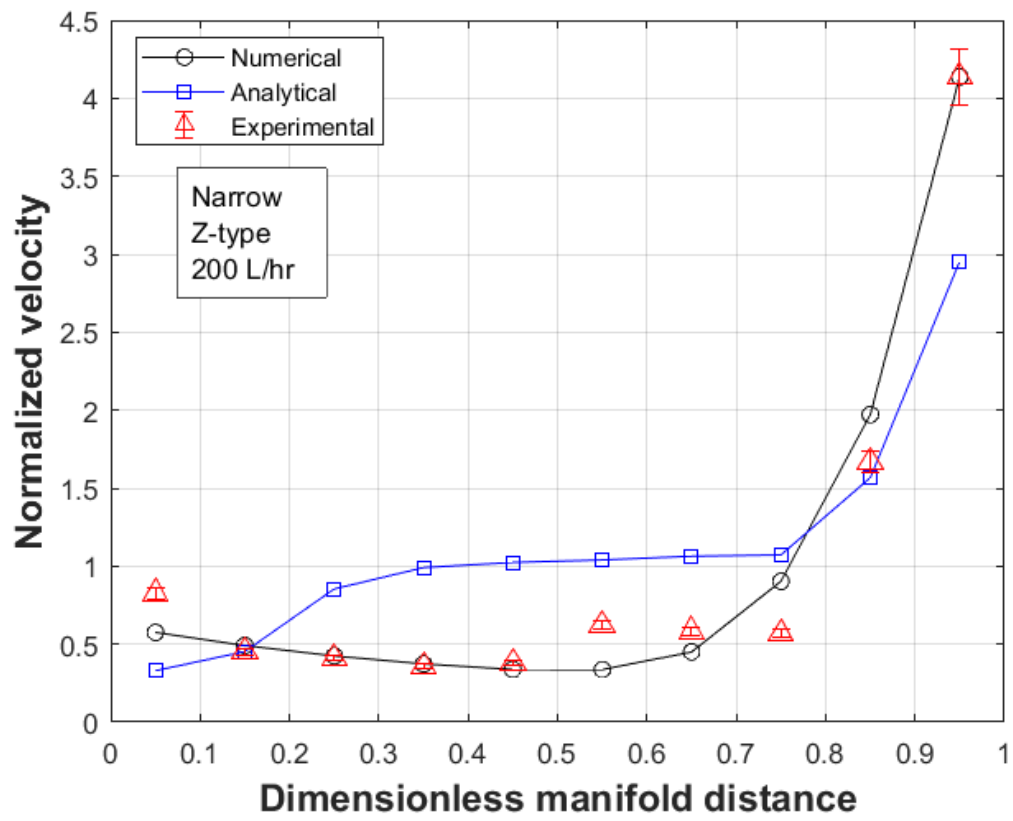


Figure 7.28. Comparison between numerical, analytical, and experimental models for the flow rate distribution in the channels. Z-type, narrow manifold, 200 L/hr.

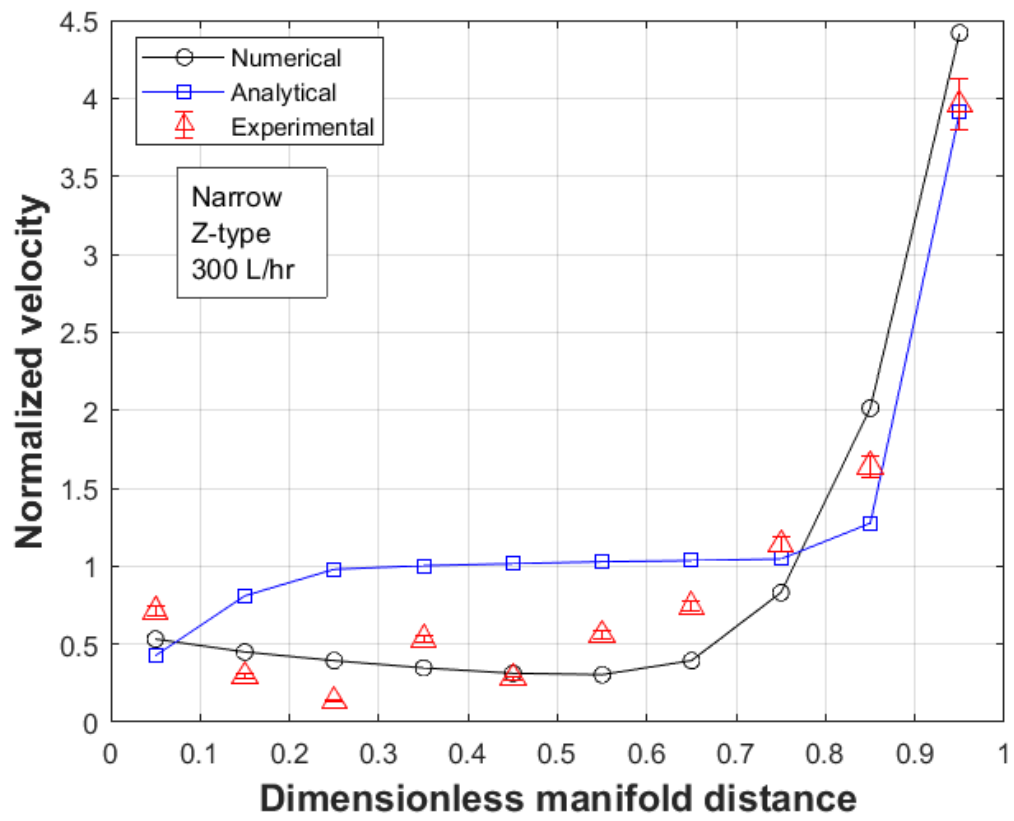


Figure 7.29. Comparison between numerical, analytical, and experimental models for the flow rate distribution in the channels. Z-type, narrow manifold, 300 L/hr.

Chapter 8

CONCLUSION AND FUTURE WORK

This chapter is divided into four sections. In the first three sections, concluding remarks on results in the previous chapter are presented. In the last section, some directions are given in which this work can be extended.

8.1 Concluding remarks

A micro-channel heat exchanger has seen numerous applications on different scales, as studied by several researchers that are discussed in this paper. Most of the work is focused on making the flow uniform across all the channels, ensuring flow uniformity is the first step in ensuring thermal uniformity. The flow uniformity reduces the pressure losses along with the enhancement of thermal performance and effectiveness of these heat exchangers.

With regards to the split flow with manifold heating, the observations can be summarized as:

- a) The comparison of the area-weighted and the mass-weighted average temperature is demonstrated, which shows mass weighted average should be

used to find the mean cross-sectional temperature. The area weighted average always overpredicts the local Nusselt number.

- b) The impact of heating of the manifold in addition to the tubes has been examined, it has been found that the boundary layer creates non-axisymmetric flow in tubes and reduces the performance of outer surfaces. This performance reduction is evident by the reduced Nusselt number at the outer periphery. Hence, in cases where the manifold cannot be isolated from the external heating, attention should be given to the reduced thermal performance of a heat exchanger.
- c) The Nusselt number is always positive for cooling or heating but for cases of non-uniform inlet temperature, a negative Nusselt number (based on classical axisymmetric assumption) can occur due to the surface temperature being lower than the mean temperature. Keeping in view that heat is being inputted into the system, a modified procedure is recommended for such non-axisymmetric flows to ensure proper positive Nusselt numbers.
- d) For non-axisymmetric cases, it has been demonstrated that the modified mean temperature calculated from the linear integral between the minimum temperature locations to the surface provides an appropriate procedure to calculate the Nusselt number in accordance with the applied wall heat flux.

- e) The performance increase for the constant wall temperature is quite prominent when moving from a single tube to 4 tubes to 37 tubes, whereas the performance improvement is very small when constant heat flux is considered as the surface boundary condition.

With regards to analogy assessment for individual cases, the results can be summarized as:

- (a) Couette flow: For a low Prandtl number, average velocity should be used while for higher Prandtl number, the maximum velocity is recommended. Significant disagreement does exist for such flow types, with Chilton-Colburn analogy ratio varying between 0.85 and 1.57.
- (b) Circular tube: Chilton-Colburn analogy with maximum velocity is suitable for laminar, while average velocity for turbulent flow. For $Pr < 1$, average velocity is preferred with decreasing error as a function of increasing Reynolds number. This behavior is similar for both the constant heat flux and constant wall temperature boundary conditions.
- (c) Parallel plate: For constant temperature cases, the profiles are almost straight, while for constant heat flux case, the profiles are rounded with end points remaining largely same. The maximum velocity is a suitable choice for the majority of flow conditions in both heat flux and temperature cases. For $Pr = 6.9$, maximum velocity for a laminar constant temperature case provides

reliable results, while average velocity for turbulent constant wall flux, seems better with analogy ratio up to 1.5.

- (d) Flat plate: Excellent results are obtained for constant wall temperature cases under laminar flow over a flat plate. For turbulent flow, the ratio starts to increase from 0.95 to 1.72 for increasing Prandtl number. For constant heat flux cases, the ratio is about 1.3 for all Prandtl number cases in a laminar flow condition. For turbulent flow, the ratio increases from 0.99 to 1.74 for increasing Prandtl number.

With regards to the flow distribution studies, the following are the major outcomes

- (a) From the numerical study, it has been found that for the U-type, the flowrate is more in the initial channels, and as the flow rate increases, the momentum of the fluid forces more fluid into the latter channels leading to better flow distribution. The narrow manifold had larger maldistribution, with better results for the wider manifold. The presence of stagnation flow at the corners of wider manifold led to higher surface temperature values, resulting in lower Nusselt number. Also, the Nusselt number is higher for the initial channels and lower for the later channels.
- (b) For the analytical study, the model has been validated for the case of wide and normal manifold width, with both the U-type and Z-type arrangements.

The flow coefficients of momentum change and turn loss coefficients are determined and presented. The analytical model is tested with the numerical model and good agreements are found between them.

- (c) For the experimental study, the manifold designs were fabricated, and particle image velocimetry was used to obtain the velocities for each channel. The designs were modelled with both U- and Z-type arrangements. The velocity profiles were obtained for the channels and good agreements were found between the experimental and numerical results. With regards to the flow distribution, the overall trend was matching for all the cases, however there were some variations which can be attributed to the laminations of the PIV system for the current application. One of the reasons was that the laser was illuminating the outer channels better, while the light was diminished when it reached the middle channels.

8.2 Future work directions

For the heat exchange design, following recommendation are made for future work directions.

- (a) The fluid may be incorporated with phase change materials, where the heat storing capability of the PCM material would result in lower temperatures, thereby enhancing the performance.

- (b) Temperature dependent properties may be used in the analytical and numerical modelling to account for the variation in the density and viscosity of the fluid.
- (c) The study of the actual temperature variation may be studied to validate numerical results with the experimental results.
- (d) Variation of the number of channels may be included in the analytical modelling, with proper calculation of the governing flow coefficients.
- (e) The coefficients for different configurations can be calculated so that they can be used for future users who intend to use the model for their variations of the manifold.

Appendix A: UNCERTAINTY ANALYSIS FOR THE PIV MEASUREMENTS

This appendix is related to the calculation of uncertainty in velocity measurements provided by PIV system. The uncertainty analysis is performed on a data that is derived from multiple experimentally determined quantities. In this regards the data reduction equation is of the form,

$$R = f (X_1, X_2, X_3, \dots) \quad (A.1)$$

The uncertainty analysis of this equation is of the following form,

$$\left[\frac{U_R}{R} \right]^2 = \left[\frac{1}{R} \frac{\partial R}{\partial X_1} U_{X_1} \right]^2 + \left[\frac{1}{R} \frac{\partial R}{\partial X_2} U_{X_2} \right]^2 + \left[\frac{1}{R} \frac{\partial R}{\partial X_3} U_{X_3} \right]^2 + \dots \quad (A.2)$$

where U represent the total uncertainty associated with a particular variable.

The uncertainty analysis equation provides the information on how the uncertainties of the individually determined quantities are propagated to affect the uncertainty of the calculated variable. With regards to the uncertainty in the velocity itself, the following equation can be used to find the relation between the measurements that affect the velocity itself.

$$u = \frac{\dot{m}_{inlet}/10}{\rho A_{ch}} \quad (A.3)$$

This relation can be explained in more detail as follows. The flowrate is being measured by a rotameter, hence we have uncertainty related to the flowrate measurement. This flow rate is divided into 10 channels, such that average flow rate is $1/10^{\text{th}}$ in each channel. This mass flow rate is converted into velocity by using the continuity equation, where the density is standard for water. The area is of the channel, which is the product of width and depth of the channel. This area has its uncertainty in its measurements. Hence, the three factors affecting the uncertainty in the velocity are width and height of channel in addition to the flowmeter.

By performing uncertainty analysis Eq.(A.2) on the data reduction Eq. (A.3), we obtain the following expression

$$\left[\frac{U_u}{\dot{m}_u} \right]^2 = \left[\frac{1}{u} \frac{\partial u}{\partial \dot{m}_{in}} U_{\dot{m}_{in}} \right]^2 + \left[\frac{1}{u} \frac{\partial u}{\partial A_c} U_{A_c} \right]^2 \quad (\text{A.4})$$

where the two terms on right side are evaluated as

$$\left[\frac{1}{u} \frac{\partial u}{\partial \dot{m}_{inlet}} U_{\dot{m}_{inlet}} \right] = \left[\frac{1}{\frac{\dot{m}_{inlet}/10}{\rho A_{ch}}} \frac{1/10}{\rho A_{ch}} U_m \right] = \left[\frac{U_{\dot{m}_{inlet}}}{\dot{m}_{inlet}} \right] \quad (\text{A.5})$$

and

$$\left[\frac{1}{u} \frac{\partial u}{\partial A_{ch}} U_{A_{ch}} \right] = \left[\frac{1}{\frac{\dot{m}_{inlet}/10}{\rho A_{ch}^2}} \frac{-\dot{m}_{inlet}/10}{\rho A_{ch}^2} U_m \right] = \left[-\frac{U_m}{\dot{m}_{inlet}} \right] \quad (A.6)$$

Hence, Eq.(A.4) becomes

$$\left[\frac{U_u}{u} \right]^2 = \left[\frac{U_{\dot{m}_{in}}}{\dot{m}_{in}} \right]^2 + \left[\frac{U_{A_c}}{A_c} \right]^2 \quad (A.7)$$

It is important to note that if there is a higher order term in the data reduction equation, the corresponding uncertainty term of that variable has power times the contribution towards the total uncertainty. In the current cases, all the terms are of first order, so a simple root-sum-square (RSS) of the uncertainties will provide the total uncertainty. Here the area can be split into the width and height of the channel separately to account for their independent uncertainties as:

$$\left[\frac{U_u}{u} \right]^2 = \left[\frac{U_{\dot{m}_{in}}}{\dot{m}_{in}} \right]^2 + \left[\frac{U_b}{b} \right]^2 + \left[\frac{U_h}{h} \right]^2 \quad (A.8)$$

The measurements of the height and width of each channel was obtained using a digital Vernier caliber of resolution 0.01mm. The maximum and minimum values, obtained, are presented in Table A.1

The standard deviation is found by summing the square of difference of each point from the mean value, divided by one less than the total number of samples. The square root of this value is the standard deviation, as shown by the equation. The normalized value is obtained in percentage by dividing the standard deviation by the average value.

$$S_x = \sqrt{\frac{\sum_{i=1}^n (x_i - \bar{x})^2}{n-1}} \quad (\text{A.9})$$

For the flow rate, it is being supplied by a continuous centrifugal pump. The flow rate is being measured with a rotameter which has a measurement uncertainty of 4%. By inserting the values of 4% for mass flow rate uncertainty of the rotameter and 5.33% for width and 0.97% for height, the total uncertainty in the velocity of the channel is about 6.85%. This is the uncertainty associated with the actual velocity, not velocity measurements.

The measurement of velocity with the use of PIV involves correlating multiple images to identify the change in position of the illuminated particles. In this process, the time is a fixed value, the value of which is provided by the imaging source, that depends on the frame rate for the images. Hence it is the distance measurement that has uncertainty associated with it. Now regarding the uncertainty associated with the PIV system, multiple values have been found in the literature. Sciacchitano et al. [185] discussed in details the procedure to calculate the actual uncertainty in the PIV measurements by super-resolution principle, where the cross-correlated distance is compared with the residual between the

particles in the paired images. This comparison was made for all the particles and in this way, they were able to demonstrate the uncertainties associated with the PIV measurements. They mentioned the use of 0.1 pixel as the accuracy for the PIV systems. For the current case, the velocity was about 1.6 pixels, which converts to about 6.25% uncertainty. They demonstrated that the use of larger image can result in large variations. It was noticed in the author's current work that if the complete channel was used, it results in error of about an order of magnitude. For this reason, only a smaller portion of properly illuminated particles was used for each channel, that resulted in excellent results. They further concluded that accuracy of 0.01 pixels was obtained for the RMS error. In another study [186], they computed the uncertainty of average velocities and found they were within 5% of the actual values. Hence, a value of 5% can be associated with the PIV system velocity measurements.

Combining this error (5%) with the previously calculated velocity uncertainty (6.85%), we can obtain the total uncertainty in velocity measurement, for the current setup, using RSS to be about 8.48% which can be presented as $\pm 4.24\%$. This value is used for all the experimental data shown in Chapter 7.

Table A.1. The characteristics of the sample data for the calculation of channel area uncertainty.

Statistic	Width (mm)	Height (mm)
Maximum	22.76	5.37
Minimum	22.00	4.55
Average	22.42	4.99
Standard deviation	0.22	0.27
Normalized Standard deviation	0.98%	5.47%

Appendix B: MATLAB CODES

B.1. Calculation of Nusselt number for non-axisymmetric flows

function

```
Nu_local_z_theta=Nusselt_number_at_crossection(input_a,input_b,input_c,input_d,input_e);
```

```
thermal_cond=0.0242;
```

```
x_hf=read_mixed_csv_xyplot(input_a);
```

```
y_hf=read_mixed_csv_xyplot(input_b);
```

```
x_st=read_mixed_csv_xyplot(input_c);
```

```
y_st=read_mixed_csv_xyplot(input_d);
```

```
y_min=min(y_hf(:,1))
```

```
y_max=max(y_hf(:,1))
```

```
y_diff=y_max-y_min
```

```
y_avg=(y_min+y_max)/2
```

```
x_min=min(x_hf(:,1))
```

```
x_max=max(x_hf(:,1))
```

```
x_diff=x_max-x_min
```

```
x_avg=(x_min+x_max)/2
```

```
diameter=y_diff;
```

```
[surface_values,n] = size(x_hf);
```

```
all_surface_data=[x_hf(:,1) y_hf(:,1) x_hf(:,2) x_st(:,2)];
```

```
surface_data_to_use=[];
```

```
for n=1:surface_values
```

```
    if all_surface_data(n,3)~=0
```

```
        surface_data_to_use=[surface_data_to_use;all_surface_data(n,:)];
```

```
    end
```

```
end
```

```
[surface_values_use,na] = size(surface_data_to_use);
```

```
%for internal data from profile-----
```

```
outlet_total_temp=read_mixed_csv_prof(input_e);
```

```

[mesh_number,aa] = size(outlet_total_temp);

actual_readings=mesh_number/5;
actual_readings_1=actual_readings*1;
actual_readings_2=actual_readings*2;
actual_readings_3=actual_readings*3;
actual_readings_4=actual_readings*4;
actual_readings_5=actual_readings*5;

outlet_total_temp_x=outlet_total_temp(1:actual_readings_1,1);
outlet_total_temp_y=outlet_total_temp(actual_readings_1+1:actual_readings_2,1);
z=outlet_total_temp(actual_readings_2+1)
outlet_total_temp_v=outlet_total_temp(actual_readings_3+1:actual_readings_4,1);
outlet_total_temp_t=outlet_total_temp(actual_readings_4+1:actual_readings_5,1);
outlet_total_temp_a=[outlet_total_temp_x outlet_total_temp_y outlet_total_temp_v
outlet_total_temp_t];

[M,I] = min(outlet_total_temp_a(:,4));
[Ik,J] = find(outlet_total_temp_a(:,4)==M,5);
Minimum_temp_cordinates=outlet_total_temp_a(Ik,1:2);
Axis_xy=mean(Minimum_temp_cordinates);
abc=zeros(surface_values_use,1);

su_dat_to_add_inter=[surface_data_to_use(:,1) surface_data_to_use(:,2) abc
surface_data_to_use(:,4)];

outlet_total_temp_a=[outlet_total_temp_a;su_dat_to_add_inter];

slope=0;
t_m=[];
utr=[];
ur=[];
arr_interp=[];
Nu_local=[];
Nu_local_z_theta=[];

```

```

thethaa=[];
for naa=1:surface_values_use

    p_1=Axis_xy;
    xp=p_1(1,1);
    yp=p_1(1,2);
    p_2=[surface_data_to_use(naa,1) surface_data_to_use(naa,2)];
    dx=(p_2(1,1)-Axis_xy(1,1));
    dy=(p_2(1,2)-Axis_xy(1,2));

    x_division=10;
    slope=((p_2(1,2)-Axis_xy(1,2))/(p_2(1,1)-Axis_xy(1,1)));
    dx_internal=dx/x_division;
    dy_internal=slope*dx_internal;

    if slope==Inf || slope==-Inf
        dx_internal=0;
        dy_internal=dy/x_division;
    end

    sum_utr=0;
    sum_ur=0;

    F_v =
    scatteredInterpolant(outlet_total_temp_a(:,1),outlet_total_temp_a(:,2),outlet_total_temp_
a(:,3));
    F_t =
    scatteredInterpolant(outlet_total_temp_a(:,1),outlet_total_temp_a(:,2),outlet_total_temp_
a(:,4));

    dr=0;
    for x=1:x_division
        x_n=xp+(dx_internal*x);
        y_n=yp+(dy_internal*x);
        Vel=F_v(x_n,y_n);
        temp=F_t(x_n,y_n);
        dr=dr+sqrt((dx_internal^2)+(dy_internal^2));
        utr=Vel*temp*dr;
        sum_utr=sum_utr+(Vel*temp*dr);
    end
end

```



```

sum_ur=sum_ur+(Vel*dr);
ur=Vel*dr;
arr_interp=[arr_interp;x_n y_n Vel temp dr (Vel*temp*dr) (Vel*dr) sum_utr
sum_ur];
end
t_m=[t_m;(sum_utr/sum_ur)];
Nu_local=[Nu_local;(p_2(1,1)) (p_2(1,2))
(((surface_data_to_use(naa,3))/(surface_data_to_use(naa,4)-
t_m(naa,1)))*diameter)/thermal_cond)];
x_theta=(p_2(1,1)-x_avg);
y_theta=(p_2(1,2)-y_avg);
thetaa=atan2d(y_theta,x_theta);

if thetaa<0
thetaa=thetaa+360;
end
Nu_local_z_theta=[Nu_local_z_theta;z thetaa
(((surface_data_to_use(naa,3))/(surface_data_to_use(naa,4)-
t_m(naa,1)))*diameter)/thermal_cond)];
end
end

```

B.2. Calculation of Nusselt number in channels

```
function data_sorted=code_channel(plane);
[x,t]=importfile_xy(strcat(plane,'-X.xy'));
[y,t]=importfile_xy(strcat(plane,'-Y.xy'));
[z,t]=importfile_xy(strcat(plane,'-Z.xy'));
[x,v]=importfile_xy(strcat(plane,'-X-V.xy'));
[y,v]=importfile_xy(strcat(plane,'-Y-V.xy'));
[z,v]=importfile_xy(strcat(plane,'-Z-V.xy'));
[x,tau]=importfile_xy(strcat(plane,'-X-taus.xy'));

total_data=[x y z v t tau];
total_data_final=[];
for i = 1:size(total_data)
    if total_data(i,3)==0.005;
        total_data_final=[total_data_final;total_data(i,:)];
    end
end
tm=importfile_tm (strcat(plane,'-mean_t.xy'));
vm=importfile_tm (strcat(plane,'-mean_v.xy'));
data_sorted = sortrows(total_data_final,1);
Width=max(total_data_final(:,2))-min(total_data_final(:,2));
Height=0.005;
D_hy=2*Width*Height/(Width+Height);
Nu=1000.*D_hy./(0.6.*(data_sorted(:,5)-tm));
Nu_star=1000.*D_hy./(0.6.*(data_sorted(:,5)-298));
St=(1000./(998.2.*vm.*4182.*(data_sorted(:,5)-tm)));
St_star=(1000./(998.2.*vm.*4182.*(data_sorted(:,5)-298)));
Cf2=(data_sorted(:,6)./(998.2*(vm^2)/2))/2;
Mean=[mean(Nu);mean(Nu_star);mean(St);mean(St_star);mean(Cf2);mean(St)/mean(Cf
2);zeros(size(Nu,1)-6,1)] ;
data_sorted=[data_sorted Nu Nu_star St St_star Cf2 St./Cf2 Mean];
end
```

B.3. Calculation of Nusselt number in manifold.

```
function data_sorted=code(plane);
[x,t]=importfile_xy(strcat(plane,'-X.xy'));
[y,t]=importfile_xy(strcat(plane,'-Y.xy'));
[z,t]=importfile_xy(strcat(plane,'-Z.xy'));
[x,v]=importfile_xy(strcat(plane,'-X-V.xy'));
[y,v]=importfile_xy(strcat(plane,'-Y-V.xy'));
[z,v]=importfile_xy(strcat(plane,'-Z-V.xy'));
[x,tau]=importfile_xy(strcat(plane,'-X-taus.xy'));
total_data=[x y z v t tau];
total_data_final=[];
for i = 1:size(total_data)
    if total_data(i,3)==0.005;%to get only surface
        total_data_final=[total_data_final;total_data(i,:)];
    end
end
tm=importfile_tm (strcat(plane,'-mean_t.xy'));
vm=importfile_tm (strcat(plane,'-mean_v.xy'));
data_sorted = sortrows(total_data_final,2);
Width=max(total_data_final(:,1))-min(total_data_final(:,1));
Height=0.005;
D_hy=2*Width*Height/(Width+Height);
Nu=1000.*D_hy./(0.6.*(data_sorted(:,5)-tm));
Nu_star=1000.*D_hy./(0.6.*(data_sorted(:,5)-298));
St=(1000./(998.2.*vm.*4182.*(data_sorted(:,5)-tm)));
St_star=(1000./(998.2.*vm.*4182.*(data_sorted(:,5)-298)));
Cf2=(data_sorted(:,6)./(998.2*(vm^2)/2))/2;
Mean=[mean(Nu);mean(Nu_star);mean(St);mean(St_star);mean(Cf2);mean(St)/mean(Cf
2);zeros(size(Nu,1)-6,1)] ;
data_sorted=[data_sorted Nu Nu_star St St_star Cf2 St./Cf2 Mean];
end
```

REFERENCES

- [1] N. Srihari, B. Prabhakara Rao, B. Sunden, S.K. Das, Transient response of plate heat exchangers considering effect of flow maldistribution, *Int. J. Heat Mass Transf.* 48 (2005) 3231–3243.
- [2] R. Karwa, N. Karwa, R. Misra, P.C. Agarwal, Effect of flow maldistribution on thermal performance of a solar air heater array with subcollectors in parallel, *Energy*. 32 (2007) 1260–1270.
- [3] J.M. Yin, C.W. Bullard, P.S. Hrnjak, Single-Phase Pressure Drop Measurements in a Microchannel Heat Exchanger, *Heat Transf. Eng.* 23 (2002) 3–12.
- [4] R.W. Knight, D.J. Hall, J.S. Goodling, R.C. Jaeger, Heat sink optimization with application to microchannels, *IEEE Trans. Components, Hybrids, Manuf. Technol.* 15 (1992) 832–842.
- [5] N. Goldberg, Narrow Channel Forced Air Heat Sink, *IEEE Trans. Components, Hybrids, Manuf. Technol.* 7 (1984) 154–159.
- [6] D.B. Tuckerman, R.F.W. Pease, High-performance heat sinking for VLSI, *IEEE Electron Device Lett.* 2 (1981) 126–129.
- [7] R.J. Phillips, Micro-channel heat sinks, In: A. Bar-Cohen and A. D. Kraus, editors. *Advances in thermal modeling of electronic components and systems*, 2, ASME Press, New York, NY., ASME, 1990.
- [8] R. Phillips, Microchannel Heat Sinks, *Lincoln Lab. J.* 1 (1988) 31–48.
- [9] S.J. Kim, D. Kim, Forced Convection in Microstructures for Electronic Equipment Cooling, *J. Heat Transfer*. 121 (1999) 639–645.
- [10] A.G. Fedorov, R. Viskanta, Three-dimensional conjugate heat transfer in the microchannel heat sink for electronic packaging, *Int. J. Heat Mass Transf.* 43 (2000) 399–415.
- [11] W.L. Qu, I. Mudawar, Experimental and numerical study of pressure drop and heat transfer in a single-phase micro-channel heat sink, *Int. J. Heat Mass Transf.* 45 (2002) 2549–2565.
- [12] J.H. Ryu, D.H. Choi, S.J. Kim, Numerical optimization of the thermal performance of a microchannel heat sink, *Int. J. Heat Mass Transf.* 45 (2002) 2823–2827.
- [13] J.H. Ryu, D.H. Choi, S.J. Kim, Three-dimensional numerical optimization of a manifold microchannel heat sink, *Int. J. Heat Mass Transf.* 46 (2003) 1553–1562.
- [14] E.G. Colgan, B. Furman, M. Gaynes, W.S. Graham, N.C. LaBianca, J.H. Magerlein, et al., A practical implementation of silicon microchannel coolers for high power chips, *IEEE Trans. Components Packag. Technol.* 30 (2007) 218–225.
- [15] S. Sarangi, K.K. Bodla, S. V Garimella, J.Y. Murthy, Manifold microchannel heat

sink design using optimization under uncertainty, *Int. J. Heat Mass Transf.* 69 (2014) 92–105.

- [16] R.K. Mathur, D.R. Mehrotra, S. Mittal, S.R. Dhariwal, Thermal non-uniformities in concentrator solar cells, *Sol. Cells.* 11 (1984) 175–188.
- [17] E. Radziemska, E. Klugmann, Thermally affected parameters of the current–voltage characteristics of silicon photocell, *Energy Convers. Manag.* 43 (2002) 1889–1900.
- [18] E. Radziemska, The effect of temperature on the power drop in crystalline silicon solar cells, *Renew. Energy.* 28 (2003) 1–12.
- [19] J.S. Coventry, Performance of a concentrating photovoltaic/thermal solar collector, *Sol. Energy.* 78 (2005) 211–222.
- [20] A. Royne, C.J. Dey, D.R. Mills, Cooling of photovoltaic cells under concentrated illumination: a critical review, *Sol. Energy Mater. Sol. Cells.* 86 (2005) 451–483.
- [21] N. Amin, C.W. Lung, K. Sopian, A practical field study of various solar cells on their performance in Malaysia, *Renew. Energy.* 34 (2009) 1939–1946.
- [22] G.N. Tiwari, R.K. Mishra, S.C. Solanki, Photovoltaic modules and their applications: A review on thermal modelling, *Appl. Energy.* 88 (2011) 2287–2304.
- [23] K.A. Moharram, M.S. Abd-Elhady, H.A. Kandil, H. El-Sherif, Enhancing the performance of photovoltaic panels by water cooling, *Ain Shams Eng. J.* 4 (2013) 869–877.
- [24] H. Bahaidarah, A. Subhan, P. Gandhidasan, S. Rehman, Performance evaluation of a PV (photovoltaic) module by back surface water cooling for hot climatic conditions, *Energy.* 59 (2013) 445–453.
- [25] D. Du, J. Darkwa, G. Kokogiannakis, Thermal management systems for Photovoltaics (PV) installations: A critical review, *Sol. Energy.* 97 (2013) 238–254.
- [26] S. Dubey, G.N. Tiwari, Thermal modeling of a combined system of photovoltaic thermal (PV/T) solar water heater, *Sol. Energy.* 82 (2008) 602–612.
- [27] S. Wu, C. Xiong, Passive cooling technology for photovoltaic panels for domestic houses, *Int. J. Low-Carbon Technol.* 9 (2014) 118–126.
- [28] J. Cremers, I. Mitina, N. Palla, F. Klotz, X. Jobard, U. Eicker, Experimental Analyses of Different PVT Collector Designs for Heating and Cooling Applications in Buildings, *Energy Procedia.* 78 (2015) 1889–1894.
- [29] S.R. Reddy, M.A. Ebadian, C.-X. Lin, A review of PV–T systems: Thermal management and efficiency with single phase cooling, *Int. J. Heat Mass Transf.* 91 (2015) 861–871.
- [30] N. Aste, C. Del Pero, F. Leonforte, M. Manfren, Performance monitoring and modeling of an uncovered photovoltaic-thermal (PVT) water collector, *Sol. Energy.* 135 (2016) 551–568.
- [31] R.R. Ratnakar, B. Dindoruk, L. Wilson, Experimental investigation of DME–water–crude oil phase behavior and PVT modeling for the application of DME-enhanced

- waterflooding, *Fuel*. 182 (2016) 188–197.
- [32] G. Evola, L. Marletta, Exergy and thermoeconomic optimization of a water-cooled glazed hybrid photovoltaic/thermal (PVT) collector, *Sol. Energy*. 107 (2014) 12–25.
 - [33] Shyam, G.N. Tiwari, O. Fischer, R.K. Mishra, I.M. Al-Helal, Performance evaluation of N-photovoltaic thermal (PVT) water collectors partially covered by photovoltaic module connected in series: An experimental study, *Sol. Energy*. 134 (2016) 302–313.
 - [34] H.M.S. Bahaidarah, A.A.B. Baloch, P. Gandhidasan, Uniform cooling of photovoltaic panels: A review, *Renew. Sustain. Energy Rev.* 57 (2016) 1520–1544.
 - [35] J.P. Chiou, The effect of nonuniform fluid flow distribution on the thermal performance of solar collector, *Sol. Energy*. 29 (1982) 487–502.
 - [36] G.F. Jones, Consideration of the heat-removal factor for liquid-cooled flat-plate solar collectors, *Sol. Energy*. 38 (1987) 455–458.
 - [37] F. Ghani, M. Duke, J.K. Carson, Effect of flow distribution on the photovoltaic performance of a building integrated photovoltaic/thermal (BIPV/T) collector, *Sol. Energy*. 86 (2012) 1518–1530.
 - [38] J. Laskar, S. Nuttinck, S. Pinel, Thermal Management of High Power Devices, 30332 (2004) 0–3.
 - [39] R. Naewngerndee, E. Hattha, K. Chumpolrat, T. Sangkapes, J. Phongsitong, S. Jaikla, Finite element method for computational fluid dynamics to design photovoltaic thermal (PV/T) system configuration, *Sol. Energy Mater. Sol. Cells*. 95 (2011) 390–393.
 - [40] G. Agrawal, N.S. Kaisare, S. Pushpavanam, K. Ramanathan, Modeling the effect of flow mal-distribution on the performance of a catalytic converter, *Chem. Eng. Sci.* 71 (2012) 310–320.
 - [41] S. Jeong, T. Kim, CFD Investigation of the 3-Dimensional Unsteady Flow in the Catalytic Converter, SAE technical paper 971025, (1997).
 - [42] W. Guojiang, T. Song, CFD simulation of the effect of upstream flow distribution on the light-off performance of a catalytic converter, *Energy Convers. Manag.* 46 (2005) 2010–2031.
 - [43] M. Badami, F. Millo, A. Zuarini, M. Gambarotto, CFD analysis and experimental validation of the inlet flow distribution in close coupled catalytic converters, SAE technical paper 2003-01-3072, (2003).
 - [44] K. Zygourakis, Transient operation of monolith catalytic converters: a two-dimensional reactor model and the effects of radially nonuniform flow distributions, *Chem. Eng. Sci.* 44 (1989) 2075–2086.
 - [45] J. Wollin, S.F. Benjamin, A Study of the flow performance of ceramic contoured substrates for automotive exhaust catalyst systems, SAE technical paper 1999-01-3626, (1999).

- [46] M.-C. Lai, J.-Y. Kim, C.-Y. Cheng, P. Li, G. Chui, J.D. Pakko, Three-dimensional simulations of automotive catalytic converter internal flow, SAE technical paper 910200, (1991).
- [47] C.D. Lemme, W.R. Givens, Flow through catalytic converters - an analytical and experimental treatment, SAE technical paper 740243, (1974).
- [48] A. Bejan, M.R. Errera, Deterministic Tree Networks for Fluid Flow: Geometry for Minimal Flow Resistance Between a Volume and One Point, *Fractals*. 05 (1997) 685–695.
- [49] C. Amador, A. Gavrilidis, P. Angeli, Flow distribution in different microreactor scale-out geometries and the effect of manufacturing tolerances and channel blockage, *Chem. Eng. J.* 101 (2004) 379–390.
- [50] B. Ramos-Alvarado, P. Li, H. Liu, A. Hernandez-Guerrero, CFD study of liquid-cooled heat sinks with microchannel flow field configurations for electronics, fuel cells, and concentrated solar cells, *Appl. Therm. Eng.* 31 (2011) 2494–2507.
- [51] Product Documentation, Fluent 15, ANSYS Inc., (2014). <http://www.ansys.com/Products/Fluids/ANSYS-Fluent>.
- [52] S. O-Charoen, O. Srivannavit, E. Gulari, Simulation and Visualization of Flow Pattern in Microarrays for Liquid Phase Oligonucleotide and Peptide Synthesis, *Biotechnol. Prog.* 23 (2008) 755–761.
- [53] M. Saber, J.M. Commenge, L. Falk, Rapid design of channel multi-scale networks with minimum flow maldistribution, *Chem. Eng. Process. Process Intensif.* 48 (2009) 723–733.
- [54] J.-M. Commenge, M. Saber, L. Falk, Methodology for multi-scale design of isothermal laminar flow networks, *Chem. Eng. J.* 173 (2011) 541–551.
- [55] K.K. Nielsen, K. Engelbrecht, C.R.H. Bahl, The influence of flow maldistribution on the performance of inhomogeneous parallel plate heat exchangers, *Int. J. Heat Mass Transf.* 60 (2013) 432–439.
- [56] H. Liu, P. Li, J. Van Lew, CFD study on flow distribution uniformity in fuel distributors having multiple structural bifurcations of flow channels, *Int. J. Hydrogen Energy*. 35 (2010) 9186–9198.
- [57] Y. Chen, P. Cheng, Heat transfer and pressure drop in fractal tree-like microchannel nets, *Int. J. Heat Mass Transf.* 45 (2002) 2643–2648.
- [58] Y. Chen, P. Cheng, An experimental investigation on the thermal efficiency of fractal tree-like microchannel nets, *Int. Commun. Heat Mass Transf.* 32 (2005) 931–938.
- [59] S.. Senn, D. Poulikakos, Laminar mixing, heat transfer and pressure drop in tree-like microchannel nets and their application for thermal management in polymer electrolyte fuel cells, *J. Power Sources*. 130 (2004) 178–191.
- [60] D. Tondeur, L. Luo, Design and scaling laws of ramified fluid distributors by the

- constructal approach, *Chem. Eng. Sci.* 59 (2004) 1799–1813.
- [61] L. Luo, D. Tondeur, Optimal distribution of viscous dissipation in a multi-scale branched fluid distributor, *Int. J. Therm. Sci.* 44 (2005) 1131–1141.
 - [62] L. Luo, Z. Fan, H. Le Gall, X. Zhou, W. Yuan, Experimental study of constructal distributor for flow equidistribution in a mini crossflow heat exchanger (MCHE), *Chem. Eng. Process. Process Intensif.* 47 (2008) 229–236.
 - [63] M.S. Gandhi, A.A. Ganguli, J.B. Joshi, P.K. Vijayan, CFD simulation for steam distribution in header and tube assemblies, *Chem. Eng. Res. Des.* 90 (2012) 487–506.
 - [64] M. Mohammadi, G.N. Jovanovic, K. V. Sharp, Numerical study of flow uniformity and pressure characteristics within a microchannel array with triangular manifolds, *Comput. Chem. Eng.* 52 (2013) 134–144.
 - [65] COMSOL Multiphysics®. Version 4.2. COMSOL, Inc., (2011). <https://www.comsol.com/comsol-multiphysics>.
 - [66] P. Minqiang, Z. Dehuai, T. Yong, C. Dongqing, CFD-based study of velocity distribution among multiple parallel microchannels, *J. Comput.* 4 (2009) 1133–1138.
 - [67] O. Tonomura, S. Tanaka, M. Noda, M. Kano, S. Hasebe, I. Hashimoto, CFD-based optimal design of manifold in plate-fin microdevices, *Chem. Eng. J.* 101 (2004) 397–402.
 - [68] G. Griffini, A. Gavrilidis, Effect of microchannel plate design on fluid flow uniformity at low flow rates, *Chem. Eng. Technol.* 30 (2007) 395–406.
 - [69] S.A. Solovitz, J. Mainka, Manifold Design for Micro-Channel Cooling With Uniform Flow Distribution, *J. Fluids Eng.* 133 (2011) 051103.
 - [70] M. Pan, Y. Tang, H. Yu, H. Chen, Modeling of velocity distribution among microchannels with triangle manifolds, *AIChE J.* 55 (2009) 1969–1982.
 - [71] M. Pan, Y. Tang, W. Zhou, L. Lu, Flow distribution among microchannels with asymmetrical manifolds, 2007 IEEE Int. Conf. Control Autom. Guangzhou. (2007) 193–197.
 - [72] E. Vásquez-Alvarez, F.T. Degasperri, L.G. Morita, M.R. Gongora-Rubio, R. Giudici, Development of a micro-heat exchanger with stacked plates using LTCC technology, *Brazilian J. Chem. Eng.* 27 (2010) 483–497.
 - [73] J.M. Hassan, T.A. Mohamed, W.S. Mohammed, W.H. Alawee, Modeling the Uniformity of Manifold with Various Configurations, *J. Fluids*. 2014 (2014) 1–8.
 - [74] M. Perlmutter, Inlet and Exit-Header Shapes for Uniform Flow Through a Resistance Parallel to the Main Stream, *J. Basic Eng.* 83 (1961) 361.
 - [75] F.A. Tereda, N. Srihari, B. Sunden, S.K. Das, Experimental Investigation on Port-to-Channel Flow Maldistribution in Plate Heat Exchangers, *Heat Transf. Eng.* 28 (2007) 435–443.

- [76] C.H. Chen, S.P. Jung, S.C. Yen, Flow distribution in the manifold of PEM fuel cell stack, *J. Power Sources*. 173 (2007) 249–263.
- [77] A.B. Datta, A.K. Majumdar, Flow Distribution in Parallel and Reverse Flow Manifolds, *Int. J. Heat Fluid Flow*. 2 (1980) 253–262.
- [78] R.A. Bajura, E.H. Jones, JR., Flow Distribution Manifolds, *J. Fluids Eng.* 98 (1976) 654–665.
- [79] S.H. Choi, S. Shin, Y.I. Cho, The effect of area ratio on the flow distribution in liquid cooling module manifolds for electronic packaging, *Int. Commun. Heat Mass Transf.* 20 (1993) 221–234.
- [80] S.H. Choi, S. Shin, Y.I. Cho, The effects of the Reynolds number and width ratio on the flow distribution in manifolds of liquid cooling modules for electronic packaging, *Int. Commun. Heat Mass Transf.* 20 (1993) 607–617.
- [81] S. Kim, E. Choi, Y.I. Cho, Effect of header shapes on the flow distribution in a manifold for electronic packaging applications, *Int. Commun. Heat Mass Transf.* 22 (1995) 329–341.
- [82] G.F. Jones, N. Lior, Flow distribution in manifolded solar collectors with negligible buoyancy effects, *Sol. Energy*. 52 (1994) 289–300.
- [83] J.C.K. Tong, E.M. Sparrow, J.P. Abraham, Geometric strategies for attainment of identical outflows through all of the exit ports of a distribution manifold in a manifold system, *Appl. Therm. Eng.* 29 (2009) 3552–3560.
- [84] R.Y. Miura, F.C.C. Galeazzo, C.C. Tadini, J.A.W. Gut, The effect of flow arrangement on the pressure drop of plate heat exchangers, *Chem. Eng. Sci.* 63 (2008) 5386–5393.
- [85] B. Prabhakara Rao, B. Sunden, S.K. Das, An Experimental and Theoretical Investigation of the Effect of Flow Maldistribution on the Thermal Performance of Plate Heat Exchangers, *J. Heat Transfer*. 127 (2005) 332.
- [86] B.P. Rao, S.K. Das, An Experimental Study on the Influence of Flow Maldistribution on the Pressure Drop Across a Plate Heat Exchanger, *J. Fluids Eng.* 126 (2004) 680.
- [87] K.L. Wasewar, S. Hargunani, P. Atluri, K. Naveen, CFD Simulation of Flow Distribution in the Header of Plate-Fin Heat Exchangers, *Chem. Eng. Technol.* 30 (2007) 1340–1346.
- [88] L.H. Gunnewiek, E. Brundrett, K.G.T. Hollands, Flow distribution in unglazed transpired plate solar air heaters of large area, *Sol. Energy*. 58 (1996) 227–237.
- [89] G. Mohan, B.P. Rao, S.K. Das, S. Pandiyan, N. Rajalakshmi, K.S. Dhathathreyan, Analysis of Flow Maldistribution of Fuel and Oxidant in a PEMFC, *J. Energy Resour. Technol.* 126 (2004) 262.
- [90] H. Fu, A.P. Watkins, M. Yianneskis, The Effects of Flow Split Ratio and Flow Rate in Manifolds, *Int. J. Numer. Methods Fluids*. 18 (1994) 871–886.

- [91] J.-H. Koh, H.-K. Seo, C.G. Lee, Y.-S. Yoo, H.C. Lim, Pressure and flow distribution in internal gas manifolds of a fuel-cell stack, *J. Power Sources*. 115 (2003) 54–65.
- [92] J.M. Commenge, L. Falk, J.P. Corriou, M. Matlosz, Optimal design for flow uniformity in microchannel reactors, *AIChE J.* 48 (2002) 345–358.
- [93] M. Pan, Y. Tang, L. Pan, L. Lu, Optimal design of complex manifold geometries for uniform flow distribution between microchannels, *Chem. Eng. J.* 137 (2008) 339–346.
- [94] M. Pan, X. Wei, D. Zeng, Y. Tang, Trend prediction in velocity distribution among microchannels based on the analysis of frictional resistances, *Chem. Eng. J.* 164 (2010) 238–245.
- [95] V. Weitbrecht, D. Lehmann, A. Richter, Flow distribution in solar collectors with laminar flow conditions, *Sol. Energy*. 73 (2002) 433–441.
- [96] B. Alm, R. Knitter, J. Haußelt, Development of a Ceramic Micro Heat Exchanger - Design, Construction, and Testing, *Chem. Eng. Technol.* 28 (2005) 1554–1560.
- [97] A.T. Mohammad, S. Bin Mat, M.Y. Sulaiman, K. Sopian, A.A. Al-abidi, Survey of hybrid liquid desiccant air conditioning systems, *Renew. Sustain. Energy Rev.* 20 (2013) 186–200.
- [98] M.R.H. Abdel-Salam, G. Ge, M. Fauchoux, R.W. Besant, C.J. Simonson, State-of-the-art in liquid-to-air membrane energy exchangers (LAMEEs): A comprehensive review, *Renew. Sustain. Energy Rev.* 39 (2014) 700–728.
- [99] H. Hemingson, Preliminary testing for run around heat and moisture exchanger. Canada: Department of Mechanical Engineering, College of Engineering, University of Saskatchewan, summer work report, (2005).
- [100] L.-Z. Zhang, Z.-X. Li, T.-S. Zhong, L.-X. Pei, Flow maldistribution and performance deteriorations in a cross flow hollow fiber membrane module for air humidification, *J. Memb. Sci.* 427 (2013) 1–9.
- [101] Z.-X. Li, L.-Z. Zhang, Flow maldistribution and performance deteriorations in a counter flow hollow fiber membrane module for air humidification/dehumidification, *Int. J. Heat Mass Transf.* 74 (2014) 421–430.
- [102] M.R.H. Abdel-Salam, R.W. Besant, C.J. Simonson, Sensitivity of the performance of a flat-plate liquid-to-air membrane energy exchanger (LAMEE) to the air and solution channel widths and flow maldistribution, *Int. J. Heat Mass Transf.* 84 (2015) 1082–1100.
- [103] M.R.H. Abdel-Salam, R.W. Besant, C.J. Simonson, Performance testing of 2-fluid and 3-fluid liquid-to-air membrane energy exchangers for HVAC applications in cold-dry climates, *Int. J. Heat Mass Transf.* (2016).
- [104] C.M. Huang, S.S. Shy, C.H. Lee, On flow uniformity in various interconnects and its influence to cell performance of planar SOFC, *J. Power Sources*. 183 (2008) 205–213.

- [105] S. Balaji, S. Lakshminarayanan, Improved Design of Microchannel Plate Geometry for Uniform Flow Distribution, *Can. J. Chem. Eng.* 84 (2006) 715–721.
- [106] E.R. Delsman, A. Pierik, M.H.J.M. De Croon, G.J. Kramer, J.C. Schouten, Microchannel Plate Geometry Optimization for Even Flow Distribution at High Flow Rates, *Chem. Eng. Res. Des.* 82 (2004) 267–273.
- [107] M. Lu, C. Wang, Effect of the Inlet Location on the Performance Parallel-channel Cold-plate, *IEEE Trans. Components Packag. Technol.* 29 (2006) 30–38.
- [108] D. Bogojevic, K. Sefiane, A.J. Walton, J.R.E. Christy, G. Cummins, H. Lin, Investigation of Flow Distribution in Microchannels Heat Sinks, *Heat Transf. Eng.* 30 (2009) 1049–1057.
- [109] D. Zeng, M. Pan, Y. Tang, Qualitative investigation on effects of manifold shape on methanol steam reforming for hydrogen production, *Renew. Energy.* 39 (2012) 313–322.
- [110] D. Kim, C.H. Yu, S.H. Yoon, J.S. Choi, Effects of manifold geometries on flow distribution to parallel microchannels, *J. Mech. Sci. Technol.* 25 (2011) 3069–3074.
- [111] A. Jiao, R. Zhang, S. Jeong, Experimental investigation of header configuration on flow maldistribution in plate-fin heat exchanger, *Appl. Therm. Eng.* 23 (2003) 1235–1246.
- [112] Z. Zhang, Y. Li, CFD simulation on inlet configuration of plate-fin heat exchangers, *Cryogenics (Guildf).* 43 (2003) 673–678.
- [113] M.A. Habib, R. Ben-Mansour, S.A.M. Said, M.S. Al-Qahtani, J.J. Al-Bagawi, K.M. Al-Mansour, Evaluation of flow maldistribution in air-cooled heat exchangers, *Comput. Fluids.* 38 (2009) 677–690.
- [114] J. Wen, Y. Li, Study of flow distribution and its improvement on the header of plate-fin heat exchanger, *Cryogenics (Guildf).* 44 (2004) 823–831.
- [115] J. Wen, Y. Li, A. Zhou, K. Zhang, An experimental and numerical investigation of flow patterns in the entrance of plate-fin heat exchanger, *Int. J. Heat Mass Transf.* 49 (2006) 1667–1678.
- [116] J. WEN, Y. LI, A. ZHOU, Y. Ma, PIV investigations of flow patterns in the entrance configuration of plate-fin heat exchanger, *Chinese J. Chem. Eng.* 14 (2006) 15–23.
- [117] S. Lalot, P. Florent, S.K. Lang, A.E. Bergles, Flow maldistribution in heat exchangers, *Appl. Therm. Eng.* 19 (1999) 847–863.
- [118] STAR-CD, CD-adapco, (2016). <http://mdx.plm.automation.siemens.com/star-cd>.
- [119] L. Sheik Ismail, C. Ranganayakulu, R.K. Shah, Numerical study of flow patterns of compact plate-fin heat exchangers and generation of design data for offset and wavy fins, *Int. J. Heat Mass Transf.* 52 (2009) 3972–3983.
- [120] A.B. Datta, A.K. Majumdar, A calculation procedure for two phase flow distribution in manifolds with and without heat transfer, *Int. J. Heat Mass Transf.* 26 (1983) 1321–1328.

- [121] P. Balasubramanian, S.G. Kandlikar, Experimental Study of Flow Patterns, Pressure Drop, and Flow Instabilities in Parallel Rectangular Minichannels, *Heat Transf. Eng.* 26 (2005) 20–27.
- [122] P. Rao Bobbili, B. Sunden, S.K. Das, Thermal analysis of plate condensers in presence of flow maldistribution, *Int. J. Heat Mass Transf.* 49 (2006) 4966–4977.
- [123] M. Martin, C. Patton, J. Schmitt, S. V. Apte, Direct Simulation Based Model-Predictive Control of Flow Maldistribution in Parallel Microchannels, *J. Fluids Eng.* 131 (2009) 111201.
- [124] A. Marchitto, F. Devia, M. Fossa, G. Guglielmini, C. Schenone, Experiments on two-phase flow distribution inside parallel channels of compact heat exchangers, *Int. J. Multiph. Flow.* 34 (2008) 128–144.
- [125] A. Marchitto, M. Fossa, G. Guglielmini, Distribution of air–water mixtures in parallel vertical channels as an effect of the header geometry, *Exp. Therm. Fluid Sci.* 33 (2009) 895–902.
- [126] A. Marchitto, M. Fossa, G. Guglielmini, The effect of the flow direction inside the header on two-phase flow distribution in parallel vertical channels, *Appl. Therm. Eng.* 36 (2012) 245–251.
- [127] J.K. Lee, S.Y. Lee, Distribution of two-phase annular flow at header–channel junctions, *Exp. Therm. Fluid Sci.* 28 (2004) 217–222.
- [128] M. Premkumar, G. Mahesh, Distribution analysis of Fluid in circular and square header, *Int. J. Adv. Mar. Eng. Renewables.* 1 (2015) 51–57.
- [129] M.K. Bassiouny, H. Martin, Flow distribution and pressure drop in plate heat exchangers-I U-type arrangement, *Chem. Eng. Sci.* 39 (1984) 693–700.
- [130] A. Acrivos, B.D. Babcock, R.L. Pigford, Flow distributions in manifolds, *Chem. Eng. Sci.* 10 (1959) 112–124.
- [131] T. KUBO, T. UEDA, On the Characteristics of Divided Flow and Confluent Flow in Headers, *Bull. JSME.* 12 (1969) 802–809.
- [132] A.K. Majumdar, Mathematical Modelling of Flows in Dividing and Combining Flow Manifold., *Appl. Math. Model.* 4 (1980) 424–432.
- [133] R. Pigford, M. Ashraf, Y. Miron, Flow distribution in piping manifolds, *Ind. Eng. Chem. Fundam.* 22 (1983) 463–471.
- [134] M.K. Bassiouny, H. Martin, Flow distribution and pressure drop in plate heat exchangers-II Z-type arrangement, *Chem. Eng. Sci.* 39 (1984) 701–704.
- [135] P.I. Shen, The Effect of Friction on Flow Distribution in Dividing and Combining Flow Manifolds, *J. Fluids Eng.* 114 (1992) 121–123.
- [136] N.P. Kikas, Laminar flow distribution in solar systems, *Sol. Energy.* 54 (1995) 209–217.
- [137] E.M. Sparrow, J.C.K. Tong, J.P. Abraham, A Quasi-Analytical Method for Fluid Flow in a Multi-Inlet Collection Manifold, *J. Fluids Eng.* 129 (2007) 579.

- [138] L. Fang, L. Young-hao, Y. Shi-ming, Analytical and Experimental Investigation of Flow Distribution in Manifolds for Heat Exchangers*, J. Hydrodyn. Ser. B. 20 (2008) 179–185.
- [139] S. Maharudrayya, S. Jayanti, A.P. Deshpande, Flow distribution and pressure drop in parallel-channel configurations of planar fuel cells, J. Power Sources. 144 (2005) 94–106.
- [140] J. Wang, Theory of flow distribution in manifolds, Chem. Eng. J. 168 (2011) 1331–1345.
- [141] J. Wang, Pressure drop and flow distribution in parallel-channel configurations of fuel cells: U-type arrangement, Int. J. Hydrogen Energy. 33 (2008) 6339–6350.
- [142] J. Wang, Pressure drop and flow distribution in parallel-channel configurations of fuel cells: Z-type arrangement, Int. J. Hydrogen Energy. 35 (2010) 5498–5509.
- [143] J. Wang, H. Wang, Discrete approach for flow field designs of parallel channel configurations in fuel cells, Int. J. Hydrogen Energy. 37 (2012) 10881–10897.
- [144] J. Wang, Theory and practice of flow field designs for fuel cell scaling-up: A critical review, Appl. Energy. 157 (2015) 640–663.
- [145] J. Wang, H. Wang, Discrete method for design of flow distribution in manifolds, Appl. Therm. Eng. 89 (2015) 927–945.
- [146] O.K. Krasnikova, Double-tube coil heat exchangers of cryogenic helium units, Chem. Pet. Eng. 44 (2008) 374–381.
- [147] K.W. Cowans, A countercurrent heat exchanger that compensates automatically for maldistribution of flow in parallel channels, in: Cryog. Eng. Conf. Atlanta, Ga., 1974: pp. 437–444.
- [148] R.B. Fleming, The effect of flow distribution in parallel channels of counterflow heat exchangers, in: Adv. Cryog. Eng., Springer US, Boston, MA, 1967: pp. 352–362.
- [149] K. Chowdhury, S. Sarangi, Effect of flow maldistribution on multipassage heat exchanger performance, Heat Transf. Eng. 6 (1985) 45–54.
- [150] T.W. Ambrose, J.G. Knudsen, Local shell-side heat transfer coefficients in baffled tubular heat exchangers, AIChE J. 4 (1958) 332–337.
- [151] K.S. Lee, J.G. Knudsen, Local shell-side heat transfer coefficients and pressure drop in a tubular heat exchanger with orifice baffles, AIChE J. 6 (1960) 669–675.
- [152] W. Zeng, Z. Zhang, Experimental Investigation on the Performances on the Shell Side of Shell-and-Tube Heat Exchangers with Multiparallel Channels, Ind. Eng. Chem. Res. 50 (2011) 13545–13553.
- [153] H. Li, V. Kottke, Visualization and determination of local heat transfer coefficients in shell-and-tube heat exchangers for staggered tube arrangement by mass transfer measurements, Exp. Therm. Fluid Sci. 17 (1998) 210–216.
- [154] J.A. Perez, E.M. Sparrow, Determination of Shell-Side Heat Transfer Coefficients

- by the Naphthalene Sublimation Technique, *Heat Transf. Eng.* 6 (1985) 19–30.
- [155] A.P. Colburn, A method of correlating forced convection heat-transfer data and a comparison with fluid friction, *Int. J. Heat Mass Transf.* 7 (1964) 1359–1384.
 - [156] T.H. Chilton, A.P. Colburn, Mass transfer (absorption) coefficients prediction from data on heat transfer and fluid friction, *Ind. Eng. Chem.* 26 (1934) 1183–1187.
 - [157] R.L. Webb, A critical evaluation of analytical solutions and reynolds analogy equations for turbulent heat and mass transfer in smooth tubes, *Wärme- Und Stoffübertragung.* 4 (1971) 197–204.
 - [158] S.P. Mahulikar, H. Herwig, Fluid friction in incompressible laminar convection: Reynolds' analogy revisited for variable fluid properties, *Eur. Phys. J. B.* 62 (2008) 77–86.
 - [159] Z. Duan, B. He, Extended Reynolds analogy for slip and transition flow heat transfer in microchannels and nanochannels, *Int. Commun. Heat Mass Transf.* 56 (2014) 25–30.
 - [160] H.-T. Lin, The analogy between fluid friction and heat transfer of laminar forced convection on a flat plate, *Wärme- Und Stoffübertragung.* 29 (1994) 181–184.
 - [161] H.-T. Lin, L.-K. Lin, Similarity solutions for laminar forced convection heat transfer from wedges to fluids of any Prandtl number, *Int. J. Heat Mass Transf.* 30 (1987) 1111–1118.
 - [162] C. Runge, Ueber die numerische Auflösung von Differentialgleichungen, *Math. Ann.* 46 (1895) 167–178.
 - [163] W. Kutta, Beitrag zur näherungsweise Integration von Differentialgleichungen, *Z. Math. Und Phys.* 46 (1901) 435–453.
 - [164] B.J. Belnap, J.A. Van Rij, P.M. Ligrani, A Reynolds analogy for real component surface roughness, *Int. J. Heat Mass Transf.* 45 (2002) 3089–3099.
 - [165] A.S. Dalkilic, B. Kundu, S. Wongwises, An experimental investigation of the Reynolds analogy and its modifications applied to annular condensation laminar flow of R134a in a vertical tube, *Arab. J. Sci. Eng.* 38 (2013) 1493–1507.
 - [166] K.S. Kulkarni, U. Madanan, R. Mittal, R.J. Goldstein, Experimental validation of heat/mass transfer analogy for two-dimensional laminar and turbulent boundary layers, *Int. J. Heat Mass Transf.* 113 (2017) 84–95.
 - [167] R.J. Goldstein, H.H. Cho, A review of mass transfer measurements using naphthalene sublimation, *Exp. Therm. Fluid Sci.* 10 (1995) 416–434.
 - [168] G.I. Gimbutis, Analogy between the processes of momentum transfer and heat transfer in turbulent flow of a liquid in a tube and in a gravitational film, *J. Eng. Phys.* 34 (1978) 645–651.
 - [169] V.F. Potemkin, Analogy between turbulent momentum and heat transfer under complex conditions, *J. Eng. Phys.* 49 (1985) 1045–1050.
 - [170] S. Han, R.J. Goldstein, The heat/mass transfer analogy for a simulated turbine blade,

- Int. J. Heat Mass Transf. 51 (2008) 5209–5225.
- [171] H.-J. Steeman, A. Janssens, M. De Paepe, On the applicability of the heat and mass transfer analogy in indoor air flows, *Int. J. Heat Mass Transf.* 52 (2009) 1431–1442.
 - [172] Z. Wang, G. Li, J. Xu, J. Wei, J. Zeng, D. Lou, et al., Analysis of fouling characteristic in enhanced tubes using multiple heat and mass transfer analogies, *Chinese J. Chem. Eng.* 23 (2015) 1881–1887.
 - [173] A.G. Laptev, E.A. Lapteva, The model of heat and mass transfer in rough and irrigated ducts, *Thermophys. Aeromechanics*. 22 (2015) 435–440.
 - [174] A.G. Laptev, E.A. Lapteva, External and internal problems of modeling the heat and mass transfer coefficients at particles motion in liquids, *Thermophys. Aeromechanics*. 24 (2017) 249–258.
 - [175] S. Churchill, Critique of the classical algebraic analogies between heat, mass, and momentum transfer, *Ind. Eng. Chem. Res.* 36 (1997) 3866–3878.
 - [176] F.P. Incropera, D.P. DeWitt, T. Bergman, A. Lavine, *Fundamentals of heat and mass transfer*, 6th ed., John Wiley & Sons Inc., 2006.
 - [177] MATLAB 2016b, The MathWorks Inc., Natick, MA, (2014). <https://www.mathworks.com/products/matlab.html>.
 - [178] S. Chandel, R.D. Misal, Y.G. Beka, Convective Heat Transfer through Thick-Walled Pipe, *Procedia Eng.* 38 (2012) 405–411.
 - [179] W.M. Kays, M.E. Crawford, *Convective heat and mass transfer*, 3rd ed., McGraw-Hill, Inc., New York City, New York, 1993.
 - [180] F.M. White, *Viscous fluid flow*, 2nd ed., McGraw-Hill, Inc., 1991.
 - [181] L.F. Moody, Friction Factors for Pipe Flow, *Trans. ASME*. 66 (1944) 671–684.
 - [182] Sundrum Solar, <http://sundrumsolar.com/index.php/products>. Accessed on 15 October 2011.,.
 - [183] Y. Cengel, J. Cimbala, *Fluid Mechanics: Fundamentals and Applications*, 2013.
 - [184] O.K. Siddiqui, Analytical investigation of flow distribution in heat exchanger manifolds, PhD thesis, KFUPM, 2018.
 - [185] A. Sciacchitano, B. Wieneke, F. Scarano, PIV uncertainty quantification by image matching, *Meas. Sci. Technol.* 24 (2013).
 - [186] A. Sciacchitano, B. Wieneke, PIV uncertainty propagation, *Meas. Sci. Technol.* 27 (2016).

VITA

Name Osman Kaleem Siddiqui

Nationality Pakistan

Date of Birth December 9, 1987

Email osmankaleem@gmail.com

Permanent Address House No. 40, Mehran Block, Allama Iqbal Town, Lahore
54570, Pakistan

Academic Background

M.S (Mechanical Engineering), May 2013,
King Fahd University of Petroleum & Minerals,
Dhahran, Saudi Arabia.

B.Sc. (Mechanical Engineering), August 2009,
University of Engineering and Technology, Lahore, Pakistan.

Publications:

- [1] **O.K. Siddiqui**, S.Z. Shuja, S.M. Zubair, Assessment of thermo-fluid analogies for different flow configurations: the effect of Prandtl number, and laminar-to-turbulent flow, Int. J. Therm. Sci. 129 (2018) 145–170. (Impact Factor: **3.361**)
- [2] **O.K. Siddiqui**, S.Z. Shuja, S.M. Zubair, Influence of manifold heating and split flow on thermal-hydraulic characteristics: Application to heat exchangers having

- non-axisymmetric flow, *Appl. Therm. Eng.* 122 (2017) 768–784. (Impact Factor: **3.771**)
- [3] **O. K. Siddiqui**, S.M. Zubair, Efficient energy utilization through proper design of microchannel heat exchanger manifolds: A comprehensive review, *Renew. Sustain. Energy. Rev.*, 74 (2017) 969-1002. (Impact Factor: **9.184**)
 - [4] **O.K. Siddiqui**, M.H. Sharqawy, M.A. Antar, S.M. Zubair, Performance evaluation of variable pressure humidification-dehumidification systems, *Desalination* 409 (2017) 171-182. (Impact Factor: **6.603**)
 - [5] B.S. Yilbas, M.K. Anwar, S.Z. Shuja, **O.K. Siddiqui**, Thermal Analysis of Mobile Thermal Battery with Aluminum Mesh Subjected to Solar-Concentrated Heating, *J. Energ. Eng.* 143 (2017). (Impact Factor: **1.944**)
 - [6] **O.K. Siddiqui**, B.S. Yilbas, S.Z. Shuja, E. Wang, Volumetric solar absorption in a channel with presence of phase change material in a carrier fluid, *Appl. Therm. Eng.* 102 (2016) 1059-1068. (Impact Factor: **3.771**)
 - [7] **O.K. Siddiqui**, B.A. Qureshi, S.M. Zubair, Dew point refrigeration systems: Normalized sensitivity analysis and impact of fouling *Int. J. Refrig.* 55 (2015) 60-71. (Impact Factor: **3.233**)
 - [8] B.S. Yilbas, **O.S. Kaleem**, Performance Characteristics of a Volumetric Solar Receiver: Presence of an Absorber Plate with a Selective Surface, *Numer. Heat Tr. A-Apl.* 67 (2015) 992-1009. (Impact Factor: **2.409**)
 - [9] S.A. Tirmizi, **O.K. Siddiqui**, P. Gandhidasan, S.M. Zubair, Performance analysis of an ejector cooling system with a conventional chilled water system, *Appl. Therm. Eng.* 66 (2014) 113–121. (Impact Factor: **3.771**)
 - [10] **O.K. Siddiqui**, B.S. Yilbas, Thermal characteristics of a volumetric solar absorption system, *Int. J. Energy Res.* 38 (2014) 581-591. (Impact Factor: **3.009**)
 - [11] **O.K. Siddiqui**, B.S. Yilbas, Solar absorption heating in horizontal channel: Influence of absorbing plate location on thermal performance, *Energy Convers. Manag.* 74 (2013) 140–148. (Impact Factor: **6.377**)